Actuator line modelling of wind turbines and their wakes



Markella Zormpa

Balliol College

University of Oxford

A thesis submitted for the degree of

Doctor of Philosophy

Hilary Term 2024

Acknowledgements

First and foremost I'd like to thank my supervisors, Prof. Richard Willden and Dr. Christopher Vogel. Their supervision has allowed me to develop a range of skills and grow as a researcher. I deeply appreciate their consistent guidance and support at every stage of this degree and I am grateful that my DPhil has been such an intellectually stimulating and enjoyable experience.

I would also like to acknowledge and thank my industrial sponsors from RWE Dr. Kester Gunn and Christopher Rodaway. Our bi-annual meetings have always provided a breath from my academic focus. They've made me think of the industrial implications of my research findings as well as given me interesting inputs from an alternative perspective.

Another collaboration that enriched my DPhil experience was that with Prof. Esteban Ferrer and Prof. Soledad Le Clainche from Universidad Politécnica de Madrid. I'm grateful to have been introduced to the world of data decomposition methods and for their time and supervision during and after my visit to UPM. Thanks to the ETSIAE-UPM CFD group students as well for all the fun times during my stay there.

I would like to gratefully acknowledge Richard Willden's EPSRC Advanced Fellowship EP/R007322/1 and RWE Renewables for providing full funding for my DPhil research. I'd also like extend my acknowledgements to the project HPC-EUROPA3 (INFRAIA-2016-1-730897), with the support of the EC Research Innovation Action under the H2020 Programme, for fully funding my 3-month visit to UPM. Moreover, Balliol College is gratefully acknowledged for financially supporting my participation to the WAKE conference in Sweden, during the summer of 2023. I'd finally like to thank the ARC support team in Oxford for being always helpful over the course of my DPhil as well as Alison May for her consistent support to our group.

I'd like to deeply thank Dr. Federico Zilic de Arcos, who has been a great mentor for the past years. Our many conversations on wind turbine modeling have been fruitful. Importantly, I thank him for providing me valuable guidance and emotional encouragement over the years whenever I needed it.

Dr. Xiaosheng (Shaun) Chen is gratefully acknowledged as he has been supportive from the start of my DPhil. His contribution to the entire group in providing technical guidance and CFD support is significant. I'd also like to thank Dr. Guiyu Cao for our fantastic chats on turbulence and beyond.

The entire Tidal and Wind Energy group has been a great environment to work in. I'm grateful to all the academics for their inputs and feedback on my research. It's been a real pleasure following the research progress of all my fellow DPhil candidates.

Another incredible community was the WAMESS CDT. Thank you to all the academics that taught us; it was invaluable being exposed to such a variety of wind and marine energy aspects. Many great memories shared with the CDT cohort during the months in Glasgow; it's been a pleasure catching up with everyone's research since then. Special kudos to Laurence Morgan for being an amazing colleague and friend from the first week in Scotland to date.

Other amazing groups: Room 11. Special love for Kathy Wen, Yixiong Jing, Zhengyou Zhang, and our incredible discussions inside and outside of Room 11. Packed lunch group also without fail made weekdays more fun.

Outside of engineering, I'd like to acknowledge my amazing Oxford family for making these past years exceptionally fun, from early covid days to our latest trip and and beyond. Some great years shared with Gabe, Lizzie, Ziski, Jake, Naomi, Lampros and Shobhan. I'm grateful for my friendship with Lampros Bisdounis, which, in addition to the great times, has been an invaluable source of support and comfort in Oxford from day one. Finally, I'd like to deeply thank Shobhan Dhir for all the love and support, the hilarious times we shared up to the very end of our DPhils, and a genuinely unique friendship which only grows stronger every year.

Even from a distance, all my Athens friends have been incredibly supportive the past years. Much love to my girls for inspiring me everyday with their incredible talent and kindness: Alina, Marilena, Irini, Annie, Alexandra, Stella.

Finally I'd like to thank my family, the strongest constant in my life and the reason I can do what I love. I'm incredibly grateful to my mother Lia, my father Giannis, and my brother Nikos for being an endless source of love, support, and inspiration during the PhD and throughout my entire life.

Abstract

Wind energy has a central role in the green energy transition, with a projected surge in installed capacity in the coming decades. Understanding and modelling wind turbine aerodynamics and their wakes is key for the economical deployment of wind energy at large scale. This is only possible if high-fidelity flow field data are available, often obtained by numerically simulating rotors using high resolution methods. One such simulation method is the actuator line method (ALM), which is the focus of this thesis. This thesis addresses evaluating and improving the numerical efficiency and accuracy of the ALM and explores the potential to use the generated high-fidelity data to validate and inspire low-fidelity models.

The ALM uses a virtual representation of each turbine blade, avoiding the complex and costly processes of meshing the blade surface. This thesis first addresses the robustness of the ALM in the prediction of rotor forces. An important step in any ALM implementation is the flow sampling: the process of obtaining a characteristic local velocity vector at each collocation point of the actuator line in order to calculate blade forces through reference to pre-defined aerofoil coefficients. It is shown that the widely-used method of sampling the flow at the collocation point that lies along the actuator line introduces a large dependence of the rotor forces on the time step. This has given rise to stringent time step limitations, typically employed by ALM practitioners. Using a line average sampling method that samples the flow at locations circumscribing the collocation point and outside the region where computed blade forces are imposed, improves robustness of predicted rotor power and thrust across a large range of time steps. This enables the use of larger time steps than those typically used in collocation point sampling ALM simulations, improving the numerical efficiency of the ALM.

The ALM is embedded in a large eddy simulation (LES) solver to perform ALM-LES of an experimental rotor and its wake. The numerical sensitivity of the rotor power and thrust to ALM parameters is first established. The sensitivity of the predicted wake on the mesh size is tested, with highly-resolved LES simulations used as a reference. It is demonstrated that in cases where the mesh is insufficient to resolve the tip vortices, the vortex breakdown mechanism is altered, with lower resolution simulations resulting in vortices merging into shear layers that then themselves develop instabilities.

The importance of the turbine support structure (nacelle and tower) for accurately simulating the turbine wake is explored. Three methods for introducing low-fidelity representation of the support structures are assessed for their ability to capture the aerodynamic interaction between the support structure and the rotor wake observed in experimental measurements. Good agreement with experiments is achieved when a low-resolution body-fitted representation of the support structure is used. Additionally, the effect that the support structure has on the far wake aerodynamics is investigated: when including the tower, the wake centre typically drops with streamwise distance. This deviation from an axisymmetric wake profile, as commonly assumed in engineering models, is quantified by comparing a Gaussian wake model against the ALM-LES data.

In order to explore the potential of reducing the dimensionality and numerical cost of simulating wake flows, the ALM-LES spatio-temporal flow data are analysed using a dynamic mode decomposition (DMD) algorithm. The merger between two turbine wakes in tandem is explored: the lower frequency background flow due to the upstream turbine is found to be more dynamically persistent, dominating local rotor dynamics.

This work evaluates and extends actuator line modelling of wind turbines and their support structures for the simulation of wind turbine wake aerodynamics. It thus supports more efficient, robust, and accurate turbine and wake modelling for wind energy research.

Nomenclature

Turbine Geometry

A	Rotor area
D	Rotor diameter
D_{nac}	Nacelle diameter
D_{tow}	Tower diameter
N_b	Number of blades
R	Rotor radius
z_h	Hub height
σ	Solidity

Velocity Triangle and Wind Turbine metrics

$\mathbf{a}$	Axial induction factor
$\mathbf{a}'$	Tangential induction factor
c	Chord
C_l	Lift coefficient
C_d	Drag coefficient
C_P	Power coefficient
C_T	Thrust coefficient
d	Sectional drag force
F	Blade force
F_{ax}	Axial force per unit span
F_{tan}	Tangential force per unit span
l	Sectional lift force
P	Power
Q	Blade torque
r	Local radius

T . . . . . Thrust

T . . . . . Rotational period

U_∞ . . . . . Freestream velocity

V . . . . . Incident velocity

V_{rel} . . . . . Relative velocity

W . . . . . Induced velocity

$\hat{x}$ . . . . . Axial direction

a . . . . . Angle of attack

β . . . . . Twist angle

$\hat{\theta}$ . . . . . Tangential direction

λ . . . . . Tip-speed ratio

ϕ . . . . . Flow angle

ω . . . . . Angular speed

Navier-Stokes Equations

F_i . . . . . External force vector component

L . . . . . Characteristic length scale

p . . . . . Pressure

Re . . . . . Reynolds number

U . . . . . Characteristic velocity

u_i . . . . . Velocity vector component

$x_i, \quad i = 1, 2, 3$. (x, y, z) 3D position vector

ν . . . . . Kinematic viscosity

ρ . . . . . Density

RANS & URANS: selected variables

$\bar{u}_i$ . . . . . Mean velocity component

$\bar{p}$ . . . . . Mean pressure

u_i' . . . . . Instantaneous velocity component

p' . . . . . Instantaneous pressure

$\overline{u_i' u_j'}$ . . . . . Reynolds stress tensor

δ_{ij} . . . . . Kronecker delta

ν_t . . . . . Eddy viscosity

k	Turbulent kinetic energy
ϵ	TKE dissipation rate
ω	Specific TKE dissipation rate
C_μ	Eddy viscosity model coefficient
Δx	Cell edge length
Δt	Time step

LES

C_S	Smagorinsky coefficient
k_{sgs}	Subgrid-scale kinetic energy
$\tilde{p}$	Resolved pressure
p''	Subgrid-scale pressure
$\tilde{S}_{ij}$	Strain rate tensor
$\tilde{u}_i$	Resolved velocity component
u_i''	Subgrid-scale velocity component
Δ	Filter width
ν_{sgs}	Subgrid-scale viscosity
τ_{ij}^{sgs}	Subgrid-scale stress tensor
$\tau_{ij}^{sgs,dev}$	Subgrid-scale stress tensor, deviatoric part

Chapter 3

Co	Courant number
N	Number of sampling points for LAS
N_x	Number of cells per rotor diameter
N_t	Number of time steps per rotor rotation
N_ε	Smearing radius to cell size ratio
r_s	Sampling radius of LAS
r_g	Gaussian smearing kernel radius
R_{core}	Lamb-Oseen viscous vortex core radius
$\langle U_x \rangle_{disc}$	Disc-averaged streamwise velocity
$\langle U_x \rangle_r$	Circumference-averaged streamwise velocity at a radius r
Γ	Circulation
Δs	Tip distance travelled in one time step

ε . . . . . Smearing parameter

ε_{rel} . . . . . Relative error

Chapter 4

L . . . . . Turbulence length scale

TI . . . . . Turbulence intensity

x/D . . . . . Non-dimensional streamwise location

y/R . . . . . Non-dimensional spanwise location

$(z - z_h)/R$ . . . Non-dimensional wall-normal location

γ . . . . . TKE ratio

δ . . . . . Percentage difference

Chapter 5

C_T^* . . . . . AD calibrated thrust coefficient

$(C_Y(x), C_Z(x))$. Wake centreline

f . . . . . CB volume fraction

k^* . . . . . Wake expansion parameter of the BP model

L . . . . . CB characteristic length scale

s_p . . . . . CB momentum source coefficient

u^* . . . . . CB characteristic velocity

$\mathbf{u}_m$ . . . . . AD monitor point velocity vector

$\mathbf{u}_0$ . . . . . AD disc averaged velocity

$U_{bypass}(x)$ . . . . Mean bypass flow velocity

U_{CFD} . . . . . Mean velocity of the ALM-LES simulation

U_{Gauss} . . . . . Mean velocity estimate of the Gaussian model

β . . . . . Parameter of the BP model

$\langle\varepsilon(U)\rangle_W$ . . . . Wake-averaged mean velocity relative error

$\varepsilon(\langle U\rangle_W)$ . . . . Relative error of the wake-averaged mean velocity

$\langle\varepsilon(U^3)\rangle_D$ . . . . Disc-averaged mean kinetic energy relative error

$\varepsilon(\langle U^3\rangle_D)$ . . . Relative error of the disc-averaged mean kinetic energy

Chapter 6: selected variables

K . . . . . Number of snapshots

$\mathbf{u}_m(\mathbf{x})$ . . . . . Mode m

α_m	Amplitude of mode m
δ_m	Growth rate of mode m
ε_1	Truncation error
ε_2	Truncation error
ω_m	Frequency of mode m

Contents

Nomenclature **vii**

List of Figures **xvii**

1 Introduction **1**
1.1 Towards a sustainable future 1
1.2 A brief history of wind energy 4
1.3 Wind turbine wakes 6
1.4 Research objectives 7
1.4.1 ALM model parameters 8
1.4.2 Evaluation of mesh resolution for ALM-LES wake simulations 8
1.4.3 Effect of the turbine support structures on wakes 8
1.4.4 Identification of dominant flow features in wind turbine wakes 9
1.5 Thesis Layout 9

2 Theory, modelling methods and rotor geometries **11**
2.1 Aerodynamic structure of wind turbine wakes 12
2.1.1 Near wake 12
2.1.2 Far wake 14
2.1.3 Ambient flow 15
2.2 Parameterisation of wind rotors in CFD simulations 17
2.2.1 Blade-resolved simulations 19
2.2.2 Actuator methods 20
2.3 The Actuator Line Method 23
2.3.1 Step 1: Flow sampling 26
2.3.2 Step 2: Force calculation 29
2.3.3 Step 3: Force smearing 34
2.4 CFD solvers 36
2.4.1 Governing equations 36
2.4.2 RANS &URANS 37
2.4.3 Large Eddy Simulation 41
2.5 Rotor descriptions 44

2.5.1 NTNU rotor 44
2.5.2 MEXICO rotor 46
2.5.3 Sch15b rotor 47
2.6 Summary 48

3 The effect of flow sampling in the robustness of the ALM 51
3.1 Abstract 51
3.2 Introduction 52
3.3 Flow sampling methods 57
3.3.1 Point sampling 58
3.3.2 Volume sampling 60
3.3.3 Line sampling 62
3.4 Time step in ALM simulations 63
3.4.1 Streamwise CFL condition 63
3.4.2 Tangential CFL condition and the ALM time step constraint 64
3.4.3 Relationship between the ALM time step condition and streamwise CFL constraint 65
3.5 Turbine Descriptions 65
3.6 Numerical Solution 68
3.6.1 Numerical and ALM set-up 68
3.6.2 Mesh size guidelines in ALM simulations 69
3.6.3 Mesh sensitivity analysis 71
3.7 Results 73
3.7.1 Power and thrust coefficients 74
3.7.2 Spanwise force distributions 78
3.7.3 Instantaneous velocity 80
3.8 Conclusions 88
3.9 Authorship statement 92

4 ALM-LES of wind turbine wakes 93
4.1 ALM-LES simulations of wind turbine wakes 94
4.1.1 LES: numerical solver, boundary conditions and mesh topology 94
4.1.2 ALM: methods and parameter selection 96
4.2 Spatial and temporal resolution of ALM-LES 101
4.2.1 Simulation suite 102
4.2.2 Convergence 103
4.2.3 Integrated metrics 104
4.2.4 Instantaneous flow field 105
4.2.5 Flow statistics 108
4.3 Synthetic turbulence 113

4.3.1 Turbulent inflow boundary conditions for LES 114
4.3.2 DFSEM: simulations of an empty domain 116
4.3.3 No- vs low- inflow turbulence for a single rotor wake 117
4.4 Summary and conclusions 121

5 Support structures in ALM-LES simulations 123
5.1 The effect of the support structure on wind energy aerodynamics . . 124
5.1.1 Rotor scale 124
5.1.2 Near wake 125
5.1.3 Far wake 127
5.1.4 Wind farm aerodynamics 127
5.2 Support structure modelling in ALM-LES simulations 128
5.2.1 Review of support structure modelling methods 128
5.2.2 Support structure models 130
5.2.3 Support structure simulation suite 136
5.2.4 Rotor and support structure axial force 137
5.2.5 Instantaneous flow 139
5.2.6 Meshed support structure influence on near wake predictions 141
5.2.7 Nacelle modelling effect on wake predictions 146
5.2.8 Tower modelling effect on wake predictions 147
5.3 Assessment of the Gaussian far wake assumption 149
5.3.1 Description of the datasets 150
5.3.2 Gaussian fitting of the ALM-LES wake 152
5.3.3 Gaussian wake modelling without centreline adjustment . . . 157
5.3.4 Gaussian wake modelling with centreline adjustment 159
5.4 Summary and conclusions 161

6 Dynamic Mode Decomposition of wind turbine wakes 163
6.1 Data decomposition methods in wind energy 164
6.2 Higher Order Dynamic Mode Decomposition 166
6.2.1 Algorithm 167
6.2.2 Calibration 170
6.3 Dynamic mode decomposition of merging wind turbine wakes . . . 171
6.3.1 Abstract 171
6.3.2 Introduction 171
6.3.3 Numerical simulations 174
6.3.4 Higher Order DMD 178
6.3.5 HODMD of two flows: a single and a downstream rotor wake 180
6.3.6 Conclusions 184
6.3.7 Authorship statement 186

7 Conclusions and future work **187**
7.1 Conclusions 187
7.2 Future work 190

Appendices

A Scaling test of OpenFOAM in ARC **195**

B Self-convergence of the line average sampling method **197**

C Extracting lift and drag coefficients from RANS BR simulations **199**

D Characterisation of the ALM viscous vortex **201**

E Robustness of flow sampling methods for ALM-LES **205**

References **207**

List of Figures

1.1 Electricity mix for the World and the UK. 2
1.2 Cumulative renewable electricity capacity up to 2030. 3
1.3 History of wind energy in pictures. 4

2.1 Characteristic vorticity magnitude contour of a wind turbine wake. 12
2.2 CFD methods for wind energy modelling. 18
2.3 Schematic of an actuator line. 24
2.4 Actuator line method flow chart. 26
2.5 Velocity triangle incident to a blade section. 27
2.6 Tip correction functions used in the ALM. 33
2.7 Integral of the Gaussian kernel for different N_ε values. 35
2.8 Illustration of the TKE spectra of a turbulent flow. 42
2.9 Schematic of the NTNU wind tunnel for BT1 and BT2. 45
2.10 Chord and twist distributions for NTNU, MEXICO and Sch15b rotors. 45
2.11 NTNU: 3D render. 46
2.12 MEXICO: 3D render. 47
2.13 Sch15b: 3D render. 48

3.1 Velocity triangle incident to a blade section. 58
3.2 Schematic of the flow sampling method types. 59
3.3 Recommended N_t values against N_x given the CFL condition 66
3.4 Chord and twist distributions for MEXICO and Sch15b 67
3.5 Render comparison between MEXICO and Sch15b 67
3.6 Mesh topology for MEXICO rotor simulations. 69
3.7 MEXICO: C_P and C_T dependence on N_x, N_ε and sampling method. 72
3.8 MEXICO: C_P and C_T dependence on N_t, N_ε and sampling method. 76
3.9 Sch15b: C_P and C_T dependence on N_t, N_ε and sampling method. . 77
3.10 MEXICO, $N_t = 400$: $F_{ax}(r)$ &$Q(r)$ for various N_ε values 79
3.11 MEXICO: $F_{ax}^{N_\varepsilon=4} - F_{ax}^{N_\varepsilon=2}(r)$ &$Q^{N_\varepsilon=4} - Q^{N_\varepsilon=2}(r)$ for various N_t . . 79
3.12 MEXICO: $F_{ax}(r)$ &$Q(r)$ of BR &ALM for various N_t &sampling methods 80
3.13 MEXICO: $u(\mathbf{x})/U_\infty$ rotor plane contours for various N_t and sampling methods 81

3.14 MEXICO, $N_\varepsilon = 2$: $u(\theta)/U_\infty$ at $r/R = 80\%$ for various N_t &sampling methods 84
3.15 MEXICO, $N_t = 1600$: $u(\theta)/U_\infty$ at $r/R = 80\%$ for various N_ε &sampling methods 87

4.1 BT1: Mesh topology for ALM-LES simulations. 95
4.2 C_l and C_d coefficients for the S826 aerofoil at Re = $1e05$. 97
4.3 BT1: C_P and C_T tip-speed ratio sweep. 99
4.4 BT1: temporal convergence of C_P and C_T. 104
4.5 BT1: far wake instantaneous velocity time series. 104
4.6 BT1: temporal convergence of the first and second order statistics. . 105
4.7 BT1: velocity and vorticity contours for various mesh refinement levels. 106
4.8 BT1: mean flow profiles for various N_x & N_t. 111
4.9 BT1: far wake energy spectra. 113
4.10 Visualization of synthetic turbulence in an empty domain. 118
4.11 Streamwise evolution of turbulence intensity 118
4.12 BT1: qualitative effect of low inlet turbulence in tip vortex breakdown. 119
4.13 BT1: mean flow profiles for various no- and low- inflow turbulence . 120

5.1 Illustrations of support structure parameterisation methods. 131
5.2 Support structure dimensions for the NTNU rotor. 131
5.3 BT1: $|\omega|$ for various support structure modelling methods. 140
5.4 BT1: mean flow wake profiles for meshed support structures. 142
5.5 Streamwise evolution of the mean flow contours ($x/D = 0 - 5$). . . 143
5.6 Streamwise evolution of the mean flow contours ($x/D = 6 - 8$). . . 144
5.7 BT1: mean wake flow for various support strcuture methods. 148
5.8 Gaussian vs ALM-LES wakes at $x/D = 8$ 155
5.9 Fit 1 &3: streamwise evolution of $k^*(x)$, $(C_Y(x), C_Z(x))$ 156
5.10 Fit 1 &3: streamwise evolution of $\varepsilon(\langle U^n \rangle)$ &$\langle \varepsilon(U^n) \rangle$. 157

6.1 BT1: Mean velocity and TKE comparison with experiments. 176
6.2 BT1&BT2: Instantaneous vorticity magnitude. 178
6.3 DMD of $C1$: $\omega - \alpha$ diagram. 181
6.4 DMD of $C1$: four of the most robust modes. 183
6.5 DMD of $C1$, $C2$ and BG: $\omega - \alpha$ diagram. 184

A.1 Scaling test of the ALM-LES solver in the ARC-HPC facility. . . . 196

B.1 MEXICO: self convergence of N and r_s/r_g for LAS 198

C.1 MEXICO: sectional C_l and C_d against angle of attack 200

D.1 Tangential velocity distribution of a Lamb-Oseen vortex 202

E.1 MEXICO: C_P &C_T for different N_t, solvers &sampling methods. . . 206

1 Introduction

1.1 Towards a sustainable future

Greenhouse gas emissions are the main driver of increasing global temperatures with catastrophic consequences for ecosystems and human life. A large proportion of those emissions originates from fossil fuels utilised in the energy, industry, and transportation sectors [1]. In the 2023 UAE Consensus that followed the 28^{th} Conference of Parties (COP28) nearly 200 nations recognised, for the first time in the history of the summit, the importance of transitioning away from fossil fuels in order to limit the global average temperature rise to within 1.5°C compared to pre-industrial era levels [2, 3]. The ever increasing global energy demand will therefore need to be satisfied largely by low carbon production methods, like renewables.

The term renewable energy refers to energy production methods that utilise natural sources "that are replenished at a higher rate than they are consumed" [4]. Examples include solar, wind, hydro, tidal energy and others. In 2022, the share of renewables in electricity generation globally was 29.5%, while their share in total energy supply was 12.3% [5].

Within renewables, solar and wind energy are the most promising sources globally. In Figure 1.1 the electricity mix over time is illustrated for the years 1990-2022, globally and also nationally, for the UK. In 2022, wind energy accounted

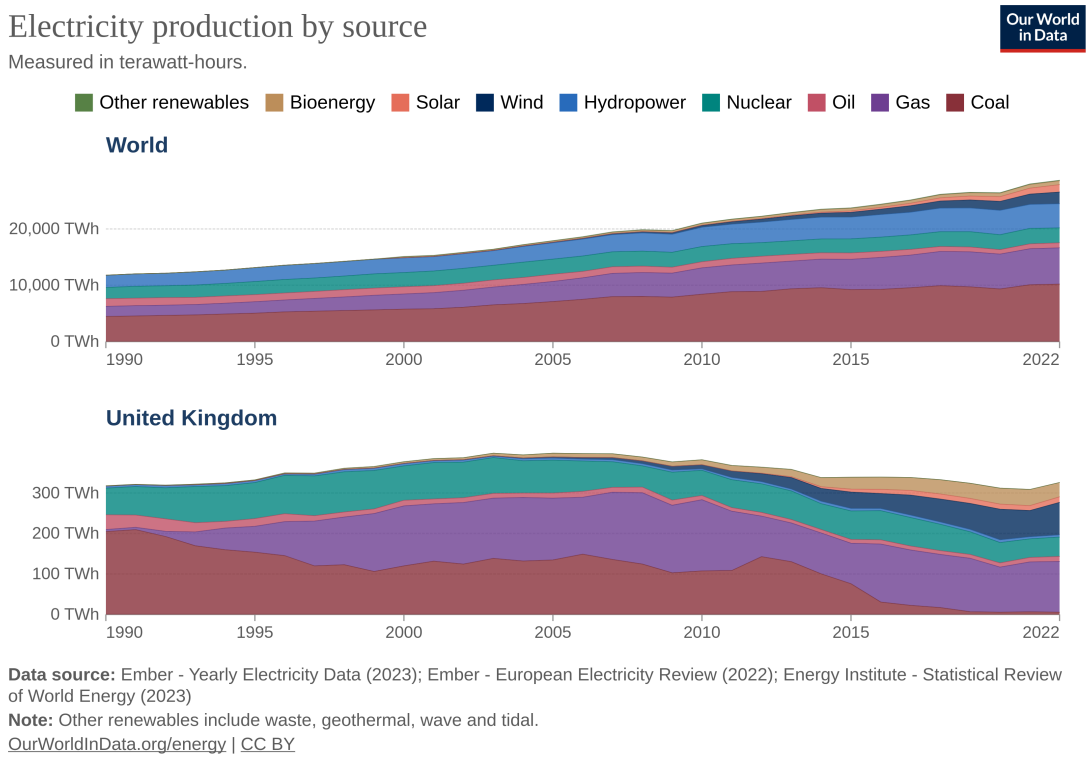


Figure 1.1: Electricity production by source for the World and the UK for years 1990-2022. Source: Our World in Data [6].

for 7% of the global electricity mix, and 24.6% of the UK's, as can be observed in Figure 1.1. These percentages mark significant increases when compared to the penetration of wind in the electricity mix in previous decades.

The ongoing increase in renewable energy penetration was reinforced in COP28, when 133 countries pledged to triple their renewable energy capacity by 2030 [2]. This ambition is expected to be met largely by solar and wind energy. Specifically, the 2030 net zero scenario by the International Energy Agency (IEA) predicts an approximately four-fold increase in solar and three-fold increase in wind capacity, as demonstrated in Figure 1.2. This could imply that by 2030, 40% of the electricity globally could come from solar and wind only. In the 2050 net zero road-map, IEA proposes a twenty-fold increase for solar and eleven-fold for wind (both compared to 2021 levels), totalling a 70% dependence of the global electricity on solar and wind power [7].

While renewable energy is plentiful, the various sources are non-uniformly

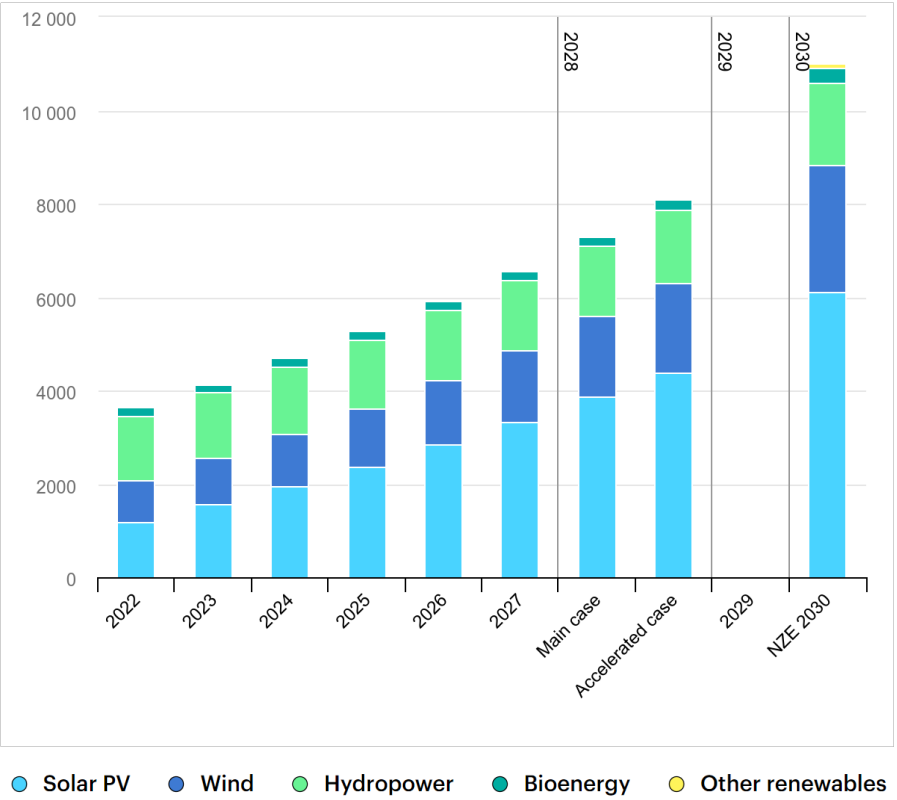


Figure 1.2: Cumulative renewable electricity capacity (in GW) for various 2030 scenarios according to the IEA. Source: IEA [5].

distributed across the planet. Given its location, geology, and climate, each country's renewable energy potential is unique and therefore for each country certain energy extraction technologies may be more suitable than others. For instance, the UK is characterised by very high wind speeds [8] and as a result is one of the global leaders in wind energy deployment, with current (2024) total installed capacity of approximately 30 GW: 15 GW of which is onshore and 15 GW offshore [9]. This significant uptake is accompanied by ambitious goals for 2030, involving the increase of the cumulative installed offshore wind capacity to 50 GW, with an additional 5 GW of floating wind [10]. This will contribute to the UK's long-term commitment of achieving net zero by 2050 [11].

Given the above global and national targets, it is evident that wind energy is anticipated to play a substantial role in the decarbonisation efforts. Consequently, the engineer's responsibility to improve the predictability and efficiency of wind energy systems contributes to a more sustainable future.

1.2 A brief history of wind energy

Evidence of wind energy harvesting dates back thousands of years. The earliest examples of wind power utilization relate to sailing. The use of windmills for tasks such as grain grinding or pumping water may date back to the 3$^{\text{rd}}$ century BCE in present-day China, Pakistan and the Middle East [12]. References to windmills used for irrigation are found in Hammurabi's Code (17$^{\text{th}}$ century BCE) [13]. Notes from 2$^{\text{nd}}$ century BCE by Heron of Alexandria propose a wind-powered musical instrument [13]. A major example of a wind plant that dates back to the 6$^{\text{th}}$-8$^{\text{th}}$ century CE and still withstanding are the Panemones, an assembly of vertical axis wind turbines used primarily for grain grinding (Figure 1.3) [13]. The traditional Dutch windmills (Figure 1.3) were widespread in Europe from the 12$^{\text{th}}$ century until the mid-19$^{\text{th}}$ century and were used for various pre-industrial processes [14].



Figure 1.3: Brief photographic timeline of wind energy harnessing systems by means of rotary machines. Upper panel (from left to right): The Panemone in Iran ($6^{th} - 8^{\text{th}}$ century CE, [13]); Windmills in the Netherlands (built 1738-1740, [15]); Blyth's Montrose Lunatic Asylum turbine (built 1895, [16]). Lower panel (from left to right): Rural turbine from the early 20^{th} century,[13]; Whitelee onshore wind farm in Scotland (commissioned 2009, [17]), Hywind floating wind farm (commissioned 2017, [18]).

The interest in electrification that marked the Second Industrial Revolution led to the use of wind turbines for electricity production. One of the first such turbines was constructed by Scottish engineer James Blyth, in 1887. The structure was a

10 m tall vertical axis wind turbine with sails (Table 1.1, [19]). Indicative of the turbine's capacity is Blyth's note "*When a good breeze was blowing, I stored as much in half a day as gave me light for four evenings*" [20].

Year	Milestone	Location	Nameplate capacity	Reference
1887	Pioneering electricity producing wind turbine	Glasgow, Scotland	[...] *stored as much in half a day as gave me light for four evenings*	[19]
1980	Among the first onshore wind farms	New Hampshire, US	20×30 kW	[21]
1991	Among the first offshore wind farms	(1 mi off) Vindeby, Denmark	11×450 kW	[22]
1991	First commercial onshore wind farm in the UK	Cornwall, UK	10×400 kW	[23]
2003	Among the first large scale offshore wind farms in the UK	(5 mi off) north Wales, UK	30×2 MW	[23]
2017	First commercial floating wind farm	(18 mi off) Peterhead, Scotland	5× 6 MW	[18]

Table 1.1: Brief timeline of major milestones in wind energy harnessing for electricity production. The list is not exhaustive and dates are indicative.

While fossil fuels overtook centralised electrification in the 20^{th} century, the development of wind turbines was still necessary to address certain challenges. For example, until rural electrification took place, small wind turbines were used at scale to provide decentralised electricity in farms and remote locations (Figure 1.3, [13]). In the second World War, fuel conservation programs re-ignited the interest in small scale wind energy [13].

After the oil crisis of 1973, renewed interest in wind energy was sparked due to the rising prices of oil. Incentives given by the U.S. government for the research and development of wind power contributed to the large-scale exploitation of wind, with 16,000 machines of a total 1.7 GW capacity installed in the U.S. in the years $1981 - 1990$ [14] (Table 1.1).

The rapid growth of wind energy (Figure 1.1) from the 1990's onwards has been marked by climate change awareness, which has led to a steady increase in scale and innovation of wind energy projects as can be observed in the milestones listed in Table 1.1. Clean energy is now a necessity as more and more countries commit to net zero goals that require an unprecedented uptake of renewables.

1.3 Wind turbine wakes

Given the ambitious targets regarding the uptake of wind energy in the coming decades, discussed in Section 1.1, as well as the historical course of wind energy innovation presented in Section 1.2, it is evident that ahead of us awaits a wind farm deployment effort of unprecedented scale. Engineers can contribute to the acceleration of this endeavour by making wind energy deployment more affordable and reliable to help reduce the levelised cost of wind energy.

One of the most significant aerodynamic challenges when it comes to wind farm efficiency is the understanding and modelling of wind turbine wakes. While wind turbine wake aerodynamics has been an active research area since the 1980's, questions regarding wind turbine wake physics persist, due to the dynamic and turbulent nature of wind turbine wakes and their merger as well as their complex interaction with the atmosphere. Another aspect that contributes to the difficulty of the problem is the limited availability of observational data, especially offshore [24].

Given the significant impact of wind turbine wakes on wind farm efficiency, it is imperative to create generalised, accurate, and fast wake models [25]. Poor fidelity of engineering wake models triggers a series of consequences as described in greater detail in [24]: inaccurate wake models may lead to loss of revenue for wind plant developers, while the large uncertainty may result in marginal projects not being developed. Inaccurate wake modelling also creates a bottleneck in exploiting wake aerodynamics for wind farm design and control, for instance using wake steering for the reduction of wake effects in wind farms.

The fast engineering models used by wind farm developers and operators during wind farm design and control need to be suitably accurate and general. To ensure

this, their predictions must be validated against the high-fidelity data for a range of flow conditions. It is therefore necessary to have access to high-fidelity wake data representative of the wake behaviour in different conditions in order to develop engineering models. However, since flow data in controlled conditions for large wind farm projects are scarce due to the cumbersome and expensive measurement procedures, it is often the case that certain flows can only be investigated numerically using high-fidelity computational fluid dynamics (CFD).

Actuator line method large eddy simulations (ALM-LES) can provide among the highest-fidelity wake predictions of commonly-used numerical methods and have therefore been extensively used the past decade to study wind turbine wake aerodynamics. Such simulations allow for an accurate representation of the near wake structures as well as an accurate reproduction of the turbulent far wake, and can be embedded in a range of background flow conditions. ALM-LES is therefore a very generalisable turbine and wake modelling tool, with fewer assumptions than alternative computational methods. High-fidelity and generalisability often comes at high computational cost, which is the case with ALM-LES simulations. Despite the computational expense, they can provide a ground-truth approximation for various wind turbine wake problems.

Improving the computational efficiency of ALM-LES simulations as well as understanding the dependence on model parameters is important in order to obtain the essential high-fidelity datasets needed to better understand wind turbine wakes. ALM-LES data can then be further used to validate engineering models, as well as to inspire the creation of new reduced order models.

1.4 Research objectives

Given the significance of the ALM-LES simulations for generating high-fidelity wake flow data, as well as their importance in validating and informing engineering models, this thesis focuses on evaluating and improving numerical efficiency and accuracy of the ALM and explores the potential to use the high-fidelity data to

validate and inspire low-fidelity models. In support of these aims, this thesis addresses the four following objectives:

1.4.1 ALM model parameters

While ALM simulations of wind rotors are considered to be among the most flexible and general turbine models, they still employ a number of user-defined parameters that can significantly affect the prediction of the blade forces. Consensus among practitioners has been reached for the determination of some of the user-defined parameters, however other parameters exhibit greater complexity and there may be interactions between them. As a result, the current best-practice recommendations for such parameters are still not fully resolved in the literature.

The first objective is therefore to understand and reduce the dependence of the ALM blade forces on model parameters, focusing on aerodynamic inputs and models, such as the aerofoil data and tip correction model as well as less explored areas in the literature on numerical parameter selections such as the ALM flow sampling sub-models and their interaction with the time step and the smearing radius.

1.4.2 Evaluation of mesh resolution for ALM-LES wake simulations

ALM-LES simulations are often used as the state-of-the-art wake prediction CFD method. The mesh resolution employed varies given the application and numerical resources, and is rarely assessed systematically.

The second objective is therefore to evaluate the effect of the mesh resolution of ALM-LES simulations of wind turbine wakes and their ability to quantitatively and qualitatively represent wake flow phenomena.

1.4.3 Effect of the turbine support structures on wakes

Evidence suggests that the support structures of wind turbines impact wind energy aerodynamics at all scales: from the rotor loads to the wind farm aerodynamics. However, there is little consensus on what is the best way to model the support

structures in an ALM-LES framework where low-fidelity approaches are necessary due to computational requirements. It is also known that the support structure leads to asymmetry in the far wake. However, the extent to which this may invalidate the assumption of a Gaussian far wake, commonly assumed in engineering models, is not known.

The third objective is therefore to investigate support structure representations in ALM-LES simulations and study their interaction with wind turbine wakes, as well as the consequences for assumptions of axisymmetry in engineering models.

1.4.4 Identification of dominant flow features in wind turbine wakes

The spatio-temporal data from high-fidelity ALM-LES simulations contain rich information about the flow in question. Processing and extracting interpretable information from three-dimensional and unsteady wake flows can be challenging. Sophisticated spatio-temporal data processing methods, such as the dynamic mode decomposition (DMD) may have the potential to reduce the dimension of the flow problem by identifying the dominant flow features.

Extending the focus to two-rotor wake interaction, the fourth objective is to explore alternative dimensionality reduction analysis methods to approach the wake problem, in order to identify and compare potential dominant flow features.

1.5 Thesis Layout

The above research objectives are addressed in the remainder of this thesis.

A literature review of the wake problem as well as the methods used to parameterise wind rotors and CFD techniques used to model the flow is presented in Chapter 2.

Chapter 3 focuses on modelling methods at the device scale. The robustness of the ALM in predicting rotor forces is studied, by exploring the interaction of the sampling method with the time step and smearing radius.

Chapter 4 focuses on the wake scale. The effect of numerical parameters in wake prediction using ALM-LES simulations is explored.

In Chapter 5, aspects of support structures are studied. The methods used to parameterise towers and nacelles in ALM-LES simulations are compared and asessed. The overall effect of support structures on far wakes is also studied.

In Chapter 6, DMD is applied to study the flow problem of the wake merger.

A summary of the conclusions of this thesis alongside future work recommendations is presented in Chapter 7.

2

Theory, modelling methods and rotor geometries

In this chapter, the aerodynamics of wind turbine wakes are reviewed in order to set the background and context for the developments and conclusions drawn in this thesis. Numerical methods for the parameterisation of wind rotors used and improved throughout the thesis are described. The different rotor geometries simulated in the following chapters are also summarised, aiming to make this thesis a self-contained read.

Section 2.1 focuses on describing the aerodynamic characteristics of a single wind turbine wake as well as acknowledging the complexities arising when turbines operate in non-homogeneous background flow. Sections 2.2, 2.3, and 2.4 all focus on the CFD-based modelling of wind energy flows. Specifically, in Section 2.2 a literature review of all methods used to model wind turbines in CFD simulations is presented, providing the context in which the ALM, detailed in Section 2.3, was developed. The governing equations and the numerical solution methods used throughout this thesis are presented in Section 2.4. The chapter concludes by summarising geometrical and operational information of three rotors studied in this thesis; Section 2.5 is therefore a rotor geometry database for the reader. A summary of the above is presented in Section 2.6.

2.1 Aerodynamic structure of wind turbine wakes

Wind turbine wakes and wind farm flows constitute a profound aerodynamic problem comprised of a combination of flow problems spanning a wide range of spatial and temporal scales. The accurate modelling of wind turbine wakes and wind farm flows is crucial for the design and optimisation of wind farm layout, wind farm energy prediction and control as well as the estimation of fatigue loads and turbine lifetime. Improvements to all of the above have the potential to contribute to making wind energy a more reliable and efficient energy source, and reduce risks and costs related to wind energy projects.

Veers *et al.* [26] define a wind turbine wake as a "low energy region in the flow caused by extracting energy from that flow". Generally, a wind turbine wake can be divided into two distinct regions: a near wake and a far wake (Figure 2.1). The near wake is characterised by coherent structures that are directly linked to the rotor's geometry and operating conditions. When these coherent structures break down, an axisymmetric and self similar velocity deficit is developed, that characterises the far wake. The main characteristics and structures of the near and far wake regions, as well as descriptions of the evolution of the mean flow quantities for a wind turbine wake with a uniform laminar inflow, are described in this section.

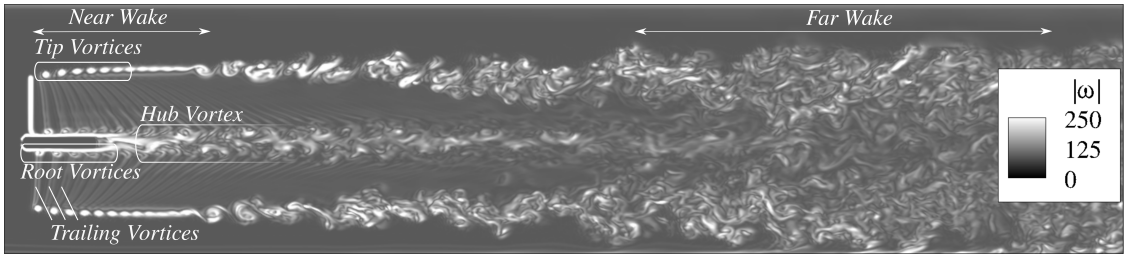


Figure 2.1: Vorticity magnitude in a cross-section through the middle of a wind turbine wake. The tip and root vortices, hub vortex, trailing vorticity and vortex breakdown, as well as the mixing processes that lead to a turbulent far wake are visualised.

2.1.1 Near wake

The near wake is located immediately downstream of the rotor and it may exist up to $2-4D$ downstream, where D is the rotor diameter. In the near wake region,

characteristic coherent structures are present.

The most distinct coherent structures in the near wake are the tip and root vortices (Figure 2.1). Both emerge from the blades due to the static pressure difference between the pressure and suction surfaces, leading to three-dimensional flow gradients that are responsible for the formation of vortical structures. For a three-bladed rotor the triple helix formed by the tip and root vortices has a characteristic frequency that is equal to three times the rotor frequency. Each vortex advects downstream and spirals in the opposite direction to that of the rotor rotation. The root vortices have been reported to break down much faster than the tip vortices [27]. The tip vortex system for an N_b bladed rotor has a geometrical pitch of [28]:

$$h = \frac{2\pi R U_c}{N_b \lambda U_\infty}, \tag{2.1}$$

where R is the rotor radius, U_c is the streamwise propagation velocity of the vortex, λ is the tip-speed ratio (TSR), and U_∞ is the streamwise velocity upstream of the rotor.

Additional to the tip vorticity, each blade sheds a helical trailing vortex sheet from its trailing edge (visible in Figure 2.1), due to non-uniform circulation distribution along the blade.

Another coherent structure that develops near the rotor is the hub vortex (Figure 2.1). The hub vortex is formed downstream of the nacelle, is centred around the wake centreline, and is preserved throughout the near wake. It is described as a single helix mode rotating opposite to the rotor's rotating direction with a frequency much lower than that of the rotor [29]. The hub vortex has been found to enhance the far wake turbulence levels by expanding radially and therefore interacting with the tip vortex envelope [30].

Coherent structures shed from the support structure may also be observed in the near wake. In addition to their influence on the availability of streamwise momentum to the rotor due to upstream flow induction, and the development of a wake that is merged with the rotor wake, support structures and their wakes have been shown to interact with the tip vortices, affecting the wake in more subtle ways. In Debnath *et al.* [31], proper orthogonal decomposition analysis of a wind turbine wake with and

without a support structure model showed that the type of instability responsible for the tip vortex breakdown changes when simulating the support structure.

For a uniform incoming flow, the mean velocity deficit in the near wake usually corresponds to the blade thrust distribution and the drag of the nacelle and therefore a profile forms, that is highly influenced by the blade geometry and forces. Turbulent kinetic energy peaks may be expected at the tip vortex locations at the edge of the wake.

The near wake characteristics gradually transform into the far wake mainly due to tip vortex breakdown. Widnall [32] derived analytically three types of instabilities for a single helix vortex system: a long wave, a short wave, and a mutual inductance instability. The last is found to be the dominant source of instability for the triple helix vortex system of a three-bladed rotor in [28], and occurs due to out-of-phase motions of adjacent helices that leads to their interaction. In the same publication, a reduced order model for the prediction of the distance between the rotor plane and the start of the breakdown of the tip vortices, l, was introduced:

$$\frac{l}{R} = \frac{-16[1 + C_2(\sqrt{1 - C_T} - 1)]^3}{N_b \lambda C_T} \log(C_1 TI). \tag{2.2}$$

where TI is the ambient turbulence intensity, C_T is the rotor thrust coefficient, and C_1 and C_2 are model parameters.

2.1.2 Far wake

While the tip vortices prevent flow from radially entraining in the near wake region [33], tip vortex breakdown transforms the coherent structures of the near wake into a turbulent wake. A common feature of turbulent wakes is that they entrain flow. This entrainment is responsible for the gradual momentum recovery of the wake. After the footprint of the near wake coherent structures has disappeared, the far wake is characterised by an approximately self similar, Gaussian velocity deficit profile.

Simplified models have been proposed to represent some of the key characteristics of the far wake. These models tend to utilise assumptions around the self similarity

of the wake to allow reduced order mathematical models to be proposed, often closed with empirical coefficients.

A simplified model to predict the velocity deficit in the far wake of a wind turbine, the Jensen model [34], is based solely on considerations of mass conservation and considers a top hat velocity shape, with uniform velocity U_w, and linear wake expansion. The velocity deficit $\Delta U/U_\infty$ at a location x in the far wake is given by

$$\frac{\Delta U}{U_\infty} = \frac{U_\infty - U_w}{U_\infty} = \frac{1 - \sqrt{1 - C_T}}{(1 + 2kx/D)^2}. \tag{2.3}$$

x is the streamwise distance and k is the empirical model parameter which encapsulates the complexity of the far wake entrainment, and in the Jensen model is a function of the ambient turbulence.

Amending the top hat shape and incorporating momentum conservation, Bastankah and Porte-Agel's (BP) [35] more recent analytical wake model employs an axisymmetric Gaussian velocity deficit, self-similar in the streamwise direction. Similar to the Jensen model, the BP model involves a single coefficient, the wake expansion parameter k^* that models similar processes to the ones modelled by Jensen's k.

2.1.3 Ambient flow

The above description of a wind rotor wake is characteristic for a uniform inflow. Such inflows can be reproduced in wind tunnel experiments; however, they are rarely encountered in the field. Despite its uniqueness, it is important to understand and model this idealised case, since it is the basis for the modelling of more complex wake flows. Understanding and modelling this idealised case is also important for the verification and validation of modelling tools under idealised conditions that can be experimentally reproduced in wind tunnels.

As a renewable energy extraction device, a wind turbine operates in complex background flow conditions. The spatially non-uniform and dynamic nature of the background flow of a wind turbine and its wake can be attributed to two main factors; first, turbines operate in the inherently non-homogeneous atmospheric

boundary layer (ABL); second, when operating in wind farms, wind turbine wakes interact with each other. Examples of major phenomena affecting the background flow of wind turbines and wakes, spanning from local wake-wake interactions to large scale ABL aerodynamics are presented below.

When wind turbines are closely spaced in wind farms, significant power losses arise due to the wake effect. This is the cumulative influence that the combined wakes of upstream rotors have on the kinetic energy available to downstream rotors. Due to the momentum deficit produced by wind turbine wakes, the wake effect is a phenomenon that reduces the overall power produced by a wind farm. Average power losses in large wind farms can be of the order of $10 - 20\%$ compared to unwaked conditions [36].

Attention has recently been directed to the observation that wind farms also decelerate the incoming flow to a greater extent than the deceleration caused by the constituent turbines. This effect, namely the wind farm or global blockage effect, is a result of the interaction between a large wind farm and the atmospheric boundary layer. It can lead to variations in upstream wind speeds of the order of 3% [37] and it was only recently accounted for in the calculations of wind farm operators [38].

Depending on their locations, wind farms may be affected by the flow induced by neighboring wind farms. In a case study used in the cost analysis by Lundquist *et al.* [39] a reference wind farm operating in an undisturbed flow as well as the same reference wind farm operating downstream another wind farm were simulated. It was estimated that the annual energy yield of the reference wind farm was decreased by 8% when the upstream wind farm was added.

Turbines operate within the lower part of the atmosphere, inside the atmospheric boundary layer (ABL). Flow quantities in the ABL present significant vertical gradients. For example, the logarithmic mean velocity profile present in the ABL, known as wind shear, significantly affects the vertical symmetry of the wake. Due to larger velocities at the top part of the wind turbine wake, higher turbulent fluxes and therefore mass entrainment predominates [40]. Wind shear has also

been shown to disturb the helical shape of the tip vortex system, present in a uniform inflow wind turbine wake [41].

Atmospheric stability can change over the course of a day, which also significantly affects wake recovery. Specifically, the convective boundary layer, characterised by high buoyancy, promotes faster mixing and therefore enhanced recovery than the stable or neutral boundary layers [42].

Local surface roughness directly influences the local turbulence levels. Due to high ground roughness onshore, high levels of turbulence are present in the atmosphere and therefore the wind turbine wakes onshore may recover faster than those offshore [40].

2.2 Parameterisation of wind rotors in CFD simulations

Solving the Navier-Stokes equations using CFD for the prediction of wind turbine flows is a physics-based approach, with few assumptions on the flow physics involved, when compared to analytical models. However, a large number of spatial and temporal scales are involved in a wind turbine problem: the smallest scales starting from the micro-scales present in the turbulent cascade, and the largest spanning kilometers, characterising meso-scale weather patterns present within the Earth's atmosphere [43].

The cost of a CFD simulation for such multi-scale phenomena quickly becomes prohibitive, as it scales with the Reynolds number. The rotor diameter-based Reynolds number in wind turbine wakes is typically of the order of $\mathrm{Re} \geq \mathcal{O}(10^6)$. Capturing the smallest scales requires very small cell sizes and time steps, while capturing larger scale phenomena requires very large domain sizes and simulation period.

Therefore, CFD simulations of wind energy applications often focus on resolving a few important scales and model the rest. Spanning from blade flow predictions to numerical weather prediction simulations, different turbine parameterisation methods may be encountered in the literature. These are summarised in Figure

2.2 and described in this section, with a focus on the mesh requirements associated with each method as well as the flow problems for which they are best suitable for.

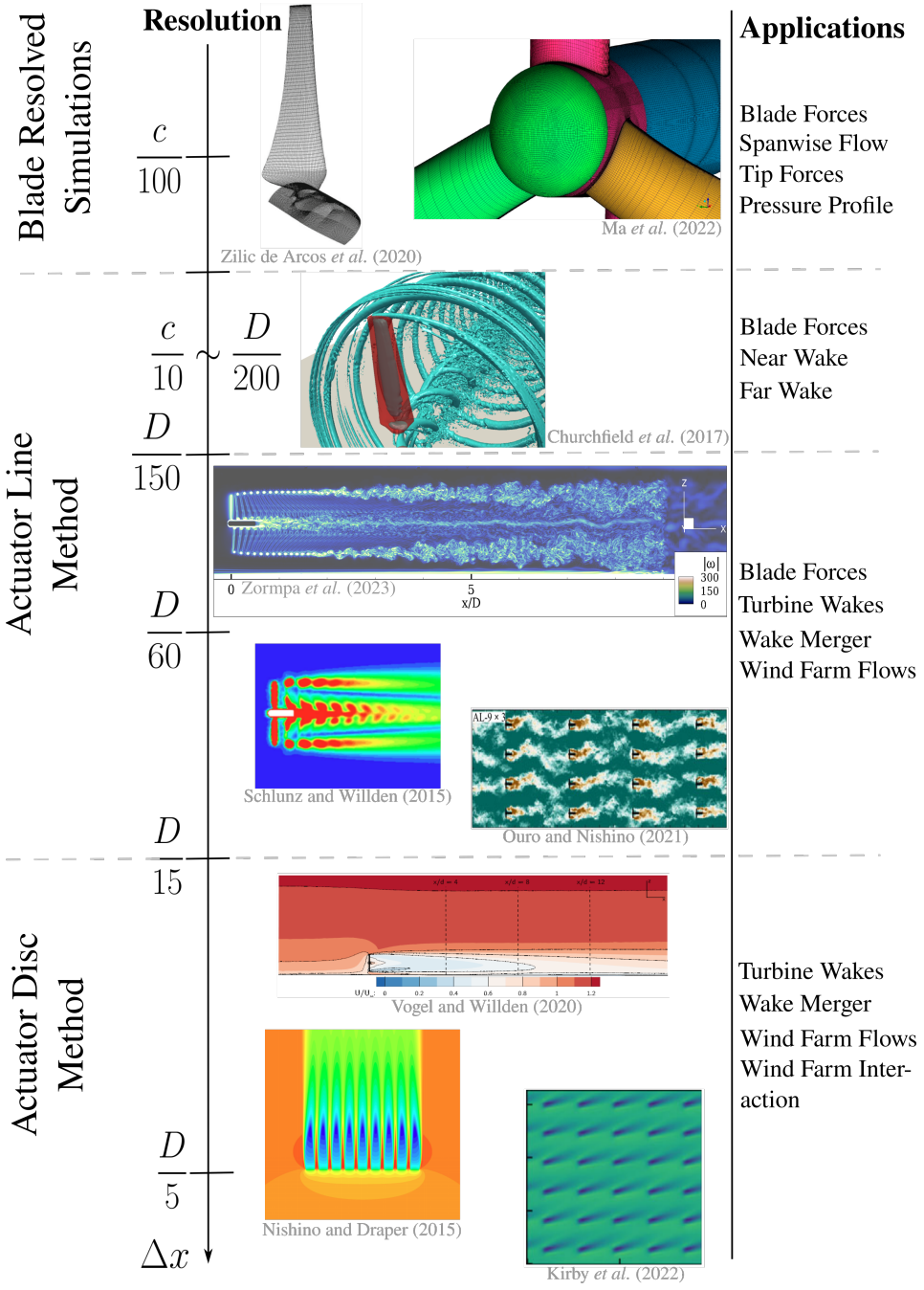


Figure 2.2: Schematic of CFD approaches for different wind energy applications: as the detail in the parameterisation method reduces, the cell size Δx increases, enabling the simulation of larger flow domains and the examination of larger-scale phenomena. References: [44],[45],[46],[47],[48],[49],[50],[51],[52]

2.2.1 Blade-resolved simulations

Blade-resolved (BR) simulations refer to simulations that resolve the geometry of the blade explicitly; the blade surface is meshed and the Navier-Stokes equations are numerically solved around it. The rotation of the rotor can either be considered in a steady or unsteady sense. In the former, the steady flow equations are solved in a static mesh with a multiple reference frame (MRF) for the rotor, which can be simplified by using a 120° wedge with periodic boundary conditions for a three-bladed rotor. However, in this approach axisymmetry of the inflow is assumed. In the unsteady approach, the unsteady flow equations are used to simulate the full geometry, often by employing a sliding mesh around the rotor. In both approaches, the boundary layer of the blade may either be fully resolved ($y+ < 5$, where y^+ is the non-dimensional wall distance) or partially, using wall functions.

The smallest scales in these simulations are related to the boundary layer of the blade, which determines the smallest cell size. In BR simulations the smallest cell size at the blade will be a fraction of the chord and may be expressed as the ratio $N_c = c/\Delta x$, where c is the local chord and Δx the chordwise cell size. Typically, $N_c \approx 100$ [53] is used in BR simulations, as is appropriate for simulating aerofoils.

BR simulations of wind turbine blades are appropriate when the viscous blade forces, spanwise flow phenomena and detailed blade pressure distributions are to be investigated. Examples include Wimshurst and Willden [53] investigating three-dimensional tip effects and blade pressure distributions for one blade using periodic boundary conditions and an MRF frame of reference to model the rotation. The method has also recently been applied in larger flow problems, for instance for the study of the near wake region [45, 54, 55]. Ma *et al.* [45] simulated a full rotor using delayed detached eddy simulations (DDES), including the three blades and a support structure, to study the effect that the support structure has on a periodic turbine array.

While BR simulations are the most accurate type of simulations available for the representation of viscous effects on 3D wind turbine blades, their computational cost limits their applicability for simulating larger scale phenomena, like wakes,

rotor-wake interactions, and wind farm flows. This limitation gave rise to a family of lower computational cost actuator methods, described in the next section.

2.2.2 Actuator methods

Considerable computational savings can be achieved if the blade geometry and boundary layer are not fully resolved but instead modelled by employing an actuator method. These savings are attributed to larger cell sizes that may also allow larger time steps. Such methods are also related to significantly less complex meshing strategies. For an unsteady simulation, like a turbomachinery flow, actuator methods may offer an easier way to implement the rotation of the blade.

Actuator methods model the presence of a solid boundary by representing its effect on the flow field. This is achieved by incorporating the force exerted by the solid onto the fluid as a source term in the momentum equations. This force may be estimated using prior knowledge and pre-defined aerofoil performance coefficients. At a distance several body dimensions away from the applied force, the resulting flow field can be a reasonable approximation to the flow field that would have been computed through an equivalent fully resolved simulation.

In what follows, three types of actuator methods with progressively decreasing level of detail in the representation of the blade geometry are briefly introduced.

Chord-resolving actuator methods

Chord-resolving actuator methods consider some geometrical features of the local aerofoil, such as the length of the local chord of the blade. This category is introduced here in order to distinguish typical ALM (discussed next), that neglects the chordwise non-uniformity of the blade force, from the more refined chord-resolving actuator methods, like the actuator surface method (ASM).

As with the ALM, chord-resolving actuator methods are embedded within an unsteady CFD solver. Each blade is represented separately and is rotated in time. The effect of the blade on the flow is represented by a set of forces geometrically located at the blade location that are implemented as a source term in the momentum equation. Chord-resolving actuator methods impose actuator forces that have both

a spanwise distribution along the blade (same as ALM), as well as a chordwise distribution around each aerofoil section, approximating the non-homogeneous force, representative of the pressure distribution, exerted by each aerofoil section.

The most commonly-used method in this category is the ASM, introduced by Shen, Zhang and Sørensen [56, 57]. Forces in both the spanwise and chordwise directions are considered, forming a blade surface that interacts with the flow. At each blade section, data from pre-determined aerofoil pressure distributions are used for the determination of the span- and chordwise forces. These forces are applied to the flow field through a regularisation kernel in order to eliminate numerical singularities.

Yang and Sotiropoulos [58] developed a variation of Shen's ASM [57], according to which the pressure distribution non-uniformity in the chordwise direction is not considered, but instead the lift and drag forces are applied uniformly in the chordwise direction. According to [58], this implementation requires lower spatial and temporal resolution than Shen's ASM.

A variation that considers the chordwise inhomogenity was also developed in Churchfield *et al.* [46], where an elliptical regularisation kernel was used, as it closer resembles an aerofoil shape, when compared to the standard spherical kernel that is most common in ALM implementations.

The smallest cell size in chord-resolving actuator methods is determined by considering the local chord. From the mesh sensitivity study performed in [56], the final resolution used is 160 cells per rotor diameter, or 8 cells along the chord at the 60% blade span location. In [58] the ASM is used with a similar cell size, equivalent to 160 cells across the rotor diameter. The mesh refinement in the cases simulated in Churchfield *et al.* [46] was similar to the ASM, approximately 7 grid cells along the tip chord. It is observed therefore that chord-resolving actuator methods tend to employ $N_c \approx 10$ cells per chord length, or typically $N_x = D/\Delta x \approx 150$ cells per rotor diameter D, where Δx is the edge length of a hexahedral element in an assumed Cartesian mesh.

The implicit representation of the viscous effects in chord-resolving actuator methods contributes to computational savings, which allows to expand the applicability of the method to larger scale phenomena, like wind turbine near wakes [46, 56]. However, the accurate calculation of the blade force distribution remains the main focus of these methods. The method has also been applied for the modelling of support structure components, like nacelles [30, 58]. It has also been applied in wind farm simulations [30], by making adjustments in the number of cells per rotor diameter required to resolve the chord length.

Actuator line method

The actuator line method is also embedded in unsteady solvers and models each blade separately. The force term added in the momentum equations in the majority of the implementations employs the total lift and drag per blade section, neglecting the chordwise inhomogeneity. A detailed description of the method is provided in Section 2.3.

The ALM has been applied in a wide range of cases, from unsteady blade loading calculations [59, 60], to wind turbine wakes [61, 62], multiple rotor wakes [47, 61, 63, 64] and wind farm calculations [49, 65, 66]. Consequently, the model is used across a large range of mesh resolutions and time steps, the implications of which are discussed in Chapter 3.

The smallest scales resolved in ALM simulations are typically determined by the domain size together with the numerical limitations. Wake resolving simulations typically employ $N_x = 60 - 150$ [47, 61, 62] cells per rotor diameter while wind farm simulations may employ $N_x = 15 - 50$ [49, 65] cells per rotor diameter.

Actuator disc method

The actuator disc concept was integral in developing early wind turbine aerodynamic theory. Contrary to the ASM and ALM that model each blade separately, the actuator disc method (ADM) represents the rotor using forces azimuthally-averaged over the rotor's swept area. This may be solved in a steady or unsteady framework.

Alternatives of different levels of complexity exist within the ADM family. The simplest implementation involves applying a single thrust force uniformly over the

disc surface. A more intricate method involves applying a spanwise, azimuthally uniform force with a tangential component, similar to the forces computed in the blade element momentum (BEM) method. This approach is denoted as ADM *with rotation* [67] and has been demonstrated to provide a more accurate representation of the resulting wake profiles. Extensions to involve unsteadiness and the development of transient phenomena have also been introduced [68].

ADM simulations have been used for the modelling of wake-wake interaction [50] where $N_x \approx 100$ cells per diameter were employed, determined by the level of accuracy required for the wake flow. The method is widely used for modelling wind farms within the atmospheric boundary layer [52, 67], where $N_x = 7$ [67] cells per rotor diameter can be employed and provide adequate representation of the far wake.

2.3 The Actuator Line Method

The actuator line method (ALM) [69] is a CFD-embedded rotor parameterisation method that allows for a discrete blade representation, relaxing the assumption of azimuthal symmetry present in methods like the ADM and BEM. The method, owing to the discrete blade representation, is capable of accurately reproducing the main features of the wake of a wind turbine like the tip vortices. Since its introduction, the ALM has been studied extensively in terms of numerical properties [61, 70], it has been validated against experimental data [64, 71, 72], and compared with lower order methods like the ADM [62, 65]. The method has been utilised for the simulation and understanding of wake phenomena that are challenging to replicate and measure experimentally [28, 30, 41]. This section provides a detailed description of the ALM, the study, improvement, and use of which is the main subject of this thesis.

The ALM models the forces exerted by a wind turbine blade on the flow and is embedded within unsteady CFD solvers. Each blade is represented by an actuator line, which is discretised into several points known as the collocation points, typically of the order of $N_x/2$ [73], visualised in Figure 2.3. At each time step, the actuator line is rotated and blade forces are evaluated: at each collocation point a characteristic blade-local angle of attack and velocity magnitude are calculated

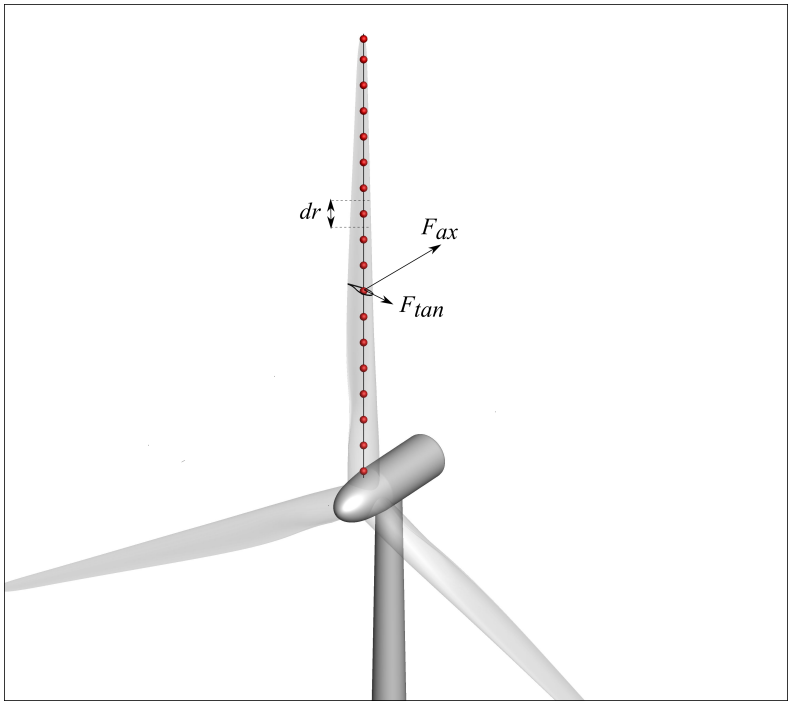


Figure 2.3: Schematic representation of the components involved in the ALM. The actuator line spans from the root to the tip of the blade. It consists of multiple collocation points represented by the red spheres. A set of axial F_{ax} and tangential F_{tan} force components, calculated at each collocation point is shown. The span that corresponds to each collocation point, dr, is denoted.

by interpolating the three-dimensional flow field. Given the predefined aerofoil data corresponding to each blade section and the calculated angle of attack, the lift and drag coefficients can be calculated at each collocation point. These are in turn transformed into a local blade force, considering the twist and pitch angles of the blade at the collocation point and the incident velocity vector. This force is introduced into the flow field as a source term in the momentum equation. After the rotor forces have been imparted into the flow, the flow solver can proceed in time, the actuator line can be rotated accordingly, and the above process is repeated until the quantities of interest reach a steady state.

The ALM has a wide appeal. This can be attributed to a number of characteristics; first, the method does not imply axisymmetry, enabling the study of non-uniform inflow conditions that correspond to realistic wind farm applications. Unsteady wind turbine flows embedded in the atmospheric boundary layer that include background shear [41] and turbulence [74] have been investigated using

the ALM. Moreover, the method has allowed for the exploration of confined rotor operation scenarios like multi-rotor interactions [75] and blockage effects [59, 76].

Secondly, the ALM offers a computationally efficient approach to simulate unsteady wakes. It bypasses the intensive task of resolving the viscous phenomena near the blade surface by modelling their overall effect on the blade force using lift and drag data. This significantly reduces the computational resources required for blade modelling, allowing for the simulation of other flow features within the same computational domain, such as tip vortices and unsteady wake evolution. Enabling the "Numerical modelling of wind turbine wakes" is a core characteristic of the ALM, in-line with the title of the original paper introducing the method to wind energy applications [69]. The method has been applied for single [61, 62] and multiple [75] wake problems.

Finally, the applicability of the ALM spans many scales: the method has recently been applied to the simulation of wind farm flows [30, 49, 65]. Given that the method was introduced for the study of rotor plane induction and near wakes, it is evident that the method has been used for the understanding a wide range of phenomena. Care must be taken when transitioning between applications, and the validity of the method must be reassessed.

The method also exhibits known modelling drawbacks, relative to the radially independent treatment of the blade, and other assumptions. The ALM neglects the development of spanwise pressure gradients and radial flows, and as a result the assumed two-dimensional nature of the lift and drag data may be invalid in certain blade locations. Such issues remain under investigation in the literature, and the evaluation and improvement of the ALM are discussed in this thesis.

The flexibility, numerical efficiency, and the broad applicability of the ALM makes it a particularly important simulation tool for wind energy research. In the next sections, the method is described in detail by breaking it down into three conceptual steps: the flow sampling, force calculation and force imposition (Figure 2.4). This breakdown is introduced here as a way to outline the fundamental structure of the ALM algorithm. While all implementations of the ALM consist of

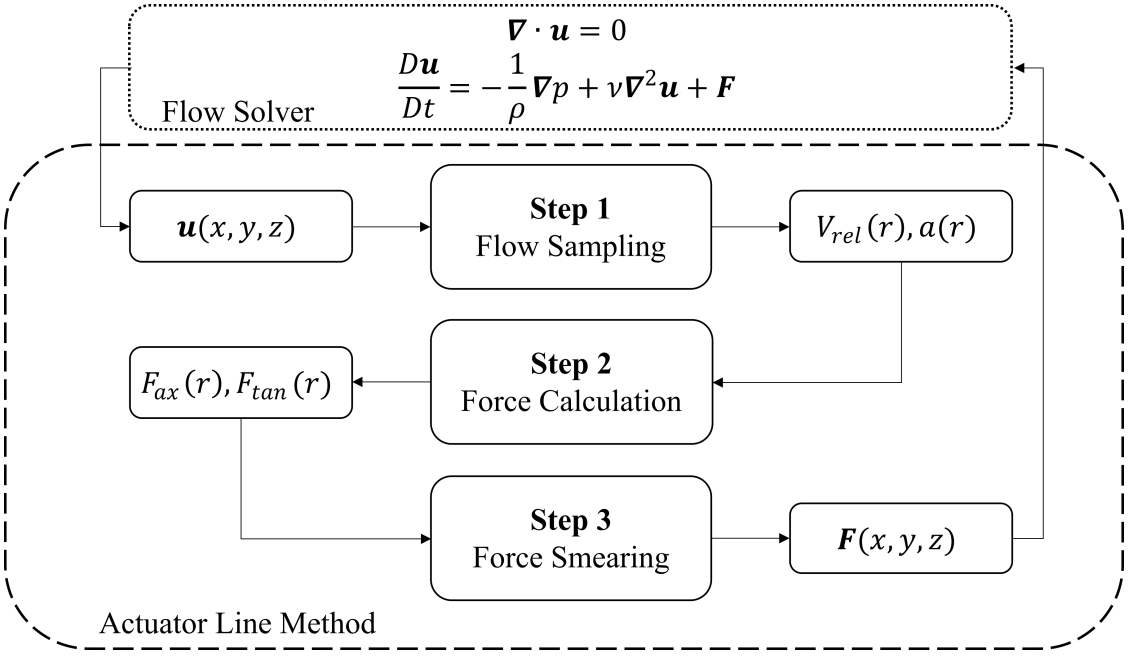


Figure 2.4: Actuator line method flow chart. The communication of the flow solver (dotted box) with the ALM (dashed box) is visualised. The velocity field calculated at the end of each iteration of the flow solver, $\mathbf{u}(x, y, z)$, is used as an input to the ALM. After performing its various steps, the ALM returns a blade force field, $\mathbf{F}(x, y, z)$, that is used by the flow solver as a momentum source.

those three steps, methods employed within each step may vary. By examining each step individually, a deeper understanding of the method is gained, and relevant literature can be categorised more effectively.

2.3.1 Step 1: Flow sampling

In this step, the three-dimensional velocity field $\mathbf{u}(x, y, z)$ simulated at each cell of the CFD mesh is processed in order to generate the characteristic incident velocity $V(r)$ at each collocation point, see the notation in Figure 2.5. By considering the local twist angle and angular velocity, $V(r)$ can be transformed into an angle of attack distribution $\alpha(r)$ and an incident relative velocity distribution $V_{rel}(r)$. As articulated in Ouro *et al.* [77], this step is concerned with the interpolation of the Eulerian flow field of the (x, y, z) coordinate system to the Lagrangian collocation point framework.

Determining a characteristic angle of attack and local velocity at an aerofoil section for a three-dimensional wind turbine flow is not a trivial task. The lift

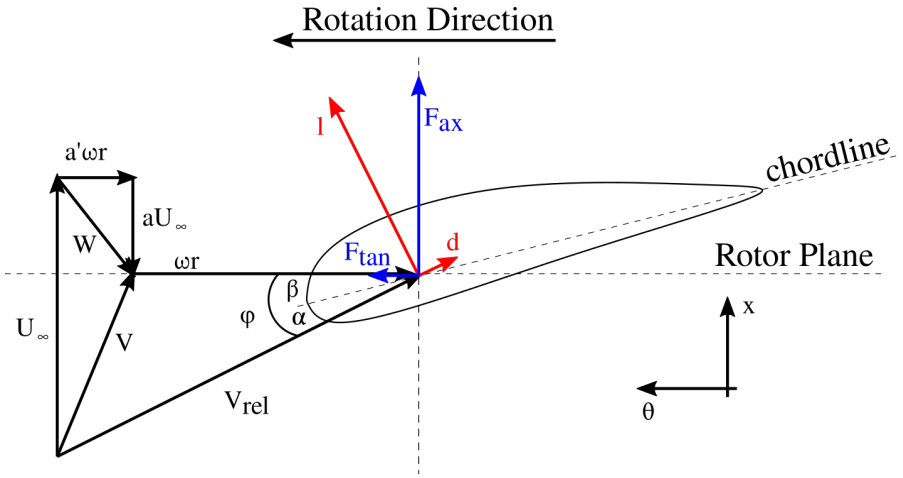


Figure 2.5: The velocity triangle relative to a blade section rotating at an angular speed ω at spanwise location r. The freestream velocity U_∞ is reduced by the induced axial velocity aU_∞, and the tangential flow velocity ωr is increased by the induced tangential velocity a$'\omega r$. The resulting velocity V is hereafter referred to as incident velocity, while once the tangential component ωr is added, the relative incident velocity V_{rel} is formed. The resulting sectional lift l and drag d forces resolved into axial (F_{ax}) and tangential (F_{tan}) components are also noted. The blade section rotates towards the left, and the axial flow velocity is aligned with the positive x direction.

and drag data used for the calculation of local aerodynamic forces generally refer to a two-dimensional aerofoil under uniform freestream velocity. However, in the case of a wind turbine blade, the flow is inherently three-dimensional and the background velocity field is spatially non-uniform.

The first issue, wherein angles of attack are inherently a two-dimensional concept while blade flows are three-dimensional, has typically been addressed by assuming radial independence of the flow at collocation points. The radial independence principle states that, given a blade that is discretised into collocation points (or annular sections in BEM theory, where the principle was first introduced) spanwise sections do not exchange momentum in the radial direction and therefore the blade only affects the flow in the axial and tangential sense. Thus, the two-dimensional local coordinate system of the aerofoil can be defined as the cylindrical surface of radius r and with an axis aligned with the turbine's rotational axis. The Cartesian velocity vectors of the CFD mesh can then be projected onto that surface. The radial independence principle is generally valid in the mid-span regions of the blade but considerable spanwise velocity gradients are found near the root and tip of the

blades. Inaccuracies related to those spanwise flows are typically treated in Step 2 of the ALM and will be discussed in the following section.

The second issue, wherein the background flow field is inhomogeneous and therefore ambiguity is introduced in the definition of a freestream velocity vector is addressed within this step. To understand the complexity of the blade flow, it is useful to describe the sources of inhomogenity of the velocity field in the vicinity of the turbine blade. Firstly, the inflow approaching the rotor plane often exhibits inhomogeneities such as wind shear or turbulence. Additionally, the freestream velocity is slowed down by the local blade forces, also known as blade induction. The presence of the blade induces rotational flow that is manifested in various types of vorticity as described in Jost *et al.* [78]: the bound and shed vorticity are both two-dimensional concepts. The bound vorticity is centred at the aerofoil quarter chord and the shed vorticity is shed by the trailing edge and advected downstream in an unsteady flow. The spanwise circulation gradients generate a trailing vortex sheet emitted by the trailing edge and advected downstream. All the above types of vorticity perturb the velocity field at the rotor plane, causing the aerofoil to operate in an inhomogeneous velocity field.

Sampling methods within the ALM framework share two features. First, they are concerned with negating the effect that the bound vorticity of the aerofoil has on the flow. The same is done in two-dimensional aerofoil flows: the freestream flow must not include effects of the local flow induction that are a result of the presence of the aerofoil, but instead must be sampled at locations undisturbed by the aerodynamic effect of the aerofoil ($r \to \infty, V_\theta \to 0$, Equation 2.4). The induced velocity due to the bound vorticity is given by the Biot-Savart law for a 2-D vortex in the (r, θ)-coordinate system, where r is the radial direction centred at the centre of the vortex, θ is the tangential direction, and Γ is the strength of the vortex:

$$\begin{aligned} V_\theta &= \frac{\Gamma}{2\pi r}, \\ V_r &= 0. \end{aligned} \tag{2.4}$$

In ALM simulations it is impossible to sample the flow at far-field locations undisturbed by the aerofoil because these locations are disturbed by other flow features (for example the adjacent blade) and are therefore not representative exclusively of the blade-local flow. Instead, the induction due to the bound vorticity is excluded by means of symmetry or other treatments based on Equation 2.4.

Secondly, all sampling approaches incorporate the inhomogeneity of the blade-local velocity field in a characteristic, or averaged sense. Methods either sample the velocity at a location that is considered the most characteristic, or average the flow sampled within a set of locations in the vicinity of the blade.

A taxonomy has been introduced in this thesis to classify the sampling methods that may be found in the literature. The taxonomy is based on the location of the sampling points relative to the collocation point. Three types of methods are encountered in the literature: collocation point sampling, where the flow is directly sampled at the collocation point, volume average sampling, where the flow is sampled at a cloud of points centred at the collocation point, and line average sampling where the flow near the collocation point is avoided and the velocity field is sampled at multiple points that lie on the circumference of a circle with local coordinate system that is centred at the collocation point. It is shown in Chapter 3 that the choice of sampling method has implications on the robustness of the ALM. The three methods are described in detail in Section 3.3.

2.3.2 Step 2: Force calculation

This step is performed entirely within the aerofoil local coordinate system of Figure 2.5. The input to this step is the local angle of attack $\alpha(r)$ and relative velocity magnitude $V_{\text{rel}}(r)$, and the output is a local blade force vector $\mathbf{F}(r)$ defined on the (x, θ) plane of Figure 2.5 that comprises an axial $F_{\text{ax}}(r)$ and a tangential $F_{\text{tan}}(r)$ force components. Within this step, a large part of the literature focuses on correcting the blade-local forces to account for inaccuracies that arise from the radial flow independence and other assumptions.

At a collocation point, given the blade-local angle of attack and relative velocity magnitude, in combination with the local blade geometry and corresponding lift and drag data that are provided as a user input, the sectional lift and drag per unit span (dr in Figure 2.3) can be calculated as

$$\begin{aligned} l(r) &= C_l(r, \alpha(r))\Big(\frac{1}{2}\rho V_{\text{rel}}(r)^2 c(r)\Big), \\ d(r) &= C_d(r, \alpha(r))\Big(\frac{1}{2}\rho V_{\text{rel}}(r)^2 c(r)\Big); \end{aligned} \tag{2.5}$$

with the direction of the lift normal to $V_{\text{rel}}(r)$ and the direction of the drag d aligned with it (Figure 2.5).

The determination of correct lift and drag coefficient data is critical for ALM simulations. The polar tables are typically generated using various methods such as panel methods (i.e. XFOIL [79]), experiments [80], or 2D CFD simulations of the flow around the aerofoil [81, 82].

Once the local lift and drag force per unit span have been calculated, the force vectors can be projected to the axial and tangential direction, given the local flow angle ϕ (Figure 2.5). This projection produces the local axial force per unit span component $F_{\text{ax}}(r)$ that contributes to the thrust, and the local tangential force per unit span component $F_{\text{tan}}(r)$ that contributes to the torque and subsequently power of the rotor:

$$\begin{aligned} F_{\text{ax}}(r) &= l(r)\cos(\phi(r)) + d(r)\sin(\phi(r)), \\ F_{\text{tan}}(r) &= l(r)\sin(\phi(r)) - d(r)\cos(\phi(r)). \end{aligned} \tag{2.6}$$

The above calculations presume that no momentum is exchanged between two collocation points, i.e. the calculations follow the radial flow independence principle. However, significant three-dimensional spanwise velocity gradients can develop along wind turbine blades, especially in the tip and root regions of the blade. Such effects lead to the invalidation of the two-dimensional lift and drag polars in these regions. *Tip corrections* have been developed to recover such inaccuracies [83, 84].

Another phenomenon that cannot be captured using two-dimensional steady aerofoil data and therefore needs to be adjusted in ALM simulations is stall delay which dominates the flow near the root of the blades of wind turbines operating at low tip-speeds. Other three-dimensional unsteady flow phenomena may be present but in this section only the aforementioned two are described in greater detail.

Tip corrections

Tip corrections in ALM generally refer to corrections that ensure that the blade force $\mathbf{F}(r) \to 0$ as $r/R \to 1$. This behaviour is encountered in real rotors due to three-dimensional effects but is not replicated in the ALM framework and therefore a manual correction of the force is applied.

The need for a tip correction first arose in the context of 2D momentum theory, in order to account for the effect that a finite number of blades has in reducing the induction near the tip. When it comes to 3D ALM simulations, the discrete blade effect is automatically accounted for by the method. However, tip losses associated with other phenomena are not fully captured in ALM simulations. Wimshurst and Willden [85] observed BR simulation data of horizontal axis rotors and attributed the tip losses to the shed vorticity developing at the tip of the blade. The term shed vorticity in [85] refers to the result of the flow wrapping around the tip of the blade due to the static pressure difference between the pressure and suction surfaces. The shed vorticity may affect the tip loads via two mechanisms: first, the velocity field induced by the shed vortex causes downwash at the outboard blade sections reducing the angle of attack; second, the velocity field induced by the shed vorticity induces spanwise flow accelerations that reduce the static pressure difference experienced by the tip aerofoils, leading to reduced sectional forces.

Since the ALM cannot fully capture the aerodynamic effects above, tip correction functions are typically used to artificially drive the tip blade loads to zero. The most widely used correction in ALM models is that introduced by Shen *et al.* [83]:

$$\begin{aligned} F_1(r) &= \frac{2}{\pi}\cos^{-1}\Big[\exp(-g_1\frac{N_b(R-r)}{2r\sin\phi})\Big], \\ g_1 &= \exp(-c_1(N_b\lambda - c_2)) + 0.1. \end{aligned} \tag{2.7}$$

Within the ALM routine, after the local sectional force $\mathbf{F}(r) = F_{\text{ax}}\hat{\mathbf{x}} + F_{\text{tan}}\hat{\theta}$ is calculated, it is multiplied by $F_1(r)$ (where $\hat{\mathbf{x}}$ the unit vector pointing in the streamwise direction and $\hat{\theta}$ the unit vector pointing in the tangential direction). In Equation 2.7, g_1 controls the strength of the tip correction. g_1 was introduced in Shen *et al.* [83] in order to calibrate the tip correction with available experimental data. It is worth noting that the above tip correction with $g_1 = 1$ resembles the Glauert correction [86], derived for the actuator disc type tip losses related to the finite number of blades in BEM simulations. The above formula was chosen by Shen *et al.* because it follows the asymptotic behaviour that the 3D-type tip losses follow. However, strictly speaking, the function was not derived for these type of losses.

In this thesis, an extension to Shen's tip correction, developed by Wimshurst and Willden [84] is used (abbreviated W&W in this thesis). In their work, Wimshurst and Willden observed that the reduction in F_{tan} near the tip is steeper than that of F_{ax}. They therefore developed an anisotropic tip correction that employed the same formula as Equation 2.7, but used different strengths $g_{1,\text{W\&W,ax}}$ for F_{ax} and $g_{1,\text{W\&W,tan}}$ for F_{tan}. Coefficients $c_{1,\text{W\&W,ax}}$, $c_{1,\text{W\&W,tan}}$, $c_{2,\text{W\&W,ax}}$ and $c_{2,\text{W\&W,tan}}$ were re-calibrated by a least square fitting to data from the MEXICO experiment [87] at a range of tip-speed ratios. While $c_{1,\text{W\&W,ax}}$ and $c_{2,\text{W\&W,ax}}$ closely matched Shen's values $c_{1,\text{Shen}}$ and $c_{2,\text{Shen}}$, respectively, a greater tip force reduction was found in the tangential direction as generally $g_{1,\text{W\&W, tan}} < g_{1,\text{Shen}}$ (Figure 2.6). The coefficients for the two models are summarised in Table 2.1.

	Axial			Tangential		
	c_1	c_2	$g_1(18)$	c_1	c_2	$g_1(18)$
Shen *et al.*	0.125	21	1.45	0.125	21	1.45
Wimshurst & Willden	0.1219	21.52	1.53	0.0984	13.026	0.61

Table 2.1: Values for the empirical coefficients c_1 and c_2 for the Shen and Wimshurst & Willden corrections. A typical value of g_1 for $N_b = 3$ and $\lambda = 6$ ($N_b\lambda = 18$) is shown, to highlight the difference between the two corrections.

It is finally noted that other tip corrections have been derived in the literature. Tip corrections may be applied to adjust the angle of attack [88, 89, 90], lift and drag coefficients, or, as described above, directly reduce the blade forces.

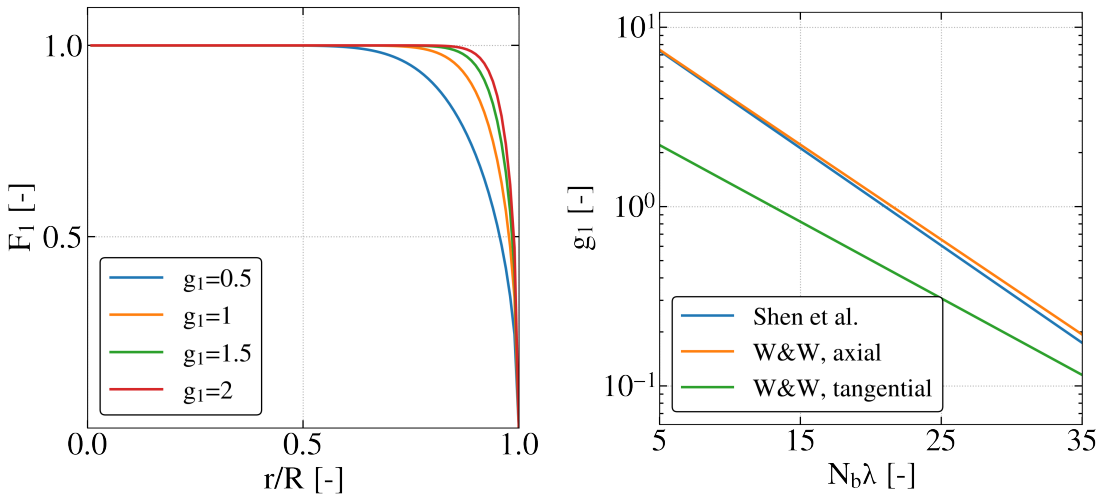


Figure 2.6: Left: Typical shape of the tip correction factor of Equation 2.7 for different values of g_1. Right: change of g_1 with $N_b\lambda$ for the calibration of Shen *et al.* [83], and that of Wimshurst and Willden [84] (noted as W&W for brevity). The latter employs different coefficients for the axial and tangential direction, with impact on g_1.

Stall delay

Another effect that cannot be captured in ALM simulations due to model assumptions is stall delay. Stall delay refers to the observation that the separation angle of attack for an aerofoil rotating as a section of an axial turbomachine is larger than the separation angle of attack of the same aerofoil in static conditions.

The mechanism behind this shifting of the separation point is related to the Coriolis force arising from the spanwise flow and normal to the radial direction. This force acts to attach the boundary layer, leading to a much larger separation angle of attack.

A typical stall delay correction developed by Snel [91] is presented here. The lift experienced by a rotating aerofoil, $C_{l,3D}$, is given by the two-dimensional lift coefficient $C_{l,2D}$ augmented by a factor that is proportional to the chord-to-radius ratio c/r:

$$C_{l,3D} = C_{l,2D} + 3\left(\frac{c}{r}\right)^2 \Delta C_l. \tag{2.8}$$

where ΔC_l is the difference between the inviscid and viscous lift coefficients. The three-dimensional drag coefficient remains the same as that in two dimensions

in Snel's model.

In this thesis, all simulations are performed at angles of attack below stall and therefore no stall delay correction is applied.

2.3.3 Step 3: Force smearing

This step is concerned with projecting the blade-local forces, $\mathbf{F}(r)dr$, calculated in the previous step, onto the three-dimensional CFD domain. This is achieved by generating a body force field $\mathbf{F}(x, y, z)$ that is added to the momentum equation.

To avoid applying a large force onto a single cell volume that could lead to numerical singularities, the spanwise force calculated in the previous step is multiplied by a kernel function $\eta(x, y, z)$ that smears the force over a number of cells ensuring smoothness. $\eta(x, y, z)$ is generally of Gaussian nature with its maximum value centred around the collocation point. When determining η, two aspects must be considered: its shape and its width.

The most widely used shape for η, introduced by Sørensen and Shen [69] and used by multiple practitioners [61, 62, 65] is a three-dimensional spherical Gaussian function, centred at the collocation point,

$$\eta_\varepsilon(r) = \frac{1}{\varepsilon^3 \pi^{3/2}} \exp[-(r/\varepsilon)^2]. \tag{2.9}$$

where r is the distance from the collocation point while ε is the standard deviation that represents the width of the smearing region. The value of the parameter ε is a matter of discussion between ALM practitioners as it may affect the simulated results.

One threshold for ε comes from the numerical considerations of the integral of $\eta(x, y, z)$. This kernel function must integrate to unity so that the total force applied to the flow field is the same as the force calculated in Step 2. Analytically, the kernel function of Equation 2.9 does integrate to 1. However, when discretised, the volume integral reaches unity for values $N_\varepsilon = \varepsilon/\Delta x > 1$ as illustrated in Figure 2.7. For smaller values of ε the integral of the kernel function is overestimated, which would result to an applied force larger than that calculated in Step 2.

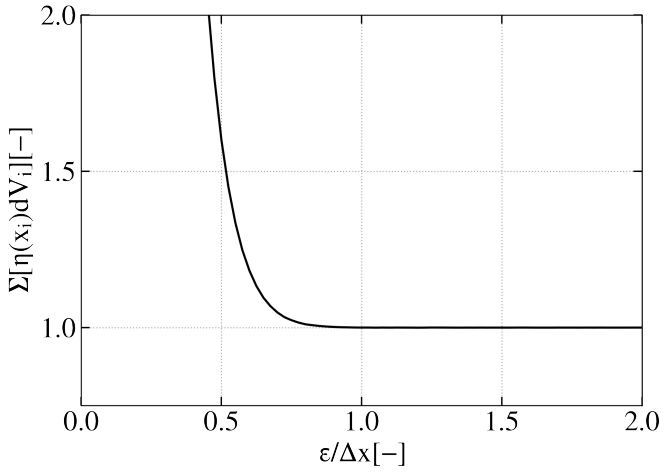


Figure 2.7: Discrete integral of the Gaussian kernel for different cell sizes. The volumetric integral is calculated as a volume-weighted (dV) sum of Function η, 2.9, at each point x_i within the smearing radius 3ε. The discretised integral reaches unity only for $N_\varepsilon \geq 1$.

In addition to the integral consideration, which requires $N_\varepsilon > 1$, researchers have attempted to define a threshold or optimal value for ε by considering how ε affects the accuracy and sensitivity of the ALM results. The literature here splits in two approaches: recommended values $\varepsilon = f(c)$, as a function of the local or average chord length; and recommended values $\varepsilon = f(\Delta x)$, as a function of the local cell size.

The first approach is followed in simulations where the focus might be on the accurate representation of the blade forces and therefore the cell size Δx is on the same order as the chord. These cell sizes typically do not permit resolution of the far wake and therefore the focus is concentrated in the rotor plane. Usually, the value of ε in this case may be calibrated by 2D aerofoil simulations. For example, in Martínez-Tossas *et al.* [92] the optimal value of ε is found to be around $14\% - 25\%$ of the chord length and is calculated by minimising the error between the 2D flow field of an aerofoil and that of a Gaussian-smeared equivalent force. Churchfield *et al.* [46] also express the anisotropic elliptical kernel widths as a function of the chord. Although this approach provides a realistic connection between the blade geometry and the induced velocity field created by the actuator line, it is often resource-heavy for simulations that focus on the far wake.

When the wake flow is of interest, larger values of $\varepsilon = f(\Delta x)$, are often used. In such simulations the cell size is typically larger than the chord in the outboard

sections of the blade, $\Delta x > c$, and the cell size is given as a function of the diameter D (i.e. $N_x = 60 - 150$). Here, the general consensus is that $\varepsilon \geq 2\Delta x$ [61] to avoid spurious oscillations. Martínez-Tossas *et al.*[62] further show that $\varepsilon \geq 5\Delta x$ makes the rotor power and thrust insensitive to the mesh size. Although a large value of ε may reduce the sensitivity of the ALM on user defined parameters such as the cell size [62] , it is important to keep the value of ε such that the actuator line width is comparable to the effective size of the blade. In the limiting case where ε is too large, the actuator lines will not generate any effective blade turbulence or tip vortices, thus generating a wake that resembles that of an actuator disc. There is therefore a trade off between accuracy and numerical stability when it comes to the choice of ε, especially in the cases where $\varepsilon = f(\Delta x)$.

Other shapes of the smearing function have been proposed in the literature, such as an elliptical kernel [46]. Jha and Schmitz [93] criticise the spherical Gaussian kernel of Equation 2.9 on the basis that since the sphere kernels overlap in the spanwise direction, points in vicinity of the actuator line are influenced by more than one spanwise force fields leading to inconsistencies in the local trailing vorticity and downwash. An additional concern with the kernel of Equation 2.9 is that its volume expands outside the tip region leading to force imposition slightly outside the rotor region, effectively increasing the length of the blade. Jha and Schmitz propose an actuator curve method where instead of a Gaussian kernel, a cylindrical kernel with its axis in the spanwise direction is employed, allowing for a better control of the applied force in the spanwise direction.

2.4 CFD solvers

2.4.1 Governing equations

Like all flows, wind turbine and wake flows are governed by the three-dimensional Navier-Stokes equations. Low speeds characterise these flows and therefore they are considered incompressible. The governing equations are here presented in

index notation and Einstein summation is employed where applicable. The three-dimensional velocity field is written as $u_i = u_i(x_i, t)$ where $i = 1, 2, 3$ denotes x, y, z component respectively. The scalar pressure field is written as $p = p(x_i, t)$.

Conservation of mass for an incompressible fluid implies that at every point the divergence of the velocity field is zero, meaning that in a fixed volume V no sources or sinks of mass may be present, i.e.

$$\frac{\partial u_i}{\partial x_i} = 0. \tag{2.10}$$

Conservation of momentum is a manifestation of Newton's second law of motion that states that the force acting on a body of a given mass is proportional to its acceleration. For an incompressible fluid in a constant volume the mass is also constant and equal to $\int_V \rho dV$, where ρ is the constant density. The acceleration is summarised in the material derivative that is comprised of two terms: the local acceleration measured by an observer at a fixed location and the convective acceleration that represents the change in velocity a fluid particle experiences as it convects through the flow. Finally, the forces acting on a Newtonian fluid of constant kinematic viscosity (or diffusivity) ν are of three types: pressure, viscous, and external forces.

$$\frac{Du_i}{Dt} = \frac{\partial u_i}{\partial t} + u_j \frac{\partial u_i}{\partial x_j} = -\frac{1}{\rho}\frac{\partial p}{\partial x_i} + \nu \frac{\partial u_i^2}{\partial x_j \partial x_j} + F_i. \tag{2.11}$$

The incompressible three-dimensional Navier-Stokes equations are the system of partial differential Equations 2.10 and 2.11; in total four equations and four unknowns.

2.4.2 RANS & URANS

Turbulent flows, such as the ones mathematically described by Equations 2.10 and 2.11, contain a large range of scales, spanning from small scales where viscous forces dominate Equation 2.11 to large scales where inertial forces are the leading term. The range is characteristic for each flow and can be described by the ratio between the inertial and viscous forces, i.e. the Reynolds number

$$\mathrm{Re} = \frac{UL}{\nu} \tag{2.12}$$

where U is a characteristic velocity and L a characteristic length scale of the inertial scales.

For many engineering applications the Reynolds number is relatively large, and therefore the task of resolving all the scales in a flow is computationally exhaustive. At the same time, even if a solution was available, it is often the case that an integrated value of the quantities is of engineering interest. In the Reynolds-Averaged Navier-Stokes (RANS) equations the temporal averaging is performed before the equations are solved numerically, a significantly faster approach than solving the full Navier-Stokes equations and averaging after.

The RANS equations were obtained by Osborne Reynolds in his 1895 paper [94]. Reynold's idea was to decompose the *instantaneous* velocity field u_i as the sum of a *mean* component $\bar{u}_i$, constant in time, and a *fluctuating* component u'_i, i.e.

$$u_i = \bar{u}_i + u'_i. \tag{2.13}$$

The mean value is defined such that when the fluctuating value is integrated over a period T, $\int_T u'_i dt = 0$. The same decomposition can be followed for the pressure $p = \bar{p} + p'$. Substituting Equation 2.13 in Equations 2.10,2.11 and subsequently time-averaging, the 3D incompressible RANS are derived:

$$\begin{aligned} \frac{\partial \bar{u}_i}{\partial x_i} &= 0 \\ \bar{u}_j \frac{\partial \bar{u}_i}{\partial x_j} &= -\frac{1}{\rho}\frac{\partial \bar{p}}{\partial x_i} + \nu \frac{\partial^2 \bar{u}_i}{\partial x_j \partial x_j} - \frac{\partial \overline{u'_i u'_j}}{\partial x_j} + \bar{F}_i. \end{aligned} \tag{2.14}$$

An unsteady version of the RANS equations can be obtained by adding a temporal acceleration term $\frac{\partial \bar{u}_i}{\partial t}$ in the LHS of the momentum balance of Equation 2.14, to formulate the Unsteady RANS (URANS) equations. For URANS time scale separation is important; the averaging period is assumed to be much larger than the turbulent time scales but smaller than the mean flow timescales. A schematic

of the length scales (an equivalent sketch can be derived for the timescales) resolved and modelled in a URANS simulation can be seen in Figure 2.8.

The Reynolds decomposition gives rise to the *Reynolds stress tensor*, $\overline{u_i' u_j'}$. The emergence of this tensor suggests that the effect of the smaller scales on the flow can be expressed as an additional stress term. However, this term is an unknown and in order to solve the RANS system of equations, 2.14, a model for $\overline{u_i' u_j'}$ needs to be determined. This question of determining an equation for the Reynolds stresses is generally referred to as the *closure problem*.

The unknown Reynolds stress tensor was first approximated by Boussinesq (see also [95]). The hypothesis was an analogy to Newton's constitutive model of the molecular stresses:

$$-\overline{u_i' u_j'} = \nu_t \left(\frac{\partial \bar{u}_i}{\partial x_j} + \frac{\partial \bar{u}_j}{\partial x_i} \right) - \frac{2}{3} k \delta_{ij}. \tag{2.15}$$

δ_{ij} is the Kronecker delta. ν_t was introduced as analogous to the molecular diffusivity, and named the *eddy viscosity* (or *eddy diffusivity*). k is the turbulent kinetic energy (TKE) and was added to ensure that the trace of the Reynolds stress tensor resulted in the TKE. However, being diagonal, this term can be balanced by an addition to the pressure term and therefore there is no need to create an equation for k at this stage.

The problem of determining the Reynolds stresses was therefore replaced by that of determining the eddy viscosity ν_t. A large family of turbulence models that determine the eddy viscosity, namely, eddy viscosity models, are routinely used in CFD simulations. From dimensional analysis, the eddy viscosity can be expressed as a function of the TKE k and the turbulent kinetic energy dissipation rate ϵ:

$$\nu_t = C_\mu \frac{k^2}{\epsilon}. \tag{2.16}$$

Given Equation 2.16, transport equations for k and ϵ are solved together with Equations 2.14 in many two-equation eddy viscosity turbulence models. Historically, the $k - \epsilon$ model [96] appeared first but shortcomings related to its ability to simulate certain wall flows gave rise to the $k - \omega$ model [97] (ω being the specific TKE dissipation rate), which however demonstrated dependence on the freestream

turbulence. A combination of the $k-\epsilon$ and $k-\omega$ models, the $k-\omega$ SST (shear stress transport) model [98] is often preferred to combine benefits from both methods. Contemporaneous to that, the one equation Spallart-Allmaras turbulence model [99] is also often common in the literature.

The $k-\omega$ SST turbulence model

In this thesis, the $k-\omega$ SST turbulence model is used to close the RANS equations and will therefore here be described in more detail. More information on the model and its exact parameters can be found in the relevant literature [98, 100, 101].

The transport equations for the turbulent kinetic energy k and the specific dissipation rate $\omega = \epsilon/(k\beta^*)$ are

$$\begin{aligned}\frac{\partial(\rho k)}{\partial t} + \frac{\partial(\rho\bar{u}_i k)}{\partial x_i} =& \tilde{P}_k - \beta^*\rho k\omega + \frac{\partial}{\partial x_i}\Big[(\mu + \sigma_k\mu_t)\frac{\partial k}{\partial x_i}\Big] \\ \frac{\partial(\rho\omega)}{\partial t} + \frac{\partial(\rho\bar{u}_i \omega)}{\partial x_i} =& \alpha\rho S^2 - \beta\rho\omega^2 + \frac{\partial}{\partial x_i}\Big[(\mu + \sigma_\omega\mu_t)\frac{\partial \omega}{\partial x_i}\Big] + 2(1-F_1)\rho\sigma_{w2}\frac{1}{\omega}\frac{\partial k}{\partial x_i}\frac{\partial \omega}{\partial x_i}.\end{aligned} \tag{2.17}$$

The blending function F_1 (Equation 2.18) depends on the wall distance y and is used to switch the turbulence model between the $k-\varepsilon$ and $k-\omega$ model, away and close to the wall, respectively.

$$\begin{aligned}F_1 =& \tanh\Big(\Big(\min\Big(\max\Big(\frac{\sqrt{k}}{\beta^*\omega y}, \frac{500\nu}{y^2\omega}\Big), \frac{4\rho\sigma_{\omega 2}k}{CD_{k\omega}y}\Big)\Big)^4\Big) \\ CD_{kw} =& \max\Big(2\rho\sigma_{\omega 2}\frac{1}{\omega}\frac{\partial k}{\partial x_i}\frac{\partial \omega}{\partial x_i}, 10^{-10}\Big).\end{aligned} \tag{2.18}$$

The production term,

$$P_k = \mu_t\frac{\partial \bar{u}_i}{\partial x_j}\Big(\frac{\partial \bar{u}_i}{\partial x_j} + \frac{\partial \bar{u}_j}{\partial x_i}\Big), \tag{2.19}$$

in the transport equation of k is limited by

$$\tilde{P}_k = \min(P_k, 10\beta^*\rho k\omega) \tag{2.20}$$

to prevent the build-up of turbulence in stagnation regions [101].

Finally, the eddy viscosity is defined as

$$\nu_t = \frac{\alpha_1 k}{max(\alpha_1 \omega, SF_2)}, \tag{2.21}$$

where S is the invariant measure of the strain rate tensor [101] and F_2 is another blending function defined as

$$F_2 = \tanh\Big(\Big(max\Big(\frac{2\sqrt{k}}{\beta^* \omega y}, \frac{500\nu}{y^2 \omega}\Big)\Big)^2\Big). \tag{2.22}$$

The updated coefficients α, β, σ_k and σ_ω of the $k-\omega$ SST turbulence model (Equation 2.17) are given as a blending between two extreme values, i.e. a blending between χ_1 and χ_2 given a blending function F results to a value of $\chi = \chi_1 F + (1-F)\chi_2$.

Using the blending function F_1 (Equation 2.18), the values for the $k-\omega$ SST model can be calculated using the extremes: $\alpha_1 = 5/9$, $\alpha_2 = 0.44$, $\beta_1 = 3/40$, $\beta_2 = 0.0828$, $\sigma_{k1} = 0.85$, $\sigma_{k2} = 1$, $\sigma_{\omega 1} = 0.5$, $\sigma_{\omega 2} = 0.856$, and $\beta^* = 0.09$.

2.4.3 Large Eddy Simulation

The turbulent energy cascade, illustrated in Figure 2.8, and the Kolmogorov hypotheses are fundamental in both the derivation of the filtered Navier-Stokes equations and the understanding of Large Eddy Simulation (LES). The reader is referred to [102, 103, 104] for more information; here, a compact outline of the key elements of LES is presented.

At sufficiently high Reynolds numbers, most of the energy in a turbulent flow is contained within the larger scales: the energy-containing range and inertial subrange (Figure 2.8). Little energy, by contrast, is contained in the dissipation range (Figure 2.8). At the same time, when performing direct numerical simulations (DNS) and thus when resolving all scales of a turbulent flow, the computational resource is mainly consumed by simulating the dissipation range [102]. The idea behind LES is to resolve the large eddies and model the smaller eddies that present a universal behaviour and contain less energy.

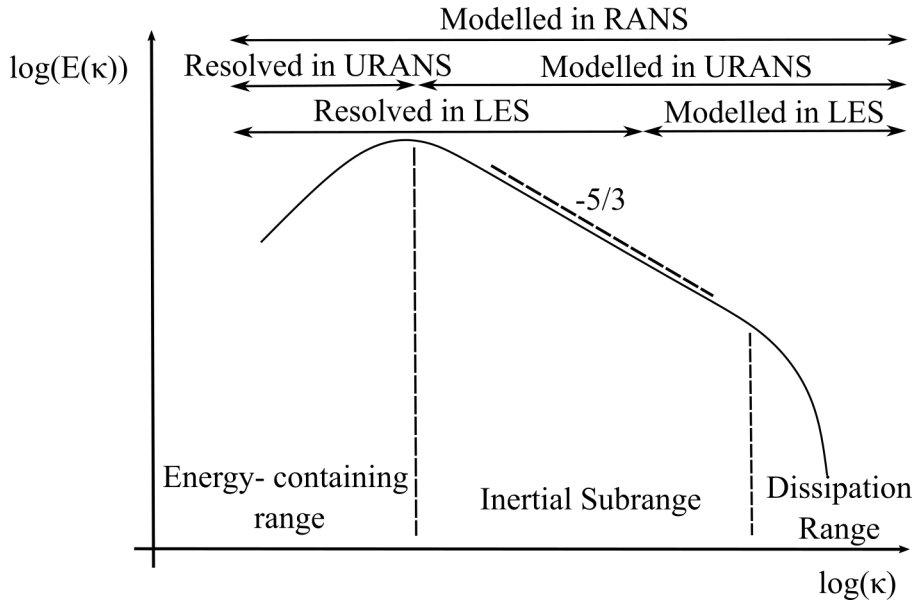


Figure 2.8: Illustration of the turbulent kinetic energy spectra of a turbulent flow. Three regions can be distinguished, from left to right: the energy-containing range, the inertial subrange and the dissipation range. Adapted from [105].

The separation of scales in LES is achieved through spatial filtering of the Navier-Stokes Equations 2.10 and 2.11. The instantaneous velocity field can be decomposed as $u_i = \tilde{u}_i + u_i''$, where $\tilde{u}_i$ is the *resolved* and u_i'' the *subgrid-scale* velocity component. The same filtering applies to the pressure field, $p = \tilde{p} + p''$. It is important to note that while this decomposition can appear to be mathematically similar to the Reynolds decomposition described in Section 2.4.2, there are inherent differences between the two, the most important being that in RANS the filtering of the equations is temporal while in LES it is spatial.

The filtered three-dimensional incompressible Navier-Stokes equations are therefore:

$$\begin{aligned} \frac{\partial \tilde{u}_i}{\partial x_i} &= 0, \\ \frac{\partial \tilde{u}_i}{\partial t} + \tilde{u}_j \frac{\partial \tilde{u}_i}{\partial x_j} &= -\frac{1}{\rho}\frac{\partial \tilde{p}}{\partial x_i} + \nu \frac{\partial^2 \tilde{u}_i}{\partial x_j \partial x_j} - \frac{\partial \tau_{ij}^{sgs}}{\partial x_j} + \tilde{F}_i. \end{aligned} \tag{2.23}$$

τ_{ij}^{sgs} is the *subgrid-scale stress tensor*, analogous to the Reynolds stress tensor. The tensor represents the effect that smaller eddies have on the filtered flow field. The closure problem in LES refers to the determination of the subgrid-scale stress

tensor. The Boussinesq approximation is here again employed for the modelling of the deviatoric part of the subgrid-scale stress tensor, $\tau_{ij}^{sgs,dev}$. For LES, the subgrid-scale turbulent kinetic energy k_{sgs} is used,

$$\tau_{ij}^{sgs} = \tau_{ij}^{sgs,dev} + \frac{2}{3}k_{sgs}\delta_{ij} = -2\nu_{sgs}\tilde{S}_{ij} + \frac{2}{3}k_{sgs}\delta_{ij}. \tag{2.24}$$

The isotropic subgrid-scale stresses can be absorbed by the pressure term in the same way as in RANS, creating the modified pressure $\tilde{p}^* = \tilde{p} + \frac{2}{3}\rho k_{sgs}$. The filtered rate of strain is denoted by $\tilde{S}_{ij} = \frac{1}{2}\left(\frac{\partial \tilde{u}_i}{\partial x_j} + \frac{\partial \tilde{u}_j}{\partial x_i}\right)$. The eddy viscosity of the subgrid-scale motions is denoted by ν_{sgs}. Similar to how eddy-viscosity models in RANS seek to approximate ν_t, eddy viscosity models in LES aim to approximate ν_{sgs}.

Smagorinsky subgrid-scale eddy viscosity model

The Smagorinsky model, developed by Smagorinsky [106], forms the basis for many LES eddy viscosity models. It is a zero-equation eddy viscosity model that is based on the balance of turbulent kinetic energy production and dissipation in the inertial subrange. The subgrid-scale viscosity in the Smagorinsky model is defined as:

$$\nu_{sgs} = (C_s\Delta)^2\sqrt{2\tilde{S}_{ij}\tilde{S}_{ij}}, \tag{2.25}$$

where Δ is the filter width and C_s is the Smagorinsky coefficient. $C_s\Delta$ represents the characteristic subgrid eddy size. The value of $C_s = 0.173$ was derived by Lilly [107] for homogeneous isotropic turbulence.

One of the most significant shortcomings of the Smagorinsky-Lilly model is the inability of the model to predict zero turbulence in the viscous sublayer of wall flows. Near-wall modifications have been proposed, like the Van Driest damping function, that limits the subgrid-scale dissipation near the wall by means of limiting the characteristic length scale. The Wall Adapting Local Eddy-viscosity (WALE) [108] model also results in a zero ν_{sgs} near the wall. Dynamic approaches have also been developed [109, 110, 111]. These approaches generally employ the Geremano identity [112] to relate the subgrid-scale stresses calculated at two test filter widths in order to then calculate the Smagorinsky coefficient, without the need to pre-define it, as is necessary in the Smagorinsky-Lilly model.

2.5 Rotor descriptions

The rotors utilised in this thesis are summarised in this section. Background information for each rotor, along with their geometry, flow conditions and other relevant details are summarised below.

2.5.1 NTNU rotor

The NTNU rotor was designed for Blind Test 1 [113] (hereafter referred to as BT1), an experimental study of the wake of a model wind turbine conducted in the Large-Scale Wind Tunnel of the Department of Energy and Process Engineering, NTNU in 2013. BT1 is unique for its detailed near and far wake measurements. Subsequently, the same rotor was used in follow-up blind tests at NTNU, including BT2 [114], which explores the merging of wakes from two rotors. In this thesis, data from the first two blind tests are utilised, while acknowledging that more blind tests have been performed recently, namely BT3-5, that focus on the effect of freestream turbulence, yawed wakes, and other wake phenomena.

The rotor is three-bladed, with a diameter of $D = 0.894$ m and the nacelle has a diameter of $D_{nac} = 0.09$ m. The wind tunnel dimensions are $(L \times W \times H) = (11.15 \times 2.7 \times 1.826)$ m or $(12.47 \times 3 \times 2)D$ (Figure 2.9), and the rotor is centred at a hub-height $z_h = 0.807$ m above ground. This configuration gives a rotor-to-tunnel area ratio of 12%. A schematic of the domain dimensions and relative position of the rotor(s) in BT1 and BT2 is presented in Figure 2.9.

The blades consist of NREL S826 [115] aerofoils along the entire span. The chord and twist distributions are plotted in Figure 3.4, and a 3D render of the rotor is presented in Figure 2.11.

The design tip-speed ratio is $\lambda = 6$. In both BT1 and BT2, the freestream velocity is $U_\infty = 10$ m/s. Therefore, at design conditions, the rotor rotates at 1280 RPM. The chord-based Reynolds number defined as $\mathrm{Re}_c = cV_{rel}/\nu$, where V_{rel} the relative velocity incident to the blade section, is here $\mathrm{Re}_c = 10^5$ at the tip. The single rotor in BT1 and the upstream rotor in BT2 are located $4D$ downstream of

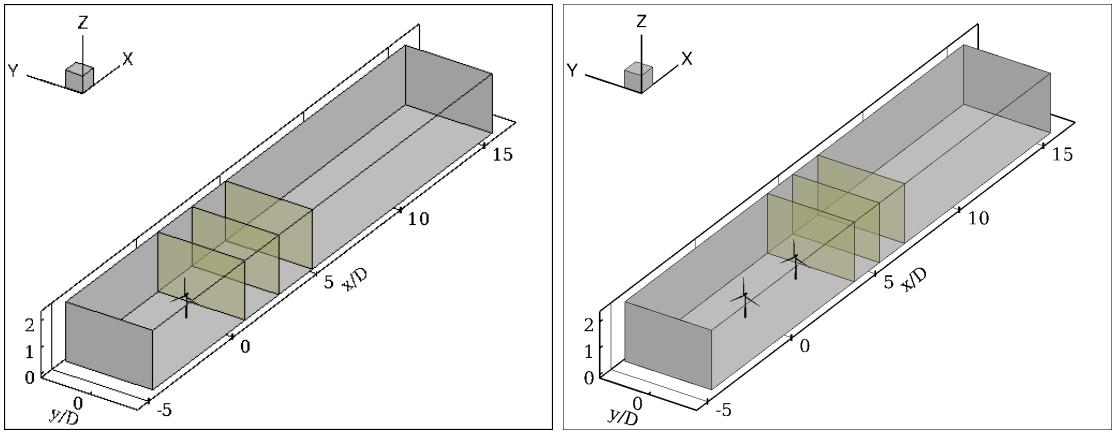


Figure 2.9: Wind tunnel dimensions for BT1 (left) and BT2 (right). The horizontal planes show the locations where wake flow field measurements are available from experiments [113, 114].

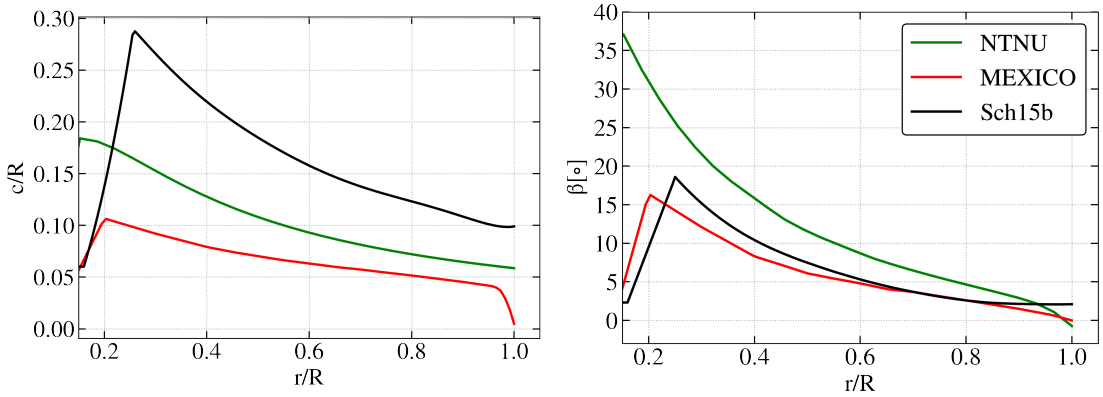


Figure 2.10: Spanwise distributions of the chord non-dimensionalised by the tip radius (left), and the blade twist angle (right) for the NTNU (green), MEXICO (red), and Sch15b (black) rotors. The MEXICO twist distribution is shown without considering the design root pitch angle of $-2.3°$

the tunnel inlet. For the laminar cases of BT1 and BT2 the turbulence intensity $2D$ downstream of the tunnel inlet is measured to be $TI = 0.3\%$.

The experimental results for BT1 consist of power and thrust curves for a range of TSR values ($2 \leq \lambda \leq 12$). Additionally, horizontal and vertical profiles of mean velocity and TKE were measured, $1, 3$ and $5D$ downstream of the rotor.

Similarly, the experimental results reported from BT2 include power curves for both rotors, alongside horizontal and vertical profiles of mean velocity and TKE, at streamwise locations $1, 2.5$ and $4D$ downstream of the second rotor.

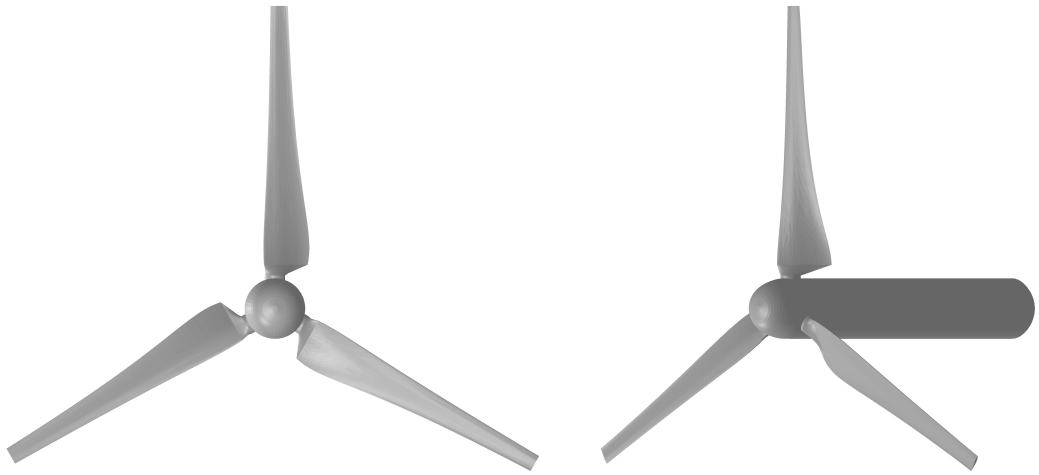


Figure 2.11: NTNU rotor: 3D render of the rotor with nacelle. Blade geometry made in QBlade [116] given [113].

2.5.2 MEXICO rotor

The MEXICO (Model rotor EXperiment In COntrolled Conditions) rotor was designed as part of IEA Wind's Task 29, which took place between 2006 and 2014. The experiments involved in the Task were performed in the Large Low speed Facility of German-Dutch Wind facilities in the Netherlands. The first phase of Task 29 [87] was concerned with the measurement of blade pressure distributions at different spanwise locations, and the PIV measurement of the near wake velocity field.

The rotor is three-bladed, with a diameter of $D = 4.5$ m and the nacelle has a diameter of $D_{nac} = 0.54$ m. The facility is an 9.5×9.5 m^2 open jet configuration of 20 m length and the rotor is placed 7 m downstream of the nozzle at a hub height of $z_h = 5.12$ m.

The blades consist of three aerofoils, DU91-W2-250 from 20% to 45.6% span, RISØ-A1-21 from 54.4% to 65.6% span and NACA 64-418 from 74.4% to the tip. The remaining spanwise length is occupied by transition pieces that ensure a gradual transition between aerofoils. The chord and twist distributions can be seen in Figure 3.4. A 3D render of the rotor is displayed in Figure 2.12.

The design tip-speed ratio is $\lambda = 6.67$. The corresponding freestream velocity is $U_\infty = 15$ m/s at a rotational speed of 424.5 RPM. The chord-based Reynolds

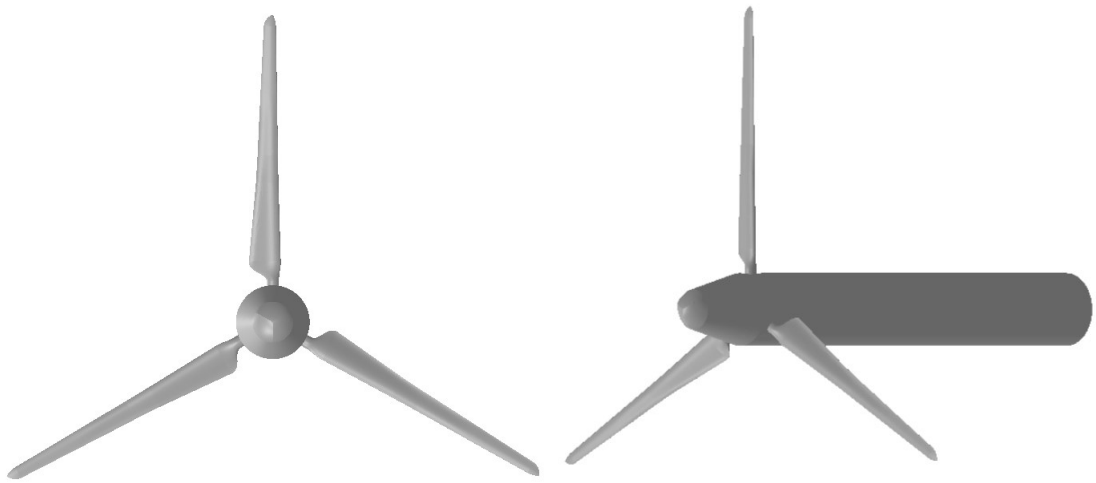


Figure 2.12: MEXICO rotor: 3D render of the rotor with nacelle. Geometry from [117].

number at the tip for this rotating speed is $\mathrm{Re}_c = 8 \times 10^5$. Inlet turbulence intensity is estimated below 0.4%.

2.5.3 Sch15b rotor

The Sch15b rotor is a tidal rotor characterised by high solidity, designed for optimal performance in blocked conditions. Contrary to the rotors presented above, the Sch15b turbine has not been manufactured and therefore existing analysis is only numerical. The rotor was introduced in Schluntz and Willden [60], and was designed for optimal performance at a blockage of $B = 19.6\%$. Later, Wimshurst and Willden [72] modified the root solidity and tip twist. Zilic de Arcos et al. [118] further modified the root for structural purposes. The latter version of this rotor is used in this thesis and referred to as the Sch15b tidal rotor.

The rotor is three-bladed, with a diameter of $D = 20\,\mathrm{m}$ and the nacelle has a diameter of $D_{nac} = 3\,\mathrm{m}$. The channel for which it was optimised has a square cross section of side $2D$ and is infinite in length. It is noted however that in this thesis, blockage is not studied or replicated when simulating the Sch15b rotor.

The blade sections comprise of RISØ-A1-24 aerofoils along the entire span and the chord and twist profiles are reproduced in Figure 3.4. A 3D render of the rotor is presented in Figure 2.13

The design tip-speed ratio is $\lambda = 5.5$ at the design blockage ratio, $B = 19.6\%$. The freestream velocity is $U_\infty = 2$ m/s, with a corresponding rotational speed of 10.5 RPM. The chord-based Reynolds number at the tip for this rotating speed is $\mathrm{Re}_c = 20 \times 10^6$.

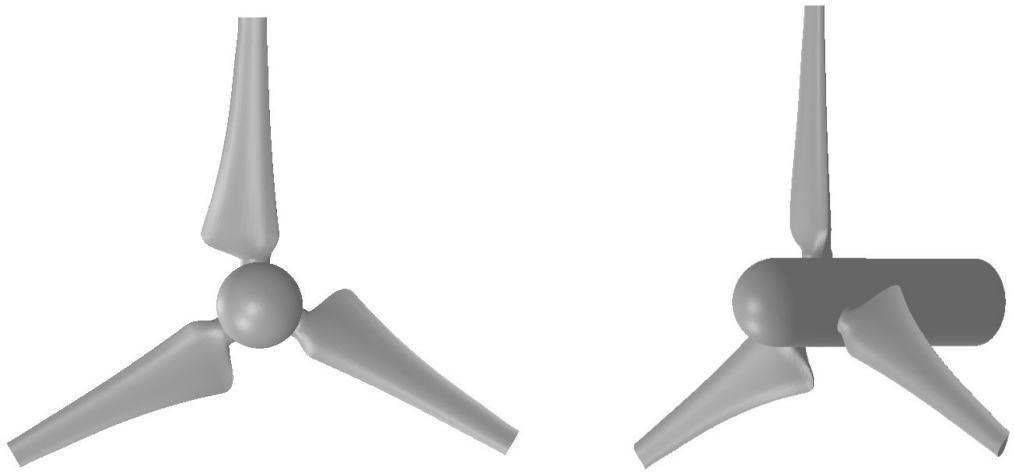


Figure 2.13: Sch15b rotor: 3D render of the rotor with nacelle. Geometry from [117].

2.6 Summary

This chapter provided an overview of the aerodynamic nature and simulation methods for wind turbine wakes. Providing definitions for near and far wake features is necessary to support discussions in upcoming chapters. Acknowledging complexity related to non-uniform background flow is also important context to justify the need for accurate and fast simulation methods, capable of resolving as many scales as possible.

A summary of modelling methods for wind energy applications allows for an improved understanding of the applicability range of each method. For each wind turbine parameterisation method, the smallest resolved scales (corresponding to the cell size) and the largest scales (corresponding to the domain size) are presented using examples from the literature. This presentation emphasises the large range of problems in which the ALM is used which in turn highlights the importance of the

method in wind energy research. Therefore, improvements of the ALM that are presented in this thesis should be a valuable input for ALM practitioners.

The ALM was presented in detail by introducing a three-step classification of the various tasks. This classification is used to categorise the existing literature. It may be used as a framework to discuss the relation and dependence between the various steps, which may facilitate the improvement of the method. Last, splitting the ALM in three steps provides an organised framework that may be used to differentiate between different implementations in the literature.

The Navier-Stokes equations are presented, together with the Boussinesq approximation. Central ideas for both RANS and LES approaches are summarised. A turbulence closure model for each approach, namely, the $k-\omega$ SST for RANS, and the Smagorinsky model for LES are presented and used in the next chapters of this thesis.

Finally, the three horizontal axis rotors utilised in this thesis were summarised.

3

The effect of flow sampling in the robustness of the ALM [1]

This chapter investigates the effect of the ALM flow sampling sub-model on the predicted blade forces and flow field. Three sampling methods are explored: the widely used collocation point sampling method, a volume average sampling method, and the line average sampling, initially introduced by Jost *et al.* [78], here adapted for use within the ALM framework. A key takeaway from this chapter is that when employing the collocation point sampling method, the simulated power and thrust present significant dependence on two user defined parameters: the time-step, Δt; and the smearing radius, ε. The proposed line average sampling method successfully reduces those dependencies, therefore leading to improved robustness and numerical efficiency of the ALM.

The chapter corresponds to a publication submitted to *Wind Energy*, expected to be published soon. The Author's statement is presented in Section 3.9.

3.1 Abstract

The actuator line method (ALM) is a widely-used tool for the modelling of horizontal axis turbines and wind and tidal farm flows. The method uses a virtual blade

[1] This chapter corresponds to a publication submitted to *Wind Energy*.

representation to simulate the dynamics of wind turbines without the computational expense associated with resolving the blade geometry. Within the ALM the flow is first sampled at each blade section, allowing for the calculation of the sectional lift and drag forces that are in turn imposed on the flow domain using a smearing kernel. In this work the effect of the flow sampling method on the robustness of the ALM is discussed. Implementations of two widely-used types of methods for horizontal axis wind turbines are tested: point sampling, where the flow is sampled at or near the collocation point, and volume average sampling where flow field information from multiple points centered at the collocation point is averaged into a representative blade-local velocity vector. A third method, line average sampling, that was initially proposed for sampling flows from blade-resolved simulations is adapted for the ALM framework. This method samples the flow symmetrically around a control element in order to eliminate the interference of the bound circulation, thus allowing the inflow velocity at the aerofoil to be determined. When evaluating power and thrust coefficients as well as the flow field at the rotor plane predicted by the ALM, the line average sampling approach is demonstrated to be more robust and converges faster with time step for two different rotors: a small wind rotor and a high solidity tidal rotor. This suggests that carefully selecting the sampling method could be key in alleviating the very strict time step restriction imposed by the ALM, a widely acknowledged limitation of the method. Such an advancement could contribute towards improving the computational efficiency and tractability of the method.

3.2 Introduction

The Actuator Line Method (ALM) [69] is a commonly used tool to model the rotor blades of axial flow turbines when performing Computational Fluid Dynamics (CFD) simulations. The ALM represents the presence of the rotating blades virtually within a CFD simulation. At each time step the blade loads are approximated based on the locally sampled flow field and sectional force data. These loads are then imposed on the modelled momentum equations and the flow field solution is advanced in time. The method attempts to capture some of the dynamics and flow

structures that emerge from the individual blades of the axial rotor, including the tip-vortices and azimuthal variations in velocity induction. In contrast to blade-resolved (BR) simulations, the ALM generates the above flow structures without resolving the boundary layers of the blades. The cost of BR simulations is high and often prohibitive, as a result of modelling smaller scales and structures. When compared to the steady flow actuator disc method (ADM), where the main focus is on capturing accurately the momentum deficit due to the rotor but none of the independent blade structures, the ALM provides greater accuracy but at increased cost.

The ALM is particularly useful for two types of investigations: firstly, it allows the loads on wind and tidal rotors to be studied in cases where the turbine inflow is not uniform. Such problems may include background shear [41], turbulence [74], multi-rotor interactions [49, 65, 75], blockage [76] and others. Secondly, aligned with its original introduction for wind turbine applications [69], the ALM enables simulation of the spatial and temporal structure of turbine wakes. Even when using high performance supercomputers, adequately resolving the wake region may be prohibitively expensive when a BR mesh is used to model the rotor.

Typical implementations of the ALM include three distinct steps that are performed within each time step of the CFD simulation. However within each step the methods and model parameters may vary depending on the implementation and focus of the particular simulation.

In step 1, the simulated velocity field is sampled to determine the angle of attack and relative velocity magnitude at a series of collocation points along each blade span. Various methods can be used to perform the sampling, with consequences for both the accuracy and robustness of the results. These methods are the focus of the current paper and are discussed in detail below.

The sectional blade forces are evaluated in step 2 using lift and drag data that can be sourced from aerofoil CFD simulations, experiments or other aerofoil tools such as panel methods. A range of corrections have been proposed [83, 84, 89, 119] to account for effects such as the reduction in forces near the blade tip, stall delay, and dynamic stall.

The calculated blade forces are projected onto the CFD mesh in step 3. To avoid numerical singularities that emerge from applying a large body force in the volume of a single mesh cell, the projection of the force from the collocation point to the CFD mesh is typically achieved using a smearing kernel. This kernel is characterised by its shape and size. The majority of implementations use a spherical Gaussian kernel proposed in the original ALM paper [69], but other shapes such as elliptical kernels have been proposed [46]. The size of the force smearing kernel that is represented by the standard deviation of the Gaussian function, ε, is a matter of ongoing discussion. The size and shape of the kernel can affect the forces predicted by the model, with corrections proposed to reduce this dependence [88, 89, 90]. The current guidelines state that in order to avoid numerical oscillations a choice of [61] $\varepsilon \geq 2\Delta x$ is appropriate, where Δx is the cell size at the rotor plane.

This paper focuses on the flow sampling of step 1. Determining the blade-local angle of attack for an aerofoil section of an actuator line is non-trivial and several methods have been proposed in the literature. Most methods attempt to eliminate the circulation-induced velocity that results from the lift force applied by the blade to yield the incident velocity that the blade experiences in the absence of the local blade-induced flow. Velocity sampling at the collocation point, has been adopted by many authors [61, 62, 65, 69, 120]. This is supported by the assumption that the perturbation velocity due to the foil's circulation vanishes at the collocation point [92]. Mittal *et al.*[120] discuss the effect of the scheme used to interpolate the velocity from the CFD mesh to the collocation point and find significant deviation in the prediction of power and thrust when different interpolation schemes are used. Single point based sampling methods remain very sensitive to the force smearing around the same point and consequently the mesh resolution.

To eliminate the concerns related to the interpolation errors as well as to allow for non-symmetrical force projection functions in step 3, Churchfield *et al.* [46] introduced an extension to the ALM that, together with the methods described above, can be found in SOWFA [121]. The method samples the velocity vectors at various points located within a pre-defined kernel that is centered at

the collocation point. The blade-local velocity is calculated as a weighted average of the various sampled velocities.

Unlike the sampling methods described above, where the velocity is sampled in locations where a blade force has been applied and the velocity field has been significantly disturbed, the approach by Schluntz and Willden [48] samples at locations outside the force smearing kernel. A three-point sampling method is introduced that, through solution of simple potential flow equivalence equations, allows the blade section's circulation, angle of attack and relative speed to be determined. By sampling the velocities just outside the region where the force has been applied, this method avoids interaction with the Gaussian force smearing kernel.

The problem of calculating angles of attack from 3D blades is not unique to the ALM; the discussion is also relevant when extracting angles of attack from a computed flow field. When the 3D flow field around the blade is already known, usually from a BR simulation, it is useful to transform it into a series of 2D aerofoils with their own angles of attack and induction factors. In this way, the extensive information coming from a 3D CFD simulation is converted into spanwise-distributed quantities that are compatible with blade-element theory, enabling comparisons with other models. Sampling angles of attack from BR simulations though, differs from sampling from ALM simulations. Different types of information are available in the two cases. For instance, the blade pressure forces are not available in ALM simulations as the geometry is not explicitly resolved. On the other hand, in BR methods the flow field sampling cannot occur at the center of pressure of the blade, as may be done in ALM, as it is occupied by the solid blade. Another difference arises from the smearing of the force in ALM simulations that can interfere with the flow sampling. Despite the differences, there is a conceptual overlap between those two bodies of literature and therefore it can be useful to carefully migrate knowledge from one to the other. Comparative studies such as [44, 57, 78, 122] have demonstrated the trade-offs between the various sampling methods available.

Zilic de Arcos *et al.* [44] presented an analysis of six different methods to extract angles of attack from BR CFD simulations. Two of these, the vortex sheet

method [57] and the pressure fitting method [123], use information from the pressure distribution on the blade surface and are therefore not appropriate in the context of the ALM. The other four methods are based on sampling the velocity field and could therefore also be used as sampling methods in an ALM framework. Between them, the stream tube analysis method, introduced in the same paper, and the line average method introduced by Jost *et al.* [78] were found to be the most robust in terms of their internal parameters when sampling BR CFD flow-fields. These two methods were also found to systematically agree with the other methods. They are relatively simple to implement and their theoretical base does not rely on assumptions, like axisymmetry, that escape the general case.

In this paper, the line average method is considered for use within the ALM. The line average method samples the velocity at a specified number of points that lie on the circumference of a circle of radius r_s that has its center at the section's collocation or centre of pressure point. According to the potential flow equivalence, the average velocity of those points should equal the freestream as long as the points are equally distributed around the circumference so that the net contribution of the blade's circulation is zero and the blade drag is not too significant. Here, the method is adapted to the actuator line model in order to sample the velocity at locations where the effect of the circulation can be eliminated, the same principle followed by Schluntz and Willden's three-point sampling method [48]. The method has been previously adapted for ALM simulations of vertical axis wind turbines [124].

In what follows, three ALM velocity sampling approaches are compared: collocation point sampling; an implementation of the volume sampling method by Churchfield *et al.* that employs a 3D Gaussian kernel for the sampling; and the line average method adapted for the actuator line framework. Two rotors are simulated: an experimental wind rotor, and a high solidity tidal stream rotor. The interplay between the sampling method, time step and force smearing radius is studied and remarks are made on the robustness of each method.

This paper is organised as follows: in Section 3.3 the sampling methods are summarised. In Section 3.4 a detailed discussion of the time step constraint present in

ALM simulations contextualises and quantifies the motivation for this work. The test cases are presented in Section 3.5 and numerical methods in Section 3.6. In Section 3.7 the robustness of the different sampling methods is presented and discussed for two horizontal axis rotors. Concluding remarks are drawn in Section 3.8.

3.3 Flow sampling methods

The lift and drag data used for the calculation of local aerodynamic forces generally refer to a two-dimensional aerofoil under uniform freestream velocity. However, the local velocity field around a blade is non-uniform due to the blade rotation, the influence of the turbine on the flow, the three-dimensionality of the flow around the blade, particularly near the tip, and the flow perturbations due to the various types of vorticity in the vicinity of the blade, as described in Jost *et al.* [78].

AL flow sampling methods perform the task of extracting blade-local flow quantities to allow the calculation of blade forces. Following the notation of Figure 3.1 at an arbitrary radial position r along the blade, the blade-local velocity V is sampled at each collocation point. Noting the tangential speed of the blade section ωr, the blade-relative velocity V_{rel} and angle of attack α, required as inputs for the calculation of the blade force in step 2 of the ALM, can then be computed.

The interplay between V_{rel} and α and the blades forces forms a feedback wherein the thrust T imparted on the flow acts to retard the flow, influencing the velocity induction W and therefore blade-local velocity V. Hence the ALM is solved iteratively to account for the feedback between flow sampling and force imposition. The relationship between these variables is non-linear and may also vary with the spanwise position of the collocation point, tip-speed ratio, type of aerofoil, tip correction, rotor design, as well as the inertial and viscous forces present in the flow.

In this section, the ALM sampling methods found in the literature are categorised into three groups. All three categories employ symmetry to eliminate the effect of the bound vorticity from the calculation of the local flow, since 2D data are employed for the force calculation of step 3. The remaining flow is sampled in various ways to obtain a characteristic local velocity vector. The underlying differences between

the three methods lie in the location and number of sampling points: the point sampling methods sample the CFD flow field at a single characteristic point, the volume sampling methods sample the flow at multiple points that are located in a 3D volume centered about the collocation point and the line sampling methods sample the flow at locations outside the projected force region of step 3. All three types of methods are described and visualised, and variations are discussed, as well as the dependence of each method on its internal parameters below.

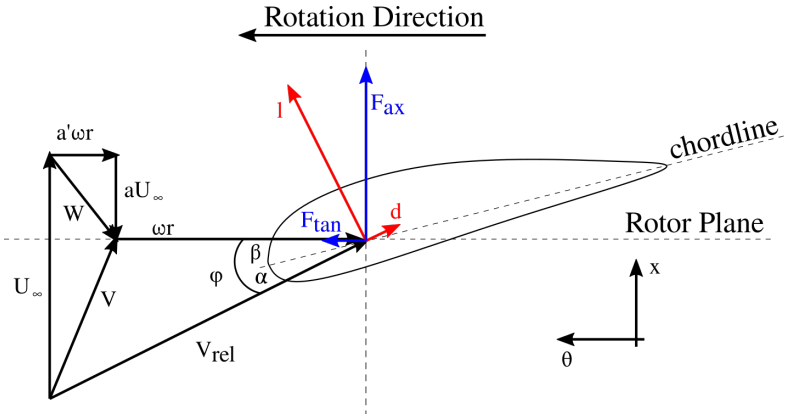


Figure 3.1: The blade-local velocity triangle relative to a blade section rotating at speed ωr at spanwise location r. The axial flow speed is reduced by aU_∞ from the freestream U_∞ and the tangential flow increased by $a'\omega r$ due to the rotor thrust and torque respectively. The resulting lift l and drag d forces resolved into axial (F_{ax}) and tangential (F_{tan}) components are also noted. The blade section rotates towards the left, and the incoming stream velocity is aligned with the positive x direction.

3.3.1 Point sampling

The methods included in this category sample the blade-local velocity at a single point that is usually the collocation point. The collocation point sampling method (hereafter CPS, Figure 3.2) is the most widely-used sampling method for actuator line applications [62, 65, 75] first introduced in the initial implementation of the algorithm for wind turbine simulations by Sørensen and Shen [69]. Sampling at the collocation point allows the freestream velocity to be obtained by eliminating perturbations due to the Gaussian force smearing kernel, as derived in Martínez-Tossas *et al.* [92].

Implementations in the literature have used locations different to the collocation point location for point sampling. In Mittal *et al.* [120] the sampling point is

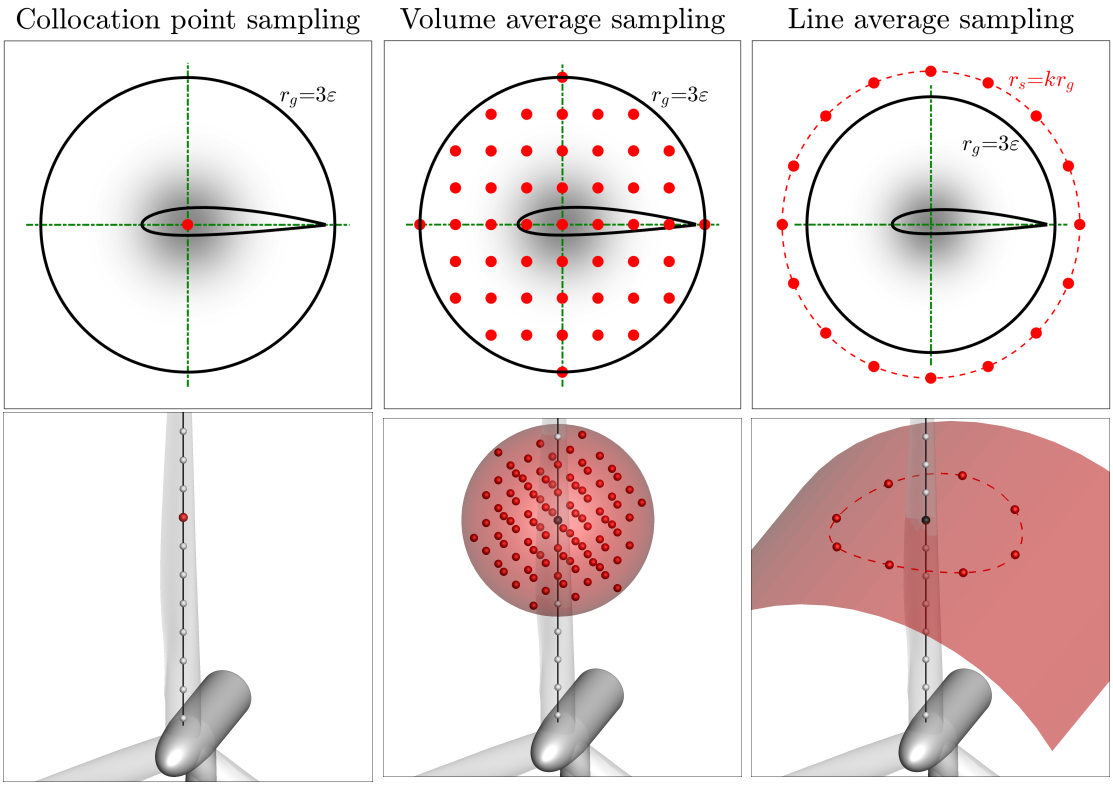


Figure 3.2: Schematic of the three flow sampling method types in two dimensions (upper panel) and three dimensions (lower panel). The red dots represent potential sampling points for each method. In the upper panels, the background gradient bounded by the black circle of radius $r_g = 3\varepsilon$ represents the force imposition region for an isotropic Gaussian smearing kernel.

defined as the cell centre that is the nearest neighbour to the collocation point, and therefore its location is mesh and rotor-speed dependent. Extensions of the method aiming to improve the accuracy and theoretical background of the method include the derivation of a correction for the drag-induced velocity [92], as well as a proposed viscous core correction for the underprediction of axial induction observed in ALM simulations with large ε/c values, where c is the local chord [88, 90].

When the velocity is sampled at the collocation point, the only user choice that influences the resulting blade-local velocity is the scheme used to interpolate the velocity from the CFD mesh to the sampling point. Mittal *et al.* [120] observed large differences in turbine power and thrust coefficients, C_P and C_T, when the interpolation scheme was varied. This sensitivity to the interpolation scheme is a direct result of the method only depending on a single point for the determination of

the blade-local velocity. It will be demonstrated in this paper that this single-point dependence introduces sensitivity to other user-defined parameters.

The most widely used version of the CPS method, as proposed by Sørensen and Shen [69], has been implemented in this paper. For the velocity interpolation, the mean value coordinates interpolation scheme is used, available in OpenFOAM [125], and is a widely-used interpolation scheme in CFD and visualization softwares. This scheme uses the field values at the vertices of the cell enclosing the sampling point together with the coordinates of the sampling point to calculate the velocity [126]. The interpolation method in this paper is kept consistent across all sampling methods in order to investigate other parameters of the ALM.

3.3.2 Volume sampling

The methods included in this category sample the flow field at multiple points, with the points located in a region that includes the collocation point (hereafter these methods are referred to as volume average sampling, VAS, Figure 3.2). Two aspects need to be determined here: the region where the sampling points are located, and the function through which the multiple sampled velocities will be weighted to generate a single blade-local velocity vector.

The most widespread method in this category is the advanced ALM developed by Churchfield *et al.*[46] implemented in SOWFA [121]. The authors test alternative sampling methods in order to circumvent the interpolation errors that emerge from the CPS method and quantified by Mittal *et al.*[120]. The mathematical derivation is based on the 2D steady incompressible inviscid momentum equations and the Kutta condition. In the 2D plane, the force applied by the aerofoil to the flow field is given as the product of a force vector multiplied by the scalar smearing function $g(x, y)$. The undisturbed 2D velocity in that case reads

$$\mathbf{V_{2D}} = \iint g(x, y)\mathbf{u}(x, y)dxdy. \tag{3.1}$$

That is, the undisturbed velocity is the weighted average of the velocity in the vicinity of the blade, where the weighting factors are given by the force projection

function. Although the method was originally developed with a 2D kernel $g(x, y)$, the authors hypothesised that a non-spherical 3D kernel that decays quickly in the spanwise direction, is a reasonable assumption. In that case, the x, y coordinates are the local coordinates at the plane of the aerofoil and $\mathbf{V_{2D}}$ the blade-local velocity $\mathbf{V}$. The authors noted that using a thin 3D kernel might be an inadequate approximation near the tip, where spanwise gradients can be very large.

Other implementations in this category include the Mittal *et al.* [120] velocity averaging from 7 or 21 nearest neighbours where the region of the sampling points is mesh dependent and the averaging involves either no weighting or weighting using the velocity gradient information. Ouro *et al.* [77] describe their sampling routine as an interpolation from the Eulerian flow field to the Lagrangian collocation point framework. The interpolation uses 64 neighbours located in a 3D kernel of width $4\Delta x_i$, where Δx_i the cell size of the Eulerian mesh. The sampled velocities are combined using the ϕ^4 δ-function by Yang *et al.* [127].

In this paper we consider a single implementation of the volume sampling method, based on that of Churchfield *et al.*[46]. The force smearing function $g(r)$ (where r is the distance from the collocation point) in this paper is constant across all simulations and given by Equation 3.4 (where $g(r) = \eta_\varepsilon(r)$), that represents a 3D spherical Gaussian kernel. Following Equation 3.1, the flow sampling points are then located within the 3D spherical Gaussian kernel used for the force smearing, and are also weighted by its kernel function. As already noted, the method in Churchfield *et al.*[46] has been derived for 2D kernels whilst thin, anisotropic 3D kernels are used in practice. Here, we use a 3D isotropic kernel, and note that it may produce inaccuracies in the spanwise direction. However, given the large number of volume sampling methods found in the literature, and that this work focuses on time step sensitivity that is mainly affected by the relative distance of the sampling points in the azimuthal direction and not in the spanwise direction, we have chosen to use the 3D spherical Gaussian kernel as the most generic volume sampling shape.

3.3.3 Line sampling

The methods included in this category sample the flow in multiple locations, similarly to the Volume Average Sampling methods, but here the location of the sampling points is outside of the force smearing kernel. Care is required when interpreting the sampled velocity in highly non-uniform and dynamic flows due to the spatial and temporal filtering effect of sampling velocities across a volume rather than a singular point. Circumventing the aerofoil region is not only preferable in ALM simulations, but it is also necessary when extracting angles of attack from BR simulations, since the region is occupied by the blade geometry.

Jost *et al.*[78] developed the line average sampling method, hereafter LAS (Figure 3.2) as a way to extract the blade-local angles of attack from BR simulations, removing the circulatory effect that the aerofoil bound circulation exerts on the flow. The method was inspired by the reduced axial velocity sampling method that also belongs in the line sampling category introduced by Hansen *et al.* [128]. There, the flow is sampled upstream and downstream of the rotor plane and the blade-local velocity is an average of the two. Similar to Schluntz and Willden [48] who developed a sampling method based on potential flow equivalence, LAS assumes that the effect of the aerofoil at each blade section is an axisymmetric induced velocity field. The sampling points for a collocation point at radius r are located on an annular surface of the same radius and therefore sample the flow field over that curved surface, as described in Jost *et al.* [78]. Exploiting symmetry, the sampling is performed at a set of locations at a constant radius r_s from the centre of the aerofoil and that are diametrically opposed. This averaging process eliminates the circulation-induced velocity yielding the local velocity at the blade section.

In this paper, the LAS method is implemented within the ALM framework for horizontal axis rotors. The method depends on two parameters: the number of circumferential sampling points N and the distance r_s from the collocation point or center of the aerofoil. A convergence study on the number of points is presented in Appendix B and it was found that $N = 16$ points is sufficient for sampling both the angle of attack and blade-local velocity over the whole span of the blade

and across different tip-speed ratios (λ) and rotors. The sampling distance r_s, is kept constant across simulations and chosen to be $r_s = 1.1r_g = 1.1 \cdot 3\varepsilon$ (where ε is the standard deviation of the Gaussian force smearing kernel) thus lying slightly outside the force imposition region, as per Appendix B.

3.4 Time step in ALM simulations

The time step used by different ALM practitioners in the literature can vary such that there are between 100 and 1500 time steps per revolution[46, 48, 49, 129]. This is because many factors play a role in selecting the timestep, including the mesh size, tip-speed ratio, and the Reynolds number of the simulation. Generally, two restrictions are considered when it comes to actuator line simulations: a streamwise and an tangential CFL condition. Both are discussed below.

In what follows, the time step is represented as the "number of time steps per rotation", $N_t = T/\Delta t$, where T is the turbine rotational period. The mesh-size is represented as "number of cells per diameter", $N_x = D/\Delta x$, where D is the turbine diameter, and x is an arbitrary direction in a presumed hexahedral mesh. The computational cost therefore scales with N_t and N_x.

3.4.1 Streamwise CFL condition

Considering the streamwise CFL condition based on the freestream velocity U_∞, the time step restriction can manifest according to Equation 3.2. It is noted that in this expression, the freestream velocity U_∞ is used instead of the local maximum streamwise velocity expected when calculating the Courant number (Co) to avoid violating the CFL condition due to local accelerations. This can however be accounted for by setting $\mathrm{Co}_{x,max} \leq 1$, where the subscript x implies streamwise direction.

The relation between N_t and N_x, established through the streamwise CFL condition varies with $\lambda = \omega R/U_\infty$:

$$\mathrm{Co}_x \leq \mathrm{Co}_{x,max} \Leftrightarrow U_\infty \frac{\Delta t}{\Delta x} \leq \mathrm{Co}_{x,max} \Leftrightarrow N_t \geq \frac{\pi}{\lambda \mathrm{Co}_{x,max}} N_x. \tag{3.2}$$

3.4.2 Tangential CFL condition and the ALM time step constraint

In ALM simulations, in addition to the main flow characterised by the freestream velocity U_∞, there is another significant characteristic velocity in the tangential direction, namely the tip velocity ωR. Since the tangential characteristic velocity is larger than the freestream, a tangential CFL condition can be written for a characteristic tangential velocity $U_\theta = \omega R$, where the subscript θ implies tangential direction, and a characteristic cell length Δx:

$$\mathrm{Co}_\theta \leq \mathrm{Co}_{\theta,max} \Leftrightarrow U_\theta \frac{\Delta t}{\Delta x} \leq \mathrm{Co}_{\theta,max} \Leftrightarrow N_t \geq \frac{\pi}{\mathrm{Co}_{\theta,max}} N_x. \tag{3.3}$$

For $\mathrm{Co}_{\theta,max} = 1$ and by defining $\Delta s = \omega R \Delta t$ as the distance travelled by the tip collocation point in one time step, the tangential CFL condition of Equation 3.3 can be rewritten as $\Delta s / \Delta x \leq 1 \Leftrightarrow N_t \geq \pi N_x$, which reads: "the distance travelled by the tip collocation point in one time step must not be larger than a cell size". This is the typical ALM time step constraint, widely-used in most ALM implementations [61, 62, 69]. Therefore, the ALM time step constraint is equivalent to a tangential CFL condition with $\mathrm{Co}_{\theta,max} = 1$ and characteristic velocity ωR.

Here, the choice of $U_\theta = \omega R$ as the characteristic tangential velocity is challenged. Given that the flow velocity simulated at the rotor plane is $\mathbf{V}$, the blade-local tangential velocity component will be $\mathrm{a}'\omega r$ (Figure 3.1). Typical values of the tangential induction factor a' suggest that at the tip $\mathrm{a}'\omega R < U_\infty < \omega R$. In the inboard sections of the blade the tangential induction factor typically increases, but it is still expected that $\mathrm{a}'\omega r < U_\infty$. Therefore, using $U_t = \omega R$ is an overestimation of the simulated tangential velocities at all spanwise locations. In fact, since typically $\mathrm{a}'\omega R < U_\infty$, restrictions imposed by tangential CFL conditions should be less constraining than the streamwise CFL condition expressed in Equation 3.2.

It is finally noted that the above discussion applies to a hexahedral mesh where the cell sizes at the streamwise and tangential directions are considered to be similar. For polar grids or alternative mesh topologies the conditions should be adjusted accordingly.

3.4.3 Relationship between the ALM time step condition and streamwise CFL constraint

Equations 3.2 and 3.3 define the minimum required number of time steps per rotor revolution as a function of mesh size and are displayed graphically in Figure 3.3. By comparing the two conditions that apply simultaneously in actuator line simulations, it is clear that the ALM time step constraint imposes a more significant restriction on the allowable time step compared to the constraint due to the streamwise CFL condition, which is a limitation widely acknowledged by the ALM community [130, 131]. In fact, for $\mathrm{Co}_{x,max} = 1$ and $\lambda = 1$ the streamwise CFL condition of Equation 3.2 reduces to the ALM time step constraint.

The ALM constraint was introduced by practitioners that use the CPS method described in Section 3.3.1. We hypothesise that potential convergence issues that led to the ALM time step constraint are in fact related to the sampling method. We therefore explore how different sampling methods perform with larger time steps. The sensitivity of the CPS method has already been challenged in Mittal *et al.*[120] in terms of mesh size and interpolation scheme and is here challenged in terms of time step.

3.5 Turbine Descriptions

Two horizontal axis turbines are analysed in this paper in order to generalise this study across different rotor geometries. The MEXICO (Model Experiments In Controlled Conditions) rotor [87] is an experimental wind rotor that has been studied extensively in the literature [44, 84, 129, 132] and has a local solidity (defined as $\sigma_r = N_B c_r/(2\pi r)$ where N_B is the number of blades and c_r is the blade chord at radius r) of $\sigma_{75\%} = 2.6\%$. The Sch15b tidal rotor [72, 133] has been optimised for blocked-flow conditions with high solidity and thrust and at 75% span it has a local solidity of $\sigma_{75\%} = 6.2\%$.

The MEXICO rotor has a diameter of $D = 4.5\,\mathrm{m}$. The blade chord and twist distributions are shown in Figure 3.4. It consists of three aerofoils: DU91-W2-250 (20% to 45.6% span), RISØ-A1-21 (54.4% to 65.6%) and NACA 64-418 (74.4% to

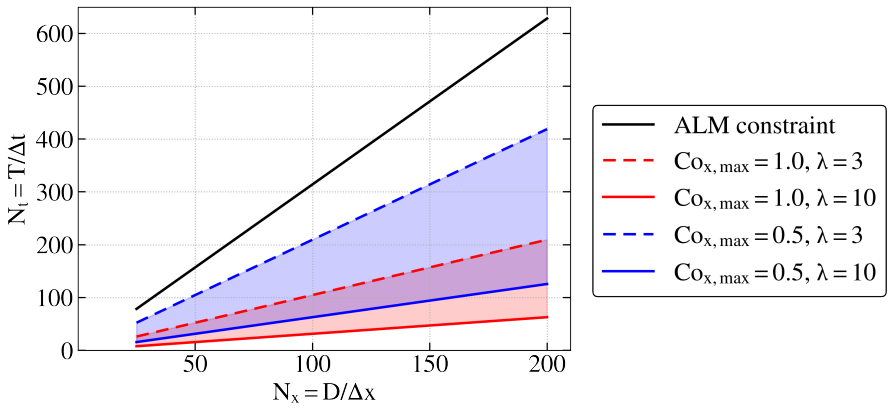


Figure 3.3: The minimum allowable number time steps N_t corresponding to different mesh sizes N_x, using the ALM time step constraint and streamwise CFL condition. While the ALM constraint is independent of λ, the streamwise CFL condition depends on λ. The shaded areas correspond to a typical λ range ($3 \leq \lambda \leq 10$) for each of the two $\mathrm{Co}_{x,max}$ values visualised here, to account for local accelerations. As an example, this diagram reads: for $\mathrm{Co}_{x,max} = 0.5$, $\lambda = 3$ and a hexahedral mesh with $N_x = 100$ cells per rotor diameter, at least $N_t \approx 310$ time steps per rotor rotation are required for the ALM constraint to be satisfied. Only $N_t \approx 210$ time steps per rotation are needed to remain within the limits of the streamwise CFL condition.

the tip). Aerofoil lift and drag data across the transition pieces between sections are linearly interpolated. The aerofoil polars used in the ALM simulations in this paper have been directly extracted from BR Reynolds-Averaged Navier-Stokes (RANS) simulations and therefore no tip-correction is needed (Appendix C). The design tip-speed ratio is 6.67 and design root pitch angle is $-2.3°$. In this paper, a tip-speed ratio of $\lambda = 10$ is simulated, as at this tip-speed no flow separation is observed at any point along the blade that could complicate the angle of attack calculations.

The Sch15b tidal rotor has a diameter of $D = 20$ m and was optimised for a blockage of $B = 19.6\%$. The spanwise distribution of blade chord and twist can be seen in Figure 3.4. The blade profile consists of the relatively thick RISØ-A1-24 aerofoil, except for the inboard region $r/R \leq 0.15$ where the blade cross-section transitions into a cylindrical profile for connection into the nacelle. As with the MEXICO rotor, the lift and drag data used for the ALM simulations are sourced from BR simulations of the same rotor (Appendix C). The design tip-speed is 5.5 and the ALM simulations are performed at $\lambda = 4.8$, which is found to be the optimal tip-speed for this rotor for unblocked conditions [72].

The design characteristics of the two rotors are summarised in Table 3.1. An overlay of the two rotors is presented in Figure 3.5.

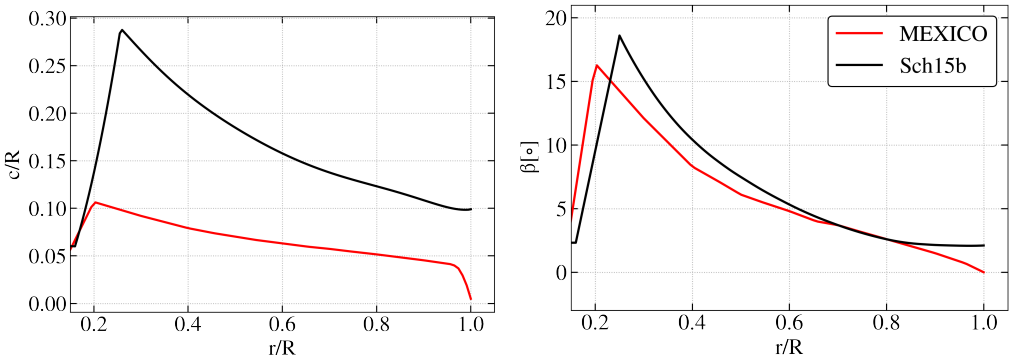


Figure 3.4: Spanwise distribution of the chord non-dimensionalised by the tip radius (left), and the blade twist (right) for the MEXICO (red) and Sch15b (black) rotors. The MEXICO twist distribution is shown without considering the design root pitch angle of $-2.3°$.

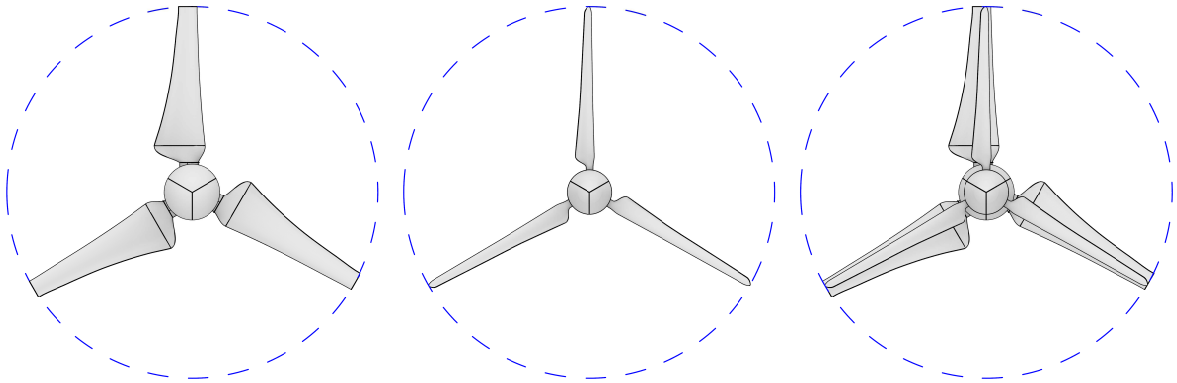


Figure 3.5: Render comparing the profiles of the Sch15b (left) and MEXICO (middle) rotors, and an overlay of both (right). The rotor profiles are non-dimensionalised by their respective radius.

Turbine	Type	N_b	D [m[	D_{nac} [m]	λ_d	U_d [m/s]	λ	U_∞ [m/s]	$\mathrm{Re}_{75\%}$
MEXICO	Wind	3	4.50	0.54	6.7	15.0	10.00	10	$\sim$0.6 $\times 10^6$
Sch15b	Tidal	3	20.00	3.00	5.5†	2.0	4.8	4.5	$\sim$ 27 $\times 10^6$

† Design tip-speed ratio for a blockage of $B = 19.6\%$

Table 3.1: Main design and operational parameters of the MEXICO and Sch15b rotors, displaying type of turbine, number of blades N_B, rotor and hub diameters, design tip-speed ratio λ_d and velocity U_d, simulated tip-speed ratio λ, velocity U_∞ and chord-based Reynolds number $\mathrm{Re}_{75\%}$ evaluated at $r/R = 0.75$ and the simulated conditions.

3.6 Numerical Solution

3.6.1 Numerical and ALM set-up

The ALM used in this study was adapted from SOWFA [121] validated by Wimshurst [134] and later transferred to OpenFOAM version v2006 [125]. The URANS equations are solved numerically using the PISO algorithm for pressure-velocity coupling. The $k-\omega$ SST turbulence model with updated coefficients [101] is adopted for turbulence closure. A second order backward differencing temporal discretisation scheme is employed, and the convective term is discretised using a blended central difference scheme. Chord-based Reynolds numbers are noted in Table 3.1. It is noted here that although the present analysis has been done using URANS, the conclusions have been confirmed for other unsteady approaches, such as LES (Appendix E).

The ALM parameters are chosen as follows: 100 collocation points are used per blade, distributed cosinusoidally with a concentration of points at the root and tip. The largest distance between collocation points, at the middle of the blade span, is smaller than the local cell size, Δx, ensuring that the kernels always overlap, a necessary condition to establish a continuous load distribution and independence of the ALM solution from the number of collocation points [73, 135]. The flow is sampled at every iterative loop of the PISO solver and the sampling method of step 1 is varied between the methods described in Section 3.3. The aerofoil polar coefficients needed in step 2 are based on interpolation of data from RANS-BR results (Appendix C). This choice ensures an accurate representation of the 3D flow effects along the blades that can be especially significant in tidal rotors.

For the last step of the ALM, the force smearing kernel shape is set to be a spherical Gaussian, introduced in Sørensen and Shen [69]:

$$\eta_\varepsilon(r) = \frac{1}{\varepsilon^3 \pi^{3/2}} \exp\left[-(r/\varepsilon)^2\right], \tag{3.4}$$

where r is the distance from the collocation point. The choice of ε in the above equation significantly affects the power and thrust prediction [62], and thus corrections for the decoupling of ε from the rotor loads have been proposed [88, 89, 90]. ε is usually

defined as a function of Δx and hereafter the ratio $N_\varepsilon = \varepsilon/\Delta x$ will be used. The lower limit $N_\varepsilon \geq 1$ ensures that the discretised integral of function 3.4 approximates to 1 for a hexahedral mesh. Another limit $N_\varepsilon \geq 2$ was established by Troldborg [61] for numerical stability. In the present work, in order to account for the effect of ε on turbine performance metrics, the width of the kernel of Equation 3.4 is varied from $N_\varepsilon = 2, 4, 8$, being a similar range as that used by Martínez Tossas *et al.* [62].

The two meshes were created for two different projects so their finest cell size is slightly different: for the MEXICO mesh it is $N_x = 160$ while for the Sch15b mesh it is $N_x = 180$. The mesh topology is of Hexcore type (Figure 3.6), created using OpenFOAM's snappyHexMesh. The domain size spans $[L, W, H] = [15D, 8D, 8D]$ for both rotors, giving a blockage ratio of ∼1.2%. Four levels of mesh refinement are used within the domain. The background mesh has a dimension of $D/10$ for MEXICO and $D/11$ for the Sch15b simulations. The cell dimension is halved in the region $[15D, 4D, 4D]$ centered on the rotor hub. Closer to the rotor, the cell dimensions halve a further three times to reach the finest cell size that occupies a cylinder of $[L, D_{cyl}] = [2D, 1.2D]$ centered on the rotor hub.

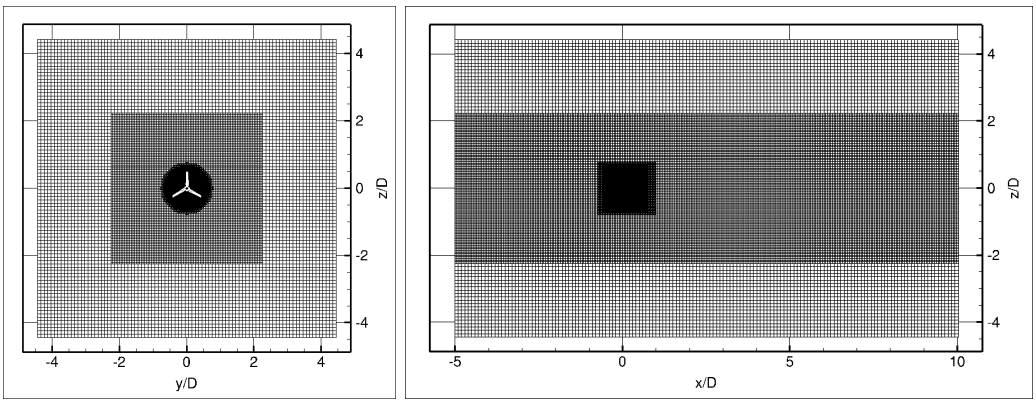


Figure 3.6: Mesh topology with a schematic of the MEXICO rotor for reference. Left: a cross section at the rotor plane $x = 0$. Right: a cross section at $y = 0$.

3.6.2 Mesh size guidelines in ALM simulations

Determining a general rule for meshing in ALM simulations is challenging; the difficulty stems from the fact that when Δx is varied, both $\varepsilon = f(\Delta x)$ and the time step, given by Equation 3.3, need adjustment. Those dependencies are combined

with other numerical considerations, for example the streamwise CFL condition of Equation 3.2. At the same time, different applications may call for different mesh topologies, such as polar grids. Finally, it may often be the case that following the ALM guidelines becomes prohibitively computationally expensive and a compromise in accuracy is required. Three types of applications for which the ALM is regularly used and their typical N_x values are described below.

In applications that focus on accurately calculating the blade loads, tip force reduction and tip vortices, very fine meshes might be employed, often with a polar topology [61, 69]. The cell dimension is often limited by the chord size as a result of ε being a function of the blade chord combined with the requirement that [70] $N_\varepsilon \geq 1$. Methods in this category might include the advanced ALM of Churchfield *et al.* [46] that focuses on representing the blade shape more accurately by employing an elliptical force smearing kernel that resembles the blade shape. They employed $N_x = 200$ and 900 for the two demonstrated cases in order to resolve the tip chord region.

Applications that focus on single rotor wakes or wakes of several rotors interacting with or without inlet turbulence, typically employ a cell size of [61, 73, 92, 135] $N_x = 60-150$. In these cases, the chord size is not considered and therefore $\varepsilon = f(\Delta x)$. At this scale, Martínez-Tossas *et al.*[62] concluded, that for mesh independence $N_\varepsilon > 5$.

In applications that focus on the large farm-scale dynamics, convergence is usually assessed using the mean flow field metrics and therefore mesh requirements are less demanding. In these cases, larger cell sizes are accepted in order to facilitate larger domain sizes, with typical values of N_x between 15 [65] and 50 [49, 136].

It is evident that depending on the focus of the simulation the mesh evolves from a very fine mesh with comparable cell count to a BR simulation, where scales are based on the local chord of the blade, to a coarse mesh with large ε values that lead to a wider force smearing, with comparable resolution to an ADM simulation, where scales are based on the diameter of the rotor.

3.6.3 Mesh sensitivity analysis

Following from the literature review of the previous section, a broad range of cell sizes is considered here: $N_x = 40, 80$ & 160. The value of ε i.e. N_ε, and time step, i.e. N_t are varied to achieve mesh convergence for the three sampling methods. Two different values of ε and two values of time step are tested for the three sampling methods described in Section 3.3. In total, 36 simulations were performed to ensure mesh convergence.

When assessing mesh independence of the ALM, two approaches for the determination of ε may be followed. First, $N_\varepsilon = const$ may be employed, where the value of ε changes with the varying mesh resolution, N_x. In this case, the effective blade size scales with the mesh size, and convergence may not be achieved [73]. Here we follow a second approach, according to which the physical width of the Gaussian force smearing kernel ε is kept constant when changing N_x so that the effective rotor geometry also remains the same.

Two values of ε are tested for convergence: $N_{\varepsilon,c} = 0.5$ and 1, where $N_{\varepsilon,c} = \varepsilon/\Delta x_c$ and Δx_c is the cell size of the coarsest mesh $N_x = 40$. Despite that $\varepsilon = 0.5\Delta x_c$ is invalid (i.e. $N_\varepsilon < 1$) for the $N_x = 40$ mesh, this ε value is valid for the other two meshes and therefore the simulations are still performed (the out-of-range simulations are represented using dashed lines in Figure 3.7). Their relative errors are naturally very high and therefore those results are not included in the following discussion. Despite the large errors for the $N_x = 40$ case, $\varepsilon = 0.5\Delta x_c$ was chosen because it corresponds to a thinner kernel (i.e. $N_\varepsilon = 2$ for a mesh $N_x = 160$) that is common in the literature.

For the time step, two values $\Delta s/\Delta x = 0.5, 1$ are tested. Here, for each mesh size N_x the time step is adjusted so that the ratio $\Delta s/\Delta x$ is kept constant.

To quantify convergence in N_x, and later N_ε and N_t, the relative error of the metric C_*, that can either be the power coefficient $C_P = P/\frac{1}{2}\rho U_\infty^3 A$ or the thrust coefficient $C_T = T/\frac{1}{2}\rho U_\infty^2 A$, where ρ is fluid density and A the rotor area, is defined as

$$\varepsilon_{rel}^{N_{ref}}(C_*^N) = \frac{C_*^N - C_*^{N_{ref}}}{C_*^{N_{ref}}}. \tag{3.5}$$

N_{ref}, the superscript to ε_{rel}, indicates the simulation that is used as the reference in calculating the relative error, usually the most converged simulation. N, the superscript of C_*, indicates the simulation for which the error is calculated. For example $\varepsilon_{rel}^{N_x=160}(C_P^{Nx=80})$ is the relative error of the power coefficient calculated for a mesh resolution of $N_x = 80$ with reference to the power coefficient calculated for the finer mesh resolution of $N_x = 160$.

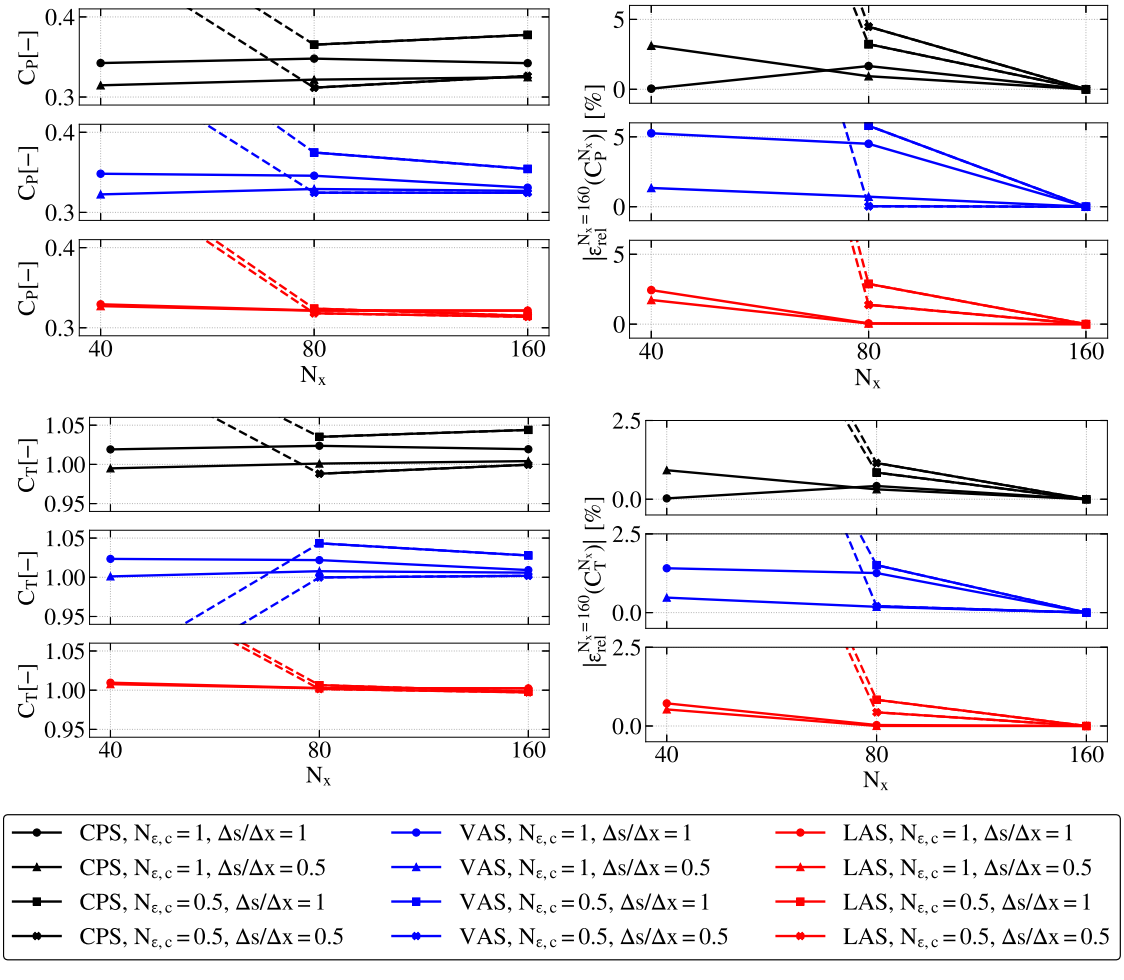


Figure 3.7: MEXICO rotor. Left: dependence of power (upper panel) and thrust (lower panel) coefficients on the mesh size, N_x for varying $N_{\varepsilon,c}$ and time step $\Delta s/\Delta x$. Velocity sampling is performed using the collocation point sampling (CPS) method, volume average sampling (VAS) and line average sampling (LAS). Right: Relative error $\varepsilon_{rel}^{N_x=160}$ with respect to the finest $N_x = 160$ simulations. Invalid simulations with $N_\varepsilon < 1$ are denoted with dashed lines.

As can be seen in Figure 3.7 all three methods for varying ε and $\Delta s/\Delta x$ ratios converge to within 6% for C_P and 1.5% for C_T for all the valid cases (solid lines). Therefore, both $N_x = 40$ and $N_x = 80$ cases are considered converged to within an error threshold of 6% for C_P relative to the most refined suite of simulations. The case $N_x = 160$ will be used in the following discussion and analysis, so that smaller ε values can be employed that might be closer in dimension to the rotor's real geometry.

Some scatter is observed in the $N_x = 160$ results as a function of different $N_{\varepsilon,c}$ and $\Delta s/\Delta x$ values. As a broad indicator, the relative difference of C_P between the largest and smallest prediction calculated as $2(C_{P,max} - C_{P,min})/(C_{P,max} + C_{P,min})$ is 15% for CPS, 8% for VAS and 2.4% for LAS. The dependence of the methods on ε and Δt will be discussed in more detail in the next sections.

3.7 Results

Simulations were performed to investigate the effect of the time step and force smearing radius on ALM simulations. As can be seen in Table 3.2 for the MEXICO and Sch15b rotors, 5 different time step values N_t were simulated at 3 different Gaussian force smearing widths N_ε and with 3 different sampling methods. It is noted that VAS was only performed for $N_\varepsilon = 2, 4$ as the number of sampling points increases with the cube of ε and $N_\varepsilon = 8$ was exhaustive for the current implementation of the method. However, this does not limit our conclusions as $N_\varepsilon = 8$ is not typically used in the literature due to the large force smearing region it involves. Therefore, a total of 40 simulations per rotor, 80 simulations in total, were performed. The power and thrust coefficients have been calculated for both rotors. Additionally for the wind rotor, angles of attack at 80% radius, instantaneous streamwise velocity contours at the rotor plane and instantaneous streamwise velocities at 80% radius and 40° azimuthal range are extracted to further analyse the interactions between the actuator line method and the simulated flow field.

Rotor	Sampling Method	N_x	N_t	N_ε
MEXICO	CPS, VAS, LAS	160	$100, 200, 400, 800, 1600$	$2, 4, 8$ †
Sch15b	CPS, VAS, LAS	180	$100, 200, 400, 800, 1600$	$2, 4, 8$ †

† For the VAS cases, $N_\varepsilon = 8$ was not performed due to computational cost.

Table 3.2: Summary of simulations performed in this study.

3.7.1 Power and thrust coefficients

The dependence of power coefficient, thrust coefficient and angle of attack at 80% span on the time step for different sampling methods and N_ε values for the MEXICO rotor at $\lambda = 10$ is plotted in Figure 3.8. A large tip-speed has been chosen to avoid stall developing on the blade, which the MEXICO rotor experiences even at moderate tip-speed ratios. However, the trends and parameter interactions observed in this tip-speed have also been confirmed for tip-speed ratios closer to the design point, not presented here. The dependence of power and thrust coefficients on the sampling method, N_ε and N_t are also presented for the higher solidity Sch15b rotor at $\lambda = 4.8$ in Figure 3.9.

The CPS and VAS methods are strictly valid only for $\Delta s/\Delta x < 1$, as explained in Section 3.4.2. For this reason, $\Delta s/\Delta x = 1$ has been noted in the graphs of Figures 3.8 and 3.9, while values above this limit are depicted using dashed lines in order to highlight that the results are not within the accepted time step range. However, the full N_t range has been simulated in order to allow for comparisons with the LAS method.

It is also worth noting that given the streamwise CFL condition of Equation 3.2, $N_x = 160$, $\lambda = 10$ and accounting for local accelerations up to $u_{local} = 2U_\infty$ by setting $\mathrm{CFL}_{max} = 0.5$, the minimum number of time steps per rotation is calculated to be $N_t = 100$ and therefore none of the MEXICO rotor cases in Figure 3.8 violate the streamwise CFL condition. Similar calculations confirm a value of streamwise Courant number less than unity for all the Sch15b rotor simulations.

Convergence in N_t is asymptotic for all sampling methods, parameter settings and rotors, with the LAS method converging the fastest and at a much lower N_t, and the CPS method the slowest. Focusing on the MEXICO rotor for $N_\varepsilon = 4$, it can be

deduced that to achieve an arbitrary convergence threshold of $|\varepsilon_{rel}^{N_t=1600}(C_P^{N_t})| < 5\%$, a practitioner would need $N_t = 800$ using CPS, $N_t = 400$ using VAS and $N_t = 100$ using the LAS. The same time step requirement holds for $|\varepsilon_{rel}^{N_t=1600}(C_T^{N_t})| < 5\%$. The Sch15b rotor also benefits from the LAS implementation, as it experiences even more pronounced dependence of power and thrust coefficients on N_t when methods such as the CPS or VAS are employed.

The dependence of the ALM on N_ε is present for all sampling methods and has long been recognised in various works [62, 70, 92], with corrections proposed in [88, 89, 90]. It is here demonstrated that the sensitivity to N_ε generally depends on N_t for both CPS and VAS methods, for the demonstrated time step range and simulated rotors. On the contrary, for LAS, the sensitivity to N_ε remains approximately constant and small for varying N_t.

While the focus of this work is on the robustness of the ALM, its accuracy is also assessed by comparing C_P and C_T calculated using the ALM against the equivalent values calculated using higher-fidelity BR simulations (Appendix C). All ALM implementations underestimate the loads for $N_t = 800$ & 1600 for the MEXICO rotor. A different trend is observed for the Sch15b rotor where CPS and VAS present parameter-dependent scatter around the BR coefficients, while LAS presents a consistent overestimation. Sources of errors against a high-fidelity method may be attributed to a number of numerical factors. Importantly, it is demonstrated here that LAS is capable of consistently reducing the sensitivity of the ALM results to two user-defined parameters, N_ε and N_t. The method therefore ensures robustness that is a pre-requisite before accuracy can be assessed.

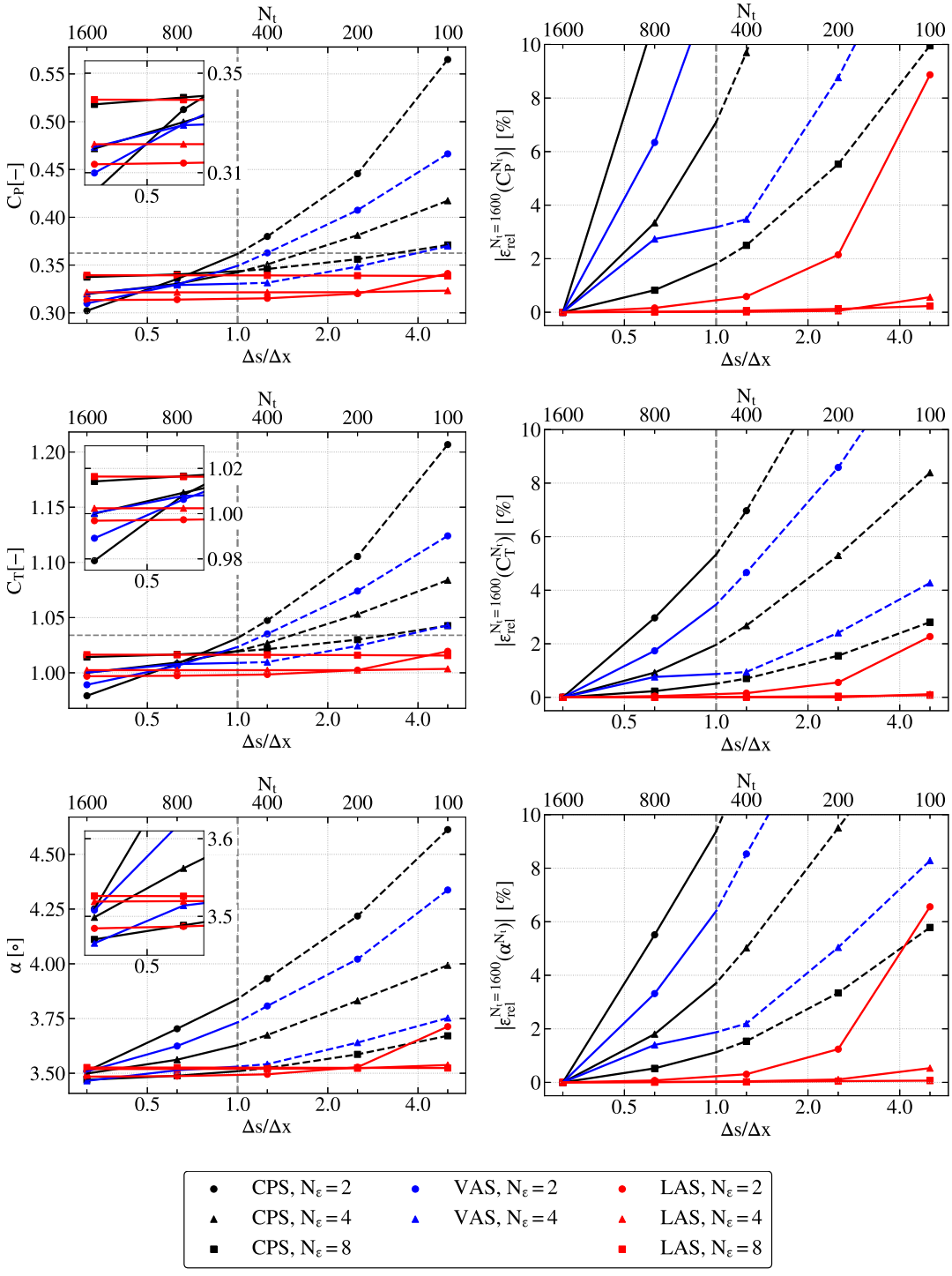


Figure 3.8: MEXICO rotor, $N_x = 160$. Left: sensitivity of power coefficient C_P (upper panel), thrust coefficient C_T (middle panel) and angle of attack α at 80% radius (lower panel) to the time step for various N_ε values and three sampling methods: CPS, VAS and LAS. The grey horizontal lines denote C_P and C_T values calculated from the BR simulations described in Appendix C. Right: relative error of the same metrics with respect to the most temporally converged case with $N_t = 1600$. $\Delta s/\Delta x$ is a proxy for time step, with $\Delta s/\Delta x = 1$ denoted by a vertical line. Invalid simulations that use CPS or VAS with $\Delta s/\Delta x > 1$ are denoted with dashed lines.

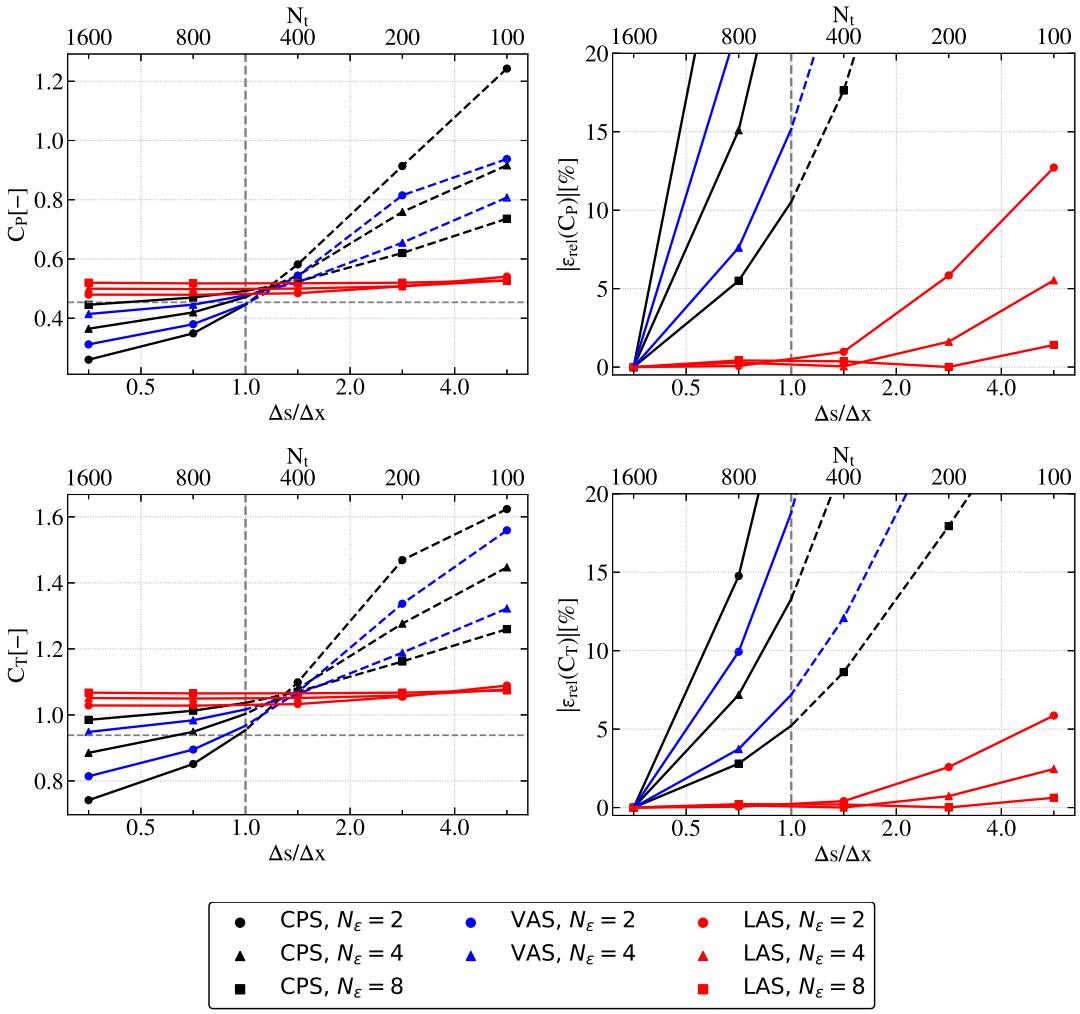


Figure 3.9: Sch15b rotor, $N_x = 180$: counterpart of Figure 3.8 for the Sch15b rotor. Left: sensitivity of power coefficient C_P (upper panel) and thrust coefficient C_T (lower panel) to the time step for various N_ε values and three sampling methods: CPS, VAS and LAS. The grey horizontal lines denote C_P and C_T values calculated from the BR simulations described in Appendix C.Right: relative error of the same metrics with respect to the most converged case of $N_t = 1600$. $\Delta s/\Delta x$ is a proxy for time step, with $\Delta s/\Delta x = 1$ denoted by a vertical line. Invalid simulations that use CPS or VAS with $\Delta s/\Delta x > 1$ are denoted with dashed lines.

3.7.2 Spanwise force distributions

In order to explore the spanwise distribution of the contributions to the errors observed in Figure 3.8, the axial force and torque per unit span (F_{ax} and Q, respectively) are examined for selected simulations. The distributions correspond to the calculated C_T and C_P values discussed in the previous Section.

The axial force and torque distributions for a time step value close to the ALM time step constraint, $N_t = 400$, and smearing radius values of $N_\varepsilon = 2$ & 4, are presented in Figure 3.10. Dependence of the spanwise loads on ε is observed for radial locations $r/R > 0.5$ for CPS and VAS methods, and for $r/R > 0.8$ for LAS method.

The dependence of the sampling methods on ε is further visualised in Figure 3.11, where the difference between predicted loads at each spanwise location using two different Gaussian kernel widths is presented. At $N_t = 400$ the dependence of the CPS and VAS methods on ε is greatest towards the mid-span, with oppositely-signed differences in the tip region providing compensation for the overall error metric. This mid-span sensitivity to ε for CPS and VAS is eliminated by increasing the number of time steps per rotation to $N_t = 1600$ in which case dependence on ε is concentrated towards the tip of the blade. For LAS, the dependence on ε is concentrated towards the tip region regardless of the N_t value. A comparison between blade resolved simulations and ALM results is presented by comparing radial distributions of axial force and torque in Figure 3.12. The comparison is made for $N_\varepsilon = 2$ and a range of time step values $N_t = 400 - 1600$. Similar to the comparison for varying N_ε, the CPS and VAS methods demonstrate greater sensitivity to N_t than the LAS method. When $N_t = 1600$, all methods generate similar predictions that follow the general trends of the blade resolved simulations including in the tip region, albeit with slight underestimation of the sectional torque across the blade span. Uncertainties near the tip emerge naturally within the ALM due to the invalidation of the two dimensional flow assumption [85] and the underestimation of the induced downwash near the tip [137]. Tip forces here are consistent across the simulations but might deviate slightly from the BR predictions.

The differences in the sectional axial force predictions are relatively smaller due to the reduced sensitivity to the flow angle and drag component of the blade force.

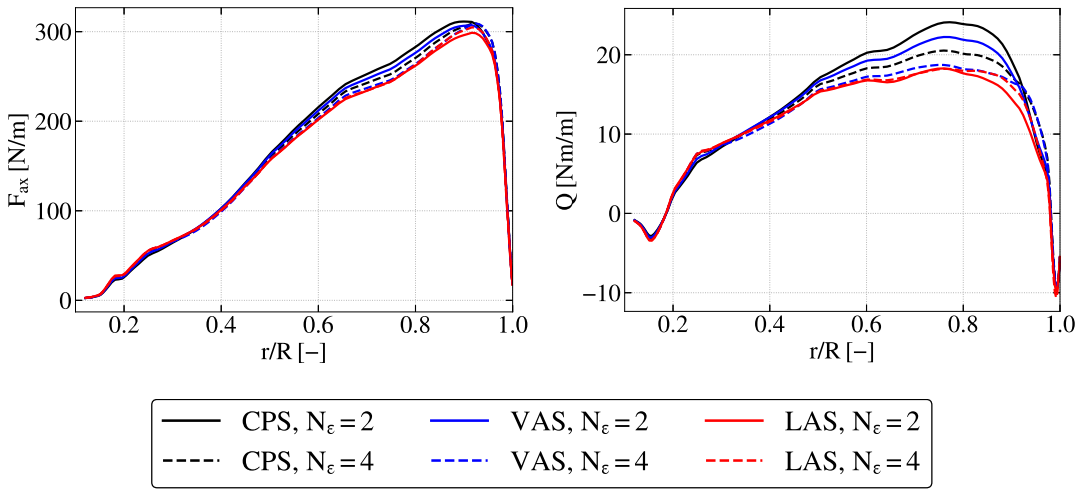


Figure 3.10: MEXICO rotor, $N_x = 160$, $N_t = 400$. Local axial force (left) and torque (right) per unit span against non-dimensional radius. The entire span is displayed in the upper panel while the tip region, $r/R \geq 0.8$, is examined closely in the lower panel. Spanwise distributions are displayed for $N_\varepsilon = 2, 4$ and three sampling methods, CPS, VAS, and LAS.

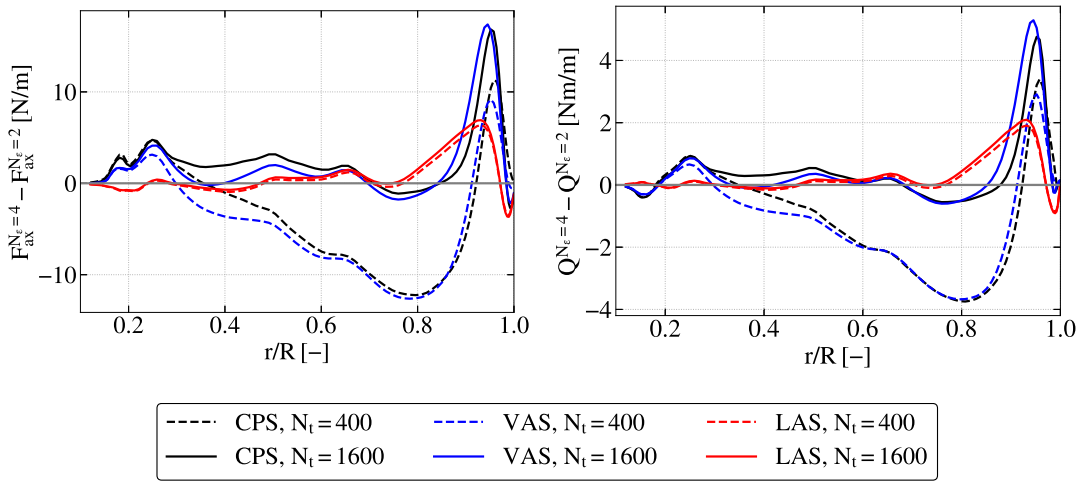


Figure 3.11: MEXICO rotor, $N_x = 160$. Difference in local axial force (left) and torque (right) per unit span between the predictions for $N_\varepsilon = 4$ and $N_\varepsilon = 2$ against the non-dimensional radius. Spanwise distributionss are presented for three sampling methods: CPS, VAS, and LAS.

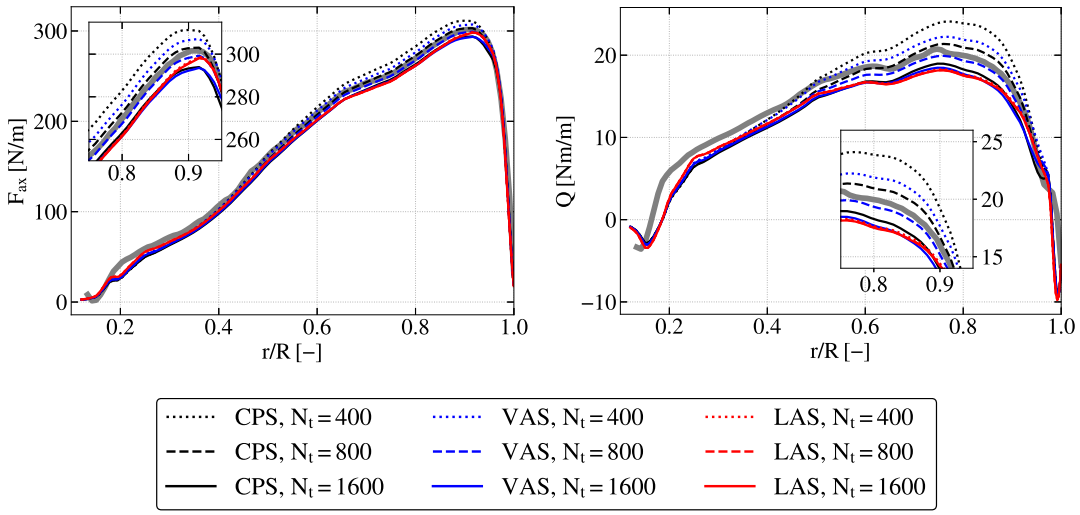


Figure 3.12: MEXICO rotor, $N_x = 160$, $N_\varepsilon = 2$. Local axial force (left) and torque (right) per unit span against non-dimensional radius. Spanwise distributions are presented for $N_t = 400$, 800, & 1600, and three sampling methods: CPS, VAS, and LAS. The grey line denotes results from BR simulations.

3.7.3 Instantaneous velocity

The values of N_ε and N_t are found to affect the instantaneous force imparted onto the flow field at each time step, resulting in differences in the simulated flow field and hence differences in the rotor performance metrics as described above. Two effects of these ALM parameters on the simulated flow field are described in further detail: the development of spurious oscillations, and the fidelity in simulating the viscous vortex represented by the actuation line.

Spurious oscillations

It is widely reported in the literature that when applying the ALM with a very small value of N_ε, spurious momentum streaks can develop in the flow field, an observation that led to the constraint [61] $N_\varepsilon \geq 2$. This constraint was derived while keeping the value of N_t within the traditional ALM limits. Here, we demonstrate that this oscillatory behaviour is a combination of the chosen N_ε and N_t, since the spurious momentum streaks arise when two subsequent actuator line positions are too far away from each other, either due to a very small Gaussian force smearing radius or due to a very large time step.

As can be seen in Figure 3.13 the spurious momentum streaks are observed for all sampling methods at $N_t = 100$ due to the large time step. When $N_t = 200$, corresponding to $\Delta s/\Delta x > 2$, the oscillatory behaviour is suppressed, meaning that disregarding the ALM time step constraint does not necessarily lead to spurious oscillations. However, at large time steps, $N_t \approx 200$, the velocity fields when using the CPS and VAS methods present an excessively large velocity reduction at the rotor region that does not correspond to the blade shape. Both methods eventually obtain a more realistic flow field as the time step is reduced to $N_t = 1600$. The LAS method on the other hand, does not experience this velocity reduction variation with time step and therefore the $N_t = 200$ and $N_t = 1600$ flow fields look qualitatively similar.

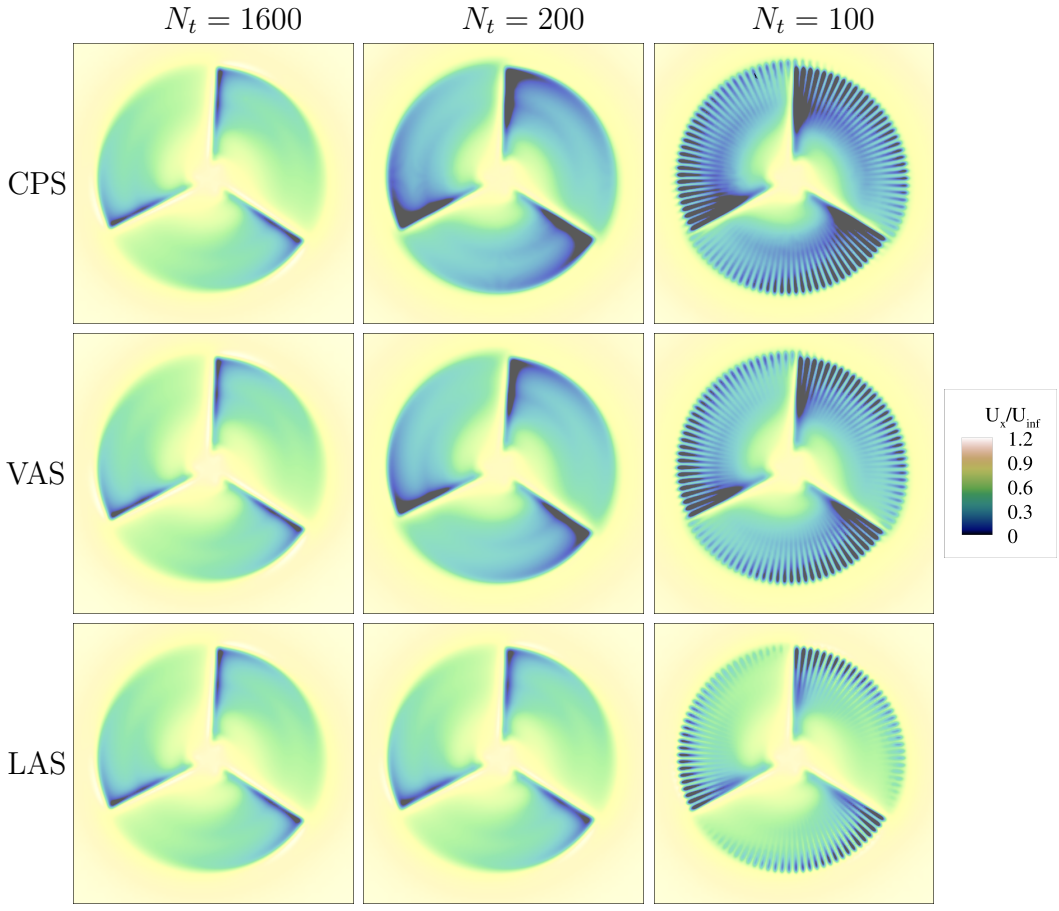


Figure 3.13: MEXICO rotor, $N_x = 160$, $N_\varepsilon = 2$: non-dimensional instantaneous streamwise velocity fields at the rotor plane arising from the three velocity sampling methods CPS (upper panel), VAS (middle panel) and LAS (lower panel) and for three different time step values $N_t = 1600$ (left), $N_t = 200$ (centre) and $N_t = 100$ (right). The procedure for calculating the blade force and imposing it on the flow remains unchanged between simulations.

Azimuthal variations of streamwise velocity

To obtain a more detailed image of the flow around the actuator line, the instantaneous streamwise velocity has been extracted at the rotor plane across an arc of $\pm 20^\circ$ at $r/R = 80\%$ radius for various N_t values and constant $N_\varepsilon = 2$ for all three sampling methods, shown in Figure 3.14. To explore the dependence on N_ε, the flow simulated at various N_ε values, constant $N_t = 1600$, and all three sampling methods is presented in Figure 3.15, for the same azimuthal range and spanwise location as the previous figure.

The two figures exhibit similarities, independent of the varying parameters. First, for each simulation $U_x(-20^\circ) > U_x(20^\circ)$, as a result of the wake of the blade. Second, the perturbation in streamwise velocity as a result of the ALM Gaussian force of step 3, is similar to a Lamb-Oseen viscous vortex as observed by Dag and Sørensen [88] and detailed in Appendix D, and can be identified in all simulations in the vicinity of the blade. It is important to note that the viscous vortex cannot be strictly characterised as a Lamb-Oseen vortex as the background flow is non-uniform and three-dimensional and significant blade drag may be present. However, approximating the flow in the vicinity of the blade as a Lamb-Oseen vortex facilitates the characterisation of the flow field at this location.

The change of the streamwise velocity at $r/R = 80\%$ when varying N_t and N_ε will be quantified and discussed. Two azimuthal locations are of particular interest: $\theta = \pm 20^\circ$, which represents the flow away from the influence region of the force smearing kernel; and $\theta = 0^\circ$, which represents the viscous vortex at the vicinity of the blade. The streamwise velocity at $\theta = \pm 20^\circ$ is related to the the rotor-scale induction. To quantify the behaviour of the rotor-scale flow, the thrust coefficient C_T and the disc area-averaged streamwise velocity $\langle U_x \rangle_{disc}$ at the rotor plane have been presented in Tables 3.3 and 3.4.

The second location of interest is the blade location around $\theta = 0^\circ$ where the distinctive shape of the velocity induced by a viscous vortex is superimposed on the background velocity field. The location of the vortex is analysed in terms of the difference between the instantaneous streamwise velocity at the blade

location, $U_x(0°)$, and the azimuthally-averaged streamwise velocity at $r/R = 80\%$, $\langle U_x \rangle_{r/R=80\%}$. The latter is subtracted from the former in order to decouple the rotor-scale induction from the blade-local flow. The strength and shape of the vortex is characterised by its strength Γ and radius R_{core} as described in Appendix D. These values are calculated in a way that decouples them from the rotor-scale induction.

Effect of N_t on the instantaneous velocity field

The streamwise velocity at $\theta = \pm 20°$ can be significantly affected by N_t, as shown in Figure 3.14. The instantaneous streamwise velocity at $\theta = \pm 20°$ for CPS and VAS increases with N_t, resulting from the reduction in C_T with increasing N_t shown in Figure 3.8, as lower values of C_T allow a higher mass flow rate through the rotor. In the case of LAS, where the C_T values are robust with the change in time step, the streamwise velocity at $\theta = \pm 20°$ is also unchanged. The disc area-averaged velocity $\langle U_x \rangle_{disc}$ presented in Table 3.3 demonstrates the same trend, confirming that the rotor-scale reduction in mass flow rate, linked to C_T, is affected by N_t. For $N_t = 800$, where the ALM time step constraint is followed, $\varepsilon_{rel}^{N_t=1600}(\langle U_x \rangle_{disc}^{N_t=800})$ is -6.03%, -4.29% and -0.55%, for CPS, VAS, and LAS respectively. It is noted that for LAS the same error is still only -3.11% for $N_t = 200$.

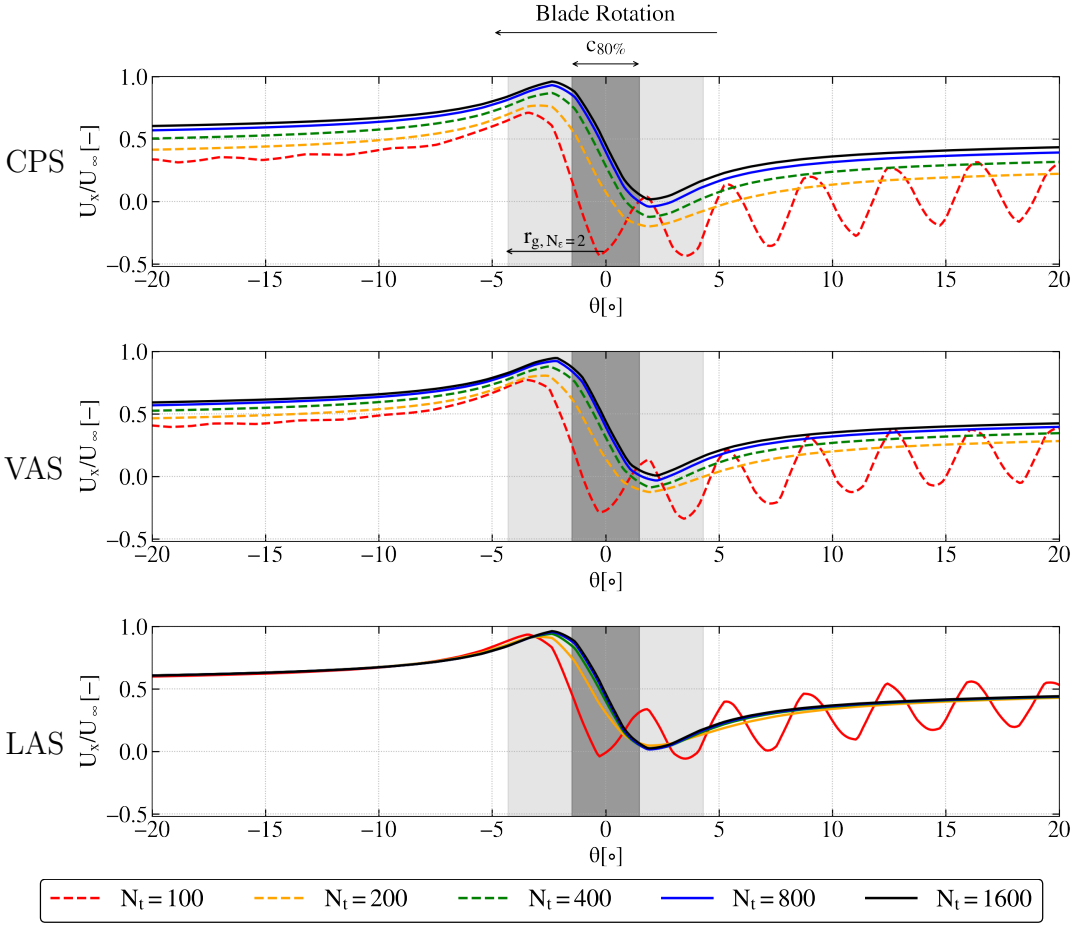


Figure 3.14: MEXICO rotor, $N_x = 160$, $N_\varepsilon = 2$: non-dimensional instantaneous streamwise velocity at $r/R = 80\%$ and at angles of azimuth in the range $\pm 20°$ around the blade ($\theta = 0$) for various N_t values, with fixed $N_\varepsilon = 2$. The three sampling methods are tested: CPS (upper panel), VAS (middle panel) and LAS (lower panel). It is noted that CPS and VAS methods for with $N_t = 100$, 200 & 400 are invalid due to violation of the ALM constraint, but are plotted in dashed lines for demonstration purposes. The dark grey shaded area corresponds to the chord dimension at $r/R = 80\%$. The light shaded area represents the maximum area of influence of the Gaussian force smearing kernel with $N_\varepsilon = 2$ (i.e. the diameter of the spherical kernel).

	N_t	200†	400†	800	1600	$\varepsilon_{rel}^{N_t=1600}(C_*^{N_t=200})[\%]$ †	$\varepsilon_{rel}^{N_t=1600}(C_*^{N_t=400})[\%]$ †	$\varepsilon_{rel}^{N_t=1600}(C_*^{N_t=800})[\%]$
C_T [-]	CPS	1.129	1.063	1.014	0.986	14.53	7.85	2.90
	VAS	1.074	1.035	1.007	0.990	8.54	4.62	1.74
	LAS	1.002	0.998	0.9973	0.9969	0.56	0.16	0.04
$\langle U_x \rangle_{disc}/U_\infty$ [-]	CPS	0.375	0.469	0.535	0.569	-34.10	-17.46	-6.03
	VAS	0.423	0.486	0.531	0.554	-23.69	-12.29	-4.29
	LAS	0.546	0.556	0.561	0.564	-3.11	-1.41	-0.55
$(U_x(0°) - \langle U_x \rangle_{80\%})/U_\infty$ [-]	CPS	-0.244	-0.132	-0.090	-0.071	-	-	-
	VAS	-0.212	-0.103	-0.074	-0.056	-	-	-
	LAS	-0.211	-0.124	-0.089	-0.071	-	-	-
R_{core} [m]	CPS	0.069	0.060	0.060	0.059	16.67	2.38	2.38
	VAS	0.064	0.062	0.063	0.063	2.22	-2.22	0.00
	LAS	0.069	0.060	0.060	0.059	16.67	2.38	2.38
Γ [m^2/s]	CPS	3.280	2.941	2.884	2.735	19.90	7.53	5.45
	VAS	2.952	2.940	2.969	2.919	1.11	0.69	1.68
	LAS	2.941	2.741	2.787	2.718	8.22	0.85	2.54

† Time steps $N_t = 200, 400$ for CPS and VAS are outside the acceptable time step range and are reported only to allow for comparisons with LAS.

Table 3.3: MEXICO rotor, $N_x = 160$, $N_\varepsilon = 2$: quantification of rotor and velocity metrics with the change in N_t, also presented in Figures 3.8 and 3.14. Five metrics are quantified: the thrust coefficient C_T, the non-dimensional area-averaged streamwise velocity over the rotor disc ($\langle U_x \rangle_{disc}/U_\infty$), the non-dimensional velocity difference $(U_x(0°) - \langle U_x \rangle_{r/R=80\%})/U_\infty$, characteristic of the change in streamwise velocity at $\theta = 0°$ and $r/R = 80\%$, and the radius R_{core} and strength Γ of the approximate Lamb-Oseen vortex. The metrics are calculated for all demonstrated N_t values, excluding the spurious solution at $N_t = 100$. The relative error for $N_t = 200, 400, 800$ using Equation 3.5 is also displayed. The procedure for calculating the blade force and imposing it on the flow remains unchanged.

The velocity in the viscous vortex region around $\theta = 0°$ also exhibits sensitivity to N_t, as shown in Figure 3.14. For CPS and VAS, the velocity around $\theta = 0°$ is affected by both the rotor-scale induction discussed above, and by the blade-local flow behaviour. To decouple the two scales, the azimuthally averaged streamwise velocity at $r/R = 80\%$ has been subtracted from $U_x(0°)$ (see Table 3.3). For all methods, the intercept approaches zero as $N_t \to 1600$. It is noted that the LAS does not provide faster convergence of the intercept to zero with N_t despite its robustness with respect to the rotor-scale metrics. The VAS method provides consistent predictions of R_{core} and Γ even for larger time steps. For LAS, the metrics are within 2.38% and 0.85% error respectively at $N_t = 400$, while for CPS a larger N_t is necessary to achieve such low errors for Γ.

It is therefore inferred from Figure 3.14 that the choice of N_t significantly impacts rotor-scale metrics like C_T and $\langle U_x \rangle_{disc}$ for CPS and VAS, justifying the ALM time step constraint of Equation 3.3. For LAS the rotor-scale metrics are insensitive to the time step, even for smaller values of N_t that may allow Δt to exceed the ALM constraint limits. When comparing the induced flow field in the vicinity of the blade ($\theta = 0°$) for a single spanwise position $r/R = 80\%$, all methods demonstrated comparable sensitivity to N_t, with the LAS showing no significant improvement in that region and VAS providing the most consistent predictions for the viscous vortex metrics. This suggests that the LAS method is capable of decoupling the blade-local and rotor-scale flows.

Effect of N_ε on the instantaneous velocity field

Figure 3.15 shows that varying N_ε and keeping N_t constant ($N_t = 1600$) does not significantly affect the streamwise velocity at $\theta = \pm 20°$ nor $\langle U_x \rangle_{disc}$, as C_T also remains approximately constant (Table 3.4). On the other hand, the viscous vortex core radius R_{core} in the vicinity of the actuator line, changes substantially with N_ε. For $N_\varepsilon = 2, 4, 8$, the physical dimension of $\varepsilon = 0.056, 0.1125, 0.225$ m, respectively. These values follow closely the R_{core} measured values for the respective N_ε for all three methods. $R_{core} = \varepsilon$ was first observed by Dag [88] for a stationary

wing. Here, depending on the method, $R_{core} \approx \varepsilon$. The difference between the observation here and Dag and Sørensen's [88] observation may be attributed to the non-uniform and three-dimensional nature of the current flow, when compared to the stationary wing case of Dag and Sørensen [88]. The circulation Γ is more consistent across different values of N_ε.

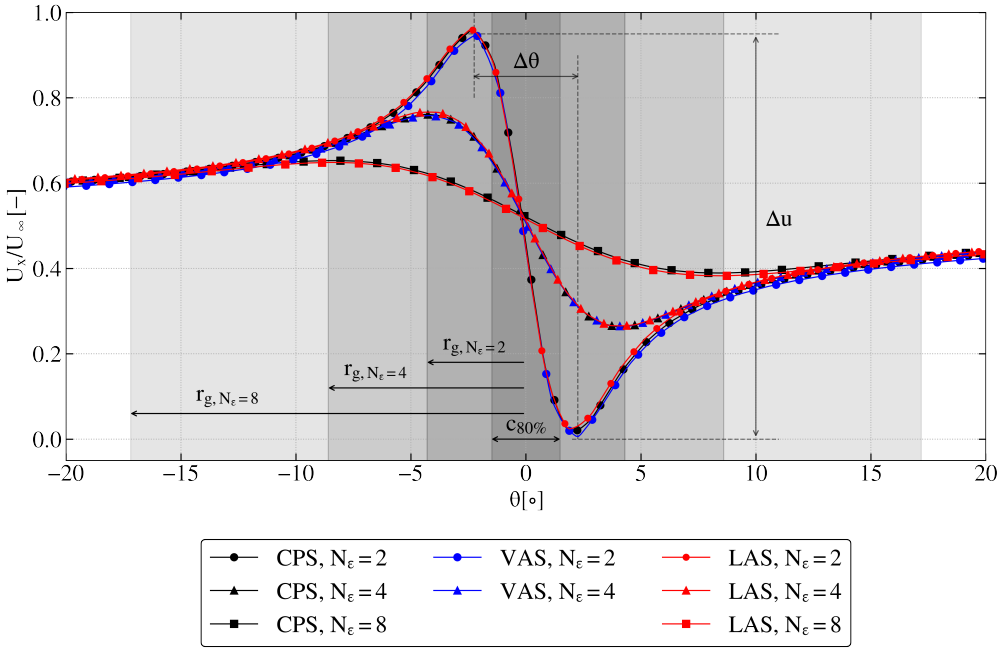


Figure 3.15: MEXICO rotor, $N_x = 160$, $N_t = 1600$: non-dimensional instantaneous streamwise velocity at $r/R = 80\%$ and at angles of azimuth in the range $\pm 20°$ around the blade location ($\theta = 0°$) for various N_ε values, with fixed $N_t = 1600$. The three sampling methods are tested: CPS, VAS, LAS. The darkest grey shaded area corresponds to the chord dimension at $r/R = 80\%$. The next grey areas from the narrowest to the widest represent the diameter of the Gaussian force smearing kernels (equal to 6ε) for $N_\varepsilon = 2, 4, 8$, respectively. These N_ε give Gaussian kernel diameters of $12\Delta x$, $24\Delta x$ and $48\Delta x$ respectively.

Finally, for a given value of N_ε and ensuring that all methods are sufficiently converged in time, agreement is observed between the three sampling methods (Figure 3.15). This suggests that ultimately the methods can all be made to be nearly equivalent in the sampled velocities and thus imposed forces but have different time step convergence requirements. Each method is equally sensitive to N_ε in terms of the resulting velocity fluctuation that is simulated around the actuator line.

To summarise the above, for a sufficient number of time steps per rotation, the

	N_ε	2	4	8	$\varepsilon_{rel}^{N_\varepsilon=4}(C_*^{N_\varepsilon=2})[\%]$
C_T [-]	CPS	0.99	1.00	1.01	1.44
	VAS	0.99	1.00	-	1.08
	LAS	1.00	1.00	1.02	0.55
$\langle U_x \rangle_{disc}/U_\infty$ [-]	CPS	0.57	0.57	0.59	0.79
	VAS	0.55	0.57	-	2.54
	LAS	0.56	0.57	0.59	1.33
$(U_x(0°) - \langle U_x \rangle_{80\%})/U_\infty$ [-]	CPS	-0.070	-0.020	-0.002	-
	VAS	-0.056	-0.011	-	-
	LAS	-0.071	-0.012	-0.002	-
R_{core} [m]	CPS	0.059	0.119	0.237	102.38
	VAS	0.063	0.122	-	93.33
	LAS	0.059	0.111	0.237	88.10
Γ [m^2/s]	CPS	2.74	2.93	3.07	6.96
	VAS	2.92	2.96	-	1.40
	LAS	2.72	2.73	3.10	0.60

Table 3.4: MEXICO rotor, $N_x = 160$, $N_t = 1600$: quantification of the variation in rotor and velocity metrics with N_ε, also presented in Figures 3.8 and 3.15. The same metrics as Table 3.3 are presented. The relative error using Equation 3.5 is also displayed.

three sampling methods produce similar flow fields and may be considered near equivalent (Figure 3.15). There is sensitivity to model parameters such as time step and ε, especially in the region in the vicinity of the actuator line where the flow field has been perturbed by the Gaussian blade force, and this sensitivity increases with increasing time step (Figure 3.14). The CPS and VAS sample within this region and become more prone to inaccuracies. These inaccuracies are magnified by the ALM itself; the ALM calculates a force that is particularly sensitive to the sampled blade-local velocity; this imposed force in turn affects the velocity field further, creating a series of compounding errors. The LAS avoids sampling the vortex region, which is the most sensitive to error, and therefore presents much faster convergence with respect to time step compared to the other two methods.

3.8 Conclusions

In this work, the dependence of ALM simulation results on the time step Δt, and the standard deviation of the Gaussian force smearing kernel ε was explored

for three velocity sampling methods: collocation point sampling, volume average sampling, and line average sampling. The three different sampling methods were tested across a range of Δt and ε. The underlying difference between the methods is the location of the sampling points: collocation point sampling calculates the blade-local velocity by sampling the simulated flow field at the collocation point; volume average sampling calculates the blade-local velocity as a weighted average of the sampled velocity values within a cloud of points centred at the collocation point and here coincident with the Gaussian force smearing kernel; and finally, line average sampling introduced by Jost [78] circumvents the region near the collocation point and samples the flow slightly outside the Gaussian force smearing kernel. Two rotors were analysed: a 4.5 m diameter wind rotor and a 20 m diameter high-solidity tidal rotor. A mesh sensitivity study employing 36 simulations and a time step and ε sensitivity study employing 80 simulations were performed.

The mesh sensitivity study for the wind rotor showed that the power and thrust coefficients for meshes with 40 and 160 cells across the rotor diameter were in close agreement, differing by less than 5% for C_P and 2% for C_T for the set of simulations tested.

After the mesh independence was established, the dependence on Δt and ε was studied for the three sampling methods. Differences in the velocity sampling method lead to different rotor performance predictions due to the coupling of the flow field with the imposed rotor forces through the actuator line method. It was found that, the LAS can achieve a valid solution for time steps two or four times larger than those required by CPS and VAS. This suggests that selecting an appropriate sampling method may help alleviate the stringent time step requirements imposed by the ALM method. The dependence of tidal rotor metrics on Δt was even more pronounced, but the conclusions remain similar. It was demonstrated that the sensitivity of the ALM to ε changes with the time step for the CPS and VAS methods. The LAS method demonstrated a limited and consistent dependence on ε across the entire time step range for both rotors.

To identify the sources of parameter sensitivity, the spanwise axial force and torque distributions were studied. It was found that for larger time steps, dependence of the CPS and VAS methods on ε could be observed in both the mid-span and tip region. The mid-span dependence was successfully suppressed by reducing the time step, although it was amplified in the tip region. The LAS on the other hand, showed limited dependence on ε that was concentrated in the tip region and independent of the time step value, enabling larger time step values.

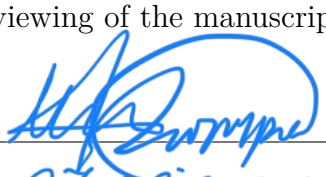
To investigate the flow further, the streamwise velocity component at the rotor plane was studied and compared for all sampling methods, time steps, and smearing radii. It was found that the flow at the rotor plane is affected by the ALM parameters in two key ways: first, the choice of the time step affected the thrust coefficient which, in turn, affected the amount of flow through the rotor and therefore streamwise velocity at the rotor plane. Second, the choice of ε affected the blade-local velocity field through the change of the core radius of the resulting viscous vortex emerging as a result of the force smearing. Sampling within the region near the vicinity of the blade, as in CPS and VAS methods, is prone to sensitivity to ALM parameters. Using LAS decouples the blade-local flow errors, that are due to the imposition of a smeared force, from the ALM sampling of the flow-field and subsequent force calculation. This leads to reduced sensitivity to ε and Δt, and hence LAS exhibits faster convergence in time step than other methods.

This work suggests that the choice of velocity sampling method could be crucial in decoupling some of the dependencies that make the ALM predictions particularly sensitive to its parameters and increase its computational cost. Notably, it introduced the use of the LAS method for horizontal axis wind turbine simulations as an effective way of achieving results comparable to traditional methods, like CPS, but with a reduced number of time steps per revolution. Moreover, the level of ε-sensitivity of the ALM was found to depend on the user-defined Δt value, for both CPS and VAS methods. The LAS suppresses this dependence by reducing the sensitivity to ε and making it consistent across a range of time steps.

The close coupling between velocity sampling and force smearing within the actuator line method has been demonstrated in this work. Future work will aim to better characterise spanwise sources of errors as well as establish the accuracy of the method with respect to higher-fidelity simulations.

3.9 Authorship statement

Publication details	
Title	The effect of flow sampling on the robustness of the actuator line method
Status	Submitted for Publication
Reference	Zormpa, M., Zilic de Arcos, F., Chen, X., Vogel, C. R., & Willden, R. H. J. (2024). The effect of flow sampling on the robustness of the actuator line method. Submitted to *Wind Energy*.

Student Confirmation	
Student Name	Markella Zormpa
Contribution to the paper	MZ: Conceptualisation of the work, analysis, processing and visualisation, manuscript. All authors contributed to ideas and reviewing of the manuscript.
Student Signature	
Date	27.09.2024

Supervisor Confirmation	
Supervisor name and title	Dr. Christopher Vogel
Supervisor comments	I confirm that Markella has made a substantial contribution to the publication, and that the description above in the Statement of Authorship is accurate.
Supervisor Signature	
Date	27. 09. 2024

Table 3.5: Statement of authorship for Chapter 3.

4

ALM-LES of wind turbine wakes

In this chapter, the ALM is embedded in an LES solver to perform wind turbine wake simulations of the NTNU BT1 experiment. The setup employed for the simulation of wind turbine wakes using ALM-LES is presented, alongside sensitivity studies on the effect that user-defined parameters have in predicting rotor and wake metrics.

In Section 4.1, the numerical details of both the LES solver as well as the ALM parameters are discussed first. While some parameters involved in the ALM are selected according to best practices, others are justified by performing sensitivity studies presented in this section. Specifically, the aerofoil data and tip corrections are selected such that the power and thrust coefficients are closest to the experimental measurements.

A spatial and temporal verification of the ALM-LES solver is performed by simulating wakes at four different meshes and various time steps, in Section 4.2. Metrics that span from the rotor plane to the far wake are discussed. A systematic and quantitative analysis of the resolution of ALM-LES simulations of wind turbine wakes is rarely performed in the literature. Insights from this chapter suggest that a spatially under-resolved near-wake may counter the benefits of the ALM discrete blade representation.

Finally, the resolution requirements of ALM-LES wake simulations are re-evaluated in Section 4.3 for the case where low turbulence intensity perturbations

are introduced in the inlet. When re-assessing the quality metrics, it is found that low turbulence levels can improve the validity of the LES. Coarser meshes may therefore be a viable option for the ALM-LES simulation of wind turbine wakes with turbulent inflow.

Summary and conclusions are presented in Section 4.4.

4.1 ALM-LES simulations of wind turbine wakes

ALM-LES simulations are widely used for the prediction of wind turbine wake flows [62, 63, 138, 139]. They involve both the large eddy simulation CFD component, responsible for the iterative solution of the Navier-Stokes equations, as well as an ALM component, within which the rotor force is calculated and imposed within the CFD solver. In this section, the details of the LES solver used in this thesis are listed. An overview of the parameters and sub-models involved in the in-house ALM code used in this thesis is also presented. Two studies on the sensitivity of ALM results to user-defined parameters are performed allowing for an informed selection of aerofoil polars and tip corrections.

4.1.1 LES: numerical solver, boundary conditions and mesh topology

All ALM-LES wake simulations in this thesis are performed for the NTNU rotor described in Section 2.5.2, in either the the single-rotor BT1 configuration (Chapters 4, 5, 6) or the two-rotor BT2 configuration (Chapter 6) .

The filtered, unsteady, incompressible 3D Navier-Stokes equations are solved using OpenFOAM [125]. Second-order centred spatial and second order backward temporal discretisation schemes are used. The PISO algorithm handles the pressure-velocity coupling. The choice of subgrid-scale model does not generally affect the ALM-LES predictions of wind turbine wakes, as long as the simulation is sufficiently well refined [64]. Therefore, the standard Smagorinsky turbulence model is employed here.

The wind tunnel of the Blind Tests is modelled using a symmetry boundary condition on the walls. A fixed value velocity is used for the inlet and a fixed pressure gradient at the outlet. Synthetic eddies are superimposed at the inlet using the Divergence Free Synthetic Eddy Method (DFSEM) by Poletto *et al.* [140] available in OpenFOAM version 1606 and above. It is noted that in some cases, no perturbations are superimposed at the inlet boundary, based on the assumption of very low inlet turbulence [61, 62, 139]. Consequently, the inlet boundary condition for velocity will be explicitly stated where applicable in this thesis.

The mesh topology employed for the various simulations of the Blind Tests is depicted in Figure 4.1. The domain contains hexahedral elements, progressively refined to achieve the target cell size in the wake region. The mesh and time step sizes are characterised using the ratios N_x and N_t, respectively, introduced in Chapter 3.

Studies in this chapter investigate the sensitivity of wake results based on both the mesh size N_x and the time step size N_t. Consequently, the mesh size and time step are varied in the studies presented, and therefore will be explicitly specified where applicable.

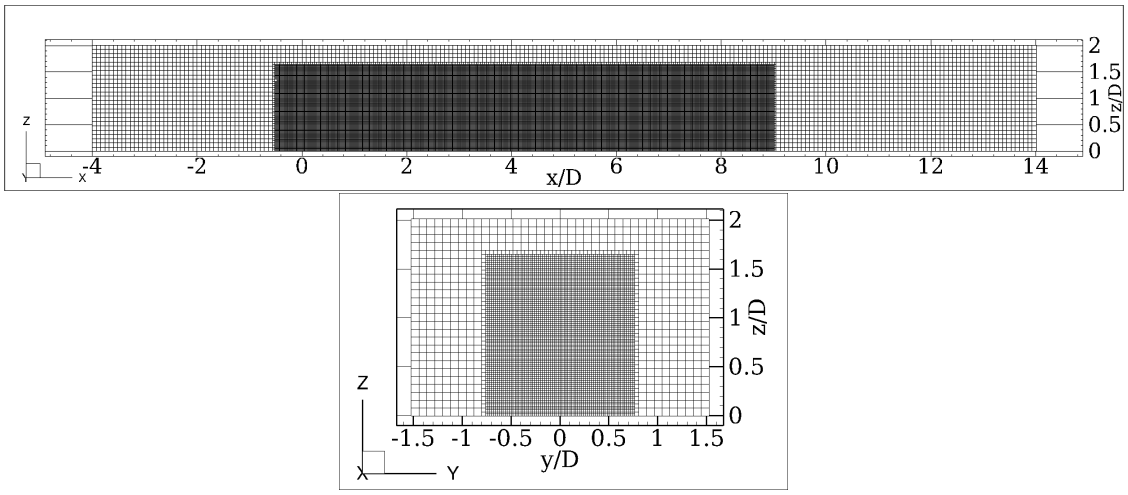


Figure 4.1: BT1: Mesh topology. The rotor is located at $x = 0$. The refined regions are characterised by the parameter N_x cells per rotor diameter.

4.1.2 ALM: methods and parameter selection

The in-house ALM used in this study was adapted by Hunter *et al.* [141] from NREL's open source OpenFOAM-based ALM solver, SOWFA [121]. It was later transferred into version 20 06 [125] for this thesis. The code has been validated for both wind [85] and tidal [141, 142] rotors.

The velocity sampling method employed in the in-house ALM solver is the LAS method introduced by Jost [78] and adapted for the ALM in Chapter 3. While the method's favourable robustness properties were demonstrated for ALM-URANS simulations, the same conclusions have been extended to ALM-LES in Appendix E. Following conclusions from Chapter 3, $N = 16$ sampling points are used and a sampling radius $r_s = 1.1r_g$.

For force smearing, the spherical Gaussian kernel of Equation 2.9 is used with $\varepsilon = 2\Delta x$, following Troldborg [61].

The choice of aerofoil polars and tip correction involved in the force calculation, discussed in Section 2.3.2, introduces parameter dependent sensitivity to the ALM calculations. Integrated power and thrust have demonstrated relative differences of the order of $5 - 23\%$ when the aerofoil polars or tip corrections were varied in [134], for a range of tip-speed ratios. Therefore, in what follows both the aerofoil polars and tip correction are investigated for the NTNU rotor in order to ensure an informed selection of the above, and quantify the dependence of the calculated power and thrust on the choice of aerofoil polars and tip correction.

Aerofoil Polars

Lift and drag coefficients for the S826 aerofoil at low to moderate Reynolds numbers are widely available from experimental campaigns that followed BT1. Those experiments aimed to increase fidelity of the aerofoil data for the S826 aerofoil in order to facilitate validation of BEM and ALM calculations of the NTNU rotor. The four experimental campaigns that have taken place since BT1, are summarised in Table 4.1, alongside the Reynolds number range at which they were performed.

Publication	Re Range	Label
Sarmast [28]	$4 \times 10^4 - 3 \times 10^5$	DTU, Sarmast
Sarlak [143]	$4 \times 10^4 - 10^5$	DTU, Sarlak
Cakmakcioglu *et al.* [81]	$7.2 \times 10^4 - 1.45 \times 10^5$	METU
Bartl *et al.* [80]	$5 \times 10^4 - 6 \times 10^5$	NTNU

Table 4.1: Summary of the experimental studies performed for the characterization of the S826 aerofoil at Reynolds numbers of the order of Re $\sim 10^5$.

The lift and drag coefficients per unit span are given by $C_l = l/(1/2\rho U^2 c)$ and $C_d = d/(1/2\rho U^2 c)$, respectively, where l and d are the lift and drag force per unit span, U the freestream velocity and c the chord length. The change of C_l and C_d with the angle of attack α at Re $= 10^5$ for the four experiments is visualised in Figure 4.2.

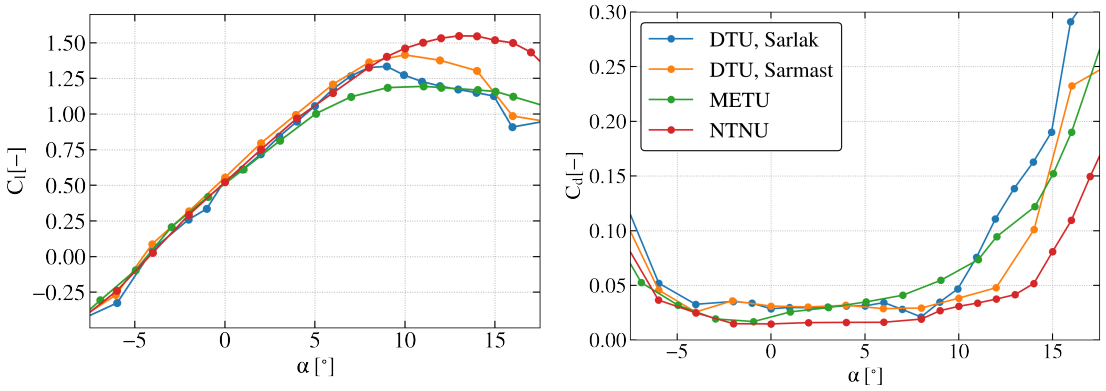


Figure 4.2: Lift (left) and drag (right) coefficient data as functions of angle of attack from the experimental campaigns of Table 4.1 for the S826 aerofoil at Re $= 10^5$.

While the four lift curves are in agreement for $\alpha < 5°$, the onset of stall differs for the four datasets, with both DTU and the METU data demonstrating an earlier stall angle that can be attributed to the larger aspect ratio employed in the DTU and METU experiments, according to Bartl *et al.* [80]. The DTU, Sarlak experiment, characterised by low turbulence intensity levels ($TI = 0.2\%$), presents an abrupt and early stall [80]. This behaviour is not observed in the NTNU experiment, which employs a larger turbulence intensity of 0.7%.

Significant deviations in drag coefficients are apparent even in pre-stall conditions. While the NTNU data show a gradual increase in drag, the experiments by DTU and METU present a steeper increase due to the earlier onset of stall.

Tip-speed ratio sweeps are generated using the ALM, employing two of the presented datasets: the NTNU and DTU, Sarlak polars. These experiments are deemed more suitable because they present significant disparity, and the Reynolds number range available is sufficient to simulate the entire TSR sweep. The power coefficient, $C_P = P/(1/2\rho U^3 A)$, and thrust coefficient, $C_T = T/(1/2\rho U^2 A)$, are compared using the *percentage difference*. The percentage difference between two values C_1 and C_2 is defined as

$$\delta_{\%}(C_1, C_2) = \frac{|C_1 - C_2|}{1/2(C_1 + C_2)} 100\%. \tag{4.1}$$

While the aerofoil data are varied in this study, all other parameters are held constant, including the tip correction (W&W, described in Section 2.3.2). The simulations performed for this study employ a hexahedral mesh, similar to Figure 4.1, with $\sim$ 2 M cells. Since only the rotor power and thrust are studied here, the refined region spans $0.5D$ upstream and $0.5D$ downstream of the rotor, and $N_x = 100$ is employed, following the mesh sensitivity analysis of Section 3.6.3. The rotor is centred in the middle of the domain, sufficiently far away from the boundaries that are modelled with freestream boundary conditions.

The two TSR sweeps that employ the NTNU and DTU, Sarlak polars are visualised in Figure 4.3 with the blue and red triangles respectively. For $\lambda = 4, 6 \& 8$, the percentage difference in C_P between the two is $\delta_{\%}^{C_P} = 18, 12.5 \& 14\%$, respectively. For thrust, the equivalent difference is $\delta_{\%}^{C_T} = 13.7, 2.4 \& 1\%$. Higher power predictions when employing the NTNU data at $\lambda = 6$, where $\mathrm{Re} = 10^5$, can be attributed to the lower drag values. At the same time, thrust appears more consistent as it is typically less dependent on the drag than on the lift coefficient. Lift coefficients for the angle of attack range at $\lambda = 6$ are in relative agreement for all datasets.

Similar disparities in C_P and C_T based on the aerofoil data are calculated when using a BEM model, employed here in order to ensure that the ALM implementation is consistent with other methods. Specifically, the percentage difference for the TSRs quoted above, using QBlade [116], is $\delta_{\%}^{C_P} = 4, 19 \,\&\, 23\%$ and $\delta_{\%}^{C_T} = 4,\ 10 \,\&\, 0.6\%$.

The above analysis underscores the importance of aerofoil data in ALM simulations. Significant dependence of the ALM (and BEM) integrated metrics on aerofoil data is found, with power presenting greater sensitivity to the aerofoil data selection than thrust, across the full TSR range evaluated here. The transitional Reynolds numbers employed here may be contributing to the discrepancies between aerofoil polars [82].

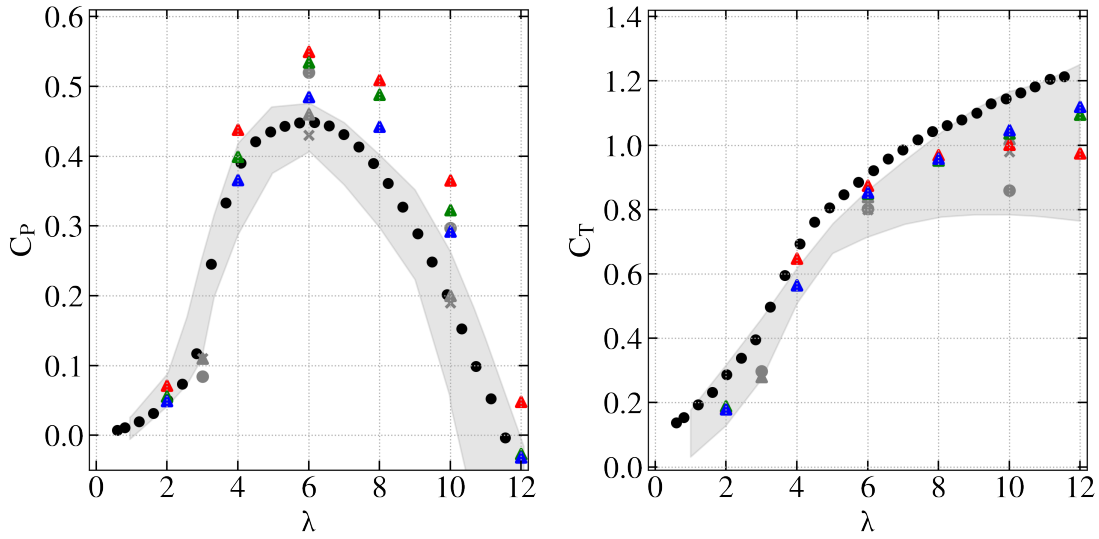


Figure 4.3: BT1: Rotor power (left) and thrust (right) coefficients as functions of TSR. **black circles** denote measurements from experiments; **grey shaded areas** denote the range of simulation results submitted to BT1 [113] (excluding the ALM-LES submission); **grey circles** denote the ALM-LES results submitted to BT1 [113]; **grey triangles and crosses** denote the ALM-LES results presented in [138]; **red triangles** are obtained using NTNU aerofoil data and W&W tip corrections; **blue triangles** are obtained using DTU, Sarlak aerofoil data and W&W tip correction; **green triangles** are obtained using DTU, Sarlak aerofoil data and Shen tip correction.

Tip correction

The influence of the tip correction on ALM predictions of power and thrust is investigated by employing two tip corrections: the Shen tip correction and the W&W tip correction, described in Section 2.3.2. All other ALM parameters are kept consistent and the aerofoil dataset used here is the DTU, Sarlak. The effect of the tip correction on the TSR sweep is depicted in Figure 4.3, with a focus on the blue and green triangles representing the W&W and Shen corrections, respectively.

For $\lambda = 4,\ 6\ \&\ 8$ the percentage differences are $\delta^{C_P}_{\%} = 8.8,\ 9.6\ \&\ 9.7\%$ respectively, and $\delta^{C_T}_{\%} = 0.008,\ 0.35\ \&\ 0.6\%$. While power is $\sim 10\%$ lower, across all TSRs, when using the W&W correction, thrust presents negligible percentage difference, as might be expected, given that the W&W tip correction was specifically developed to account for the larger drop in tangential force when compared to that experienced in the axial direction. It is therefore demonstrated that, tip corrections may also affect integrated power by a factor of $\sim 10\%$.

Validation of the power and thrust curves

When compared to the experimental results, namely, the black circles of Figure 4.3 it is evident that the ALM simulations employing DTU, Sarlak's aerofoil data and the W&W tip correction yield the closest approximation and therefore this aerofoil dataset and tip correction are selected for subsequent analyses. Percentage difference between experiments and simulations (DTU, Sarlak, W&W), for $\lambda = 4,\ 6\ \&\ 8$ are $\delta^{C_P}_{\%} = 3.5,\ 7.96\ \&\ 15.76\%$ and $\delta^{C_T}_{\%} = 17.68,\ 6.1\ \&\ 9.08\%$.

The grey shaded areas of Figure 4.3 have been digitised from [113] and represent the range of simulations submitted to BT1, although ALM-LES simulations have been separated out for more in-depth comparison. Therefore, the data in the grey shaded areas are results from BEM, ADM, and BR simulations. The results in this thesis lie above the shaded region for the $C_P - \lambda$ curve and within the range of predicted values for the $C_T - \lambda$ curve.

For a fair comparison, grey markers (circles, triangles and crosses) in Figure 4.3 represent three ALM-LES predictions from [113] and [138]. Predictions within this thesis tend to overestimate the power coefficient, similar to the ALM-LES results from the original Blind Test [113] (grey circles).

All simulations, ALM and others, consistently underpredict the experimental C_T. The simulations in this thesis result in a satisfactory estimate of the thrust when compared to ALM-LES simulations from the literature. Additionally, analysis from this section suggests that thrust is a consistent comparison metric, being less influenced by user-defined parameters such as aerofoil polars and tip corrections,

in contrast to the power, which is more sensitive. Given that thrust is the main contributor to the overall induction, accurately evaluating C_T is a priority when it comes to wake predictions.

4.2 Spatial and temporal resolution of ALM-LES for wind turbine wake simulations

Evaluating numerical resolution is often overlooked in ALM-LES: while authors may recommend cell sizes spanning from $N_x = 60$ [61, 64] to $N_x = 120$ [62], different metrics are often employed to evaluate convergence. In this section, the impact of spatial and temporal resolution on the prediction of wind turbine wakes up to $8D$ downstream, in the absence of inlet turbulence is investigated.

The resolution study is performed for BT1 at $\lambda = 6$, with $U_\infty = 10$ m/s and the solver and boundary conditions are described in Section 4.1.1. The mesh topology can be seen in Figure 4.1. The domain employs two main refinement levels: an outer coarser region and an inner finer region. The finer region spans $(L \times W \times H) = (10 \times 1.5 \times 1.7)\, D$ and has a resolution of N_x, that is varied in this section. The transition from the coarser region to the finer region is done by gradually halving the cell size three consecutive times and therefore the edge dimension in the coarser region is eight times larger than that in the finest.

No turbulence is imposed at the inlet boundary. Within the context of ALM-LES wake simulations it has been observed that small amounts of background turbulence may accelerate tip vortex breakdown, contributing to a more significant increase in the far wake turbulence [64, 139]. When inlet turbulence is present in the domain, sensitivity to numerical parameters may be expected to be less significant as the breakdown of tip vortices is quickly dominated by their interaction with the turbulent fluctuations. Therefore, performing the refinement study under non-turbulent inflow allows more conservative conclusions on resolution to be drawn.

Aerofoil data used here are obtained using XFoil [79], as the analysis of Section 4.1.2 was performed at a later stage. However, the focus in this section is on the sensitivity to the mesh and time step and therefore the aerofoil data, being

consistent across simulations herein, are not expected to affect the conclusions. For the force projection, the value of ε is chosen such that always $N_\varepsilon = \varepsilon/\Delta x = 2$. Note that keeping N_ε constant while changing Δx, implies that the virtual size of the blade, i.e. over which its presence is imposed through blade forces, changes for the different simulations involved in the mesh analysis. This may in turn affect the production of turbulence at the blade location, the size of the tip vortices and other metrics that depend on the Gaussian kernel width. Therefore, it should be noted that implicit in the refinement study below is a linear but non-trivial change in the effective chord of the blade across simulations.

The nacelle is modelled using the cell blocking method, a meshless forcing method similar to that introduced in [76]. This method is described and evaluated in detail in Chapter 5. It is worth noting that for BT1, the tower has a significant impact on the wake evolution, as observed by other validation studies [31, 71, 138, 144, 145, 146]. In this section, the tower, which is the focus of Chapter 5, is omitted, and therefore only the verification of the ALM-LES method is investigated. The validation of the wake measurements against experimental data follows when the tower is added in Chapter 5.

4.2.1 Simulation suite

The suite of six simulations performed in this section are described in Table 4.2. Four different mesh refinement levels are simulated $N_x = 50, 100, 150, \& 200$. For the two coarsest mesh refinement levels, a time step sensitivity study is also performed. Typical time step recommendations for ALM limit the time step to be such that the distance travelled by the tip collocation per time step (Δs) is no greater than one cell dimension (i.e. $\Delta s/\Delta x < 1$) [61]. For the $N_x = 50 \,\&\, 100$ cases of one cell per time step ($\Delta s/\Delta x = 1$) and two cells per time step ($\Delta s/\Delta x = 2$) are explored. The latter choice is enabled when using line average sampling, as described in Chapter 3. All simulations present a valid Courant number less than unity.

The core hours for a single rotor rotation for each simulation are presented in Table 4.2. It is noted that the total core hours per rotation for each simulation

N_x	Cell Count	N_t	$\Delta s/\Delta x$	ε [m]	Core hours/rotation
50	3.1 M	80, **160**	2, **1**	0.03576	1.2
100	22.3 M	160, **320**	2, **1**	0.01788	18.7
150	79.5 M	240	2	0.01192	111
200	188.9 M	320	1.7	0.00894	461

Table 4.2: Suite of simulations performed for the investigation of the impact of the spatial and temporal resolution of ALM-LES simulations of wind turbine wakes. In bold are the two refined time steps tested for $N_x = 50$, 100. In what follows, unless otherwise stated, the non-bold time step values are used so that the ratio $\Delta s/\Delta x = 2$ is consistent across all simulations (with the exception of $N_x = 200$ where 1.7 is set). It follows therefore that the core hours per rotation stated here refer to $N_t = 80$ & 160 for $N_x = 50$ & 100, respectively.

are dependent on both the mesh resolution N_x and the number of time steps per rotation, N_t. All simulations were performed in the Advanced Research Computing (ARC) facility of the University of Oxford. A scaling test for the above simulations and high performance supercomputing facility is presented in Appendix A.

4.2.2 Convergence

The convergence of integrated metrics and higher order statistics in the far wake are plotted. All simulations are terminated at $t/T = 150$, with the exception of the finest simulation ($N_x = 200$) that is terminated at $t/T = 105$ due to computational cost. A convergence analysis is performed here specifically for that simulation, suggesting that $t/T = 105$ is sufficient to obtain converged metrics.

First, both power and thrust coefficients are converged within just $t/T = 10$ simulated periods for all meshes (Figure 4.4).

However, the wake of the rotor arrives at the furthermost sampled streamwise location, $x/D = 8$, at approximately $t/T = 20$, as can be observed from the time series of the streamwise velocity component in Figure 4.5. Qualitatively it may be observed that while the time series resulting from the finest three meshes exhibit a similar nature, the $N_x = 50$ results trend towards an apparently more significant wake deficit at this location with little high frequency content.

The analysis of the flow statistics starts at $t/T = 40$, by which point the flow has arrived at the furthermost sampling location $x/D = 8$ and transients have

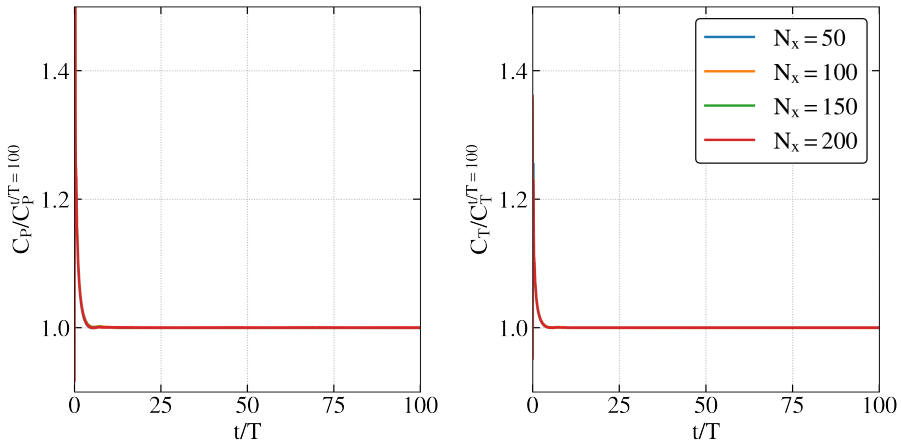


Figure 4.4: BT1: Temporal convergence of power and thrust coefficients for the simulations of Table 4.2.

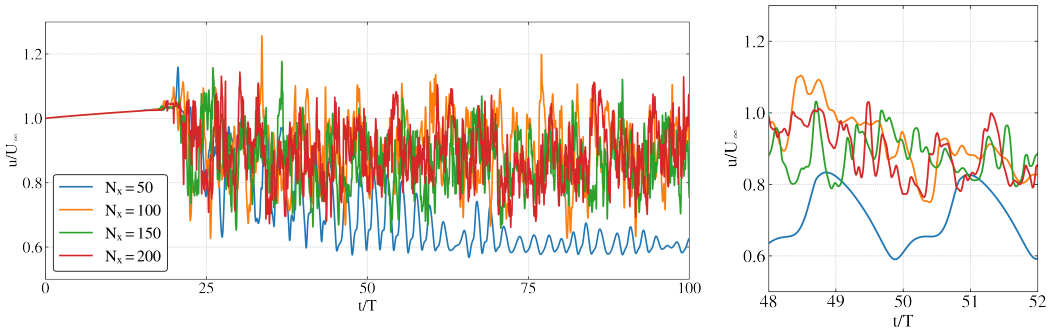


Figure 4.5: BT1: Non-dimensional instantaneous streamwise velocity sampled for 100 periods in the far wake, $(x, y, z) = (8D, 0.5D, z_h)$ for the simulations of Table 4.2.

elapsed. To ensure convergence of the first and second order statistics, the horizontal velocity and TKE profiles (both logarithmic and linear scales) at the furthermost sampled location, $x/D = 8$, for the case with $N_x = 200$ are plotted for different times (Figure 4.6). Negligible discrepancies in time averaged values are observed after a sufficiently long averaging time has elapsed.

4.2.3 Integrated metrics

The power and thrust present limited sensitivity to N_x and N_t. Specifically, no simulation presented relative errors larger than 2.1% in power, and 0.5% in thrust when compared to the $N_x = 200$ case (Table 4.3). It was demonstrated in Chapter 3 that resolutions with $N_x < 40$ and time steps with $\Delta s/\Delta x > 4$, lead to significant errors in the ALM. These limitations are not an issue in the current suite of

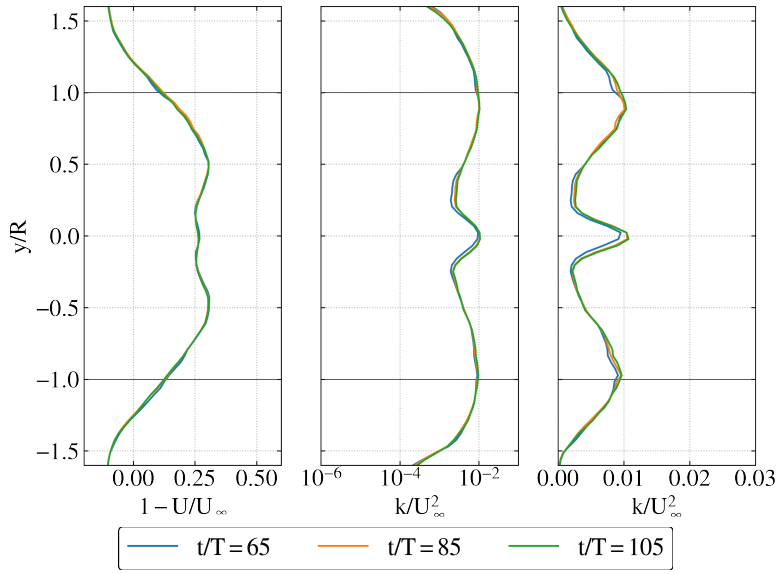


Figure 4.6: BT1, $N_x = 200$, $x/D = 8$: Horizontal profiles of mean velocity deficit and TKE in both linear and logarithmic scales after 25, 45 and 65 rotation periods. Note that analysis starts at $t/T = 40$.

simulations. However, convergence in rotor C_P and C_T does not imply convergence of the wake characteristics, which are studied next.

N_x	N_t	$\frac{C_P - C_P^{N_x=200}}{C_P^{N_x=200}}$ [%]	$\frac{C_T - C_T^{N_x=200}}{C_T^{N_x=200}}$ [%]
50	80	2.05	0.15
50	160	2.05	0.15
100	160	1.24	0.45
100	320	0.98	0.36
150	240	0.46	0.18
200	360	-	-

Table 4.3: Sensitivity of the integrated metrics on the spatial and temporal resolution for the simulations of Table 4.2. Errors are given relative to the finest case, $N_x = 200$.

4.2.4 Instantaneous flow field

The instantaneous velocity and vorticity fields resulting from the four refinement levels studied here are presented in Figure 4.7. Qualitative observations can be drawn by comparing the velocity and vorticity fields between the various simulations.

In Figure 4.7 it is apparent that the $N_x = 50$ simulation is under-resolved, as a very limited number of cells per diameter is employed. Tip vortices are hardly

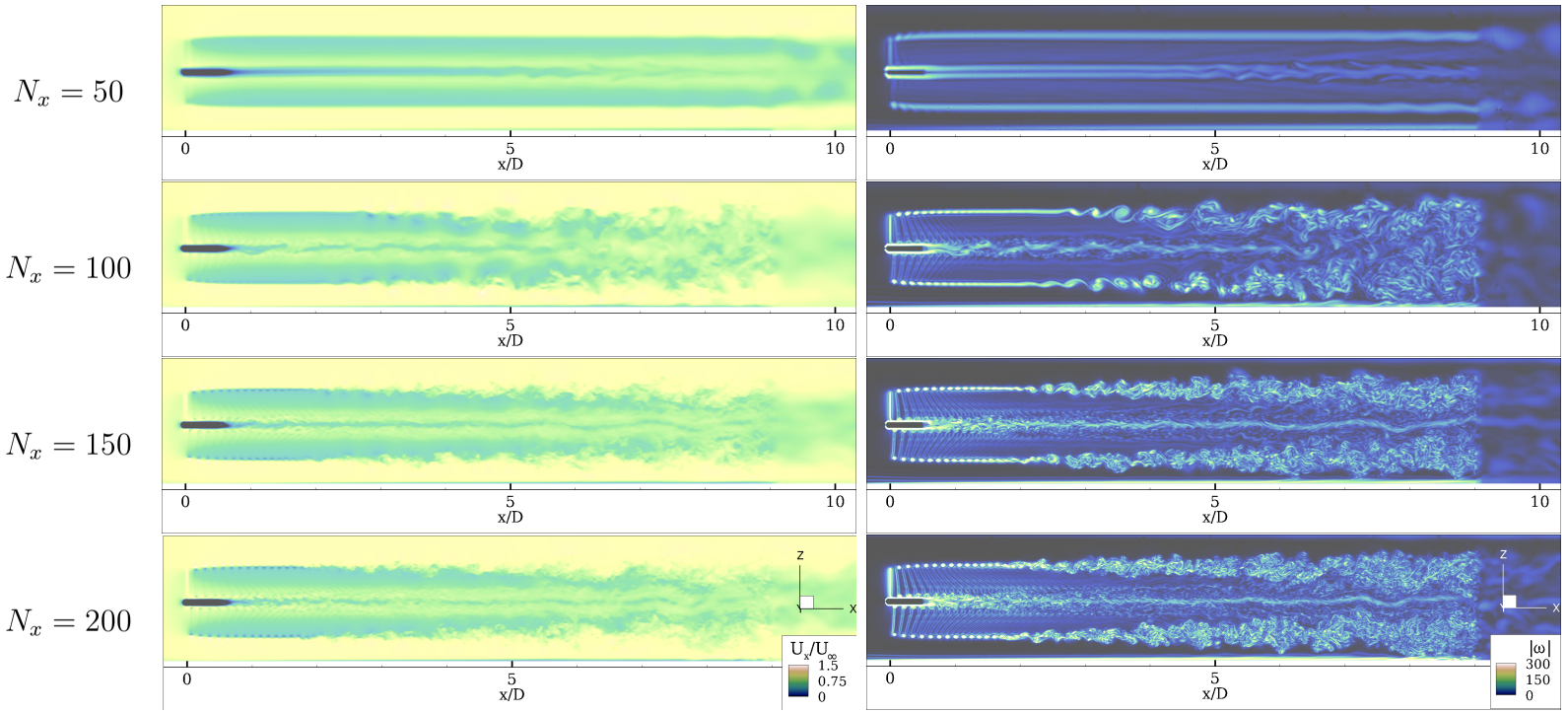


Figure 4.7: BT1, $N_x = 50, 100, 150$ & 200: Contours of non-dimensionalised instantaneous streamwise velocity (left) and instantaneous vorticity magnitude (right) at a vertical plane through the middle of the rotor for the simulations of Table 4.2.

sustained past the rotor plane. On the other hand, tip vortices can be observed in all higher-resolution simulations, $N_x = 100, 150$ & 200. For the $N_x = 100$ case however, they are only preserved up to $x/D \approx 1$, at which point they are artificially dissipated by the mesh, creating a spurious cylindrical surface of high vorticity at the edge of the wake. In both $N_x = 150$ & 200, tip vortices are preserved until $x/D \approx 2$ downstream of the rotor plane. Their shape at locations just before breakdown is clearer in the $N_x = 200$ instantaneous vorticity contours.

Both the location and wake breakdown mechanism, responsible for the transition to turbulence, varies across simulations. The $N_x = 50$ case does not transition to turbulence at all. In the $N_x = 100$ case, a shear layer instability causes the transition to wake turbulence at $x/D \approx 2.5$. Both $N_x = 150$ and $N_x = 200$ cases transition to turbulence at $x/D \approx 2$. While it is more clearly observed in the vorticity contours of the $N_x = 200$ case, in both high resolution cases an interaction between the helical tip vortices appears to be the leading mechanism responsible for the tip vortex breakdown. Interactions between tip vortices are a leading instability mechanism for helical vortex systems under non-turbulent inflow, such as wind turbine wakes [28].

A significant feature of the wakes downstream of the NTNU rotor is their interaction with the hub vortex. In all cases, the hub vortex structure is pronounced. For $N_x = 100$ the hub vortex is sustained as a separate structure until $x/D = 6$, at which point it merges with the rest of the wake. In contrast, in both $N_x = 150$ and $N_x = 200$ simulations the hub vortex is preserved until the end of the high resolution domain at $x/D = 9$.

We define "edge turbulence" as the turbulence at the edge of the wake and "centreline turbulence" as the turbulence at hub height. The merging of the edge and centreline turbulence in the $N_x = 100$ case, may be attributed to the higher edge turbulence levels present in that case. The edge turbulence in this simulation is caused by the transition due to a shear layer instability. In contrast, in the $N_x = 150$ & 200 cases, the edge of the wake transitions to turbulence due to the interaction of tip vortices. In those cases, the edge of the wake at $x/D = 3 - 6$ is more radially confined and no interaction with the hub vortex is observed prior

to $x/D = 9$. Therefore, the inability of the $N_x = 100$ mesh to resolve the tip vorticity at streamwise locations $x/D = 1 - 2$, subsequently affects the far wake prediction by triggering a shear layer instability that creates excess turbulence (compared to the $N_x = 150$ & 200 cases) at the edge of the wake which in turn leads to the acceleration of the interaction with the hub vortex. This interaction will be further explored in subsequent sections.

Qualitatively, the present analysis suggests that the $N_x = 50$ case is incapable of capturing important dynamics of the wake, such as the tip vortices and vortex breakdown. The $N_x = 100$ simulation resolves tip vortices up to a modest streamwise location. The turbulent breakdown is then due to a shear layer instability, which is a different flow feature than that observed in the more refined simulations. As a result of the numerically induced shear layer instability, an early merging of the centreline and edge turbulence takes place. The most computationally demanding simulations $N_x = 150$ & 200 demonstrate agreement with each other regarding the tip vortex propagation, breakdown, and the persistence of the hub vortex into the far wake. Qualitatively, convergence is achieved for the two finest meshes.

4.2.5 Flow statistics

Horizontal profiles of flow statistics at four locations downstream of the turbine, $x/D = 1, 3, 5$ & 8, are presented in Figure 4.8. The mean streamwise velocity deficit $(1 - U_x/U_\infty)$ is presented, alongside non-dimensional TKE (Equation 4.2). The TKE profiles are presented in both linear and logarithmic scales. The former representation allows to visualise peaks in turbulence, such as the ones in the centreline and edge of the wake. The log-scale TKE graphs are used to visualise smaller turbulent scales such as the turbulence between the centreline and the edge of the near wake. Both the total $k = \langle k_{sgs} \rangle + k_{res}$ and resolved k_{res} components of the TKE are plotted in the TKE graphs, with the shaded region denoting the amount of subgrid-scale turbulence. Finally, the ratio between the resolved and total TKE, denoted γ (Equation 4.2, [147]) is presented. To ensure that LES is resolving rather than modelling most of the turbulence, it is typically recommended

that $\gamma > 80\%$, while lower values of γ characterise very large eddy simulations (VLES) [102]. Energy spectra for the three velocity components and the various meshes are also presented in Figure 4.9 to investigate the location of the cut-off of the different LES simulations with respect to the inertial sub-range.

$$\gamma = \frac{k_{res}}{\langle k_{sgs} \rangle + k_{res}}, \quad k_{res} = \frac{1}{2}\langle u_i' u_i' \rangle \tag{4.2}$$

Velocity Deficit

Tip vortices are associated with a pronounced velocity deficit at $|y/R| = 1.05$ in the near wake ($x/D = 1$). This is not evident in the experimental results presented in [113], as will be discussed later in the thesis, and may be influenced by the ε value and the subsequent tip vortex produced by the ALM. The tip vortices are the most challenging structure to reproduce and most simulation tools are incapable of capturing such detail.

In the mid-span regions of the near wake, $0.25 < |y/R| < 0.8$, $x/D = 1$, all mean velocity deficit profiles are in close agreement, as they typically follow the blade force distribution, which is also in agreement between simulations.

The hub vortex manifests as a local peak in mean velocity deficit at the centreline that is eliminated moving downstream. The deficit peak generated in the $N_x = 50$ case is the most pronounced due to the lack of turbulence. The merging of the hub vortex with the wake at $x/D = 6$, discussed above, is evident by observing velocity profiles at $x/D = 8$: while in $N_x = 150$ & 200 simulations, a local maxima at velocity deficit can be observed at the centreline $|y/R| \approx 0$, a Gaussian-like profile is developed by the $N_x = 100$ mesh.

In summary, the $N_x = 50$ case is again demonstrated to be spurious and fails to capture some of the key wake dynamics. The $N_x = 100$ case agrees with $N_x = 150$ & 200 up to $x/D = 5$, with the exception of a lower momentum recovery at the edge of the wake at $x/D = 3$ that can be attributed to the difference in tip vortex breakdown mechanism. At $x/D = 8$, the wake shape of $N_x = 100$ has deviated from that of the most refined cases. However, this deviation may be

acceptable to practitioners, as, overall momentum availability is not significantly different for the three finest simulations. $N_x = 150$ and $N_x = 200$ are in agreement across all streamwise stations investigated here.

Limited time step dependence for the $N_x = 50$ and $N_x = 100$ simulations can be observed. For $N_x = 100$, differences between the $N_t = 160$ and $N_t = 320$ cases may be observed at $x/D = 3, 5 \,\&\, 8$ mainly at spanwise locations with high turbulence, near $|y/R| = 0$ and $|y/R| = 1$. However, the overall shape of the profiles produced by the two $N_x = 100$ simulations remains aligned and overall differences are dominated by N_x rather than N_t.

Turbulent Kinetic Energy

Significant dependence of TKE on the mesh size can be observed in the near wake ($x/D = 1$), by examining both linear and logarithmic TKE plots. The tip vortex TKE (at $|y/R| \approx 1$) increases with increasing mesh refinement level. Even for the two finest simulations the TKE of the tip vortices are mesh dependent. This appears to be the most challenging region to reproduce, given that the tip vortices are the smallest coherent structures present in the wake. Moving further inboard at the same streamwise location, mesh size is found to affect the simulated turbulence across $0.25 < |y/R| < 1$, only readily visible in the logarithmic plots. The turbulence statistics, are mainly related to the Gaussian smearing kernel size and may be equally affected by the varying cell size as well as the varying ε size. As the cell size is reduced, ε also reduces and therefore steeper velocity gradients are produced by the actuator line, leading to higher turbulence levels around the mid-sections of the blade. In reality, turbulence in this region is mainly produced by the blade's boundary layer. Actuator methods, characterised by the lack of wall modelling, do not reproduce this source of turbulence and therefore this is a limitation of the method rather than the mesh. Consequently, it can be said that convergence can not be reached for most spanwise locations at the $x/D = 1$ station, due to both ALM limitations, as well as the inability of the tested meshes to fully resolve the tip vortices.

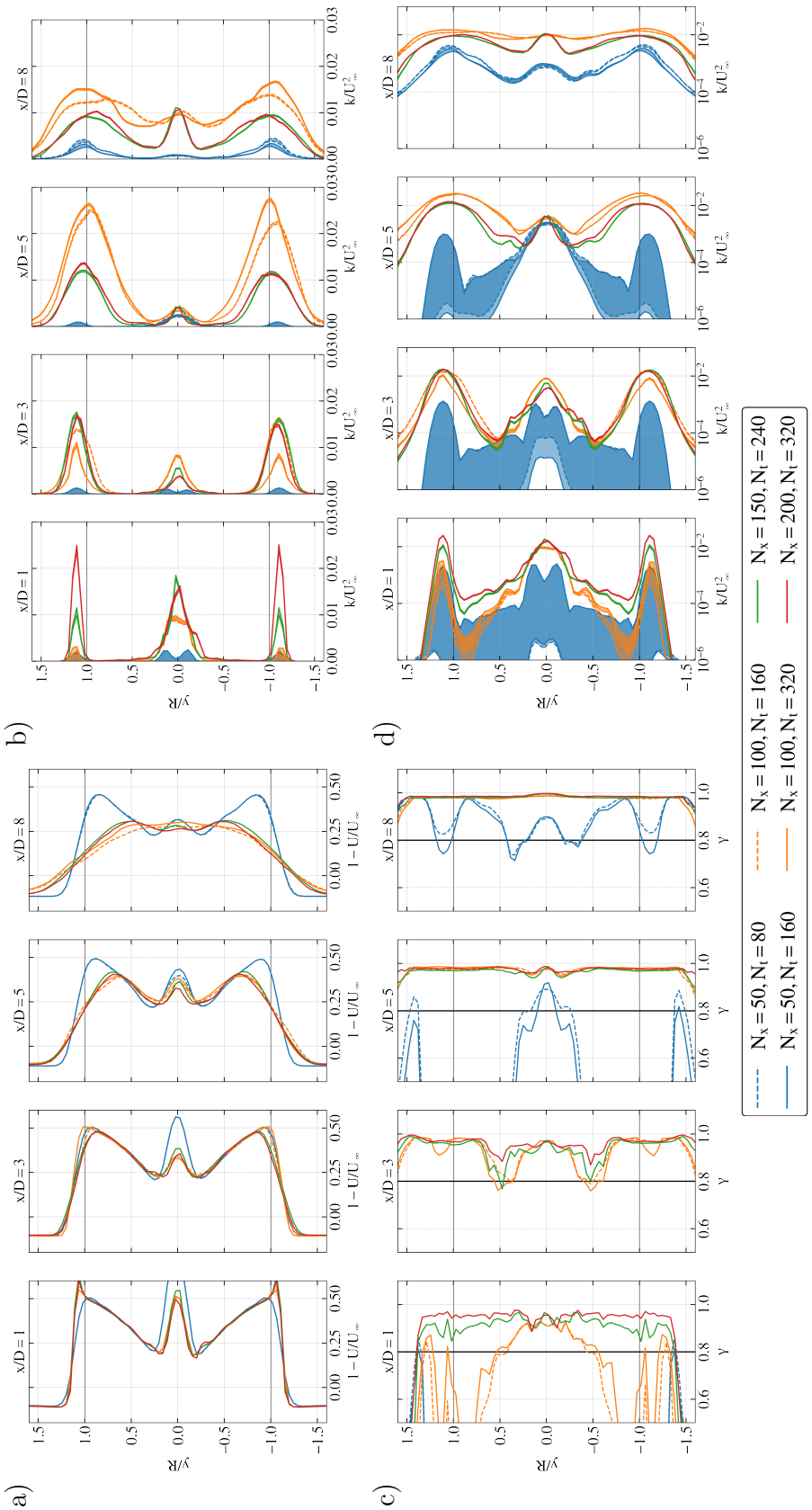


Figure 4.8: BT1: Horizontal mean flow profiles downstream of the rotor plane for the simulations summarized in Table 4.2, at downstream locations $x/D = 1, 3, 5$ & 8. (a): Mean velocity deficit; (b): TKE plotted in linear scale; (c): TKE ratio; (d) TKE plotted in logarithmic scale. The shaded region in the TKE profiles denotes the modelled TKE.

The difference in wake breakdown mechanisms between the $N_x = 100$ and $N_x = 150$ & 200 simulations, discussed in the previous section is further explored here by observing TKE profiles at a linear scale.

At $x/D = 3$, the $N_x = 100$ case has just transitioned to turbulence (at $x/D = 2.5$, as observed earlier in the instantaneous vorticity contours) and therefore the TKE peaks at the edge of the wake appear to be lower than those produced by the $N_x = 150$ & 200 cases that exhibit transition to turbulence earlier (at $x/D = 2$).

This trend changes at $x/D = 5$ where the shear layer instability experienced in the $N_x = 100$ simulation appears to generate stronger TKE peaks, producing higher turbulence than that produced by the tip-vortex interaction instability experienced in the $N_x = 150$ & 200 cases at the same streamwise station.

While the TKE at the edge of the wake for $N_x = 100$ appears to have a large radial extent (i.e. $0.5 < |y/R| < 1.5$, $x/D = 5$), turbulence peaks produced by the finer cases are more radially concentrated around $|y/R| \approx 1$. The wider radial extent of the TKE peaks in the $N_x = 100$ case then gives rise to the merging of the hub vortex with the edge of the wake at $x/D = 6$.

At $x/D = 8$, cases $N_x = 100$ and $N_x = 150$ & 200 present overall different TKE profiles, clearly observed in both the linear and logarithmic scales. This coincides with the difference in mean velocity deficit at the same station.

Dependence of the $N_x = 100$ flow fields on time step is more pronounced in the TKE profiles than in the mean velocity deficit. However, the profiles follow similar progression. The turbulent breakdown mechanisms, that appear to be the main source of differences between simulations, are dominated by N_x rather than N_t.

TKE Ratio

To evaluate the resolution of the LES at the various significant regions in the wake, the TKE ratio γ is plotted in Figure 4.8. $N_x = 50$ generally presents $\gamma < 80\%$ at all streamwise stations. While this changes at $x/D = 8$, the flow that has arrived at this station is affected by the low resolution upstream. $N_x = 100$ achieves $\gamma > 80\%$ at locations $x/D = 3$, 5 & 8. However, in the near wake, at $x/D = 1$, a

substantial portion of the γ profile presents values below 80%. It is in this region that the $N_x = 100$ prediction starts deviating from the $N_x = 150$ & 200 ones. The inability to resolve tip vortices at $x/D = 1 - 2$ is followed by a series of interactions that produce a different wake for the $N_x = 100$ case. In both $N_x = 150$ and $N_x = 200$ simulations more than 80% of the TKE is resolved which indicates that well resolved LES is performed in both cases.

Energy Spectra

Energy spectra for all four meshes and for the three velocity components are calculated using the open source toolbox of [148], and presented in Figure 4.9. The data for the spectra are sampled at the edge of the far wake, at $(8D, D/2, H)$, where turbulence is expected to be homogeneous and isotropic. The characteristic $-5/3$ slope is followed, suggesting that the cut-off wave number is within the inertial sub-range for the three finest simulations.

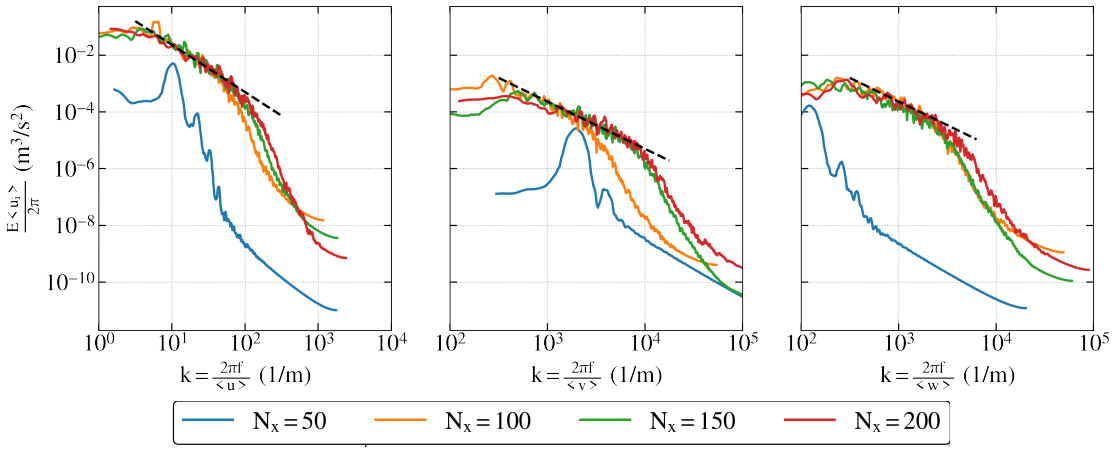


Figure 4.9: Energy spectra calculated for the time series at position $(x, y, z) = (8D, 0.5D, H)$, for the simulations presented in Table 4.2. From left to right the spectra are calculated for u, v, w time series. $-5/3$ decay indicated by the black dashed line.

4.3 Synthetic turbulence

In this section, the effect of low-turbulence inflow on the wakes of ALM-LES simulations is investigated. It is well established that an inflow turbulence intensity (TI) of approximately $TI = 5 - 10\%$ strongly affects the resulting wake recovery

by promoting breakdown of the tip vortices and enhancing mixing [61]. In [92], inclusion of 5% turbulence intensity in the inflow make the wake turbulence statistics predicted by various ALM-LES codes less sensitive to the numerical discretisation scheme and Smagorinsky coefficient. In [64], a low-turbulence inflow ($TI = 0.23\%$) increased the turbulence levels in the wake of the downstream rotor of BT2. In what follows, the effect of a low-turbulence inflow (i.e. $TI = 0.3\%$, employed in the BT1 experiment [113]) on the development of the wake of BT1 will be investigated. The wake will be compared with the non-turbulent inflow case. For the inclusion of turbulence, the Divergence Free Synthetic Eddy Method (DFSEM), widely available in OpenFOAM, will be tested.

4.3.1 Turbulent inflow boundary conditions for LES

Velocity boundary conditions for LES simulations must exhibit spatio-temporal variation at the boundary in order to be consistent with the premise of the filtered Navier-Stokes equations: a substantial proportion of the turbulent fluctuations must be resolved by the filtered equations. Therefore, the inlet velocity must vary in both space and time. In wind energy applications, two methods are often used to introduce turbulence in the flow domain: a precursor simulation, or a synthetic eddy method.

Turbulence statistics may be generated numerically by running a precursor simulation. A precursor simulation is an LES simulation of an empty domain with a wall boundary condition on the solid wall boundaries, capable of generating turbulence, and a cyclic boundary condition on the side boundaries. The precursor simulation eventually converges to a horizontally homogeneous isotropic flow; such flow is the atmospheric boundary layer where wind turbines operate. Communication between the precursor and the final wind turbine simulation occurs at each time step: a vertical plane of the turbulent fluctuations is extracted from the precursor simulation and used as the inlet velocity profile in the final wind turbine simulation. Precursor simulations are computationally demanding but are often preferred to synthetic methods for ABL modelling as they generally generate good quality turbulence statistics [149].

Turbulence statistics may also be generated artificially, using synthetic methods. Synthetic eddy methods generate turbulence statistics at a low cost using physics-based approaches and assumptions. A widespread method to replicate ABL statistics, is the Mann method [61, 71, 150] whereby velocity fluctuations are superimposed on the flow by means of small body force fluctuations located in a plane upstream of the wind turbine.

The simulations performed in this section replicate the NTNU Blind Test wind tunnel experiments. The mean velocity and turbulence intensity measured upstream of the rotor are uniform across the swept area of the rotor [113]. Limited information is available regarding the turbulence characteristics of the tunnel in the streamwise direction, but it is known that the turbulence intensity two diameters upstream of the rotor and across the rotor swept area is $TI = 0.3\%$ [114]. Given the above, no detailed atmospheric flow profile or turbulence statistics are required for ALM-LES simulations of the BT1 experiments. For this reason, the synthetic DFSEM method available in OpenFOAM v 20 06 and beyond is tested here [140]. Additionally, the DFSEM method is a viable alternative to the Mann method that requires implementation and is not readily available in OpenFOAM. The precursor methods also involve implementation of the time-dependent LES boundary conditions and come at a higher cost. Validating the DFSEM in the ALM-LES framework will provide a low cost alternative to non-turbulent inflow for OpenFOAM users.

The DFSEM, introduced by Poletto [140] is a synthetic eddy method that calculates a mass conserving velocity field at the inlet boundary surface. The user first defines a mean velocity profile, Reynolds stress tensor and turbulence length scales at each cell of the inlet boundary. An eddy bounding box that encapsulates the inlet boundary surface is defined by the method. Within it, at random locations, a user-defined number of eddies is generated, the average shape and size of which satisfies the statistics and length scales specified by the user. At each time step the eddies are convected at a bulk velocity, following Taylor's frozen turbulence hypothesis. u_i' is calculated at a plane within the eddy bounding box

and superimposed onto the mean velocity profile to generate the instantaneous velocity field at the inlet of the wind turbine simulation.

4.3.2 DFSEM: simulations of an empty domain

The information on TI given by BT1 is limited, as it is only stated that $TI = 0.3\%$ at $x/D = -2$, while no turbulence length scales are provided. As mentioned above, the DFSEM boundary condition requires the determination of the mean velocity vector $U_i(\mathbf{x})$, Reynolds stress tensor $R_{ij}(\mathbf{x})$ and length scale $L(\mathbf{x})$ at each location in the inlet boundary. Here, all three variables are assumed uniform at the inlet boundary, following velocity and TI measurements from BT1, so only one value for the entire inlet boundary is specified (U_i, R_{ij}, L). The mean velocity at the inlet is defined by the experiments and is $U_\infty = 10$ m/s. In order to simplify the determination of the Reynolds stress tensor, an assumption of isotropic turbulence is made: $R_{ij} = 2/3k\delta_{ij}$. The remaining unknown, the turbulent kinetic energy k at the inlet is found using a trial-and-error approach, with a target of achieving $TI = 0.3\%$ at $x/D = -2$ for a given length scale (Figure 4.11). The length scale is undetermined, given the experimental data available, and therefore the problem remains open. One approach is to choose $L = 0.045$ m which is the value measured in a subsequent Blind Test in the same wind tunnel with no turbulence grid [151]. However, in the present simulations a symmetry boundary condition is employed at the walls instead of boundary conditions that generate wall shear stresses. Therefore, no turbulence is generated in the domain and as a result, the background turbulence will dissipate faster in the simulation than in the wind tunnel. To compensate for this loss of TKE production, a larger length scale $L = D/3 = 0.3$ m, is employed at the inlet, which helps to retain (instead of generate) turbulence in the streamwise direction. The wakes developed in low turbulence inflow with both a small and a large length scale were compared and no significant dependence of the first and second order statistics on the inlet L was found as long as the turbulence intensity upstream of the rotor was matched to 0.3%.

The DFSEM was first tested for a flow domain identical to that described in Figure 4.1, that however employs a much smaller refined region $-0.5 \leq x/D \leq 2$. The boundary conditions are described in Section 4.1.1, with additional DFSEM-generated fluctuations in the inlet boundary. Firstly, the instantaneous velocity field for $R_{ij} = 0.00125$ m^2/s^2 $(i = j)$ and $L = 0.3$ m is inspected qualitatively in Figure 4.10, in order to ensure that no spurious features have emerged. Turbulence intensity measurements based on the total turbulent kinetic energy, are shown in Figure 4.11 for various spanwise and wall normal locations. It can firstly be observed that $TI \approx 0.3\%$ is matched at $x/D = -2$. Secondly, homogeneity of the mean flow can be observed in the spanwise and wall normal directions: the TI does not vary more than 4% at any streamwise location. This scatter is similar to that observed in measurements in the NTNU wind tunnel [152]. In the streamwise direction, the development region is mainly concentrated upstream of the rotor while the TI stabilises after $x/D = -0.5$. Small deviations between the profiles in all directions and deviations from $TI = 0.3\%$ at the corresponding upstream location are not expected to generate significant asymmetries in the wake flow.

4.3.3 No- vs low- inflow turbulence for a single rotor wake

To investigate the effect of DFSEM-generated turbulence on the wake of BT1, the $N_x = 100$ simulation from Table 4.2 was performed again here, now including turbulent fluctuations at the inlet boundary. The instantaneous vorticity magnitude for such a flow is demonstrated in Figure 4.12. In the same figure, the non-turbulent inflow case is also presented for comparison. Qualitatively, it can be inferred that the wake breaks down faster in the low-turbulence case (at $x/D = 1.5$) prior to the generation of a spurious shear layer instability in the tip region such as that discussed in Section 4.2 that is visible in the no-turbulence case of Figure 4.12 at $1 \leq x/D \leq 2.5$. The faster breakdown of the low-turbulence case promotes a faster merging of the hub vortex with the edge of the wake leading to a more homogeneous snapshot of the wake at $x/D > 6$.

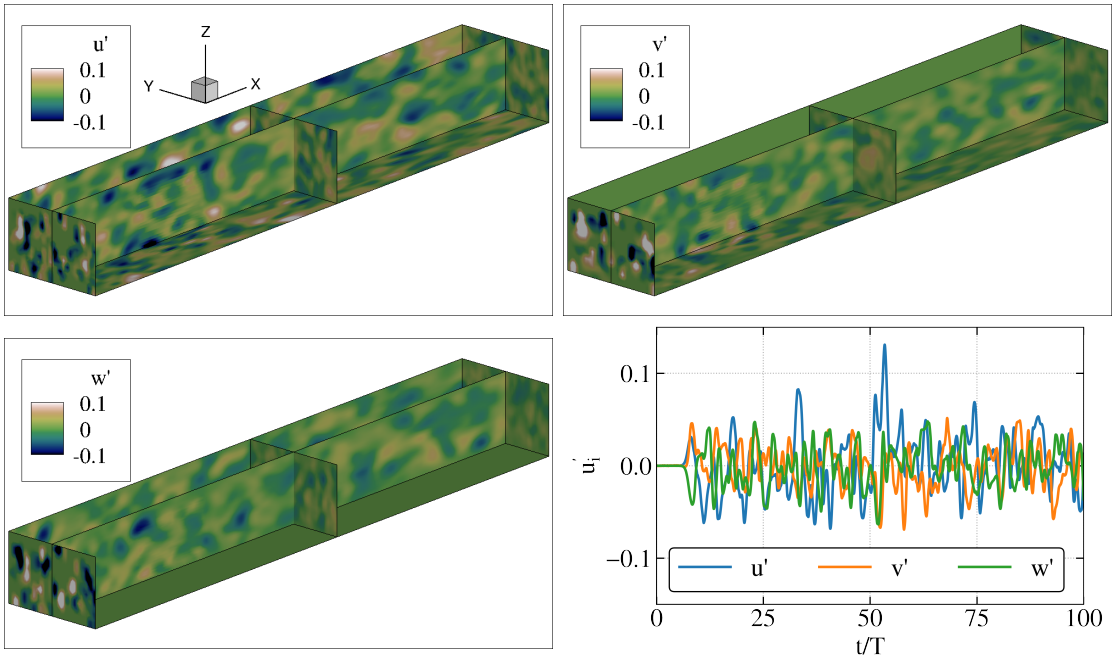


Figure 4.10: Fluctuating velocity components u_i' created by the DFSEM method in an empty domain (domain described in Figure 4.1). The flow is sampled (lower panel, right) at the hub location $(0, 0, z_h)$ to demonstrate that no spurious results are produced from the DFSEM method when used in an empty domain.

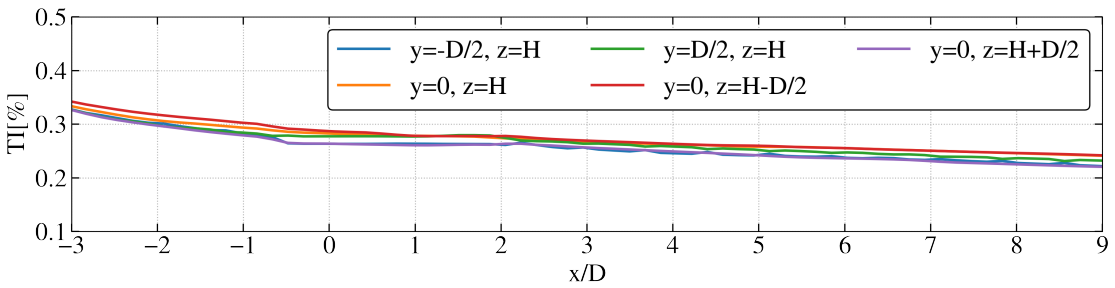


Figure 4.11: Streamwise evolution of turbulence intensity: sampled TI along axial paths passing through the perimeter and centre of the rotor disc.

The time-mean statistics of the simulations of Figure 4.12 are presented in Figure 4.13. At $x/D = 1$ it can be observed that the no- and low-turbulence cases both present the same momentum deficit and similar turbulence peaks in the linear scale. Differences are visible in the logarithmic scale plots of TKE in the background flow $|y/R| > 1$ as well as the mid-wake sections $0.3 < |y/R| < 1$ where the turbulence is low and therefore the low-turbulence inflow provides a relative increase in those regions. The TKE ratio, γ, at $x/D = 1$ is significantly improved for the low-turbulence case compared to the no-turbulence inflow. At the tip vortex locations,

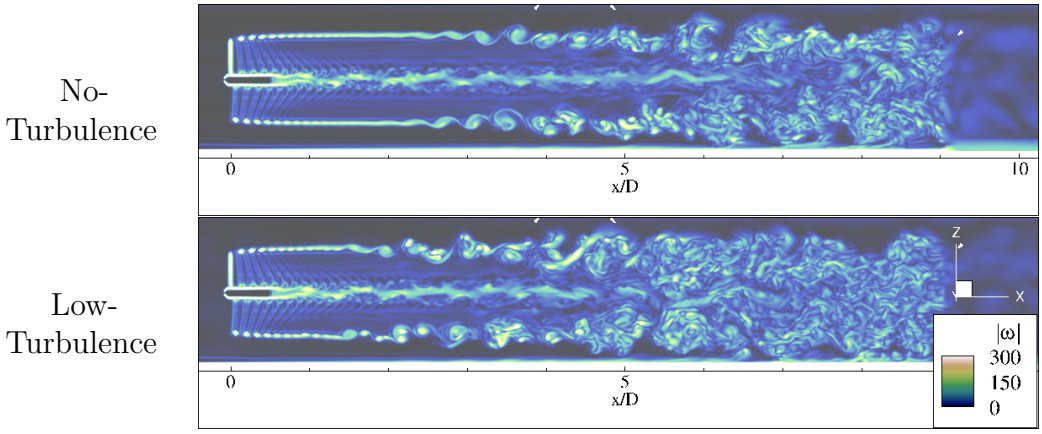


Figure 4.12: BT1, $N_x = 100$: Contours of instantaneous vorticity magnitude at a vertical plane through the middle of the rotors for no-turbulence and low-turbulence. The no-turbulence case is the same simulation as that presented in Figure 4.7.

$|y/R| \approx 1.2$, a drop to $\gamma \approx 0.5$ is observed for the low-turbulence case, but other than that the ratio remains sufficiently high to be described as an LES simulation.

This is a significant difference between the no- and low-turbulence cases, as adding a limited amount of turbulence may allow for large savings in resources by enabling a larger TKE ratio that increases the fidelity of the $N_x = 100$ case.

The higher mixing rate of the low-turbulence case due to quicker tip vortex breakdown is visible in the profiles of the turbulence statistics sampled at $x/D = 3$ and $x/D = 5$. The faster merging of the hub vortex with the rest of the turbine wake is evident in the $x/D = 5$ mean velocity deficit profile, where a less pronounced peak around $|y/R| \approx 0$ is observed. In both linear and logarithmic scale plots, the turbulence levels of the low-turbulence case are naturally higher than those of the no inflow turbulence case. $\gamma > 0.9$ for the panels $x/D = 3, 5$ &8 in both the no- and low-turbulence cases.

In the far wake, $x/D = 8$, both simulations have developed into a Gaussian-shaped velocity deficit with the low-turbulence case presenting a slightly quicker recovery due to the higher mixing undergone.

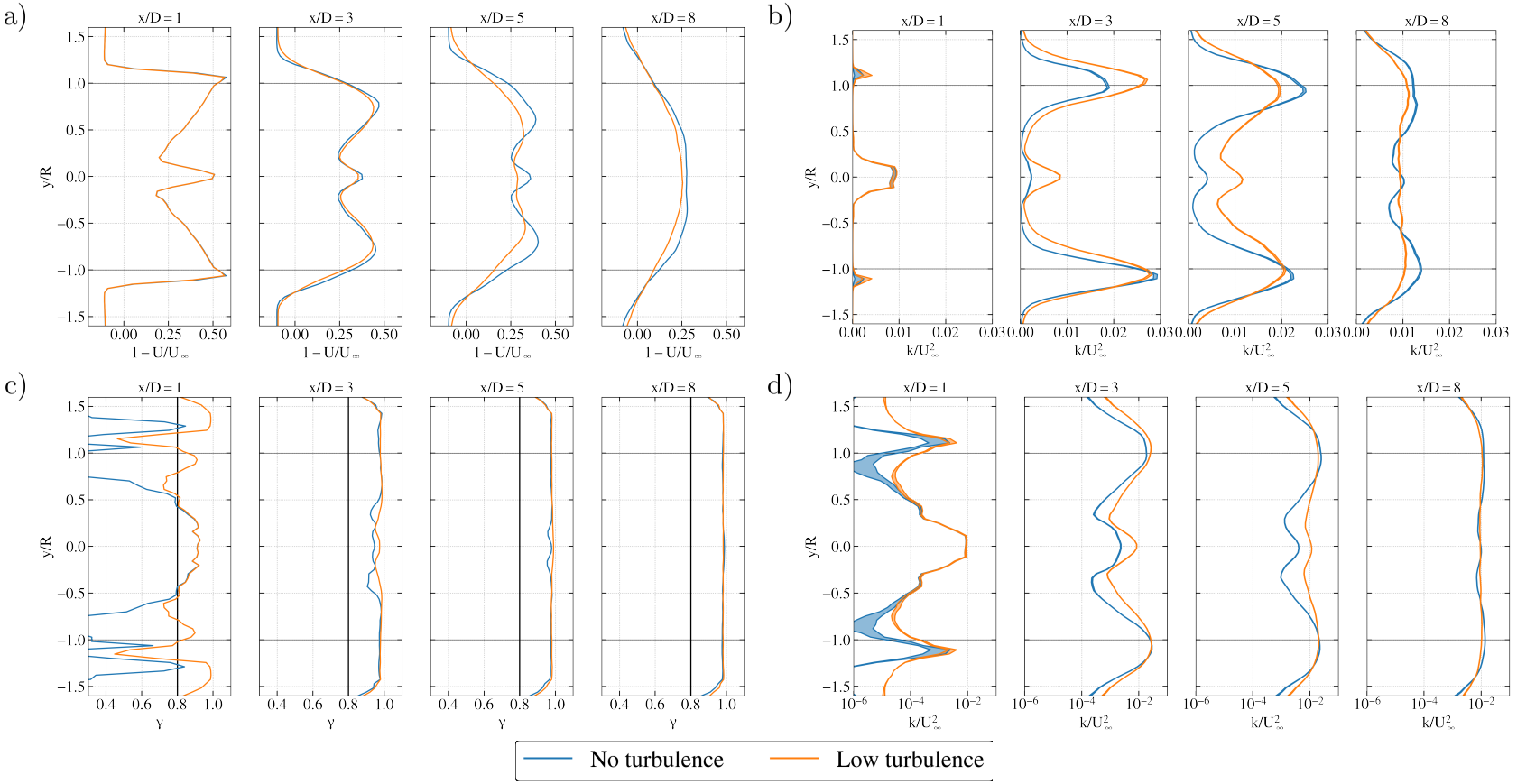


Figure 4.13: BT1: Horizontal mean flow profiles downstream of the rotor plane for two simulations: a no-turbulence and a lo-turbulence inflow, at downstream locations $x/D = 1, 3, 5$ & 8. (a): Mean velocity deficit; (b): TKE plotted in linear scale; (c): TKE ratio; (d) TKE plotted in logarithmic scale. The shaded region in the TKE profiles denotes the modelled TKE.

4.4 Summary and conclusions

In this chapter, a wide range of parametric studies relevant to ALM-LES simulations of wind turbine wakes were presented.

First, the set up of the LES and ALM solvers are described. The modelling decisions concerning the ALM were either justified with reference to relevant literature or investigated by performing sensitivity studies. Specifically, two studies are performed in order to justify the selection of the aerofoil data and the tip corrections. Differences of up to 18% in power and 14% in thrust are found when varying the lift and drag coefficients. The choice of tip correction led to up to 10% variation in power.

A mesh and time step sensitivity study for ALM-LES wakes up to 8D downstream was performed. Meshes significantly finer than the ones typically used in the literature were employed (i.e. up to $N_x = 200$), creating a well-resolved reference wake simulation. When wakes with resolutions typically found in the literature (such as $N_x = 100$) are compared to the reference wake, mesh dependence is observed. Specifically, while the velocity deficit does not vary significantly and the peaks of turbulence are generally found in similar radial locations, the tip vortex breakdown mechanism is different between the two meshes with the lower resolution mesh generating a spurious shear layer wake instability. This difference triggers a series of interactions responsible for further deviation from the reference case. This study is an example of how numerical modelling choices can affect the flow field predictions in indirect ways in flows where multiple scales are involved.

The qualitative nature of the far wake of the $N_x = 100$ simulation here may be considered closer to an ADM simulation, where wake shear is responsible for the transition of the near wake. This conclusion is in line with observations that suggest that ADM and ALM predictions at the far wake are similar, such as [62]. This study suggests that if not sufficiently resolved, ALM-LES is prone to tip vortex merging which might counter the benefits of employing a discrete blade description of the rotor.

Limitations in the above study include the non-turbulent inflow boundary condition that naturally makes flow predictions more sensitive to numerical parameters. For this reason, the effect of low-turbulence inflow is investigated. The DFSEM turbulent inflow boundary condition is tested in an empty domain and the target turbulence intensity for the NTNU experiments with low-turbulence is achieved. A wake simulation, employing low levels of inflow turbulence generated using the DFSEM is performed. It is found that the near wake turbulent kinetic energy ratio is improved when compared to the non-turbulent case and no artificial merging of the tip vortices, followed by shear layer instability, is observed for the $N_x = 100$ case. Therefore, low-turbulence inflow improves the reproduction of the near wake features of the $N_x = 100$ case leading to a higher validity solution.

5

Support structures in ALM-LES simulations

While advancements in the prediction of wind turbine loads and wakes within the ALM-LES framework have been an active research topic in recent years, the modelling of the tower and nacelle within ALM-LES simulations has received comparatively less attention. Here, the combined structure consisting of a tower and a nacelle is referred to as the "support structure". This chapter investigates both the numerical modelling of support structures within ALM-LES simulations, and their effect on the mean flow of the near and far wake.

In the absence of a published review on the interaction of wind energy rotors and their support structures at the various scales of the wind energy problem, a literature review is presented in Section 5.1, discussing the mean flow and dynamic effects of support structures on wind turbines, wind turbine wakes, and wind farms.

Modelling options for the representation of support structures in ALM-LES simulations are discussed in Section 5.2. Three methods are implemented: a meshed body representation, a meshless cell-blocking representation and an actuator disc/line representation. It is found that modelling the support structure using a meshed or a cell-block representation allows for the reproduction of distinct non-axisymmetric features observed in the experimental measurements, owing

to the ability of both methods to create a separated wake. The cell-blocking method is found to introduce high levels of turbulence intensity downstream of the tower, when compared to the meshed representation or the experimental data. On the other hand, the actuator representations implemented here are less effective in introducing turbulence and therefore are unable to capture the asymmetries introduced by the support structure.

The wake features related to the tower challenge the assumption of far wake axisymmetry. The effectiveness of the Gaussian far wake model is quantified in Section 5.3 by comparing a standard Gaussian wake model against the high-fidelity ALM-LES velocity fields. The Gaussian model is rarely challenged against such high fidelity data that present inherent asymmetries that could also be present in wind farm flows. It is found that there is a non-negligible effect of the support structure on the far wake axisymmetry assumption.

The conclusions of the work are summarised in Section 5.4.

5.1 The effect of the support structure on wind energy aerodynamics

Given the multi-scale nature of wind energy aerodynamics, the effect of the support structure can be observed at different spatial scales. A brief review of the current understanding of the effect of support structures in wind energy problems is presented in this section. The interaction between wind turbine flows and their support structures is reviewed at four different levels: the rotor aerodynamic loads, the near and far wake flows, and the wind farm effects.

5.1.1 Rotor scale

The tower and nacelle impact the overall power and thrust of the rotor. The tower structure decelerates the local incident velocity and, as a result, when the blade is located upstream of the tower, local blade forces are typically reduced due to both a reduction in available kinetic energy and a deviation of the incident flow from the optimal angle of attack. The presence of the nacelle on the other hand,

may lead to a slight increase in the incident velocity on the inboard sections of the rotor when compared to simulations that ignore the presence of the nacelle and allow air to flow through the low-resistance centre of the rotor instead.

Rotor fatigue loads caused by tower shadow, wind shear, yaw misalignment and other factors are regularly considered in wind turbine design [91]. The tower shadow loads are among the fatigue loads that cause the most abrupt force changes. Shkara et al. [153] studied the blade-tower interaction for a 5 MW three-bladed upwind rotor operating at design conditions: the interaction between a blade and the tower was recorded as a 3.1% drop in thrust and a 7% drop in torque, at the 1P frequency, i.e. once time per rotor rotation. Averaged over the three blades, these fluctuations resulted in a 2.3% drop in both rotor power and thrust, at the 3P frequency, i.e. three times per rotor rotation.

While significant and sudden aerodynamic changes may occur at the blade level at a 1P frequency, or at the rotor level at a 3P frequency, when averaged over an entire rotation the reduction in power and thrust due to tower shadow may eventually be marginal. However, the wake deficit and coherent structures downstream of the nacelle and tower interact with the rotor's near wake, with implications on the far wake and wind farm aerodynamics, discussed in the next sections.

5.1.2 Near wake

The near wake of an upwind turbine directly interacts with both the nacelle and tower wakes. Pierella and Sætran [144] studied the near wake velocity fields up to a downstream location of $x/D = 3$. They identified the wake of the tower as a low velocity region that developed directly downstream of the tower and disrupted the rotor wake axisymmetry. Moving downstream, the tower wake was rotated by the rotor wake, intensifying the introduced asymmetry. This asymmetry eventually led to an azimuthal imbalance in momentum entrainment into the wake, causing a vertical drop of the centre of the wake.

Coherent structures shed from the tower and nacelle interact with the wind turbine wake structures changing the overall near wake vorticity map as demonstrated in Debnath *et al.* [31]. POD analysis of a wind turbine wake excluding and including the support structure showed that the principal tip vortex breakdown mechanism was altered due to the presence of the tower. In the case without the support structure, a split instability was responsible for the tip vortex breakdown, while in the case that included the support structure, a pairing instability was identified among the dominant POD modes. Additionally, the presence of the nacelle was found to eliminate the root vortices, an observation also made in [27].

The effect of the nacelle alone has been studied in the literature and linked to near and far wake features. The mean centreline velocity downstream of the nacelle has been reported in measurements and simulations as either a local minimum [154, 155] or a local maximum [156]. Abraham *et al.* [156] noted that in studies that employ utility scale rotors, a local maximum can be expected. Utility scale rotors are characterised by a small nacelle to rotor diameter ratio, $D_{nac}/D \approx 5\%$, and the inboard sections of their blades consist of cylindrical sections with low axial induction that may be responsible for the observed acceleration at hub height. On the other hand, small experimental rotors are characterised by $D_{nac}/D \approx 10\%$ and blades with higher axial induction factors near the root. For such rotors, the nacelle wake centre manifests as a velocity minimum. In either case, the large velocity gradients found downstream of the nacelle produce a shear layer concentrated at the middle of the rotor wake, that expands radially with increasing streamwise distance, eventually interacting with the tip shear layer further downstream [145, 157].

In addition to dominating the mean flow features in the inboard region of the near wake, the nacelle is responsible for the generation of dynamical features, such as the hub vortex. The hub vortex has been described as a spiral vortex core downstream of the nacelle, centred at hub height that rotates in the opposite direction to the rotor [155]. As the hub vortex spiral develops downstream, its radius increases until it eventually meets the tip shear layer [155]. The implications of this interaction on far wakes and farm aerodynamics are discussed below.

5.1.3 Far wake

The effect of the support structure on the mean flow of the far wake of a wind turbine was studied, among others, by Santoni *et al.* [146]. The inclusion of the support structure in their ALM-LES simulations increased the momentum entrainment and led to quicker momentum recovery in the far wake. Therefore, when the support structure is simulated, a hypothetical downstream rotor in tandem may experience higher power availability. On the contrary, not simulating the support structure created a jet through the middle of the wake that stabilised the wake.

The low-frequency motion of the rotor far wake, known as wake meandering affects both the overall farm power and dynamic loads experienced by downstream turbines in wind farms. Its origin and magnitude is still under discussion [158]. Among other phenomena, authors have observed that the interaction of the precessing hub vortex with the tip shear layer enhances the intensity of wake meandering [154, 155]. Therefore, coherent structures shed from the nacelle can have a significant impact on far wake aerodynamics via the enhancement of wake meandering.

5.1.4 Wind farm aerodynamics

At the farm scale, Ma et al. [159] identified that for high density wind farms the optimal rotor thrust reduces and therefore the relative importance of the tower increases. Incorporating the tower thrust within the momentum balance of a two-scale model showed that optimal wind turbine spacing of infinite and very large wind farms is affected by the tower thrust. Support structure considerations may therefore affect the design of large wind farms.

Stevens *et al.* [65] also found that the inclusion of a tower and nacelle model in ADM and ALM wind farm simulations improved mean flow predictions compared to experimental data. Specifically, higher turbulence and velocity deficit directly downstream of the turbines at various rows were observed.

The effect of the hub vortex on large wind farms was also assessed by Foti *et al.* [160]. In their work, a large wind farm excluding and including a nacelle model was simulated using ASM-LES. Including a nacelle model increased the

meandering amplitudes across the wind farm and especially in the first rows, when compared to farm flow without a nacelle model. This is due to the interaction of the hub vortex with the tip shear layer that energises the wake, promotes turbulence generation and enhances wake meandering.

5.2 Support structure modelling in ALM-LES simulations

Given the significance of the interaction between wind turbine flows and their support structures, discussed in Section 5.1, a better understanding of numerical modelling methods of support structures is required. In this section, support structure modelling options in ALM-LES simulations are discussed. Three methods are implemented and assessed against the experimental measurements of BT1. The mechanism responsible for the observed far wake asymmetries is discussed, by analysing the ALM-LES far wake data of simulations that model the tower.

5.2.1 Review of support structure modelling methods

Low-fidelity approaches are typically employed to model the support structure in ALM-LES simulations of wind turbine wakes for several reasons. Firstly, the wind turbine wake problem already consists of many scales requiring resolution that drives the numerical cost towards the upper limit of the available resources for most practitioners. Added to this, the problem of calculating the forces and wake of a support structure is that of a bluff body flow problem in transitional or super-critical Reynolds numbers that in itself is a resource-intensive CFD problem. Adequately resolving both the support structure and the far wake is expensive and impractical. Additionally, even if the support structure is adequately resolved, uncertainty exists when it comes to roughness or other geometrical details of utility scale flow towers in such high Reynolds number flows. Finally, the blades, arguably a more important contributor to the wake flow, are represented using a lower-fidelity representation, and therefore the same principle may also be applied to the support structure modelling.

Various methods have been used in the literature to model support structures. Some of the most common methods will be discussed below, starting with the higher-fidelity parameterisation methods that involve limited assumptions and ending with representations that require pre-defining metrics related to the support structure forces.

Among the most accurate but also computationally expensive ways to simulate support structures is to explicitly mesh the solid boundary, using either a no-slip boundary condition with $y^+ \sim 1$ or a wall function with the first cell located in the log-law region. In the work of Muchala and Willden [161] URANS with a fully resolved tower and nacelle are employed, while in the work of de Oliveira *et al.* [54] a wall function approach was preferred. In the work of Ma *et al.* [45] a detached delayed eddy simulation (DDES) was chosen as the Wall-Modelled LES (WMLES) approach.

Immersed-boundary methods (IBM) offer a meshless alternative to solid boundary modelling, avoiding the excessive meshing effort typically associated with the latter. These methods represent the presence of the modelled structure by adding an appropriate source term in the momentum equations. Studies such as those by [31, 146, 162] employ an IBM implementation based on that of Orlandi and Leonardi [163]. Apsley *et al.* [76] modelled the support structures of tidal turbines using an alternative momentum source approach: in their implementation the solid boundary is represented by means of adding a large source term in the momentum equations that drives the velocity locally to zero, effectively blocking the flow entering the volume occupied by the solid boundary. An implementation of this method, hereafter referred to as the cell-blocking method, is tested in the subsequent sections for the prediction of the mean flow downstream a wind turbine with support structure.

Yang and Sotiropoulos [58] developed the ASM for both the modelling of wind turbine blades and the nacelle within LES simulations. The ASM generally explicitly considers more geometrical aspects than other actuator methods, such as the ALM. When employing the ASM for the nacelle, two forces are calculated and applied using a delta function at each location occupied by the boundary of the nacelle: the

normal force, ensuring no-penetration and the tangential force, calculated using an empirical friction coefficient formula and information from the upstream flow.

Consistent with the blade modelling in ALM-LES simulations, towers and nacelles are often modelled using the actuator line and disc method, respectively [63, 64, 65, 67, 138, 164]. For both components, a drag coefficient corresponding to that of a cylinder or disc is pre-defined and a characteristic inflow velocity vector has to be attained by sampling the surrounding flow. Sarlak *et al.* [64], further employed a pre-defined lift coefficient alongside a Strouhal frequency to introduce unsteadiness when modelling the tower of a model rotor; the inclusion of unsteadiness using such approaches has been subsequently employed in other validation studies [63, 138]. Other extensions to the actuator representations of the tower involve considerations of the pressure distribution around the surface of the tower [164].

While all of the above methods have been validated against experimental data or high-fidelity simulation results, little work exists in comparing methods with each other and understanding the trade-offs between them. Churchfield *et al.* [164] performed a comparison of various actuator methods for the support structure modelling and found relative differences between them.

5.2.2 Support structure models

In this section, three support structure modelling methods are discussed: a body-fitted approach, a cell-blocking momentum source approach, following Apsley *et al.* [76], and an actuator disc/line approach, following Sarlak *et al.* [64]. Schematic representations of the three methods are illustrated in Figure 5.1.

All three approaches are classified as low fidelity in the context of bluff body flows, and therefore near wake predictions of the independent bluff bodies will not be studied. Instead, the methods are assessed in the next sections based on their ability to interact correctly with the rotor wake. This is determined by evaluating the capability of each method to reproduce features observed in the experimental measurements of the NTNU rotor wake, and increase overall predictive capabilities of ALM-LES simulations.

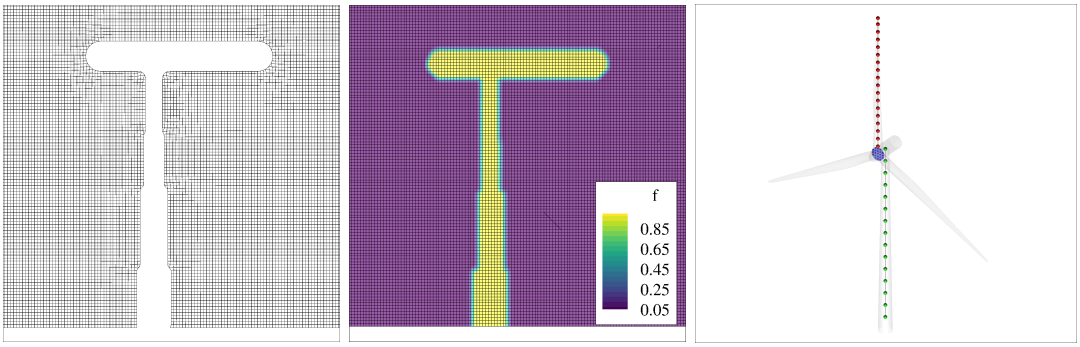


Figure 5.1: Illustrations of three support structure parameterisation methods used in ALM-LES simulations. Left panel: a body-fitted mesh around a support structure; middle panel: the f field (Equation 5.3), characteristic of the support structure geometry, employed in the cell-blocking method; right panel: schematic of the actuator disc/line representation. The tower is represented by the green collocation points, the nacelle by the blue actuator disc, and the blades by the red collocation points.

Body-fitted mesh: Geometry, meshing and boundary conditions

The geometry of the BT1 tower has been sketched in Figure 5.2, following [165]. The dimensions of the tower and nacelle are kept close to these given in the report, but adjustments such as fillets between the different tower sections were added to facilitate meshing. The hub height is $H = 0.807$ m, $\sim 1\%$ shorter than described in [165], and the average tower diameter is $\bar{D}_{tow} = 0.075$ m, while the nacelle diameter is $D_{nac} = 0.09$ m.

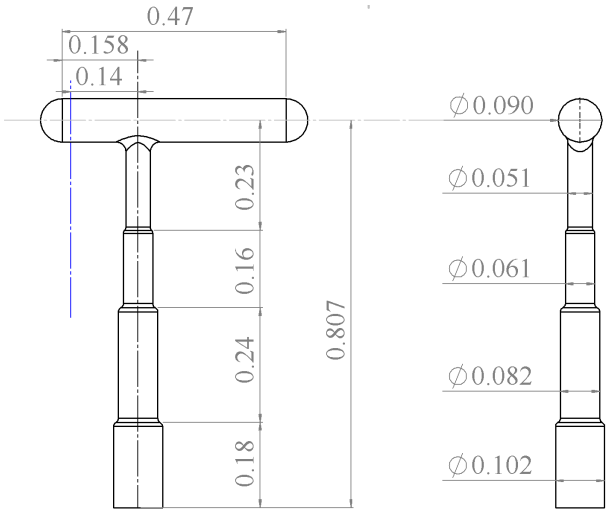


Figure 5.2: Dimensions of the NTNU rotor's support structure. The design generally follows [165].

The computational domain employed is identical to that described in Section 4.1.1, with $N_x = 100$. The support structure has been meshed by snapping hexahedral elements onto the solid boundary (Figure 5.1), using existing meshing tools available in OpenFOAM [166]. No additional refinement near the tower has been employed to ensure that the first cell remains in the log-law region. The y^+ has been calculated at the last time step and was found to be in the range of $20 < y^+ < 300$. The employed cell size corresponds to $\bar{D}_T/\Delta x \approx 8$ and $D_{nac}/\Delta x \approx 10$.

The support structure boundary condition is an analytical shear stress wall function, based on the law of the wall. Other numerical details of the simulation are summarised in Section 5.2.3.

Employing the above numerical set up ensures that the cost of the ALM-LES simulation is not overtaken by the resolution requirements of the support structure. Two aspects of the bluff body flow are compromised as a result: one relates to the force calculation, and the other to the support structure wake.

To model the boundary layer of the support structure within an LES simulation, a WMLES approach is necessary. Here, a RANS-type analytical wall function is employed that uses the law of the wall to estimate the velocity at the centre of the first cell adjacent to the wall. Subsequently this velocity is imposed on the boundary cell by artificially increasing the wall shear stress through adjusting the sub-grid scale viscosity. While the law of the wall is derived for the time-mean, rather than spatially-filtered velocity, its application in LES has been justified for coarse meshes that do not resolve the inner layer. The inner layer dynamics in such simulations may be considered in the mean sense and therefore the log law can be a good approximation [167]. Studies such as [167, 168] have demonstrated that by using analytical WMLES approaches good accuracy can be achieved at a low cost.

The wake of a cylinder flow at sub-critical Reynolds numbers, such as those experienced by the NTNU support structure, is separated and turbulent, therefore, a large number of cells is required to fully resolve the majority of scales using LES. Here, 8 cells across the average tower diameter and 10 cells across the nacelle diameter are employed uniformly around and downstream of the support structure.

Although the dynamics in the near wake of the support structure are not expected to fully converge, the primary focus here is on the interaction of the support structure with the rotor wake. In works that explore the same flow interaction, comparable mesh refinement levels have been used. For example, in Yang and Sotiropoulos [58], the velocity deficit as well as the dynamics downstream of a hydrokinetic turbine including the nacelle (represented by an ASM) were accurately captured using a mesh with $D_{nac}/\Delta x = 8$ ($D_{nac} = 0.08$ m [155], $\Delta x = 0.01$ m).

Cell-blocking representation

The cell-blocking method was introduced in Apsley et al [76] as a flexible method to model support structures of tidal rotors. It has been used in various tidal rotor simulations [76, 142, 169]. The method employs a momentum source term that is non-zero only within the cells occupied by the support structure. Its value is large enough to effectively block the mass flux from entering into a computational cell, acting as a non-penetration condition.

Once discretised, the i^{th} direction momentum equation in matrix form reads

$$Au = b \Rightarrow \alpha_P u_P - \Sigma_F \alpha_F u_F = b_P \tag{5.1}$$

where A is the discretisation matrix, b is the source vector, and u is the i^{th} velocity component vector. Au can be further separated into the diagonal and non diagonal parts, with corresponding subscripts $_P$ and $_F$, respectively. By adding an implicit source term $s_P u_P$ the diagonal of matrix A is artificially altered, and control over u_P can be obtained:

$$(\alpha_P - s_P)u_P - \Sigma_F \alpha_F u_F = b_P. \tag{5.2}$$

Setting $s_P \to \infty$ is balanced by $u_P \to 0$ so that a no-penetration condition can be enforced at the P^{th} cell. s_P needs to be infinite only in the numerical sense, and an appropriate value can be found by dimensional analysis. Equation's 5.2 terms are expressed in Newtons. Therefore, s_P can be expressed according to [76] as

$$s_P = -f\rho\frac{u^*}{L}V_P \tag{5.3}$$

where f takes values of $f \in (0, 1)$ (Figure 5.1) and represents the volume fraction calculated as the volumetric proportion of the cell that is occupied by the solid boundary. ρ is the fluid density; u^* represents a large velocity value that is taken as 10 times the inflow speed, larger than any velocity anticipated within the domain; L is the characteristic cell length taken as $V_{ave}^{1/3}$, where V_{ave} is the average cell volume.

Due to its simple implementation as an implicit source term, the cell-blocking technique lacks a wall treatment, commonly considered in immersed boundary approaches. Given that the typical cell size in ALM-LES simulations does not resolve the inner layer, a large boundary layer that scales with the mesh size has been observed to emerge from solid boundaries represented using the cell-blocking method, resulting in an overprediction of the body force as a result. Finer meshes yield thinner boundary layers and a more realistic body force. The objective of the current study is to evaluate the ability of the tested methods to improve the wake predictions without increasing the computational expense. Therefore, the mesh here was not refined to accommodate a better prediction of the support structure force. Another argument against attempting mesh refinement is that achieving satisfactory agreement with a baseline cylinder flow using a cell-blocking model at such Reynolds numbers is computationally virtually impossible requiring DNS level resolution, and case-specific. The significance of spurious features such as the thick boundary layer is tested in the context of wind turbine wakes in the following sections.

Actuator disc/line representation

In this approach, the nacelle is represented using an actuator disc (AD) and the tower using an actuator line (AL), similar to [63, 64, 164]. Such AD/AL approaches have been demonstrated to improve wake predictions of the NTNU rotor [138].

For the nacelle, an actuator disc approach may be employed to limit the flow through the centre of the rotor. Here, the variable-scaling ADM is used [170], as

implemented in OpenFOAM version 2.2.0 and above [171]. The method uniformly imposes a thrust force of magnitude

$$T = \frac{1}{2}\rho|\mathbf{u_0}\cdot\mathbf{n}|^2 A C_T^*, \tag{5.4}$$

and direction $\mathbf{n}$, where $\mathbf{n}$ is the unit vector normal to the actuator disc surface A. C_T^* is the calibrated thrust coefficient

$$C_T^* = C_T\Big(\frac{|\mathbf{u}_m|}{|\mathbf{u}_0|}\Big)^2, \tag{5.5}$$

introduced to account for the deceleration of the upstream flow. C_T is the user-defined thrust coefficient, based on a freestream velocity measurement and $\mathbf{u}_m$ is the freestream velocity sampled at a user-defined monitoring point m. The user-defined parameters in this method are therefore the thrust coefficient C_T and the location of the monitoring point m.

In the absence of a reference drag coefficient for the nacelle, the thrust coefficient for the following simulations is calculated using the body-fitted simulation results. In order to impose a constant thrust, the monitoring point is placed at the disc centre such that $\mathbf{u}_m \approx \mathbf{u}_0$. Then C_T is calculated such that the AD force is the same as the body-fitted nacelle force.

The tower is modelled using the actuator line method along its length, with a constant drag component and a fluctuating lift component, following Sarlak *et al.* [64]. All parameters here are taken from [64] that used this approach for the same rotor. Other works have also utilised the same method and parameters to model the NTNU turbine tower [63, 138].

The drag coefficient is set to $C_D = 1.2$, following measurements on cylinders with sub-critical Reynolds numbers up to $\mathrm{Re} \sim 2\times10^5$. The dynamic lift coefficient is expressed as

$$C_L(t) = A\sin(2\pi f t) + B(t). \tag{5.6}$$

The Strouhal number is set to $St = fD/U = 0.2$, where D is the tower diameter, U is the inflow velocity, and f is the frequency of the lift force fluctuation in

Hz. The root mean square of the lift coefficient is set to $A = 0.3$, representative of cylinder flows in similar Reynolds numbers. White noise $B(t)$, with standard deviation $\sigma = 0.25C_L$ is used to introduce random perturbations that mimic turbulent fluctuations in the shedding process.

As has been explored in this thesis, the parameters at each stage of the ALM algorithm may affect the calculated forces and resultant flow field. Here, the CPS method is used for the sampling, as in Sarlak *et al.*. Since the tower remains stationary, the implications discussed in Chapter 3 are not an issue here. The smearing parameter of the spherical Gaussian kernel is set to a typical value of $\varepsilon = 2\Delta x$, but a different value could affect the downstream flow field. A valid concern when employing the ALM in separated flows has been discussed in [172]: the ALM accuracy was found to deteriorate when predicting unsteady separated flows, and calibrations of the smearing parameter were suggested in order to improve the predictive capabilities of the ALM for such flows.

5.2.3 Support structure simulation suite

The three modelling methods described in Section 5.2.2 are applied for the modelling of the support structure of the NTNU rotor. Seven simulations are performed, listed in Table 5.1. The nomenclature for each case consists of two words separated by a hyphen: the first refers to the nacelle and the second one to the tower modelling method. "MSH" corresponds to body-fitted modelling of the support structure component, "CB" corresponds to cell-blocking, "AD" to actuator disc nacelle representation and "AL" to actuator line tower representation. "X" denotes that the structural component is not modelled.

All simulations employ the same numerical set up apart from the support structure modelling method that is varied. The computational domain employed is identical to that described in Section 4.1.1, with $N_x = 100$ in the region $[W \times H \times L] = [1.5D \times 2D \times 10D]$. The boundary conditions are as follows: a turbulent inflow is synthesised using the DFSEM boundary condition described in Section 4.3. The inflow velocity is $U_\infty = 10$ m/s and the turbulence intensity $2D$ upstream

of the rotor plane is $TI = 0.3\%$. The side walls of the tunnel are modelled using slip boundary conditions.

The ALM parameters are consistent across all simulations of Table 5.1. The LAS method is employed for the sampling, with $N_t = 400$, following conclusions of Chapter 3. The aerofoil data used here are those of DTU, Sarlak (Table 4.1) following the validation study of Chapter 4. The Wimshurst & Willden [84] tip correction, described in Chapter 2, is employed. A typical value of $\varepsilon = 2\Delta x$ is used and a spherical Gaussian smearing kernel, also discussed in Chapter 2.

Nacelle Modelling	Tower Modelling	Label
none	none	X-X
mesh	none	MSH-X
mesh	mesh	MSH-MSH
cell-blocking	none	CB-X
cell-blocking	cell-blocking	CB-CB
actuator disc	none	AD-X
actuator disc	actuator line	AD-AL

Table 5.1: Summary of the support structure simulations performed alongside the nomenclature used to indicate the support structure modelling method.

5.2.4 Rotor and support structure axial force

The axial force on the nacelle, tower and combined support structure as well as the thrust of the rotor for each simulated case of Table 5.1 are presented in Table 5.2. Reported values have been averaged across the last five rotor rotations, to capture the mean effect of the turbine dynamics and turbulence.

The diameter-based Reynolds number of the nacelle, using the freestream velocity $U_\infty = 10\,\mathrm{m/s}$, is $\mathrm{Re} = 5 \times 10^4$. The axial force calculated using MSH-X, is $F_{ax,nac}^{MSH-X} = 0.29\mathrm{N}$. This gives an overall drag coefficient of $C_D = 0.74$ for the nacelle, and the ratio between the rotor thrust and nacelle drag is $F_{ax,R}/F_{ax,nac}^{MSH-X} \approx 113$. The CB-X simulation applies a drag force ~ 1.5 times larger, which is related to the thick boundary layer produced by the method due to the lack of wall treatment and consequent increase in momentum deficit. The thrust coefficient for the AD-X method has been calculated based on MSH-X and therefore the force is the same as

Simulation	Nacelle Drag $F_{ax,nac}$ [N]	Tower Drag $F_{ax,tow}$ [N]	Support Structure Drag $F_{ax,ss}$ [N]	Rotor Thrust $F_{ax,R}$ [N]
X-X	0	0	0	33.59
MSH-X	0.29	0	0.29	33.74
MSH-MSH	-	-	1.59	33.59
CB-X	0.49	0	0.49	33.71
CB-CB	-	-	3.45	33.43
AD-X	0.29	-	0.29	33.68
AD-AL	0.28	0.919	1.19	33.55

Table 5.2: Mean axial force values for the support structure components alongside the mean rotor thrust for the simulations of Table 5.1.

$F_{ax,nac}^{MSH-X}$. In all three nacelle-only cases the presence of the nacelle contributes to a slight increase in rotor thrust when compared to the X-X case due to diversion of flow around the hub towards the inner sections of the blades.

The Reynolds number based on the average tower diameter $\bar{D}_T$ and freestream velocity $U_\infty = 10$ m/s, is $\mathrm{Re}_{tow} = 4.2 \times 10^4$. An approximation of the force experienced by the tower component only can be given by $F_{ax,tow} = F_{ax,ss}^{MSH-MSH} - F_{ax,nac}^{MSH-X} = 1.3$N, giving $C_D = 0.35$ and $F_{ax,R}/F_{ax,tow} = 25.8$. The support structure force predicted by the cell-blocking method is approximately 2.1 times larger than the body-fit force. The AD-AL support structure force is 0.75 of $F_{ax,ss}^{MSH-MSH}$.

Pierella and Sætern discuss the rotor to tower axial force ratio, $F_{ax,R}/F_{ax,tow}$, in [144]. For the NTNU rotor, they assumed a tower drag coefficient of $C_D = 1.2$ giving $F_{ax,R}/F_{ax,tow} = 7$. Here, a smaller tower drag is calculated using body-fitted simulations, giving a ratio $F_{ax,R}/F_{ax,tow} = 25$. This ratio is closer to the ratio predicted by Pierella and Sætern for a utility scale rotor: the rotor to tower thrust ratio for the DTU 10 MW rotor, assuming a tower drag coefficient of $C_D = 0.7$ is estimated as $F_{ax,R}/F_{ax,tow} = 39$. While this ratio is highly dependent on the assumed C_D, this observation may suggest that the discussion of the following sections regarding the interaction between rotor and support structure wakes may transfer to utility scale turbines. However, estimating the tower drag coefficient based on the freestream velocity is likely to be inaccurate in all cases, as the majority of the tower downstream of the rotor swept area experiences a mean flow that is

subject to an average induction of the order of 1/3 in design conditions. Additionally, the tower experiences highly dynamic flow related to the blade rotation.

The body force prediction of the various methods considered has been estimated to vary by a maximum factor of 2.1. This difference stems from the different treatments inherent to different methods, the cell size and the user-defined values of various parameters. The variance of force predictions between methods is deemed reasonable when compared to the rotor thrust. In the absence of an accurate tower force estimate to be used as a baseline, the methods are employed with a recognised inconsistency in forces: the effect that the force may have on the wind turbine wake is considered part of the wake problem and is tested in the following sections.

5.2.5 Instantaneous flow

A qualitative comparison of the instantaneous vorticity magnitude of the wakes from each simulation of Table 5.1 is presented in Figure 5.3.

While root vortices can be identified in the X-X simulation, they are weakened or broken down in all other simulations.

The tip vortex breakdown in the upper side tip region is consistent in all simulations and occurs at approximately $x/D = 1.5$. However, the lower side tip vortices are significantly affected by the presence of the tower, leading to an immediate breakdown of the tip vortices that interact with it. This feature is less well captured in the AD-AL case, where tip vortical features below hub height persist after their interaction with the tower.

The region downstream of the tower for both MSH-MSH and CB-CB simulations is characterised by a strong presence of turbulent eddies. This is related to the ability of the two methods to promote flow separation downstream of the modelled tower, generating a more realistic bluff body wake. In the AD-AL case, dynamic features can be observed in the lower part of the wake and downstream of the tower as a result of the imposed dynamic lift described in Equation 5.6. However, these structures do not resemble turbulent eddies. This is likely linked to the inability of the ALM model to represent separated flows, [172], if ε is not adjusted.

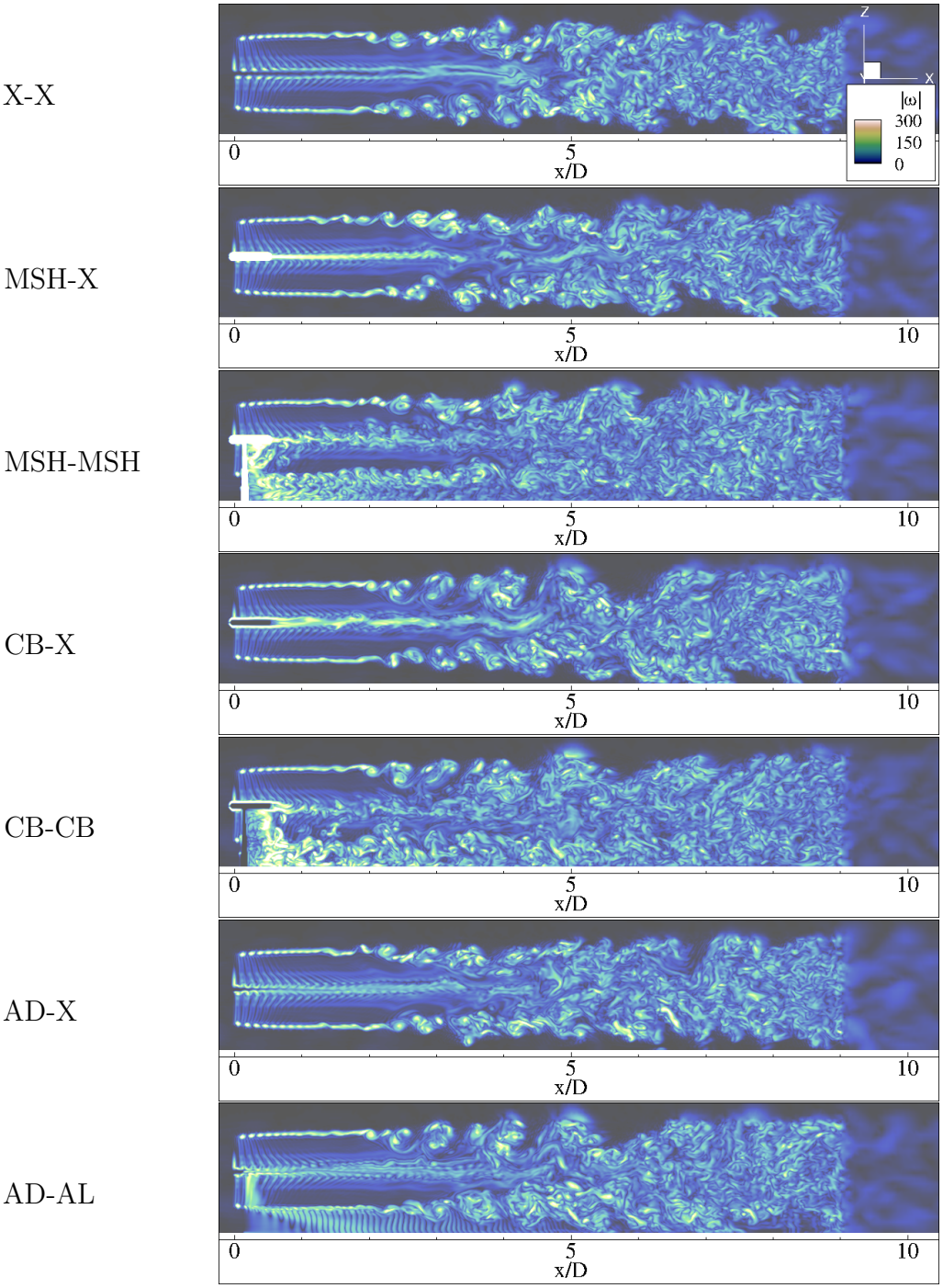


Figure 5.3: BT1, $N_x = 100$: Contours of instantaneous vorticity magnitude across a vertical plane through the centre of the rotors. See Table 5.1 for nomenclature.

In the far wake, for example at $x/D = 8$, the centreline and tip vorticity have merged into a seemingly homogeneous turbulent wake in all simulations. In the three tower cases, turbulent structures extend to the lower wall of the simulation ($z = 0$), while in the axisymmetric cases the wake has expanded at a similar rate below and above hub height.

5.2.6 Meshed support structure influence on near wake predictions

The near wake mean velocity and TKE profiles of simulations X-X, MSH-X and MSH-MSH are presented in both the horizontal and vertical planes in Figure 5.4, for three downstream locations $x/D = 1,\ 3\ \&\ 5$. The effect of including first the nacelle and then the tower as meshed structures in ALM-LES simulations of wind turbine wakes is explored. Numerical predictions are compared with the measured experimental data of BT1.

Alongside the flow profiles, the interaction between the wake of the support structure and the wake of the rotor, captured in the MSH-MSH simulation is further explored. The evolution of the mean velocity and TKE contours in the near and far wake, spanning $x/D = 0 - 8$, is visualised in Figures 5.5 & 5.6.

Streamwise location $x/D = 1$:

The ALM-LES prediction of the horizontal and vertical mean flow profiles at $x/D = 1$ benefit significantly from the inclusion of both the tower and nacelle when compared to the experimental measurements.

The $-0.2 < y/R < 0.5$ inboard section of the wake, measured in the horizontal plane, is characterised by a peak in mean velocity deficit together with a peak in TKE (Figure 5.4, (a), (c), $x/D = 1$). Both peaks correspond to the tower wake being swept upwards by the rotor wake, as observed in the $x/D = 1$ flow contours of Figure 5.5. This behaviour is accurately captured by the MSH-MSH simulation.

The mean flow prediction in the region below the lowest blade point, $(z - z_h)/R < -1$, visualised in the vertical profiles of Figure 5.4, (b) & (d), is somewhat improved when the MSH-MSH support structure representation is used: the presence of the

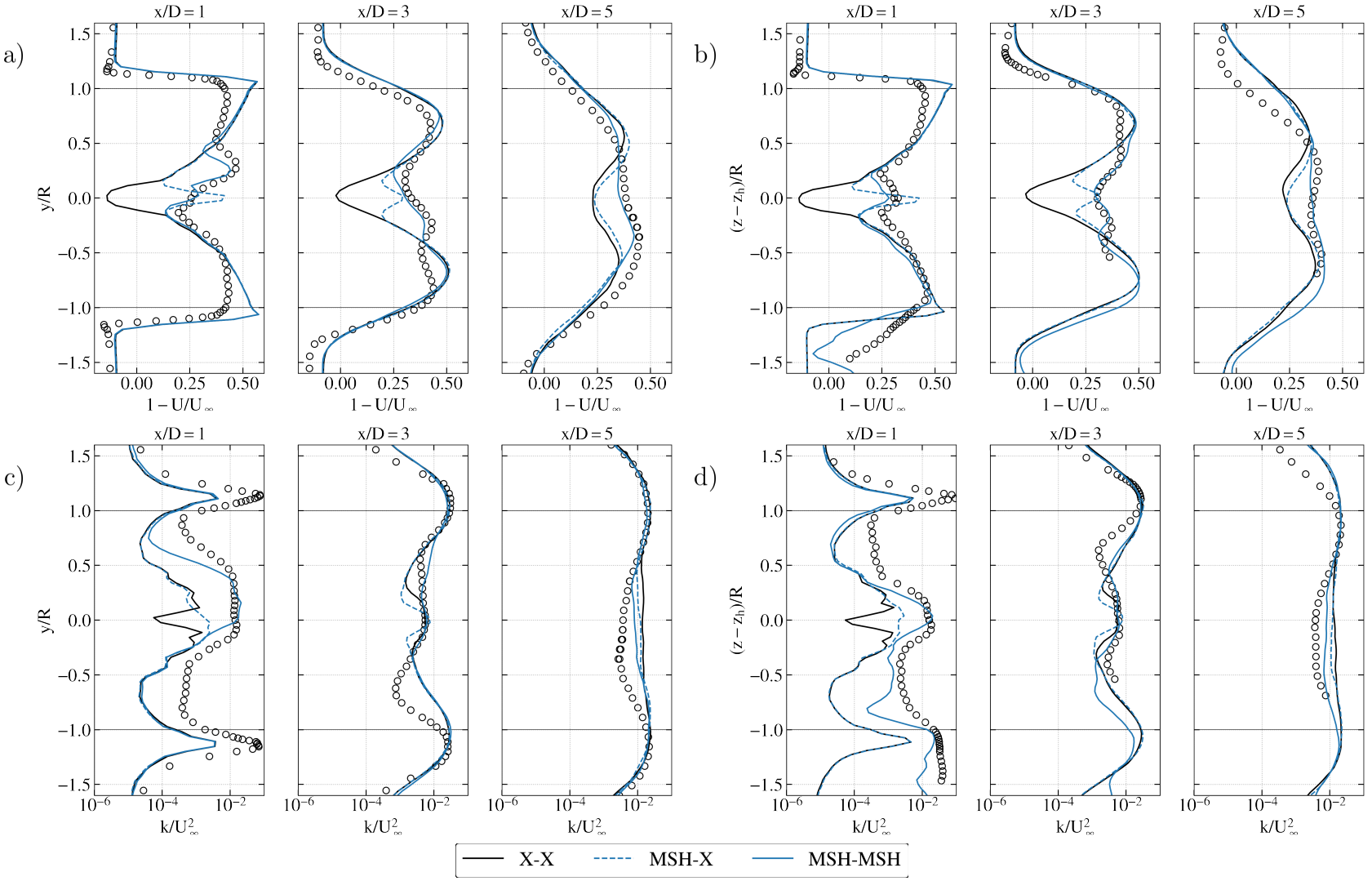


Figure 5.4: BT1: Horizontal and vertical mean flow profiles downstream of the rotor plane for the body-fitted simulations summarized in Table 5.1, at downstream locations $x/D = 1$, 3 &5. (a): Horizontal plane mean velocity deficit; (c) Horizontal plane TKE; (b): Vertical plane mean velocity deficit; (d) Vertical plane TKE. Black circles denote experimental measurements presented in [113].

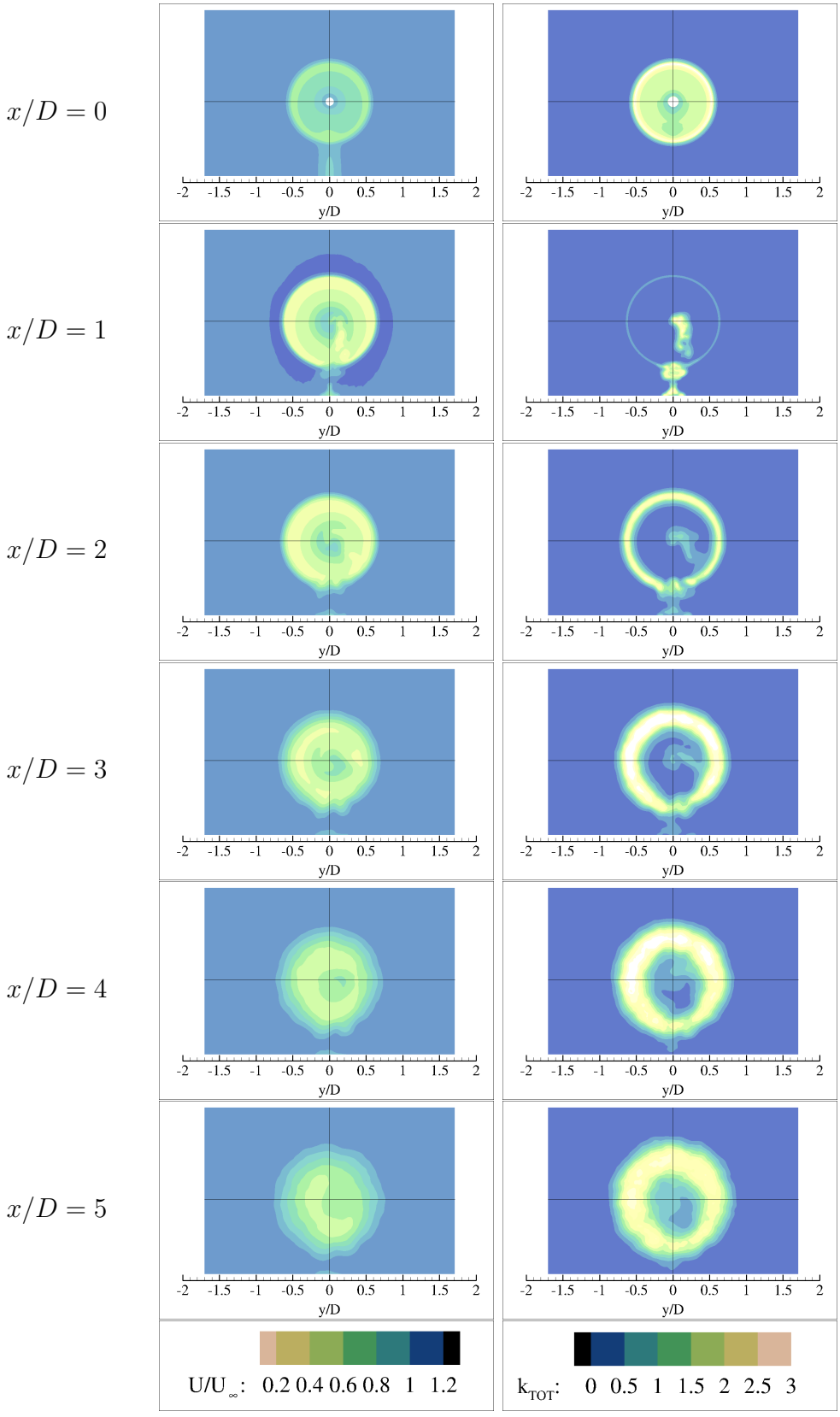


Figure 5.5: MSH-MSH: Streamwise evolution of the mean velocity (left) and TKE (right) downstream of the rotor plane. Two-dimensional planes have been extracted at streamwise locations in the range of $x/D = 0 - 5$.

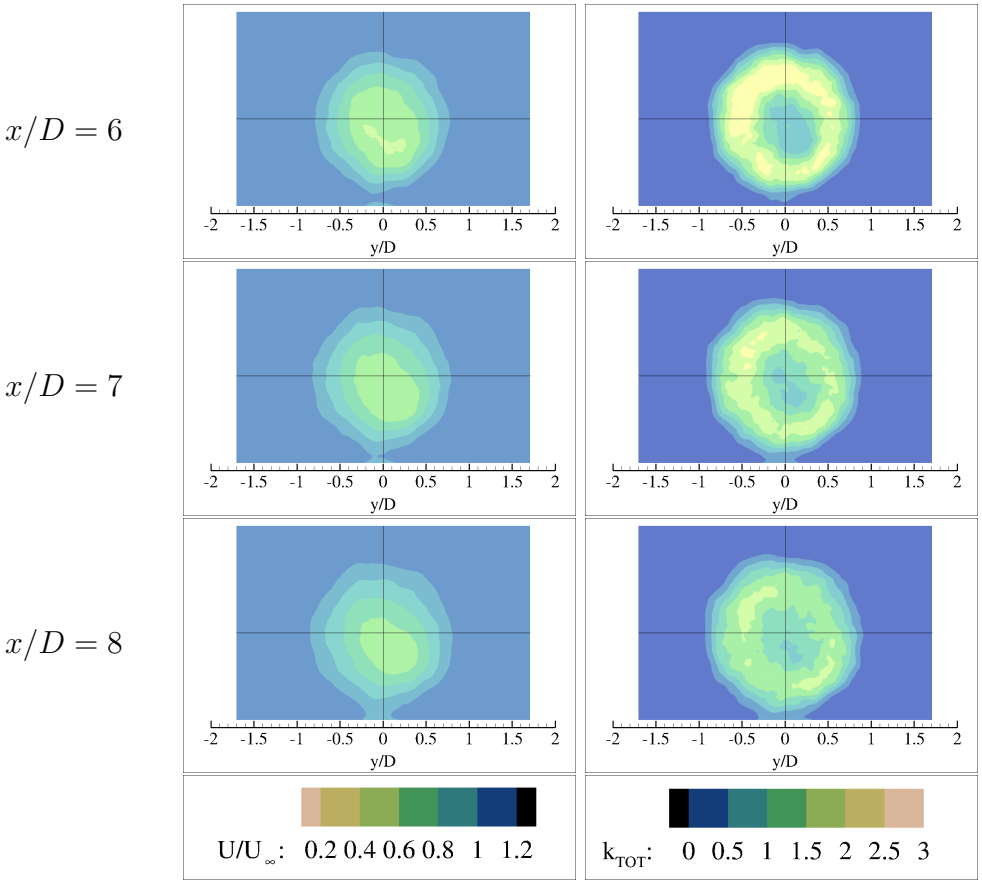


Figure 5.6: MSH-MSH: Streamwise evolution of the mean velocity (left) and TKE (right) downstream of the rotor plane. Two-dimensional planes have been extracted at streamwise locations in the range of $x/D = 6 - 8$.

tower contributes to an increase in the velocity deficit and the TKE in these locations. However, the measured deficit on this lower side is still greater than the simulated.

The inclusion of the nacelle only (MSH-X) generally suppresses the spurious jet through the rotor centre and therefore improves the mean velocity and TKE prediction at $x/D = 1$ in comparison to the simulation without any support structure (X-X). However, the asymmetric features observed in the experimental measurements and closely matched by the MSH-MSH simulations are not captured by the MSH-X simulation, the wake of which remains axisymmetric.

All simulations of Table 5.1 consistently overpredict the momentum deficit at the tip of the wake, $|y/R| \approx 1$. This behaviour results from several compounding factors, such as the blockage of the domain, the low turbulence levels that allow the tip vortices to be more persistent, and the choice of the Gaussian kernel width

of the actuator line. Similar peaks at the edge of the near wake have been observed for the same rotor in [139, 145]. Away from the overprediction of momentum deficit at the edge of the near wake, the effect of the support structure can be identified in the inboard sections of the wake for all streamwise stations in the range $1 \leq x/D \leq 5$ (Figure 5.4).

Another aspect of the ALM that can be observed consistently for all simulations is the underprediction of blade-induced TKE, visible in the mid-span region of the TKE profiles of Figure 5.4, (b), (d), $x/D = 1$). Similar behaviour is generally observed in most ALM near wake predictions [113].

Streamwise location $x/D = 3$:

The mean velocity deficit predicted by the MSH-MSH simulation, sampled at the horizontal plane three diameters downstream of the rotor plane (Figure 5.4, (a), $x/D = 3$) also follows the experimental measurements closely. In both the experimental dataset and the MSH-MSH results, the local velocity deficit peak in the inboard section of the wake has switched side of the centreline when compared to its position at $x/D = 1$. This is attributed to the swirling of the tower wake by the rotor wake as visualised in the mean velocity contours between $x/D = 1 - 3$ of Figure 5.5. MSH-MSH predictions also follow closely the experimentally measured mean velocity deficit at the vertical plane (Figure 5.4, (b), $x/D = 3$).

Adding only a nacelle model (MSH-X) affects the wake at $x/D = 3$ in the same way that it does at $x/D = 1$: the spurious jet is suppressed and, as a result, MSH-X can predict wakes that are in better agreement with experimental measurements than the predictions of X-X simulation. However, nacelle-only methods are unable to predict the asymmetry introduced into the wake by the tower.

Streamwise location $x/D = 5$:

At $x/D = 5$, the MSH-MSH simulations still outperform the other simulations in terms of agreement with the experimental measurements. The MSH-MSH wake follows closely the experimental data and presents asymmetric features. Mean flow profiles of X-X and MSH-X simulations are in close agreement, contrary to

observations in upstream streamwise locations where MSH-X outperformed the X-X predictions by suppressing the spurious centreline jet behaviour.

The asymmetry observed in the flow profiles at this streamwise station can be explained by observing the three-dimensional evolution of the rotor wake. The TKE contours at $x/D = 1$ demonstrate an increased TKE at $(z - z_h)/R \approx -1$ and $r/R = 1$, as a result of the interaction between the tip vortices and the tower structure and wake. The sections of the rotor wake edge that have interacted with the tower develop less shear at $x/D = 2$ onwards, compared to those that have not interacted with the tower. This imbalance is rotated by the rotor wake. The combined result of the interaction with the tower and the wake rotation leads to higher tip region turbulence in quadrant $y/R < 0, (z - z_h)/R > 0$ and lower tip turbulence in quadrant $y/R > 0, (z - z_h)/R < 0$ at downstream locations. This evolution explains the asymmetry observed in the experimental measurements and MSH-MSH predictions at $x/D = 5$.

The observation that satisfactory agreement with experiments at $x/D = 5$ can only be achieved by fully modelling the tower suggests that the influence of the tower evolves into the far wake and is not insignificant compared to the rotor wake, even though the associated support structure may be small compared to the rotor.

The above flow contours and discussion also confirm and extend the work of Pierella and Sætran [144]. In their work, mean velocity contours of the same rotor were measured using a five-hole Pitot tube at locations $x/D = 0.6,\ 1,\ 1.5,\ 2\ \&\ 3$. Observations allowed them to identify, among other features, an interruption in the azimuthal symmetry of momentum entrainment. Discussion here further explains the interaction between the support structure wake and the rotor wake by means of turbulence quantities. The extended available data range, up to $x/D = 8$, allows the study of the effect of the support structure in the far wake.

5.2.7 Nacelle modelling effect on wake predictions

The contribution of different nacelle modelling options on the near wake are compared in this section. Horizontal mean velocity and TKE predictions of the

NTNU rotor are presented in Figures 5.7, (a),(c) respectively, for four downstream locations $x/D = 1$, 3, 5 & 8. A comparison with experimental data is not performed, since a tower model is omitted in these simulations.

AD-X and MSH-X nacelle representations impose the same resistance on the flow given the axial force measurements presented in Table 5.2. This is also depicted by the close agreement of the methods in predicting the mean velocity deficit at all downstream locations of Figure 5.7, (a), (c). MSH-X introduces slightly higher TKE peaks owing to the ability of the body-fitted method to generate separated flow.

CB-X imposes a large force in the flow and thus introduces a high velocity deficit accompanied by high TKE, at $x/D = 1$ when compared to the MSH-X simulation.

Regardless of the nacelle representation, all wakes predict similar mean flow profiles at $x/D = 8$ across the wake span suggesting that all methods might be appropriate for a nacelle-only representation if the focus is on the mean flow of the far wake.

5.2.8 Tower modelling effect on wake predictions

Having established that the MSH-MSH support structure model closely follows experimental measurements of the NTNU rotor near wake, the capability of the CB-CB and AD-AL simulations to capture the same features is assessed. Horizontal profiles of the mean velocity deficit and TKE profiles at four downstream locations $x/D = 1$, 3, 5 & 8 are presented against experimental measurements [113] in Figure 5.7, (b), (d).

At $x/D = 1$, the peaks of mean velocity deficit and TKE at $-0.2 < y/R < 0.5$, identified as a result of the tower/rotor wake interaction, are captured by both MSH-MSH and CB-CB methods. This is attributed to the ability of the two methods to generate a turbulent wake downstream of the tower that interacts with the rotating wake of the rotor. On the other hand, while AD-AL simulation presents some wake asymmetry, the mean velocity and TKE profiles do not follow the experimental data.

At $x/D = 3$ both the CB-CB and AD-AL methods deviate from the experimental measurements. The mean velocity deficit peak at $y/R \approx -0.25$, observed in the

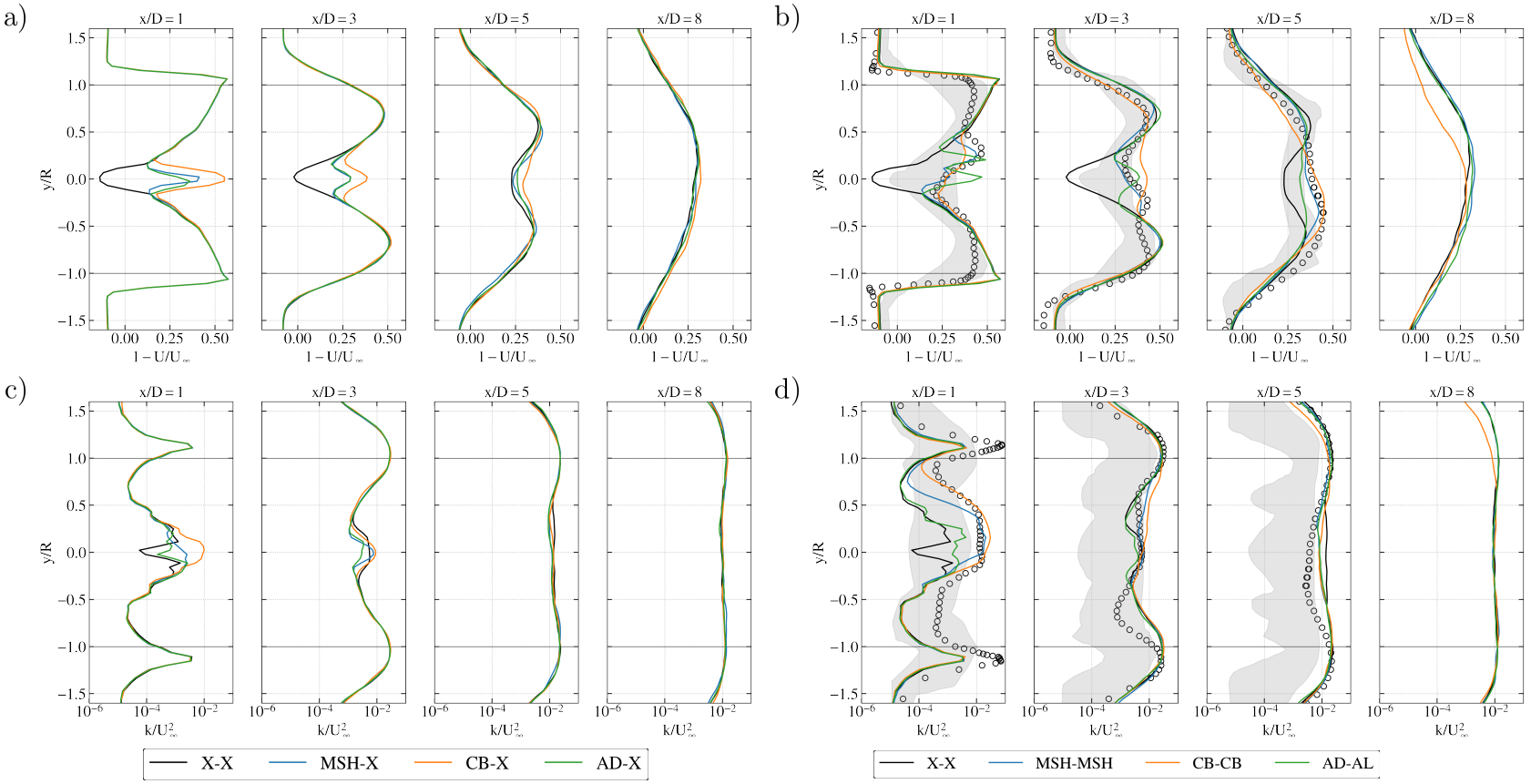


Figure 5.7: BT1: Horizontal mean flow profiles downstream of the rotor plane for the simulations summarized in Table 5.1, at downstream locations $x/D = 1$, 3, 5, & 8. The left panels present wake profiles of nacelle-only simulations, with (a) Mean velocity deficit and (c) TKE; The right panels present wake profiles of nacelle&tower simulations, with (b) Mean velocity deficit and (d) TKE; Black circles denote experimental measurements and shaded areas correspond to the range of numerical predictions from various modelling methods, presented in [113].

experimental data, cannot be identified in the CB-CB mean velocity profiles, as the deficit appears to have mixed with the surrounding flow, as implied by the enhanced TKE at $x/D = 3$ as a result of the CB-CB implementation. The prediction of the AD-AL method has returned to a symmetric wake, suggesting that the tower wake created by the actuator line was not sustained in the far wake of the turbine. This may be attributed to the lack of separation from the tower ALM if not properly calibrated, as discussed by Rocchio *et al.* [172].

At $x/D = 5$ the experimental measurements present a slightly higher velocity deficit around $y/R \approx -0.4$. Both MSH-MSH and CB-CB also capture this asymmetric behaviour. The AD-AL method improves the wake prediction at that streamwise station, when compared to the X-X case as well as the AD-X case (Figure 5.7, (a)). TKE predictions at $x/D = 5$ are slightly improved for all methods when compared to the X-X case.

At $x/D = 8$, the mean velocity deficit predictions for all simulations apart from CB-CB are in close agreement. The latter predicts significant asymmetry of the flow deficit at the horizontal plane due to a highly turbulent tower wake caused by both a large body force and the lack of wall treatment within the cell-blocking technique.

5.3 Support structure impact on far wake axisymmetry

The mean velocity deficit in the far wake of a wind turbine is often regarded as axisymmetric and self-similar [173], which has given rise to Gaussian-based engineering wake models such as the Bastankhah-Porté-Agel model (BP) [35]. However, wakes are often observed to be non-axisymmetric in experiments [113, 174]. Additionally, it is rarely the case that the entire azimuth of the wake is measured, which only allows assessment of the assumption of axisymmetry for a portion of the wake azimuth [175]. Pierella and Sætern [144] measured the mean velocity field around the entire azimuth at streamwise locations $x/D = 0.6 - 3$ downstream of the NTNU rotor. Strongly non-axisymmetric behaviour was observed in the near wake,

which was attributed to the interaction with the tower wake. The persistence of this behaviour in the far wake of the NTNU rotor is demonstrated in Section 5.2.6.

In the present section, the validity of the Gaussian assumption for the far wake is tested by comparing the MSH-MSH wake data with a Gaussian wake model. The validity of a Gaussian representation is also compared against the MSH-X and X-X far wake data in order to assess the proportion of the error of the Gaussian model that can be attributed to the asymmetry introduced by the tower.

5.3.1 Description of the datasets

CFD data and blockage correction

The non-negligible blockage of 12% for the NTNU BT1 experiment has been discussed in many studies. Sarlak *et al.* [139] dedicated a study to the effect of blockage on wind turbine wakes using the NTNU rotor, considering blockage ratios of up to 20%. They concluded that blockage ratios within the explored range did not significantly impact the wake mixing rate. While blockage affected the overall velocity profile (especially at higher ratios, close to 20%), the difference between the maximum and minimum velocity remained fairly constant, suggesting that the mixing rate was not significantly affected by blockage.

The ALM-LES blocked wakes here are corrected by the mean velocity at the bypass at each streamwise location, $U_{bypass}(x)$, sampled at radial locations outside of the wake region where the velocity only varies by less than 1%. Hereafter, with U_{CFD} we refer to the blockage-corrected CFD data:

$$U_{CFD}(x,y,z) = U_{CFD}^{uncorrected}(x,y,z)\frac{U_\infty}{U_{bypass}(x)}. \tag{5.7}$$

Therefore, U_{CFD} asymptotes to U_∞ with radial distance. Similar wake corrections based on the bypass velocity have been developed in [176]. In this study it is important to correct for blockage in order to be consistent with subsequent comparisons with an unblocked Gaussian wake model. All three X-X, MSH-X, MSH-MSH simulations have been corrected using the same method, and additionally the support structure is not found to affect U_{bypass} significantly, therefore, the

subsequent analysis is considered to have already accounted for blockage related effects. Any remaining blockage related artefacts are expected to be consistent across the three wakes.

Gaussian far wake model

To explore how accurately a Gaussian assumption can represent the far wake of ALM-LES simulations, the widely used BP Gaussian far wake model is employed. The model assumes a Gaussian far wake, employs mass and momentum conservation and assumes linear wake expansion.

The wake deficit $\Delta U/U_\infty$ at a streamwise location x downstream of a rotor of diameter D can be described by a two-dimensional Gaussian function centred at the hub height, z_h:

$$\begin{aligned}\frac{\Delta U}{U_\infty} = \Big(1 - \sqrt{1 - \frac{C_T}{8\big(\frac{k^* x}{D} + \frac{\sqrt{\beta}}{4}\big)^2}}\Big) \exp\Big(- \frac{1}{2\big(\frac{k^* x}{D} + \frac{\sqrt{\beta}}{4}\big)^2}\Big\{\big(\frac{z - z_h}{D}\big)^2 + \big(\frac{y}{D}\big)^2\Big\}\Big),\\ \frac{\Delta U}{U_\infty} = \frac{U_\infty - U_{Gauss}}{U_\infty},\\ \beta = \frac{1 + \sqrt{1 - C_T}}{2\sqrt{1 - C_T}}.\end{aligned} \tag{5.8}$$

The model depends on the thrust coefficient C_T and the wake expansion parameter k^*. C_T is set using the thrust coefficient of the ALM-LES simulation, that is relatively unaffected by the presence of the tower. The wake expansion coefficient k^* is best-fitted to the ALM-LES data using the MATLAB genetic algorithm (GA) optimisation function [177]. By best-fitting k^*, the ability of the Gaussian model to predict an ALM-LES wake is assessed. The objective functions and optimisation processes for the best fit are further discussed in the next section.

A wake centreline correction is added to the Gaussian model in order to assess the potential to model the drop of the far wake centreline observed in Figures 5.5 and 5.6. The centreline is added by introducing (C_Y, C_Z), and the Gaussian deficit model reads:

$$\frac{\Delta U}{U_\infty} = \Big(1 - \sqrt{1 - \frac{C_T}{8\Big(\frac{k^* x}{D} + \frac{\sqrt{\beta}}{4}\Big)^2}}\Big) \exp\Big(-\frac{1}{2\Big(\frac{k^* x}{D} + \frac{\sqrt{\beta}}{4}\Big)^2}\Big\{\Big(\frac{z - z_h - C_Z}{D}\Big)^2 + \Big(\frac{y - C_Y}{D}\Big)^2\Big\}\Big). \tag{5.9}$$

5.3.2 Gaussian fitting of the ALM-LES wake

The ALM-LES wake field U_{CFD}, and Gaussian wake U_{Gauss} are compared in this section to explore the validity of the Gaussian assumption for the high-fidelity simulation data of a far wake of a wind turbine with and without support structures. Four different fits are performed using GA optimisation of the Gaussian parameters. Two different sets of model parameters and two different types of minimisation functions are employed, presented in Table 5.3.

Fit	Model parameters	Minimisation Function	U_{Gauss} Equation
1	$k^*(x)$	$\langle \varepsilon(U) \rangle_W$	5.8
2	k^*	$\Big\langle \langle \varepsilon(U) \rangle_W \Big\rangle_{FW}$	5.8
3	$k^*(x)$, $C_Z(x)$, $C_Y(x)$	$\langle \varepsilon(U) \rangle_W$	5.9
4	k^*, C_Z, C_Y	$\Big\langle \langle \varepsilon(U) \rangle_W \Big\rangle_{FW}$	5.9

Table 5.3: Summary of the variables and minimisation functions of the optimisations.

The model parameters, i.e. the design variables of the GA optimisations are:

- a single variable, namely the wake expansion coefficient, k^*, used in Fits 1 and 2. k^* is the only undefined parameter in the typical implementation of the Gaussian model of Equation 5.8;
- three design variables, k^*, (C_Y, C_Z), used in Fits 3 and 4. This introduces a wake centre to the Gaussian model, as described in Equation 5.9.

The minimisation functions employed in the GA optimisations are as follows:

- First, the local relative error field is calculated, $(U_{Gauss}(y,z) - U_{CFD}(y,z))/U_{CFD}(y,z)$, representative of the ability of the Gaussian model to approximate the ALM-LES results at each point across a wake plane. A visualisation of such fields is presented in Figure 5.8. To obtain a representative value of the local error at a spanwise station, the absolute value of the local error above is averaged across the wake. This averaging is denoted by $\langle\rangle_W$, where the $_W$ subscript implies averaging in the region $-0.75 < y/D < 0.75$ and $-0.75 < (z - z_h)/D < 0.75$. The wake-averaged mean velocity absolute relative error is denoted $\langle\varepsilon(U)\rangle_W$ (see Equation 5.10) and is used as a minimisation function in Fits 1 and 3. A best-fit value for the design variables is therefore found independently for each streamwise location. Distributions of the optimal $k^*(x)$ and $(C_Y(x), C_Z(x))$ are obtained that represent the best ability of the Gaussian model to imitate the ALM-LES wake at each streamwise location.

- An average error estimate considering the entire far wake can be obtained by further averaging $\langle\varepsilon(U)\rangle_W$ in the streamwise direction. Streamwise averaging is here denoted by $\langle\rangle_{FW}$, where $_{FW}$ subscript implies far wake. The far wake here is considered to be in the range $5.5 \leq x/D \leq 8.5$. Various criteria have been considered in the literature to identify the onset of the far wake. In Neunaber *et al.* [175] the onset of the far wake coincides with the onset of the decrease in TI at the wake centreline, which in all present simulations, regardless the support structure modelling, occurs at $x/D \approx 5$. Additionally, as will be discussed in the following Sections, a plateau in $k^*(x)$ is observed for $x/D \geq 5$ which suggests that the wake can be accurately represented by a constant k^* model, often assumed for far wakes. Contrary to Fits 1 and 3, where streamwise distributions of the design variables were sought, in Fits 2 and 4 a single optimal value of k^* and (C_Y, C_Z) is obtained that represents the entire far wake. A single fitted-value of the wake parameters may be preferred to one that varies with x when it comes to engineering models.

Various error definitions are employed in this analysis to describe the differences in mass flux, directly represented with the Gaussian model, and proportional to u, and the associated kinetic energy flux, proportional to u^3. Four definitions are presented in Equations 5.10-5.13, depending on how the errors are averaged. Errors 5.10 and 5.11 represent the wake flow field and are averaged across the entire sampled wake using the $\langle\rangle_W$ notation. Errors 5.12 and 5.13 represent the power availability to a hypothetical rotor located at a downstream location. The yz plane averaging in this case is only performed over the rotor disc area that corresponds to the area of power extraction of a downstream turbine, and is denoted as $\langle\rangle_D$.

The averaging can be performed either before or after the local relative error calculation. In the cases where the $\langle\rangle_W$ or $\langle\rangle_D$ averaging is performed after the local relative error calculation, an average value of the relative error is obtained. Thus, local flow field inconsistencies between the CFD and Gaussian wakes are highlighted (Equations 5.10 and 5.12). In the cases where $\langle\rangle_W$ or $\langle\rangle_D$ averaging is performed first, producing an average velocity or cubed velocity value, the relative error is used to compare the averaged values (Equations 5.11 and 5.13). These errors are used to highlight the ability of the Gaussian wake model to predict an area-averaged velocity or power prediction.

$$\langle\varepsilon(U)\rangle_W(x) = \left\langle \frac{|U_{Gauss} - U_{CFD}|}{U_{CFD}} \right\rangle_W (x)\ 100\ [\%] \tag{5.10}$$

$$\varepsilon(\langle U\rangle_W)(x) = \frac{|\langle U_{Gauss}\rangle_W - \langle U_{CFD}\rangle_W|}{\langle U_{CFD}\rangle_W}(x)\ 100\ [\%] \tag{5.11}$$

$$\langle\varepsilon(U^3)\rangle_D(x) = \left\langle \frac{|U^3_{Gauss} - U^3_{CFD}|}{U^3_{CFD}} \right\rangle_D (x)\ 100\ [\%] \tag{5.12}$$

$$\varepsilon(\langle U^3\rangle_D)(x) = \frac{|\langle U^3_{Gauss}\rangle_D - \langle U^3_{CFD}\rangle_D|}{\langle U^3_{CFD}\rangle_D}(x)\ 100\ [\%] \tag{5.13}$$

The streamwise evolution of errors for Fits 1 and 3 is visualised in Figure 5.10 and errors 5.10-5.13 are quantified in Table 5.4. The streamwise evolution of the design variables for Fits 1 and 3 is plotted in Figure 5.9. The errors for Fits 2

and 4 are quantified in Table 5.5. Additionally, a comparison between a Gaussian wake and an ALM-LES wake for Fit 1 at $x/D = 8$ is presented Figure 5.8 for X-X, MSH-X and MSH-MSH simulations.

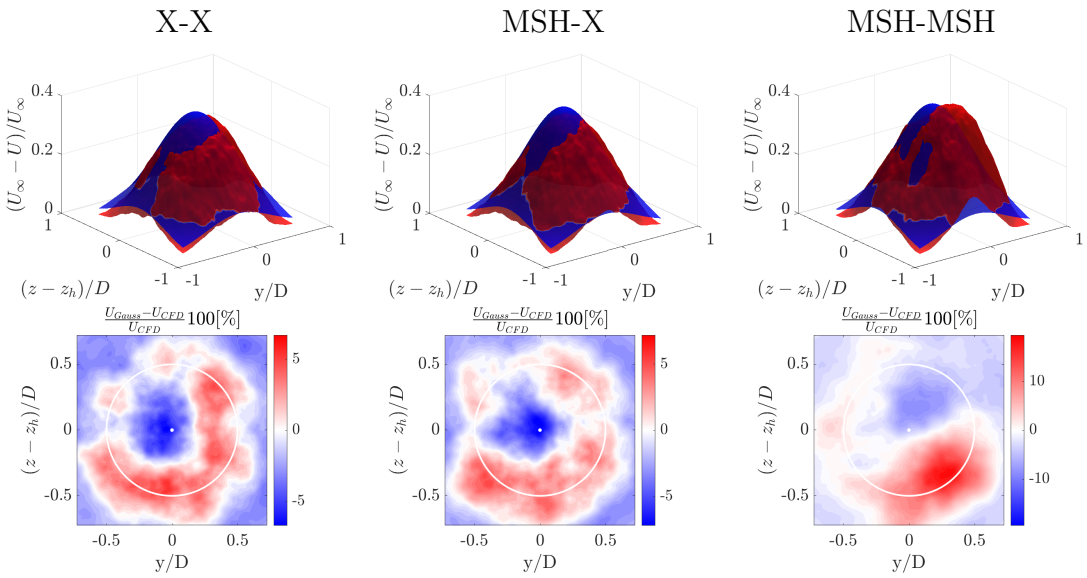


Figure 5.8: Qualitative and quantitative comparison between the wake predicted by an optimal fit Gaussian model (Fit 1) and the ALM-LES simulation results for X-X, MSH-X and MSH-MSH simulations, at $x/D = 8$. Upper panel: surface representation of the mean velocity deficit for the Gaussian (blue) and ALM-LES (red) wakes. Lower panel: mean velocity relative error field between the optimal fit Gaussian model prediction and the ALM-LES prediction.

Fit	Simulation	$k^*(8D)$	$C_Y/D(8D)$	$C_Z/D(8D)$	$\langle\varepsilon(U)\rangle_W(8D)[\%]$	$\langle\varepsilon(U^3)\rangle_D(8D)[\%]$	$\varepsilon(\langle U\rangle_W)(8D)[\%]$	$\varepsilon(\langle U^3\rangle_D)(8D)[\%]$
1	X-X	0.0191	-	-	1.93	7.14	0.19	1.55
1	MSH-X	0.0181	-	-	1.76	6.17	0.12	0.53
1	MSH-MSH	0.0175	-	-	3.61	15.46	0.61	2.62
3	X-X	0.0189	0.0121	-0.0218	1.77	6.25	0.27	0.99
3	MSH-X	0.0181	0.0076	-0.0214	1.63	5.48	0.12	0.64
3	MSH-MSH	0.0172	0.0178	-0.0835	2.63	9.71	0.57	3.34

Table 5.4: Optimal fit of k^*, (C_Y,C_Z) for the streamwise location $x/D = 8$. The errors defined in Equations 5.10-5.13 are calculated at $x/D = 8$.

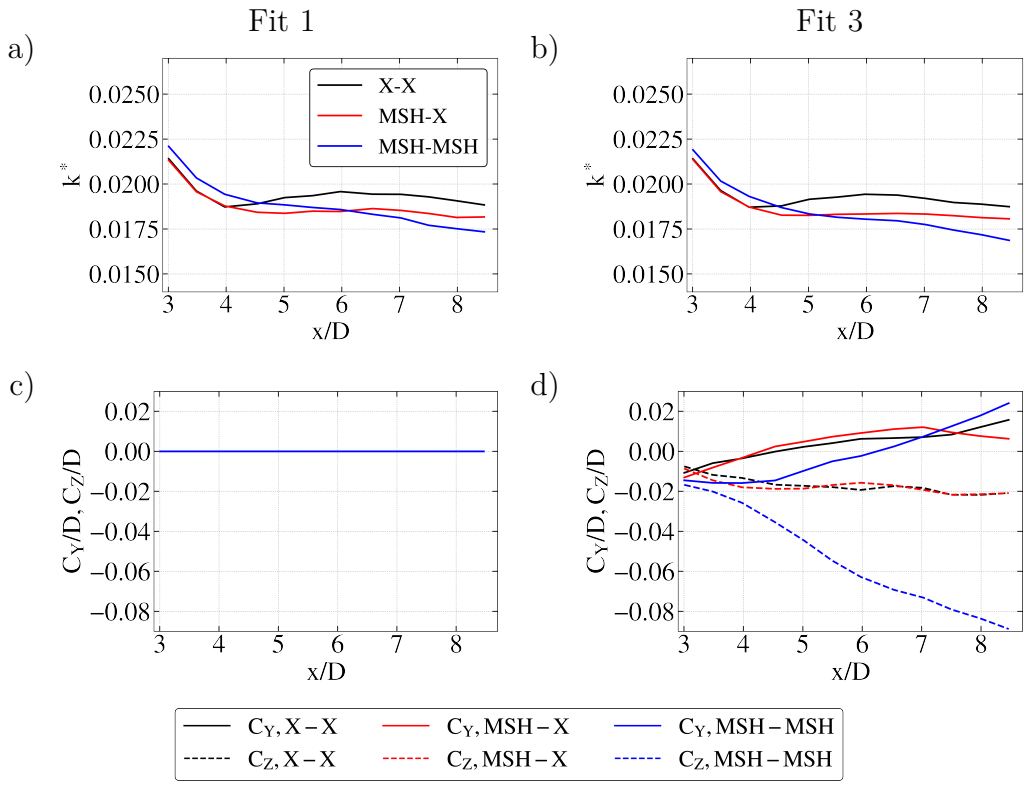


Figure 5.9: Streamwise evolution of the best fit k^*, (C_Y,C_Z) Gaussian far wake parameters for Fits 1 (left) and 3 (right).

Fit	Simulation	k^*	C_Y/D	C_Z/D	$\left\lceil\left\lceil\varepsilon(U)\right\rceil_W\right\rceil_{FW}$ [%]	$\left\lceil\left\lceil\varepsilon(U^3)\right\rceil_D\right\rceil_{FW}$ [%]	$\left\lceil\varepsilon(\left\lceil U\right\rceil_W)\right\rceil_{FW}$ [%]	$\left\lceil\varepsilon(\left\lceil U^3\right\rceil_D)\right\rceil_{FW}$ [%]
2	X-X	0.0191	-	-	2.82	12.00	0.54	1.18
2	MSH-X	0.0182	-	-	2.65	11.03	0.47	0.71
2	MSH-MSH	0.0179	-	-	4.13	18.55	0.56	4.43
4	X-X	0.0190	0.0088	-0.0198	2.72	11.48	0.58	1.07
4	MSH-X	0.0182	0.0090	-0.0192	2.54	10.37	0.50	0.55
4	MSH-MSH	0.0176	0.0050	-0.0711	3.25	13.48	0.51	4.68

Table 5.5: Counterpart of Table 5.4, for Fits 2 & 4. The errors are here averaged in the far wake.

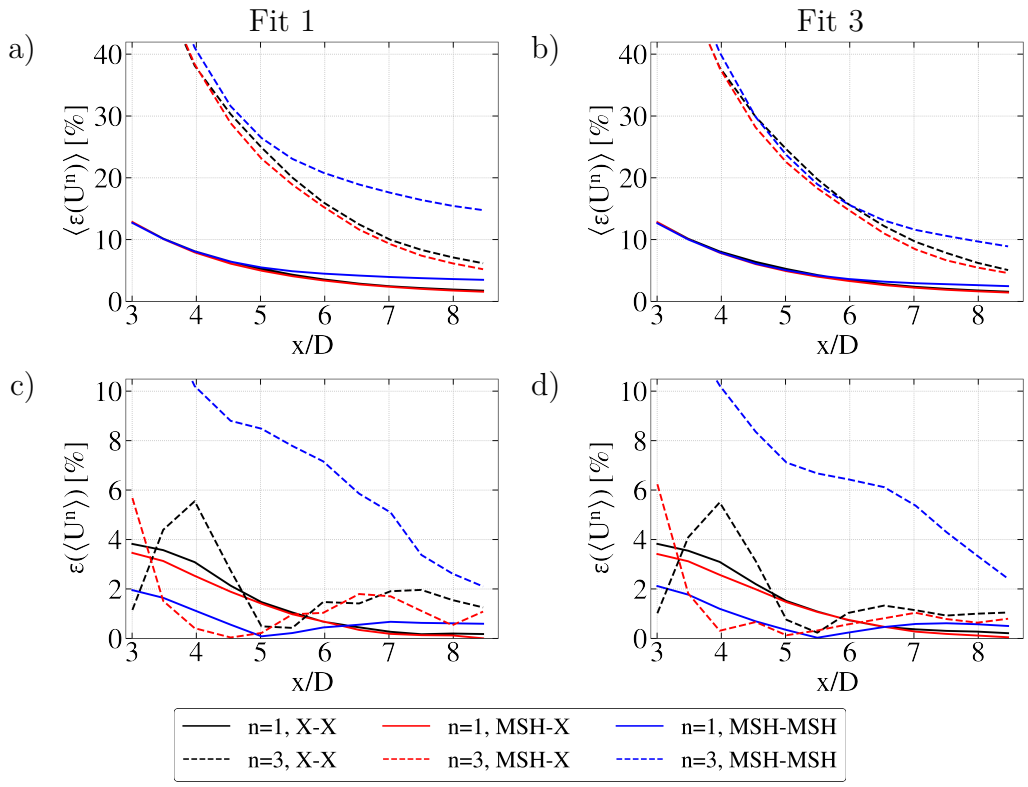


Figure 5.10: Streamwise evolution of errors 5.10, 5.12 (upper panel) and 5.11, 5.13 (lower panel) for Fits 1 and 3.

5.3.3 Gaussian wake modelling without centreline adjustment

Fit 1

The distribution of $k^*(x)$ that minimises the error for Fit 1 is presented in Figure 5.9 (a). Downstream of $x/D = 4.5$, the magnitude of dk^*/dx reduces, and k^* tends to a plateau, although k^* changes for the MSH-MSH case are monotonic and larger than for the other cases. This is consistent with the flow contours shown in Figure 5.6: the MSH-MSH wake shape continues to evolve far downstream due to the presence of the tower.

Errors $\langle \varepsilon(U) \rangle_W$ and $\langle \varepsilon(U^3) \rangle_D$ decrease with streamwise distance for all simulations, X-X, MSH-X and MSH-MSH (Figure 5.10, (a), (c)). While the errors of the X-X and MSH-X wakes remain consistent across the entire x/D range, MSH-MSH errors begin to deviate at $x/D \approx 5$ (Figure 5.10, (a)). Upstream of this location, differences between U_{CFD} and U_{Gauss} are dominated by the near

wake features of the CFD simulations for all cases. The Gaussian model's ability to approximate the far wake flow field of a high-fidelity ALM-LES simulation is reduced when the tower is explicitly simulated, and this error becomes more pronounced at greater streamwise distances.

At $x/D = 8$, the Gaussian model effectively represents the velocity field of the X-X, MSH-X and MSH-MSH wakes with wake averaged relative errors of 1.93%, 1.76%, and 3.61%, respectively. However, the corresponding errors for the prediction of the U^3 field at $x/D = 8$ are 7.14%, 6.17% and 15.46%, respectively (Table 5.4).

The relative errors between the averaged U and U^3 predicted by the Gaussian and CFD models, $\varepsilon(\langle U \rangle_W)$ and $\varepsilon(\langle U^3 \rangle_D)$ respectively, generally remain below 2% in the far wake for all simulations, with the exception of $\varepsilon(\langle U^3 \rangle_D)$ for the MSH-MSH case (Figure 5.10, (c)). The small value of these errors, relative to $\langle \varepsilon(U) \rangle_W$ and $\langle \varepsilon(U^3) \rangle_D$ may be explained by the local error contours of Figure 5.8. Both positive and negative local errors are experienced across the wake for all three simulations. Consequently, when evaluating $\langle U \rangle_W$ or $\langle U^3 \rangle_D$, the inconsistencies in local errors are masked as a result of local positive and negative errors cancelling out.

The Gaussian model's ability to predict the average U or U^3, compared to an ALM-LES simulation, experienced by a rotor eight diameters downstream, gives an error of less than 1.2% for all support structure representations (Table 5.4). The MSH-MSH case is an exception, where $\varepsilon(\langle U^3 \rangle_D) = 2.62\%$. In this case, as the flow is averaged over a disc area, there is less compensation of positive and negative local errors.

Therefore, the Gaussian model may provide a reasonable estimate of the mean velocity or power availability downstream of a rotor for cases with or without a tower. However, when considering the ability of the Gaussian model to predict the local flow field at each point in the far wake, the validity of the Gaussian wake approximation deteriorates when compared to the high-fidelity far wake that has interacted with a tower.

Fit 2

In Fit 2 the same design variables as Fit 1 are optimised, but a single value k^* is sought, representative of the entire far wake $5.5 \leq x/D \leq 8.5$. This value will likely be sub-optimal for individual streamwise stations but will provide the best fit of the Gaussian to the ALM-LES data for the entire far wake field, which is more representative of how the parameter is specified in practice.

The errors for a single far wake k^* are presented in Table 5.5. The constant k^* Gaussian model best reproduces the MSH-X far wake, with a slightly higher error calculated when reproducing the X-X far wake. The entire three-dimensional far wake flow field of the MSH-MSH simulation can be approximated by the constant k^* Gaussian model with an overall relative error in velocity field prediction of $\langle\langle\varepsilon(U)\rangle_W\rangle_{FW} = 4.13\%$ and an overall relative error in cubed velocity field prediction of $\langle\langle\varepsilon(U^3)\rangle_D\rangle_{FW} = 18.55\%$. Both errors are ~ 1.5 times larger than the corresponding X-X or MSH-X errors.

Similar to Fit 1, Fit 2 naturally performs better when the goal is to approximate an average value of U or U^3 (Table 5.5) due to compensation of errors, as discussed above.

5.3.4 Gaussian wake modelling with centreline adjustment

Fits 3 and 4 explore the possible improvement in Gaussian far wake modelling that could be achieved by introducing parameters (C_Y, C_Z) to trace the drop of the wake centreline that may arise due to the interaction with the tower wake. The standard Gaussian far wake model is modified as given in Equation 5.9.

Fit 3

The evolution of $k^*(x)$ in Figure 5.9, (c), is similar to that of Fit 1 (Figure 5.9, (a)). A non-zero centre $(C_Y(x), C_Z(x))$ is identified for all three support structure cases, however the effect of this centreline displacement for the measured errors of X-X and MSH-X is small, when compared to Fit 1. A significant drop in $C_Z(x)$

with increasing streamwise distance x is observed for the MSH-MSH case, which at $x/D = 8$ is approximately $C_Z(8D) = 8\%D = 16\%R$.

Errors $\langle\varepsilon(U)\rangle_W$ and $\langle\varepsilon(U^3)\rangle_D$ decrease with streamwise distance, similarly to Fit 1. The averaged local relative error for the X-X and MSH-X cases is marginally improved when compared to the case without wake centre displacement. The most significant improvement is observed when the MSH-MSH wake data are reproduced by the Gaussian model with a non-zero centreline. Adding a Gaussian wake centre reduces $\langle\varepsilon(U)\rangle_W(8D)$ by a factor of 1.4 when compared to the same error in Fit 1, and $\langle\varepsilon(U^3)\rangle_D(8D)$ by a factor of 1.6. However, the error at $8D$ even when employing a non-zero wake centre is not as small as that of the X-X and MSH-X wakes, suggesting that adjusting the wake centreline alone is not capable of fully accounting for the inaccuracies of the Gaussian model when it comes to representing the MSH-MSH wake.

The Gaussian model's capability to predict the average velocity $\langle U\rangle_W$ and cubed velocity $\langle U^3\rangle_D$ is minorly affected by the inclusion of a wake centre, as seen by comparing Figures 5.10 (c) to (d).

Fit 4

C_Z/D reduces approximately linearly with downstream distance, as opposed to k^* that plateaus. As a result, employing constant design variables in Fit 4 limits the predictive capabilities of the Gaussian model with centreline correction, when compared to Fit 3. The optimal $C_Z/D = -0.0711$ obtained by Fit 4 corresponds to an average value of $C_Z(x)/D$ in the range $5.5 \leq x/D \leq 8.5$ found in Fit 3.

An improvement of $\langle\langle\varepsilon(U)\rangle_W\rangle_{FW}$ by a factor of 1.2 in MSH-MSH case when compared to the Fit 2 is recorded in Table 5.5. This suggests that a constant (C_Y, C_Z) correction is unlikely to significantly improve the predictive capabilities of the Gaussian model when it comes to approximating wakes that have been influenced by the support structure.

5.4 Summary and conclusions

In this chapter, multiple aspects surrounding the interaction between support structures and wind turbine wakes are studied. Three low-cost, low-fidelity methods for representing the tower and nacelle were implemented and compared: a body-fitted method that uses an analytical wall function, a cell-blocking meshless forcing method, and an actuator disc/line approach.

The body-fitted method was found to successfully generate a turbulent wake downstream of the tower and nacelle without significantly adding to the numerical cost of the ALM-LES simulation, despite the meshing requirement to model the structure. It was capable of capturing all asymmetric near wake features observed in BT1 measurements, without the need for user-defined parameters. Two significant consequences of the interaction between the support structure and the rotor wakes were identified: (i) a non-axisymmetric flow in the inboard sections of the near wake and (ii) a tower-induced imbalance in the breakdown of tip vorticity that led to an asymmetry in the TKE in the outboard regions of the far wake. This in turn generated a non-axisymmetric far wake velocity deficit characterised by a vertical drop in the wake centre.

The cell-blocking method, which does not require mesh modifications and is also free of user-defined tuning parameters, was capable of introducing a turbulent wake downstream of the support structure, correctly capturing many non-axisymmetric aspects of the interaction of the support structure and rotor wakes. However, the method introduced a large force and relatively high TKE when compared to the experimental data, which in turn impacted the far wake mean velocity deficit in an amplified way. This behaviour is attributed to the lack of boundary layer modelling in the cell-blocking implementation.

Finally, the widely-used actuator disc/line representation of the nacelle and tower was tested using standard non-dimensional force coefficients from the literature. While the AD nacelle generated a good approximation of the flow when compared to the body-fitted nacelle, the same cannot be said for the AL tower. Representing

the tower using an actuator line was found to not be able to produce a turbulent separated wake given the current parameter setup.

The far wake asymmetry behind a rotor may challenge the validity of the Gaussian assumption employed in engineering models. In this chapter, a Gaussian wake model was fitted to the ALM-LES with body-fitted support structure data in order to quantify the errors related to the Gaussian far wake assumption. It was found that the Gaussian model performs better at predicting area-averaged values than local fields, in all cases whether or not the support structure was included. While errors in both area-averaged and local velocity values remained below 5%, predicting the cubed velocity field in the far wake was found to challenge the Gaussian assumption with local errors in the range of $15 - 18\%$. The inclusion of the tower challenged the Gaussian assumption as well by increasing all errors studied here by a factor between $1 - 9$ when compared to the case with the nacelle only. Adding a non-zero centreline to the Gaussian model, in order to account for the drop in the wake centre provided limited improvement in the prediction of the Gaussian model, suggesting that the shape as well as the centre of the wake are altered by the presence of the tower.

The current study employed the NTNU rotor in the conditions specified by BT1, with a high tower-to-rotor diameter ratio of approximately 10% and an upstream turbulence intensity of 0.3%. These conditions are ideal to study the rotor/support structure interaction, as the interaction between the two is accentuated by the large tower-to-rotor diameter ratio and the low background turbulence. Methods from this study may be applied for the study of the interaction between utility scale rotors and their support structures. It is noted that, the tower-to-rotor diameter ratio for utility scale rotors is half that of the NTNU rotor and TI can be significantly higher than studied here, potentially reducing the influence of the support structure on the far wake.

6

Dynamic Mode Decomposition of wind turbine wakes

In this chapter, the dynamic characteristics of wind turbine wakes are explored by means of dynamic mode decomposition (DMD). The substantive part of this chapter, Section 6.3, explores the dynamic differences between the wakes of a rotor operating at a clear inflow and that of a rotor operating downstream another rotor in tandem. The dynamic modes of these two wakes are compared in order to explore the difference in dynamic content between the wakes of a potential first and second turbine in a wind farm. It is found that the dynamic content of the downstream turbine is different to that of the upstream one. While the latter presents distinct characteristic frequencies at $1P$ and $3P$, the former flow is dominated by low frequency modes at frequencies below $1P$. The dynamic content between the two flows therefore differs significantly, suggesting that engineering models should treat the two flows differently.

Section 6.3 was published as a paper at the WAKE 2023 conference[1]. Sections

[1]This work was carried out alongside Professor Esteban Ferrer and Professor Soledad Le Clainche during a three-month visit to Universidad Politécnica de Madrid. The visit was funded by the Project HPC-EUROPA3 (INFRAIA-2016-1-730897), with the support of the EC Research Innovation Action under the H2020 Programme. Simulations were performed in the supercomputers of the Barcelona Supercomputing Center (BSC). The funding and facilities are gratefully acknowledged. The culmination of the project was published in the proceedings of the WAKE 2023 conference in Visby, Sweden [47]. The author of this thesis is also the lead

6.1 and 6.2 provide relevant background to the published paper covering a brief review of decomposition methods applied to wind energy aerodynamics, and the higher order DMD (HODMD) algorithm, respectively.

6.1 Data decomposition methods in wind energy

Data decomposition methods are widely used in fluid dynamics to extract spatio-temporally coherent structures from numerical or experimental data series [178]. Among the most widespread methods are the proper orthogonal decomposition (POD) and the dynamic mode decomposition. The former was first applied in turbulent flows by Lumley in 1967 [102]. The latter originates from works such as Schmid's 2010 publication [179].

In recent years, both POD or DMD methods have been applied to wind energy aerodynamic problems. Such works are here classified into four broad categories, based on the objective of the study: (1) flow extrapolation in time and space, (2) stability analysis, (3) dimensionality reduction, and (4) identification of coherent structures.

1. Flow decomposition has the potential for creating models capable of predicting flows outside of the simulated or experimentally measured range, in both time and space. Such capabilities unlock exciting potential in flow control as well as reduced order modelling (ROM). Such ROMs have been generated for wind energy flows.

   Le Clainche and Ferrer [180] constructed a DMD-based ROM using snapshots of the LES-simulated flow around a vertical axis wind turbine blade. The ROM was employed for the prediction of future flow states, and found to outperform low-fidelity models such as 2D RANS simulations, both in accuracy and efficiency. Hamilton *et al.* [181] used POD spatial modes alongside a fitted ODE representing the dynamics of the flow in order to get future

author of the publication. Slight edits may be found in this thesis document when compared to the publication.

state predictions of a wind turbine wake. While the error compared to the simulation data accumulates over time, proposed re-calibrations of the ODE coefficients allow the control of the accuracy of the ROM. Le Clainche *et al.* [182] performed a DMD decomposition of LiDAR snapshots upstream of a wind turbine. By extrapolating the modes in space they demonstrated the possibility of obtaining fast and accurate predictions of the flow outside of the LiDAR measurement region.

2. Data decomposition methods have also been used in the study of the stability of helical vortex systems such as those arising from wind turbine blade tips. Sarmast *et al.* [28] imposed stochastic perturbations upstream of the blade and identified the most unstable modes responsible for the near wake breakdown. Specifically, a mutual inductance between consecutive tip vortex filaments was found to relate to the tip vortex breakdown. Given this conclusion, a stable wake length model was developed to predict the location of wake breakdown and transition to a turbulent wake. A similar analysis framework was later performed by Kleine *et al.* [183] to study the interaction between two helical vortex systems corresponding to the interaction between two wakes in tandem.

3. The potential to reduce the dimensionality of the flow problem and the efficiency of such a reduction in representing flow quantities of interest is often explored using data decomposition methods. VerHulst and Meneveau [184] studied large wind farm aerodynamics: they identified counter-rotating vortex modes with length scales much larger than the turbine diameter as the most energetic structures using POD. $20-30\%$ of the TKE could be captured using a small number of those modes. While POD analysis often focuses on best capturing the overall TKE of the flow field, Bastine *et al.* [185] related each dominant mode to a problem-specific quantity such as the power availability for a downstream turbine. Thus, a deeper understanding of the influence of flow structures on specific quantities of interest could be obtained.

4. Finally, data decomposition methods have been used to identify coherent structures within a flow. In most cases the coherent structures characterising the flow are used to compare a flow field against another. For example Debnath *et al.* [31] compared the dynamic modes between two wind turbine wake flows: one employing a tower and nacelle and one excluding it. A non-trivial change in the tip vortex breakdown mechanism was identified when the tower and nacelle were added, a feature that could not have been identified by mean flow observations. De Cillis *et al.* [162] compared the dynamic modes of wind turbine wakes with and without background turbulence. They found that the exogenous turbulent streaks overtake endogenous dynamics of the turbines such as tip vortices.

The work presented at WAKE 2023 (Section 6.3) falls into the last category. It focuses on identifying differences between wake flows based on their coherent structure content.

6.2 Higher Order Dynamic Mode Decomposition

Since its initial introduction [179], the DMD algorithm has undergone several variations as reviewed in [186]. While all variants aim to the identification of coherent structures, each comes with trade-offs. In this thesis, the HODMD is employed.

The HODMD was introduced by Le Clainche and Vega [187] and has been applied to a number of of turbulent flows including wind turbine wakes [188] and wind resource data [182]. The method combines the standard DMD with Takens' delay embedding theorem [189], leading to enhanced noise filtering properties, robustness and flexibility as well as numerical efficiency as has been demonstrated in various studies [187, 190, 191].

Applying DMD or HODMD to a spatio-temporal field $\boldsymbol{v}(x, y, z, t)$, which could for example be the fluctuating component of the velocity field of a 3D flow, results in the decomposition of Equation 6.1. The flow is decomposed into a sum of M complex modes $\mathbf{u}_m$, each of which is multiplied by its temporal dynamics

characterised by an angular frequency ω_m and a growth rate δ_m. The modes are ranked by their real amplitude α_m.

$$\boldsymbol{v}(x, y, z, t_k) \simeq \sum_{m=1}^{M} \alpha_m \mathbf{u}_m(x, y, z) e^{(\delta_m + i\omega_m)t_k}, \qquad k = 1, ..., K. \tag{6.1}$$

The DMD algorithm can be compared to the POD, in the sense that they both decompose the flow into a set of separate spatial and temporal functions accompanied by a ranking scalar value. The application of POD to turbulent flows is described in [102] as

$$\boldsymbol{v}(x, y, z, t) = \sum_{m=1}^{\infty} \alpha_m^{POD}(t) \boldsymbol{\phi}_m(x, y, z) \tag{6.2}$$

In the context of POD and the equation above, $\alpha_m^{POD}(t)$ are random functions of time and $\boldsymbol{\phi}_m(x, y, z)$ are spatial basis functions.

Comparing Equations 6.1 and 6.2 it can be seen that the main difference between POD and DMD is that for the POD the function of the temporal evolution of modes may contain many different frequencies while in DMD each mode is linked to a single frequency, ω_m and a growth rate δ_m (Equation 6.1). This property enhances the capabilities of the DMD as it allows for a clearer interpretation of the DMD modes, as well as the ability to predict the flow in a future time, since the time-series are periodic.

6.2.1 Algorithm

The HODMD algorithm is presented in this section. An implementation of the algorithm in MATLAB is provided in [191] and used in this thesis. The description below aligns with descriptions found in [187, 191]. The interested reader is referred to those original publications for further insights on the method.

The HODMD can be described in two steps. Before the algorithm starts, the data must first be gathered and organized in a snapshot matrix of dimensions $J \times K$. For a 3D domain with N_x, N_y and N_z points in the three directions, the spatial dimension is given by $J = N_x N_y N_z$. The number of snapshots is denoted as K,

and the snapshots are equidistant in time by a time-step Δt. If $\boldsymbol{v}_k$ is a snapshot at time k (dimension $J \times 1$) then the snapshot matrix is given by

$$\boldsymbol{V_1^K} = [\boldsymbol{v}_1, \boldsymbol{v}_2, \cdots, \boldsymbol{v}_K]. \tag{6.3}$$

Step 1: Dimension Reduction

In the first step, the dimension of Matrix 6.3 is reduced in order to remove spatial redundancies, filter out noise and increase the computational efficiency of the DMD. The reduction is done via truncated singular value decomposition (SVD):

$$\boldsymbol{V}_1^K \simeq \boldsymbol{W}\boldsymbol{\Sigma}\boldsymbol{T}^{\boldsymbol{T}}. \tag{6.4}$$

The singular values σ_i of the diagonal matrix Σ together with a user-defined tolerance ε_1 define the new spatial dimension $N < J$ as $\sigma_{N+1}/\sigma_1 \leq \varepsilon_1$. It therefore follows that $\boldsymbol{W^T W = T^T T = I_N}$.

The *reduced snapshot matrix* can now be defined as a matrix of dimension $N \times K$ given by:

$$\widehat{\boldsymbol{V}}_1^K = \boldsymbol{\Sigma}\boldsymbol{T}^T. \tag{6.5}$$

Step 2: HODMD algorithm

Contrary to other DMD implementations that employ the Koopman assumption $\boldsymbol{V}_1^{K-1} = \boldsymbol{R}\boldsymbol{V}_2^K$, HODMD applies the *higher order Koopman assumption* to the *reduced snapshot matrix* from Equation 6.5, i.e.:

$$\widehat{\boldsymbol{V}}_1^K \simeq \widehat{\boldsymbol{R}}_1\widehat{\boldsymbol{V}}_1^{K-d} + \widehat{\boldsymbol{R}}_2\widehat{\boldsymbol{V}}_2^{K-d+1} + \cdots + \widehat{\boldsymbol{R}}_d\widehat{\boldsymbol{V}}_d^K. \tag{6.6}$$

where $\widehat{\boldsymbol{R}}_k = \boldsymbol{W}\boldsymbol{R}_k\boldsymbol{W}^T$, for $k = 1, \cdots, d$, where d is a user defined degree used to enhance the *reduced snapshot matrix* by d-index lagged snapshots.

This equation can be re-written in a more compact form in terms of the *modified snapshot matrix* $\widetilde{\boldsymbol{V}}_1^{K-d+1}$ (dimension $dN \times (K-d)$) and the *modified Koopman operator* $\widetilde{\boldsymbol{R}}$ (dimension $dN \times dN$) giving:

$$\widetilde{\boldsymbol{V}}_2^{K-d+1} = \widetilde{\boldsymbol{R}}\widetilde{\boldsymbol{V}}_1^{K-d} \tag{6.7}$$

The *modified snapshot matrix* will still experience redundancies and is therefore reduced further by another SVD decomposition using the same user defined error as in the previous SVD decomposition with $\widetilde{\sigma}_{N'+1}/\widetilde{\sigma}_1 < \varepsilon_1$ and $\widetilde{\boldsymbol{U}}^T\widetilde{\boldsymbol{U}} = \widetilde{\boldsymbol{V}}^T\widetilde{\boldsymbol{V}} = \boldsymbol{I}_{N'}$:

$$\widetilde{\boldsymbol{V}}_1^{K-d+1} \simeq \widetilde{\boldsymbol{U}}\widetilde{\boldsymbol{\Sigma}}\widetilde{\boldsymbol{T}}^T \simeq \widetilde{\boldsymbol{U}}\bar{\boldsymbol{T}}_1^{K-d+1}. \tag{6.8}$$

Pre-multiplying Equation 6.7 by $\widetilde{U}^T$ and using Equation 6.8 results in the Koopman assumption

$$\bar{\boldsymbol{T}}_2^{K-d+1} = \bar{\boldsymbol{R}}\bar{\boldsymbol{T}}_1^{K-d}, \tag{6.9}$$

where the snapshot matrix $\bar{T}_1^{K-d+1}$ is of dimension $N' \times (K-d+1)$ and the Koopman operator $\bar{R}$ of dimension $N' \times N'$. This operator can be found by pseudo-inverting matrix $\bar{T}_1^{K-d}$ using SVD decomposition, i.e. $\bar{T}_1^{K-d} = U\Lambda V^T$. Post-multiplying Equation 6.9 with the pseudo-inverse gives:

$$\bar{\boldsymbol{R}} = \bar{\boldsymbol{T}}_1^{K-d+1}\boldsymbol{V}\boldsymbol{\Lambda}^{-1}\boldsymbol{U}^T. \tag{6.10}$$

The N' eigenvalues μ_m and eigenvectors $\bar{\boldsymbol{q}}_m$ of matrix $\bar{\boldsymbol{R}}$ lead to the reduced tensor eigenvalues and eigenvectors through matrix $\widetilde{\boldsymbol{U}}$, with $\widehat{\boldsymbol{q}} = \widetilde{U}\bar{\boldsymbol{q}}_m$ and with the frequencies and damping rates given by:

$$\delta_m + i\omega_m = log(\mu_m)/\Delta t \tag{6.11}$$

.

The counterpart of Equation 6.1 for the reduced snapshot matrix of step 1 (Equation 6.5) is:

$$\widehat{\boldsymbol{v}}(x,y,z,t_k) \simeq \sum_{m=1}^{M} \widehat{\alpha}_m \widehat{\mathbf{u}}_m(x,y,z)e^{(\delta_m+i\omega_m)t_k}, \qquad k = 1,...,K. \tag{6.12}$$

The full DMD expansion of Equation 6.1 is obtained by pre-multiplying Equation 6.12 with the left singular vectors $\boldsymbol{W}$ of the SVD decomposition of step 1 in Equation 6.4.

Step 3: Computation of HODMD amplitudes

The amplitudes $\widehat{\alpha}_m$ are calculated using a least-squares approach equivalent to optimized DMD [192].

The number of retained modes M in Equation 6.1 is calculated through a second user-defined tolerance ε_2, $\alpha_{M+1}/\alpha_1 \leq \varepsilon_2$.

6.2.2 Calibration

The DMD and HODMD algorithms depend on certain user-defined variables such as the SVD and DMD errors ε_1 and ε_2, the degree d, the number of snapshots K and sampling frequency f_s. It is important to ensure that the modes selected for analysis and flow characterization are robust and therefore independent from the above parameters. For this reason, mode selection in HODMD is done through a calibration process where the user-defined parameters are varied and multiple HODMD decompositions are performed. The resulting modes are compared with each other in terms of frequency and shape in order to identify clusters of modes that characterize a robust structure. Those clusters must have similar frequency, that according to Le Clainche *et al.* [193] can be within a specified range $|f_{m,i} - f_{m,j}| < \epsilon$ where ϵ is an order of magnitude larger than the largest ε_1 involved in the calibration. The shape of modes is also checked by means of projection of one mode onto another $|\mathbf{u}_{m,i} \cdot \mathbf{u}_{m,j}| > 0.9$. If modes satisfy both conditions, then they belong to the same cluster. A cluster is robust if it contains modes from 75% of the decompositions performed as per [193].

6.3 Dynamic mode decomposition of merging wind turbine wakes [2]

6.3.1 Abstract

The design and operation of wind farms is significantly affected by the impact that upstream turbine wakes have on the power production and fatigue loading of subsequent turbines; often called the wake effect. In this work, two types of flows are considered: the wake of a single turbine with a laminar inflow and the combined wake of two turbines operating in-line where the upstream wake results in an unsteady inflow for the downstream turbine. Those two scenarios are simulated using large eddy simulation (LES) and the actuator line method (ALM). The spatio-temporal velocity fields are analyzed by means of higher order dynamic mode decomposition (HODMD), a well established variant of the DMD.

6.3.2 Introduction

Moving away from carbon-intensive energy generation methods will likely require a drastic increase in the deployment of large wind farms. One of the greatest challenges when it comes to wind farm aerodynamics is the complex turbine-turbine interaction that arises from their persistent wakes. The adverse impact of these wakes on the performance of downstream turbines relative to unwaked turbines, often called the wake effect, can be significant. For example a 10-20%, reduction of average power production was attributed to the wake effect for an offshore wind farm [36]. The losses for turbines at the second row of an onshore wind farm in unstable atmospheric conditions were estimated to be 20-40%, and 40-60% under stable conditions [194]. Better understanding and modelling of the wake effect could contribute towards reducing losses of such significance.

The wake effect has been investigated in the literature by employing a number of approaches. The single turbine wake has been studied through stand-alone rotor experiments [113] as well as numerical simulations such as actuator line

[2] This section corresponds to the WAKE 2023 publication.

method large eddy simulations (ALM-LES) [62]. Understanding of single wake flow mechanisms has been incorporated into analytical models [34, 35]. However, the multi-turbine problem is more complex.

The impact of turbine clustering on power production has been observed using wind turbine operational data [36, 194]. Such results are challenging to reproduce due to the large range of scales present in wind farm flows. Simple analytical models can fail to predict the velocity deficit and how wakes combine accurately [50], resulting in the increasing use of simulation when investigating the dynamics of multi-turbine configurations. One approach has been to use actuator disk method (ADM) simulations [184], where the rotors are represented in a disk-averaged sense, allowing the mean momentum deficit and mean power to be solved, but omitting important unsteady dynamics associated with rotating blades. Greater fidelity can be achieved using inherently unsteady ALM-LES simulations, but this is computationally prohibitive for very large wind farms due to the considerable associated computational requirements.

A further challenge when simulating large wind farms is extracting coherent structures and developing an understanding of wake evolution and merger. Dynamic mode decomposition (DMD), together with proper orthogonal decomposition (POD) are decomposition algorithms that have been used to gain insight into characteristics of turbulent flows. These algorithms analyze spatio-temporal data by decoupling spatial structures from temporal dynamics. Specifically, DMD ensures that the temporal dynamics of each mode are characterized by a single frequency. POD and DMD analysis has been applied to data-sets of various wind energy problems, including wakes, wind farm flows, and prediction of the wind resource.

By considering the wind turbine wake as a vortex system, it is possible to apply DMD to investigate the instability mechanisms of the system. Sarmast *et al.* [195] characterized the interaction between neighbouring vortex filaments for a rotor wake simulated using the ALM. Similar modes in the near wake emerge when the rotor is fully resolved in Sun *et al.* [55]. The interaction between the tip vortex systems of two rotors in tandem was investigated by Kleine *et al.* [183]. By understanding

the fundamental structures of the flow downstream of a rotor, low order models can be developed [195] for the prediction of the breakdown of those structures.

DMD can also be used to identify coherent structures of turbulent flows. Bastine *et al.* [185] applied POD in ADM-LES simulations with turbulent inflow and identified wake meandering as the most energetic structures. POD analysis of ADM-LES of a very large wind farm by VerHulst and Meneveau [184] identified vortical structures much larger than the turbine scale as the most energetic modes. Debnath *et al.* [31] observed that the inclusion of the tower and nacelle in ALM-LES simulations with laminar inflow altered some of the tip vortex breakdown mechanisms identified in the case without supporting structures. De Cillis *et al.* [74] applied DMD to the flow of a wind turbine wake with and without background turbulence and concluded that in the turbulent case, the exogenous background flow dynamics prevail compared to the endogenous higher frequency dynamics of the wake. Additionally to the diagnostics, the modes can also be used to build reduced order models for the temporal prediction of the flow by either projection in the case of POD [181], or by directly using the known mode frequencies in the case of DMD [180]. Le Clainche *et al.* [182] used Higher Order DMD (HODMD) as a predictive tool, to spatially extrapolate velocities outside the span of available LiDAR measurements upstream of a wind turbine.

This study employs DMD to explore the impact of an upstream rotor on the wake dynamics of a downstream rotor. Kleine *et al.* [183] investigated the interaction of the tip vortices of two rotors in tandem. Here, the first wake is allowed to breakdown to create an unsteady inflow to the second turbine. This is similar to De Cillis *et al.* [74], except that the source of the unsteady inflow in the present study is the upstream turbine wake. De Cillis *et al.* found that atmospheric turbulence drastically altered the dynamics of the wake when compared to the laminar inflow case. To explore how the dynamics and coherent structures in a turbine wake are affected by the presence of an upstream rotor, two data sets are generated: the spatio-temporal velocity data of the wake of a single turbine, and the wake of the second turbine, in-line and downstream of the first. The two data sets are

generated using ALM-LES. Once the flow results have been validated using available experimental data, they are processed using HODMD, a flexible and efficient variant of the DMD. The dominant modes and frequencies for the two data sets are presented and compared. Thus, the two wakes are compared in a dynamic sense.

This paper is organized as follows: in section 6.3.3 the sensitivity study and numerical results are presented. In section 6.3.4 a brief description of the HODMD algorithm is given. The DMD analysis of the two data sets is presented and discussed in Section 6.3.5. Conclusions are drawn in section 6.3.6.

6.3.3 Numerical simulations

We simulate the NTNU Blind Test (BT) experimental rotor, a $D = 0.894$ m diameter, three bladed wind turbine with blades composed of NREL S826 aerofoils [113, 196]. The wind tunnel dimensions are $[L \times W \times H] = [11.15 \times 2.71 \times 1.8]$ m. The inflow velocity profile is uniform and the turbulence intensity levels are low (0.3%).

The set-up and data from two experiments are used here. BT1 [113], presents data of a single wind turbine wake at various tip speed ratios (λ). Horizontal and vertical profiles of mean velocity and turbulence statistics are available at three locations downstream of the rotor. The results of this experiment at the optimal tip speed ratio $\lambda = 6$ were used to validate the ALM and flow solver.

BT2 [196], a follow up experiment, involves two rotors placed in-line spaced three diameters apart. As in BT1, profiles are available at three locations, this time downstream the second rotor. In this paper the case where both rotors are operated at their optimal tip speeds is simulated, with $\lambda_1 = 6$ and $\lambda_2 = 4$ for the first and second rotor respectively.

Numerical scheme

LES computational fluid dynamics (CFD) simulations were performed by solving the filtered, unsteady, incompressible 3D Navier-Stokes equations with Smagorinsky turbulence closure using OpenFOAM. Second order central spatial and second order backward temporal descretization schemes are used. The PISO algorithm is used

for pressure-velocity coupling and the maximum CFL values are kept at around 0.5. The boundary conditions for the wind tunnel walls are Spalding wall functions, fixed value velocity for the inlet and fixed pressure gradient for the outlet. No inlet turbulence is introduced in the domain.

The in-house ALM used in this study introduced in [48] was implemented in OpenFOAM v2.3.1 by Hunter *et al.* [141] and later transferred to version 20 06 [125]. The three steps of the ALM are briefly summarized as follows: (1) sampling of the relative flow velocity and angle of attack at each collocation point, (2) the calculation of the blade force, and (3) the imposition and smearing of the force using a kernel function. The sampling (1) here is done using the potential flow-based method described in [48]. This method samples the flow outside the force smearing region which leads to improved convergence of blade forces with time-step. The allowable time-steps using such methods are generally larger than the time-steps permitted in methods that sample the flow field at the collocation point [62, 69]. Nevertheless, the time-step used herein ensures that spurious momentum oscillations that can arise due to overly large time steps are not present, as illustrated in Figure 6.2. For step (2), the airfoil data were calculated using XFoil [79] as per Krogstad and Lund [82]. The anisotropic tip correction model of Wimshurst and Willden [84], which has been calibrated for a similar scale rotor as the one simulated here, is used. Finally, the smearing kernel used here is the three dimensional Gaussian kernel, used in Sørensen and Shen [69] with a kernel width of $\varepsilon = 2.5\Delta x$, as per Martínez-Tossas *et al.* [62]. The supporting structures are modelled using a volume of fluid approach introduced by Apsley *et al.* [76].

Convergence

The meshes are of Octree type. The domain size in all cases is equivalent to the wind tunnel size with a slightly elongated streamwise direction to enclose longer wakes $[L \times W \times H] = [15D \times 3D \times 2D]$ and the mesh in both cases is refined in the wake regions. The refined region for BT1 spans $[L \times W \times H] = [10D \times 1.5D \times 2D]$, centred 1 diameter upstream of the rotor and 9 downstream in the streamwise direction,

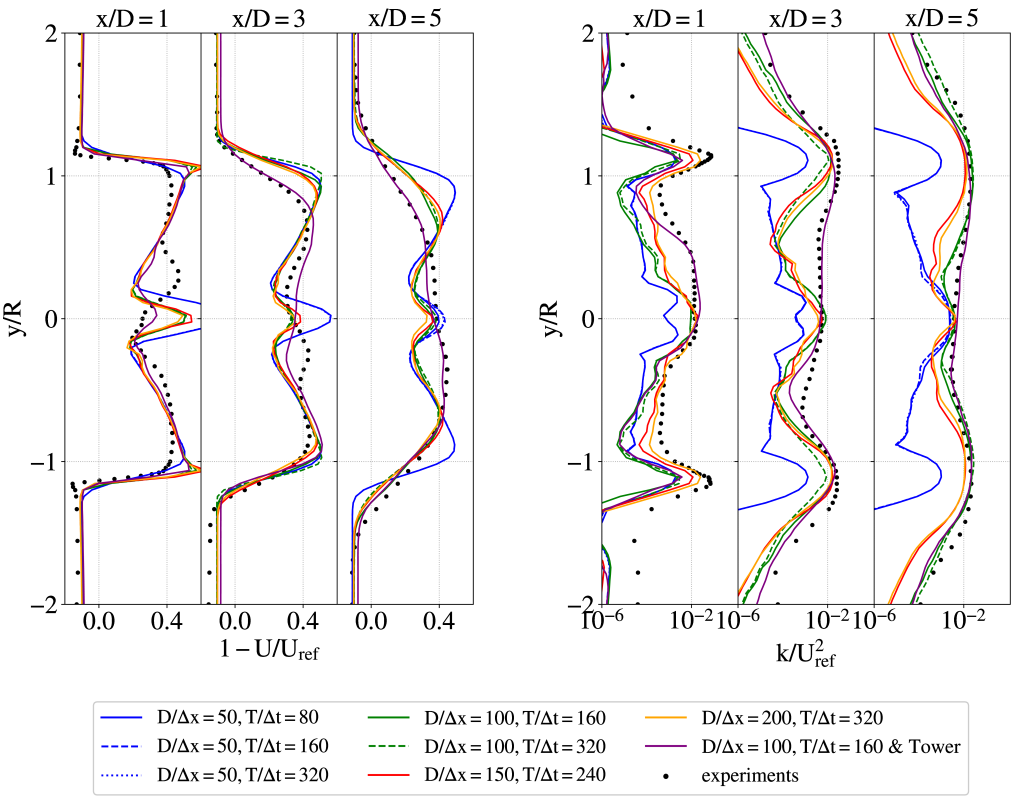


Figure 6.1: Blind Test 1: Horizontal profiles of mean streamwise velocity deficit (left) and turbulent kinetic energy (right) at three downstream positions x/D for varying cell sizes $D/\Delta x$ and time-steps $T/\Delta t$ and comparison with experimental data. The nacelle is modelled in all cases but the tower is only modelled in one (& Tower, purple).

and symmetrical around the center of the rotor in the other two directions. For BT2 the refined region spans $[L \times W \times H] = [13D \times 1.5D \times 2D]$, i.e., 3 diameters more than the single rotor case in the streamwise direction in order to resolve both wakes.

Independence from the mesh has been established for BT1 by simulating the rotor in four different refinement levels $D/\Delta x = 50, 100, 150, 200$, where Δx refers to the most refined cell size of each mesh. It can be seen in Figure 6.1 that the coarsest mesh, $D/\Delta x = 50$, under-predicts turbulence leading to limited mixing moving downstream. The case of $D/\Delta x = 100$ is very similar to the more refined cases, $D/\Delta x = 150, 200$, in terms of mean velocity, and for turbulence captures the main features even at the far wake $x/D = 5$ but slightly over-predicts turbulence at this location. The velocity and turbulence profiles for $D/\Delta x = 150$ and 200 largely agree with each other. From this comparison, it is concluded that the $D/\Delta x = 150$

simulations give a reasonable trade-off between convergence and computational cost and the data from these simulations will be used in the proceeding analysis. When it comes to comparison with the experimental data, it is important to note that all simulations model the nacelle but only one (purple line in Figure 6.1) models the tower as well. This simulation agrees better with the experimental data, providing both confidence in the mesh convergence and the accuracy of the results. However, in this work we have excluded the tower for simplicity.

The effect of time-step $T/\Delta t$, where T is the rotor period, is also investigated in the same figure. Three different time-steps are investigated for the $D/\Delta x = 50$ case, and two for the $D/\Delta x = 100$. In none of the cases simulated does the time-step affect the mean velocity or turbulent kinetic energy in any wake location (Figure 6.1), leading to the conclusion that the largest time-step can be used for numerical efficiency.

Simulation setup

The wake data produced for DMD analysis are based on BT1 and BT2, but have been slightly adapted to ensure that the two flows are equivalent in the mean sense. In what follows, the single turbine simulation is referred to as $C1$, case 1, and corresponds to a single rotor simulation with a uniform and laminar inflow, and the two rotor simulation as $C2$, case 2.

$C2$ has the same set up as BT2: the upstream and downstream rotor TSRs are $\lambda_1^{C2} = 6$ and $\lambda_2^{C2} = 4$. The reference velocity for both rotors is $U_{ref} = 10$ m/s, which is also the upstream velocity of the first rotor. The upstream rotor rotates at $\omega_1^{C2} = 134\,\text{rad s}^{-1}$ and the downstream at $\omega_2^{C2} = 89\,\text{rad s}^{-1}$.

In order for the wake of $C1$ to be comparable to the wake of $C2$, the same rotational speed is employed, i.e. $\omega^{C1} = \omega_2^{C2} = 89\,\text{rad s}^{-1}$ as well as the same levels of momentum extraction. It follows that the thrust and power produced by both rotors must be the same. For this to be achieved, the U_{ref} of case $C1$ was varied until the thrust and power of the rotor matched that of the downstream rotor of $C2$. The reference velocity at $C1$ is found to be $U_{ref}^{C1} = 6.2$ m/s, with $\lambda^{C1} = 6.47$. In $C2$

azimuthal velocity variations have been introduced, and as a result the blade loads are not completely equivalent in the spanwise sense, but the overall momentum extraction in the two cases is the same. Snapshots of the instantaneous vorticity magnitude fields of the two cases, $C1$ and $C2$ are shown in Figure 6.2, where the wake breakdown of $C1$ and $C2$ is clearly visible.

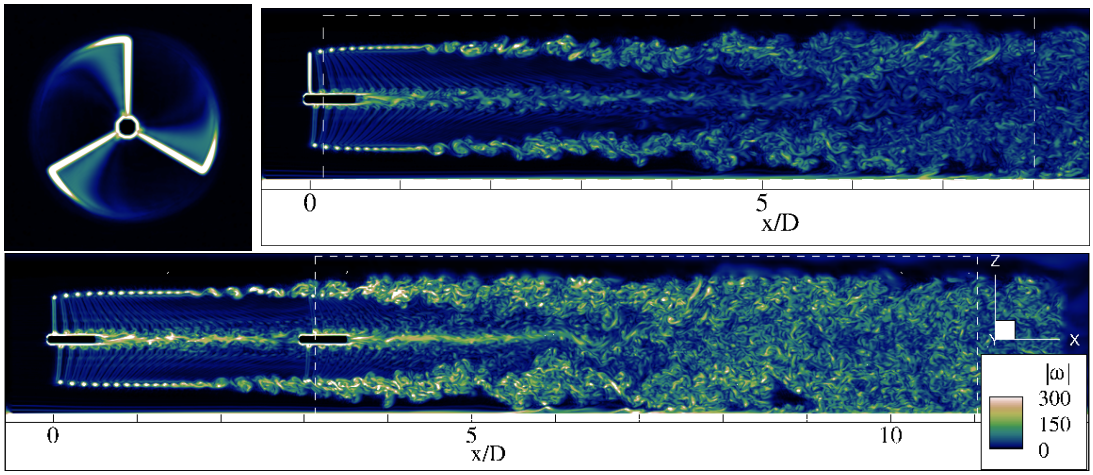


Figure 6.2: Upper panel: instantaneous vorticity magnitude contours for case $C1$ at the rotor plane $x = 0$ (left) and at a vertical plane through the middle of the rotor (right). Lower panel: instantaneous vorticity magnitude contours for case $C2$ at a vertical plane through the middle of the rotors. The domains where the DMD analysis is performed for the two cases are shown in white dashed lines.

6.3.4 Higher Order DMD

The HODMD was introduced by Le Clainche and Vega [187] and has been applied to a number of of turbulent flows including wind turbine wakes [188] and wind resource data [182]. The method combines the standard DMD with Takens' delay embedding theorem [189], leading to enhanced noise filtering properties, robustness and flexibility as well as numerical efficiency [187].

Algorithm

Applying DMD or HODMD to a spatio-temporal field $\mathbf{v}(x, y, z, t)$, which could be the fluctuating component of the velocity field of a 3D flow, results in the decomposition of Equation 6.13. The flow is decomposed into a sum of M complex modes $\mathbf{u}_m$, each of

which is multiplied by its temporal dynamics characterized by an angular frequency ω_m and a growth rate δ_m. The modes are ranked by their real amplitude α_m.

$$\mathbf{v}(x, y, z, t_k) \simeq \sum_{m=1}^{M} \alpha_m \mathbf{u}_m(x, y, z) e^{(\delta_m + i\omega_m)t_k}, \qquad k = 1, ..., K. \tag{6.13}$$

In this paper, the multi-dimensional HODMD is used where, instead of two dimensional matrices, multi-dimensional tensors are used. The algorithm has two steps: in the first step, truncated higher order singular value decomposition (HOSVD) is applied to the snapshot tensor in order to reduce its dimension and filter noise. The truncation is done using a user-defined error ε_1 where, r singular values σ_i are retained according to $\sigma_{r+1}/\sigma_1 \leq \varepsilon_1$. In the second step the DMD-d algorithm is applied that seeks the eigenvalues and eigenvectors of the modified Koopman matrix that is defined by modifying the initial snapshot tensor by adding d-index lagged snapshots, where d is the user-defined degree of the HODMD decomposition. The amplitudes α_m are calculated using a least-squares approach equivalent to optimized DMD [192]. The number of retained modes M in Equation 6.13 is calculated through a second user-defined tolerance ε_2, $\alpha_{M+1}/\alpha_1 \leq \varepsilon_2$.

Calibration

The DMD and HODMD algorithms depend on certain user-defined variables such as the SVD and DMD errors ε_1 and ε_2, the degree d, the number of snapshots K and sampling frequency f_s. It is important to ensure that the modes selected for analysis and flow characterization are robust and therefore independent from the above parameters. For this reason, mode selection in HODMD is done through a calibration process where the user-defined parameters are varied and multiple HODMD decompositions are performed. The resulting modes are compared with each other in terms of frequency and shape in order to identify clusters of modes that characterize a robust structure. Those clusters must have similar frequency, that according to Le Clainche *et al.* [193] can be within a specified range $|f_{m,i} - f_{m,j}| < \epsilon$ where ϵ is an order of magnitude larger than the largest ε_1 involved in the calibration. The shape of modes is also checked by means of projection of one mode onto

another $|\mathbf{u}_{m,i} \cdot \mathbf{u}_{m,j}| > 0.9$. If modes satisfy both conditions, then they belong to the same cluster. A cluster is robust if it contains modes from 75% of the decompositions performed as per [193].

Data collection

For the DMD analysis in this paper, spatio-temporal data are extracted from the simulations $C1$ and $C2$ described in Section 6.3.3. Although the CFD mesh has a cell size of $D/\Delta x = 150$ in the wake region, the DMD mesh has a cell size of $D/\Delta x = 50$ due to the large memory requirements of the analysis. The 3D DMD domain spans from $0.1D$ downstream of the rotor of interest (that is, the single rotor of $C1$ and the downstream rotor in $C2$) to $8D$ downstream as indicated by the white dotted rectangles in Figure 6.2 and has a $1.5D \times 1.5D$ square cross section in the YZ plane, centered on the hub. The frequency of data collection f_s corresponds to 10 snapshots per period. This gives a Nyquist frequency of $5/T$. It is acknowledged here that prior studies have indicated the presence of higher frequencies in wind turbine wakes ([55, 195]). Nonetheless, the present investigation is primarily concerned with lower frequencies. The number of snapshots in both cases is $K = 300$ which means that data are collected for 30 periods and therefore the minimum detectable frequency, $1/(30T)$, is much smaller than the rotor frequency. The sampling frequency and duration used here are similar to Debnath *et al.* [31]. This choice provides a satisfactory trade-off between memory requirements and frequency range. Various sets of (K, f_s) were tested in order to ensure that our conclusions not depend on those parameters. This investigation has been omitted from this paper for brevity.

6.3.5 HODMD of two flows: a single and a downstream rotor wake

Dependence of the results on user-defined parameters

All cases have been calibrated using the same user-defined variables, following Le Clainche *et al.* [193]. 90% of the highest amplitude modes are visualized in the frequency-amplitude plots of Figure 6.3. The circled modes, are the most robust

ones according to the criteria detailed in section 6.3.4 and are therefore the ones that describe coherent structures that exist in the flow.

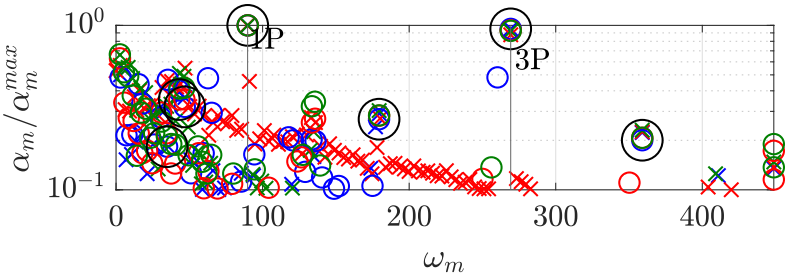


Figure 6.3: HODMD calibration for $C1$: Angular frequency ω against amplitude normalized by the maximum value α, for different SVD tolerances ε_1 and degrees d. The crosses indicate $\varepsilon_1 = 0.05$ and the circles, $\varepsilon_1 = 0.01$. Blue, red and green colours correspond to degrees 125, 93 and 75 respectively for $K = 300$ snapshots. The black circles correspond to clusters of modes that appear in at least 75% of the decompositions performed. $1P$ and $3P$ frequencies are noted, based on the rotation frequency $\omega^{C1} = \omega_2^{C2} = 89$ rad s^{-1}.

In addition to the dependence on user-defined parameters discussed above, the DMD modes may also exhibit sensitivity to the numerics of the CFD simulations, particularly in situations where the inflow is laminar, such as case $C1$. For this reason, investigations of tip vortex interactions in wind turbine wakes [183, 195] explicitly introduce known disturbances to the flow in order to eliminate the uncertainty arising from the unknown numerical perturbations. However, the present study aims to compare two distinct flow cases that are subjected to the same numerical treatment, similar to [31, 74]. Consequently, the primary focus of this study will be to analyze the differences between the cases $C1$ and $C2$, in order to minimize the influence of those numerical perturbations. It is important to note that the absence of explicit perturbations in this study represents a limitation, and as a result, only qualitative conclusions are drawn.

HODMD of a single rotor wake

The most robust modes selected for case $C1$ are identified in Figure 6.3. The highest amplitude mode has a frequency of $\omega_{1P} = 89$ rad s^{-1}. The $3P$ mode identified at $\omega_{3P} = 3\omega_{1P} = 269$ rad s^{-1} also ranks very highly. Further robust and high amplitude modes are found at lower than $1P$ frequencies. The remaining of

the robust modes are harmonics or modulation of the above mentioned dominant modes and are not discussed further.

The $1P$ mode is very active in the transition region between $x/D = 1 - 3$ (Figure 6.4) and mainly occupies the edge of the wake, around $r = R$, where r is the spanwise coordinate and R the rotor radius. When compared with the vorticity magnitude contour in Figure 6.2 it is clear that at $x/D \approx 1.2$ the tip vortex instability is triggered and the structures emerging from it persist until $x/D = 3$, where some mixing with more complex structures occurs. This mode resembles in shape and frequency the $1P$ mode identified in the blade-resolved wakes of Sun *et al.* [55], indicating that some of the dynamics emerging from ALM simulations are similar to the ones identified in higher-fidelity rotor representations. However, higher resolution simulations with explicit perturbations could potentially reveal additional frequencies in this region of tip vortex breakdown, such as mutual-inductance instability of merging tip-vortices [195] of various wavelengths and frequencies, but these are not evident in our computations.

The $3P$ mode corresponds to the tip-vortex structures that are only significant in the near wake. The tip structures are even more confined at an annular ring at $r = R$ and are also visible in the instantaneous vorticity magnitude contour of Figure 6.2. The $3P$ mode is typically found in all DMD analysis of wind turbine wakes [31, 74].

The lower frequency modes are more spatially persistent, characterizing the region starting from $x/D = 1.5$ and extending to the end of the domain and likely correspond to the larger and more energetic turbulent eddies. The appearance of robust low frequency modes, at frequencies approximately 10 times lower than the blade passing frequency are also evident in the DMD decomposition of a stand-alone rotor in laminar flow of [74], although the tower was also included in that case. In the same study, the $3P$ mode was also evident, but no $1P$ modes were observed, potentially due to the interaction with the tower.

Overall, moving from the near to the far wake of a single rotor, three types of structures of decreasing frequency and increasing radial width are identified (Figure 6.4). The near-wake tip vortices start off as very predictable helical structures

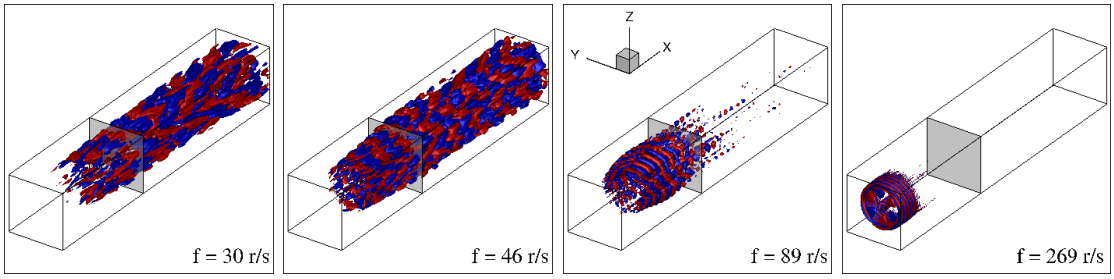


Figure 6.4: Isosurfaces of the streamwise real part of four of the most robust dynamic modes for case $C1$. The x-surface shaded in the top figures is located at $x/D = 3$, where the second rotor in $C2$ is situated.

emanating from the blade tips at $3P$ and dominant at $x/D < 1$. A $1P$ frequency, with slightly greater radial extent but still predominantly near the tip radius, is associated with the breakdown of the tip vortices and characterizes the transitional wake at $1 < x/D < 3$. This is also visible in Figure 6.2 in the instantaneous vorticity magnitude. Finally, structures with $\omega_m < 89\,\text{rad s}^{-1} \simeq 0.2P - 0.4P$, are associated with the transitional and far wake.

HODMD of a downstream wake and comparison with the single wake

In order to discuss the dynamic modes of case $C2$, the frequencies incident at the second rotor of $C2$ are first characterized. For this, HODMD has been performed in the same domain as the one in the white box of the lower panel of Figure 6.2 but in the absence of the second rotor. Essentially, this reveals the far wake modes of the upstream rotor in $C2$ which is operating at $\lambda = 6$. These modes, following the discussion in Section 6.3.5, are spatially persistent and occur at low frequencies and their modal shape is similar to the low frequency modes of Figure 6.4. Those modes are referred to as the background (BG) flow.

A comparison of the dynamics of $C1$, $C2$, and BG is presented in Figure 6.5. It can be seen that, when a rotor operates in the wake of an upstream rotor (case $C2$), the lower frequencies of the background flow become dominant. Most frequencies are below $1P$, with the only high frequency mode identified is the $3P$ frequency, that occurs at notably lower amplitudes compared to $C1$.

The modal shape of the $3P$ mode of $C2$ is not shown here as it closely resembles that of the same frequency in case $C1$, with a shorter streamwise extent. Notably,

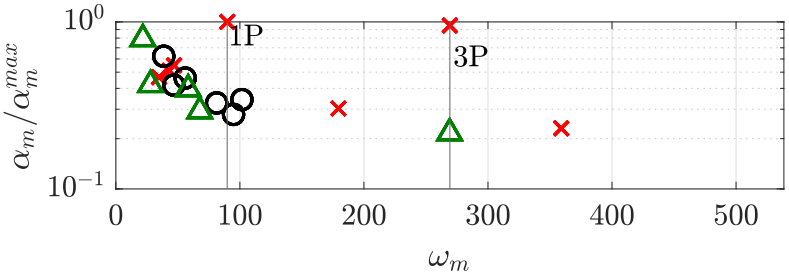


Figure 6.5: The most robust modes for case $C1$ (×), $C2$ (△) and BG of $C2$ (O). All modes shown here are a result of a calibration that employs the same parameters as the ones used in Figure 6.3. Only the modes that are independent of the user defined parameters are presented.

the $3P$ frequency loses its dynamic significance in case $C2$ as it exhibits lower values of α_m. Following the discussion of the previous section, this frequency is linked to the turbulent breakdown of the wake of $C1$. Therefore, its elimination in case $C2$ suggests that turbulent wake breakdown is done at an earlier stage and may be due to a different mechanism than in case $C1$.[3]

The prevalence of the background low frequencies over the "endogenous dynamics" as characterized by De Cillis *et al.* [74] have been identified in a similar case where atmospheric turbulence with a turbulence intensity less than 10% was imposed on the flow. There, the authors observed that when background turbulence is imposed upstream a rotor, high frequency modes are not selected by the sparsity-promoting DMD and the flow is characterized by the low frequencies. Similarly in the present work, in $C2$ the average turbulence intensity at the rotor plane is less than 8% (as indicated in Figure 6.1) and only one higher ($> 1P$) frequency is present at a low amplitude.

6.3.6 Conclusions

In this work the wake merger of two wind turbines in-line is under consideration, with the upstream wake having broken down to turbulence. Two wakes, a laminar inflow stand-alone rotor wake and a downstream wake that operates in the turbulent wake of an upstream rotor, are simulated using ALM-LES and validated using published experimental data. The datasets are investigated using HODMD. The

[3]This paragraph is not part of the original paper, [47].

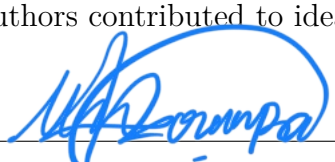
two sets of resulting modes are compared in order to investigate the similarities and differences between the combined wake and the single turbine wake.

When a rotor operates in the turbulent wake of an upstream turbine, the high frequency content identified in the laminar case is highly suppressed meaning that the background structures that characterize the far-wake of the upstream rotor are more dynamically persistent than the higher frequencies identified in the laminar case, a conclusion also drawn by [74] for atmospheric inflow turbulence. This conclusion qualitatively shows that within the wind farm, the rotor geometry and rotation might be less important than when compared to the stand-alone case, suggesting that other turbine modelling approaches, such as the ADM could also adequately capture important far-wake dynamics.

This work has developed a framework for the analysis of wind turbine wakes using HODMD that can be used for the exploration of other types of wakes as well as the development of reduced order models. The framework has been used to explore how the dynamics of a wind turbine wake are affected when it is operating within an upstream wake. HODMD at higher resolution data, with explicitly imposed perturbations as well as the simulation of different turbine spacings and layouts or modelling of the tower are necessary to generalize the conclusions and are a direction for future study.

6.3.7 Authorship statement

Publication details	
Title	Dynamic Mode Decomposition of merging wind turbine wakes
Status	Published
Reference	Zormpa, M., Le Clainche, S., Ferrer, E., Vogel, C. R., & Willden, R. H. J. (2023). Dynamic Mode Decomposition of merging wind turbine wakes. *Journal of Physics: Conference Series*, 2505(1). doi:10.1088/1742-6596/2505/1/012020

Student Confirmation	
Student Name	Markella Zormpa
Contribution to the paper	M.Z: Conceptualisation of the work, analysis, processing, visualisation, manuscript; SLC: provided the HODMD software. All authors contributed to ideas and reviewing of the manuscript.
Student Signature	
Date	27.09.2024

Supervisor Confirmation	
Supervisor name and title	Dr. Christopher Vogel
Supervisor comments	I confirm that Markella has made a substantial contribution to the publication, and that the description above in the Statement of Authorship is accurate.
Supervisor Signature	
Date	27.09.2024

Table 6.1: Statement of authorship for Section 6.3.

7 Conclusions and future work

Actuator line representations of wind turbines embedded within large eddy simulations are widely used for studying turbine and wake aerodynamics. This thesis has evaluated and improved the numerical efficiency of the ALM, contributing to best practice in simulations of turbines and their wakes. The work centred around the core themes of ALM improvements and robustness, support structure modelling, and wake analysis. In this chapter, the main conclusions of this thesis are presented as well as recommendations for future work directions.

7.1 Conclusions

An important prerequisite to simulating wind turbine wakes using ALM-LES is obtaining an accurate and robust prediction of the blade forces, in order to drive the development of the near and far wake. While the ALM is generally a flexible rotor parameterisation method, it exhibits certain numerical shortcomings. The method is sensitive to certain user-defined parameters. It also imposes a significant constraint on the simulation time step that reduces the numerical efficiency of ALM-LES simulations.

To understand better the interplay between ALM parameters and how their significance propagates through the method, the ALM algorithm is described in

this thesis as a three step process: Step 1 corresponds to the flow sampling; Step 2 to the force calculation; and Step 3 corresponds to the force smearing.

The interaction between three of the ALM parameters is studied in Chapter 3: the sampling method employed in Step 1, the force smearing width in Step 3 and the time step of the simulation. In order to explore the potential for improving the robustness of the ALM through changing the sampling location of Step 1, three sampling methods are tested: collocation point sampling; volume average sampling; and line average sampling.

The line average sampling method, previously introduced in the literature in the context of sampling blade resolved flows is here employed for AL flow sampling. The method samples the flow outside of the force imposition region and is therefore capable of decoupling the parameter-dependent blade-local flow field from the calculated ALM force. As a result, the line average sampling method was demonstrated to be more robust with larger time steps, allowing for faster temporal convergence of both rotor forces and rotor plane flow, and therefore enabling the relaxation of the ALM time step constraint. It was also found to limit the dependence of the calculated rotor forces on the smearing parameter. The conclusions were confirmed for two rotors: one wind and one tidal. They were also confirmed for two types of flow solvers, URANS and LES.

The dependence of the ALM power and thrust coefficients of the NTNU rotor on Step 2 parameters is quantified in Section 4.1.2. Significant sensitivity to the employed aerofoil data was found: the percentage error in power coefficients when using two different aerofoil polar datasets was found to be of the order of 10% at the optimal TSR and that of the thrust coefficients was of the order of 2%. Two tip corrections were tested: the Shen tip loss model and the Wimshurst & Willden one. The ability of the Wimshurst & Willden tip corrections to improve power estimates for the NTNU rotor was confirmed.

While an accurate and robust blade force calculation is important for the development of the wake, the accuracy of the numerical prediction of wind turbine

wakes using ALM-LES simulations also depends on numerical parameters such as the mesh refinement level of the wake.

Four different cell refinement levels, namely $\Delta x = D/50, D/100, D/150, \& D/200$ were compared in Section 4.2. It was found that the coarsest case, $D/50$ was insufficient to develop a turbulent wake downstream of a rotor with a non-turbulent inflow. The cases $D/150$ & $D/200$ converged in all examined metrics.

The case with $D/100$, a resolution level often employed in the literature, presented distinct features: while the mesh was capable of producing a turbulent far wake, and the mean velocity deficit profiles were close to those of the $D/150 \& D/200$ simulations, the far wake TKE differed significantly to that of the finest resolution simulations. This was attributed to the inability of the employed mesh to sustain the tip vortices which led to them merging into a shear layer that developed a different breakdown mechanism than that observed in the $D/150$ & $D/200$ cases.

Introducing synthetic eddies characterised by low turbulence intensity in the inlet of the $D/100$ simulation was found to be beneficial. The spurious tip vortex merging observed in the case with no turbulence did not emerge in the case with a low turbulence inflow. Introducing turbulent fluctuations was therefore found to relax ALM-LES resolution requirements.

To further improve the ability of the ALM-LES model to predict real rotor wakes, the inclusion of a support structure model, often omitted in such simulations, was explored in Chapter 5. Including the tower in simulations of rotor wakes has been found to promote asymmetries in the far wake mean flow.

Three methods were compared: a body-fit wall modelled LES approach; a cell-blocking method; and an actuator disc/actuator line method. The body-fit method was found to closely capture all important features of the asymmetric wake of the NTNU rotor. The cell-blocking method generated asymmetric wake behaviour but diverged from the experimental measurements at various streamwise locations. The actuator disc/line approach was not capable of capturing the asymmetric features induced by the tower.

The effect of the support structure on the validity of the Gaussian far-wake assumption was also explored in this work. A three-dimensional comparison between the high-fidelity ALM dataset and a Gaussian engineering model was performed. Such a comparison is not often done in the literature, as researchers usually focus on comparing actuator disc wakes with engineering models.

The Gaussian model performed better in capturing the area-averaged mass and kinetic energy fluxes than the local flow field. It also performed better in capturing the wake of a flow without a tower than that with a tower. Adding a centreline to account for the asymmetry of the wakes with support structures slightly improved the predictive abilities of the Gaussian model, however did not fully reproduce the simulated wakes. The significance of the error between the modelled and simulated wakes depends on the engineering problem in question.

The ALM-LES analysis of the dynamic wake flows generates valuable spatio-temporal flow datasets. However, such simulations come at a high numerical cost. Desirable cost reductions could be achieved by reducing the dimensionality of the flow problem. One way to do this is by applying data decomposition methods, explored in Chapter 6.

DMD was applied in order to compare dynamic modes between two flows: a wind turbine wake with non-turbulent inflow; and the wake of a rotor located downstream of another rotor in tandem. The two flows were found to exhibit significant dynamic differences with distinct 1P and 3P frequency modes observed in the single rotor wake experiencing lower amplitudes in the wake merger case. Lower frequencies, characteristic of the background flow, were found to dominate the wake merger problem. However, due to the extremely rich frequency content of both flows it was challenging to identify a single dominant mode inherent to the flows.

7.2 Future work

The studies and methods developed in this thesis pave the way for new directions with potential for further improving of the ALM-LES method and its sub-models.

While the ALM was found to be significantly affected by the flow sampling method, it is important to investigate further the mechanisms that give rise to these dependencies and therefore generalise the conclusions. Additionally, identifying differences in the spanwise force distributions of ALM and BR simulations could be an appropriate avenue to improve the accuracy of the former through better accounting for the three-dimensionality of rotor blade flows.

ALM-LES resolution was found to qualitatively and quantitatively impact the wake development, with an improvement in the robustness of results when low inflow turbulence is added. The evaluation of resolution of ALM-LES wind turbine wake simulations must be performed for a range of turbulence intensity levels and operating conditions with special attention to resolution metrics, such as the turbulent kinetic energy ratio.

The analysis of support structure modelling methods suggested that there is room for improvement and calibration of the cell-blocking and actuator disc/line modelling methods. It is also important to explore the effect of the tower to utility scale rotors, characterised by a smaller tower-to-rotor diameter ratio and high levels of background turbulence.

Finally, the DMD framework can be used to investigate dynamic differences of a range of wake flows, highlighting important dynamics and identifying potential dominant modes.

Appendices

A

Scaling test of OpenFOAM in ARC

Most of the simulations in this thesis were performed in the Advanced Research Computing (ARC) service at the University of Oxford [197]. Given that a large range of mesh sizes has been simulated for the mesh sensitivity analysis of Chapter 4, a scaling test was performed for each mesh to ensure adequate parallel properties and acquire the optimal number of nodes for each mesh. For meshes at the order of 10 M cells, OpenFOAM performance typically peaks at $\sim 100,000$ cells per processor [198], which is confirmed here for the $N_x = 50$ simulation. For the two largest meshes, performance peaks are observed at $\sim 400,000$ cells per processor. For those simulations, when the number of cores exceeded 400, no significant speed-ups could be obtained.

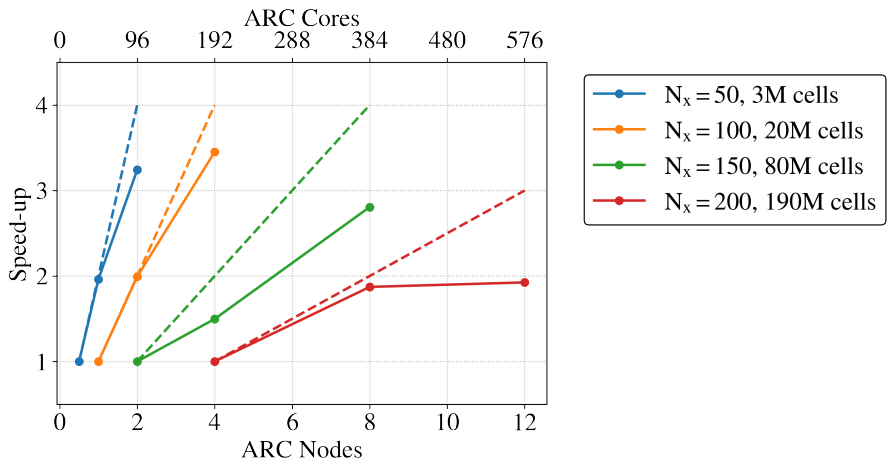


Figure A.1: Scaling test for the ALM-LES simulations of Table 4.2, performed in the ARC-HPC facility. Speed-up is defined as iterations per hour, non-dimensionalised by the value obtained for the simulation with the lowest number of cores. Dashed lines denote linear increase of the speed-up with the number of nodes.

B

Self-convergence of the line average sampling method

The line average sampling method depends on two internal parameters: the even number of points N as described in Section 3.3.3, and the sampling distance r_s (Figure 3.2). In the main body of this paper, two other ALM parameters, ε and Δt are varied in order to ensure that this self-convergence is valid when those values are altered in Section 3.7. The mesh size is not varied and mesh independence has been ensured (Section 3.6). The rotor used here is the MEXICO rotor described in Section 3.5 ($N_x = 160$).

To investigate the number of points N required for the averaging process, the points are placed at a constant radius $r_s = 1.1r_g$, just outside the Gaussian kernel of radius $r_g = 3\varepsilon$. In order to ensure independence from the value of ε and time step, three cases are explored $(N_\varepsilon, N_t) = (2, 200)$,$(N_\varepsilon, N_t) = (2, 800)$ and $(N_\varepsilon, N_t) = (4, 200)$. The change in both C_P and C_T for MEXICO rotor (Figure B.1) shows that the relative error $\varepsilon_{rel}^{N=64}(C_P^{N=16})$ is less than 1% if the number of points $N \geq 16$. Figure B.1 is in line with the conclusions of Jost *et al.* [78] that found that little accuracy is sacrificed when the number of points is reduced from 96 to 6. It is also worth noting that for the current OpenFOAM implementation,

the increase in wall-clock time per rotation between the cases $N = 2$ and $N = 64$ is a factor of 1.1 that is related to the sampling algorithm.

The sensitivity to the sampling radius r_s is also investigated in Figure B.1. The same three combinations of N_ε and N_t are explored as above. The sampling radius is a function of the radius of the Gaussian, $r_g = 3\varepsilon$. It is observed that for a region between $1 \leq r_s/r_g \leq 2$, the values of C_P and C_T remain within less than 1.5% difference from each other. For $r_s = 0$, the method reduces to the CPS sampling method. For larger r_s values, the sampling might be affected by the flow field of adjacent blades which is also undesirable. Therefore a value between 1 and 2 should be chosen where the sampling takes place outside of the Gaussian force smearing kernel, but without interacting with the velocity field of the other blades, ensuring that the captured velocity information is local. We choose $r_s = 1.1r_g$ as there appears no significant further benefit of using larger r_s.

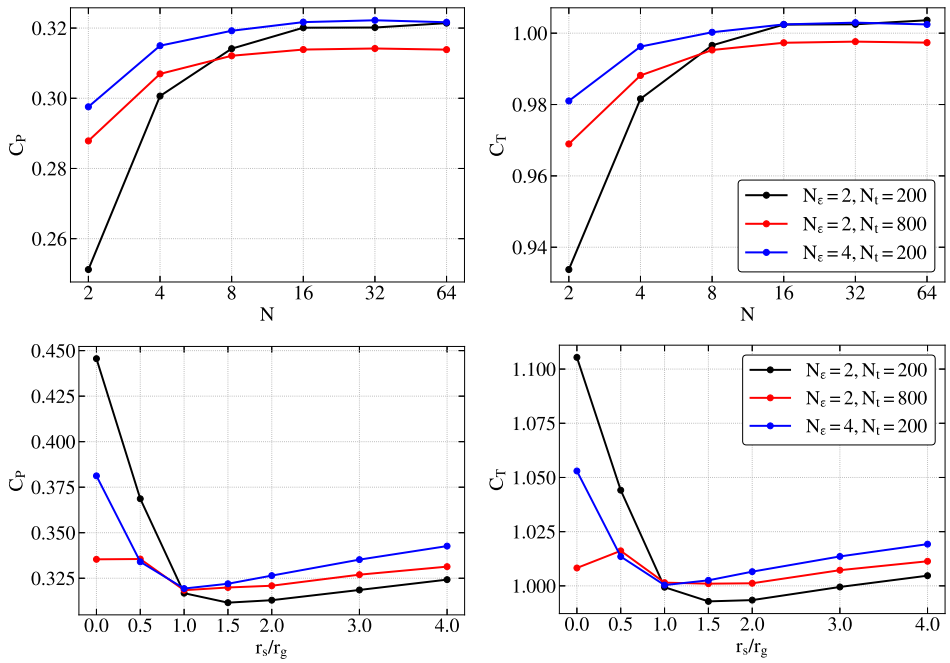


Figure B.1: MEXICO rotor, $N_x = 160$: Upper panel: change in C_P (left) and C_T (right) with number of line average sampling points N for various N_ε and N_t values ($r_s/r_g = 1.1$). Lower panel: change in C_P (left) and C_T (right) with the sampling radius r_s/r_g for various N_ε and N_t values ($N = 8$).

C

Extracting lift and drag coefficients from RANS BR simulations

The lift and drag coefficients for the ALM are calculated by processing results from 3D BR simulations. This approach circumvents the need for tip or spanwise flow corrections, as the tip effects are included in C_L and C_D values, that are allowed to vary over the blade span.

For both rotors the RANS equations with $k-\omega$ SST turbulence closure are solved. The rotation is modelled using the multiple reference frame (MRF) approach. More information about the BR simulations software, meshing, and convergence can be found in Zilic de Arcos *et al.* [44].

For the MEXICO rotor six different tip-speed ratios are simulated; $\lambda = 4.17, 5.56, 6.67, 8.34, 10, 13.3$. Likewise, for the Sch15b rotor the simulated tip-speed ratios are $\lambda = 3.0, 4.0, 5.0, 6.0, 7.0, 8.0, 9.0$ [44]. For each blade section at different radii, each tip-speed ratio simulation is used to extract a different (α, C_L, C_D) triplet. The angles of attack at each section are sampled using the line average sampling method following Zilic de Arcos *et al.* [44]. The number of points for the line averaging, centered at the quarter chord, were $N = 8$, as, increasing the number of points did not alter the sampled velocity. The sampling radius used was $r_s = 1.5c$, where c is the local chord, as per [44]. By considering multiple

tip-speed ratios which each yield a different α, C_L and C_D, variations with α can be developed for each radial position. In order to use the information in the ALM simulations, the data points are interpolated or extrapolated as required to cover the whole angle of attack range required. The value of the angle of attack in the ALM simulations is expected to be close to that extracted from the BR simulation, and extrapolation to a wider α is mainly for numerical stability purposes. For reproducibility, the lift and drag coefficients at different sections for the two turbines simulated in this paper are presented in Figure C.1.

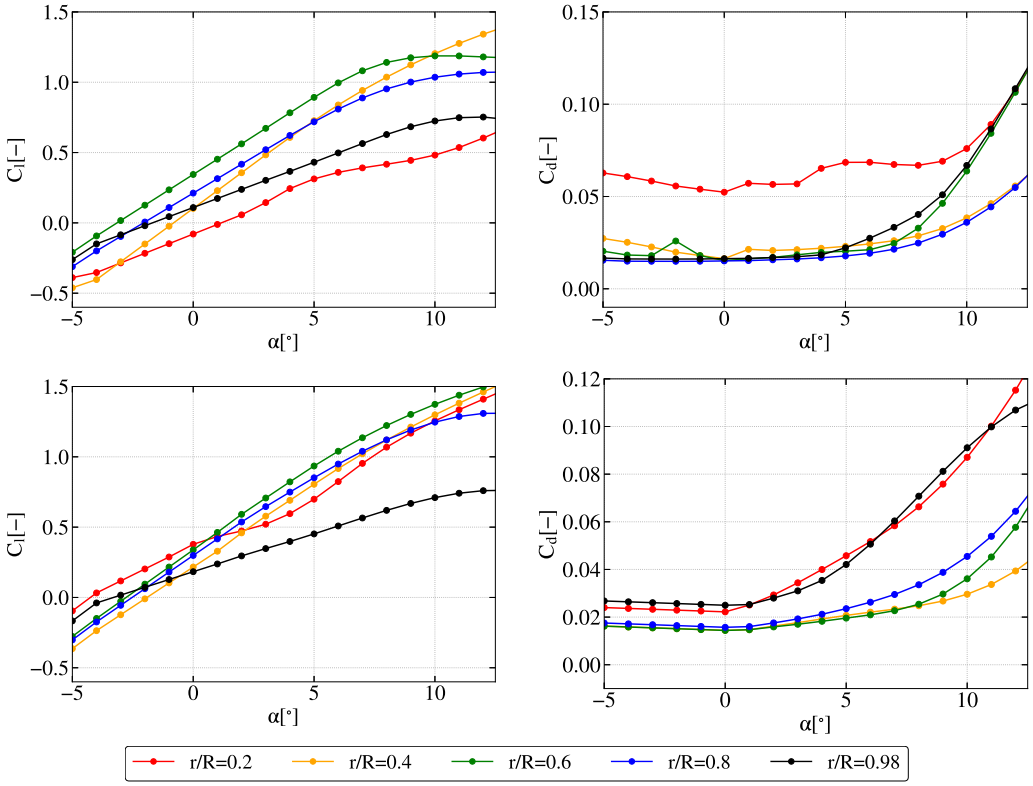


Figure C.1: Sectional lift (left) and drag (right) coefficients as functions of angle of attack at different spanwise locations, extracted from flow analysis of BR simulations for MEXICO rotor (upper panel) and Sch15b rotor (lower panel).

D

Characterisation of the ALM viscous vortex

The blade force smearing in step 3 of the ALM was originally introduced to ensure the numerical stability of the algorithm [69]. Dag and Sørensen [88] observed that the actuator line of a stationary wing that uses a Gaussian force smearing function of standard deviation ε (Equation 3.4) induces a velocity field nearly identical to that of a Lamb-Oseen viscous vortex with a core radius of $R_{core} = \varepsilon$. The observation was subsequently derived in Meyer Frosting *et al.* [90] and Martínez-Tossas and Meneveau [89].

The change in tangential velocity induced by a Lamb-Oseen vortex, varies with distance s from the centre of the vortex as:

$$u_\theta(s) = \frac{\Gamma}{2\pi}\frac{1}{s}(1 - e^{-s^2/R_{core}^2}). \tag{D.1}$$

where Γ is the circulation or strength of the vortex, and R_{core} the radius of the core. Those two parameters fully characterise the Lamb-Oseen vortex.

Given Dag and Sørensen's observations on the induced flow-field of actuator lines and the streamwise velocity fields of Figures 3.14 and 3.15, it is useful to describe the perturbed velocity field near the blade in terms of the Lamb-Oseen

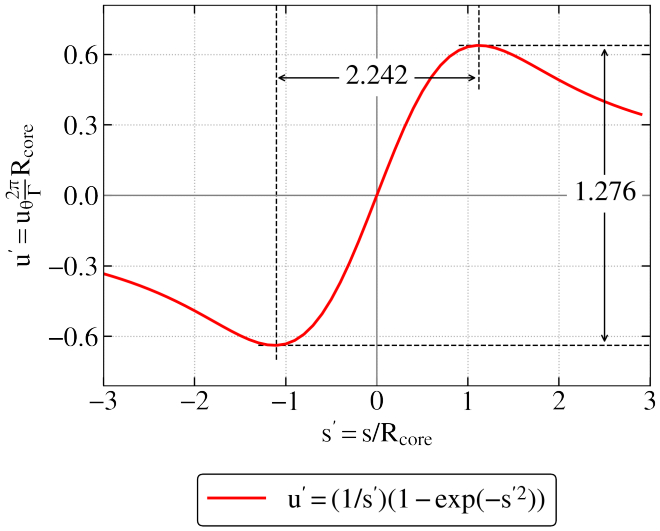


Figure D.1: Non-dimensional tangential velocity of the Lamb-Oseen viscous vortex $u' = u_\theta \frac{2\pi}{\Gamma} R_{core}$ as a function of non-dimensional distance $s' = s/R_{core}$ from the centre of the vortex.

vortex parameters. In order to fit equation D.1 to the simulated velocity fields of Figures 3.14 and 3.15, the peak-to-trough distances $\Delta s = r\Delta\theta$ and Δu, identified in Figure 3.15, are measured.

From the non-dimensional Lamb-Oseen vortex of Figure D.1 it can be deduced that a viscous vortex with an induced velocity field which has a measured circumferential peak-to-trough distance Δs, has a core radius of $R_{core} = \Delta s/2.242$. Similarly, the circulation of a viscous vortex is proportional to the peak-to-trough height of the resultant velocity field, Δu, and is given by $\Gamma = \Delta u R_{core} 2\pi/1.276$.

For a zero-velocity background flow, any two values of the given flow field would be sufficient to calculate the two parameters characterizing a fitted Lamb-Oseen viscous vortex. The fitting approach described above is a useful and pragmatic way to decouple the viscous vortex from the non-zero and non-uniform background flow.

It is finally noted that, in the results of Figures 3.14 and 3.15, the viscous vortex is not strictly a Lamb-Oseen vortex, and therefore the calculated vortex strength and radius are only approximate. Firstly, the background flow is non-uniform. Additionally, the applied forces may not be fully orthogonal to the onset flow. Also, due to the grouping of the collocation points, more than one force kernels may contribute to the velocity field of a point near the blade. Non-negligible drag can

also be present in turbine blade flows that further differentiates the resulting velocity perturbation from an ideal Lamb-Oseen vortex. The non-uniform background flow and the three-dimensionality of the field are key differences between the analysis here and that presented by Dag and Sørensen, where the background flow was uniform and the flow over the wing can be considered quasi-2D in the mid-span regions. However, the approximation that a Lamb-Oseen viscous vortex has been superimposed on an unsteady non-uniform background flow to allow quantification of the blade-local flow characteristics using vortex theory.

E

Robustness of flow sampling methods for ALM-LES

The robustness analysis of Chapter 3 was performed using an ALM-URANS solver. However it is important to extend the conclusions of this chapter for ALM-LES simulations. In ALM-LES simulations of wakes, time step savings are typically more important, as it is often the case that the computational requirements are excessive.

For both solvers, the eddy viscosity term is expected to be small at the rotor plane for a laminar or low turbulence inflow, and therefore little difference between URANS and LES can be expected, when it comes to C_P and C_T predictions. To validate this hypothesis some cases from Chapter 3 were re-simulated using ALM-LES. It can be seen in Figure E.1 that URANS and LES are indeed similar, with LAS improving the results for the LES simulations at the same degree that it does for the URANS simulations.

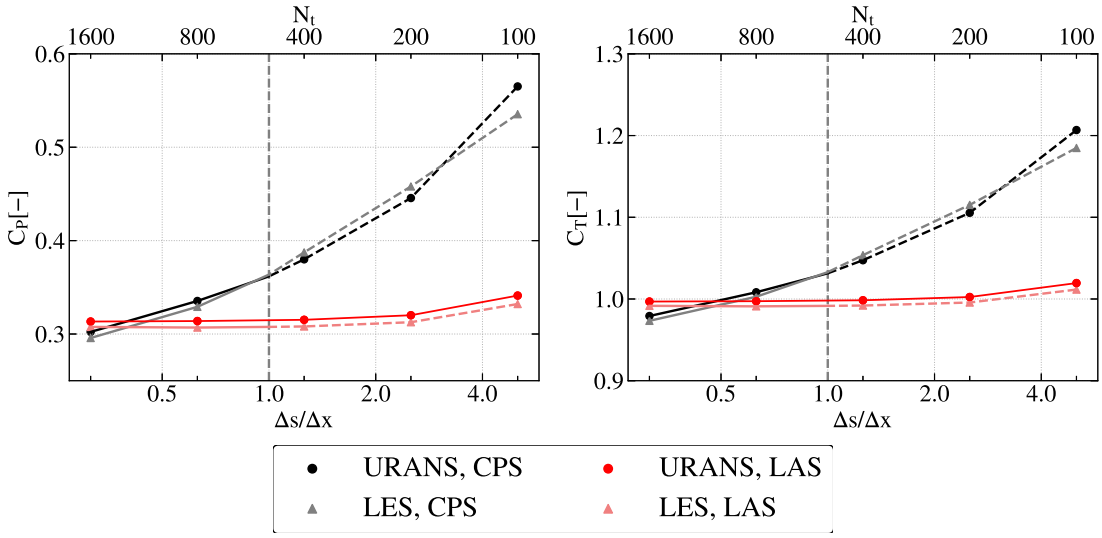


Figure E.1: MEXICO rotor, $N_x = 160$, $N_\varepsilon = 2$: convergence of power (left) and thrust (right) coefficients against N_t using two different sampling methods, CPS and LAS, and two different solvers, URANS used in Chapter 3 (results same as those presented in Figure 3.8), and LES used in Chapter 4.

References

1. Intergovernmental Panel on Climate Change (IPCC). (2023). Climate Change 2021 – The Physical Science Basis: Working Group I Contribution to the Sixth Assessment Report of the Intergovernmental Panel on Climate Change. Cambridge University Press. https://doi.org/10.1017/9781009157896.002
2. United Nations Climate Change. (2024a). *COP 28 UAE Concensus*. Retrieved 2024, from https://www.cop28.com/
3. United Nations Environment Programme. (2015, December). Paris agreement [T.I.A.S. No. 16-1104]. https://wedocs.unep.org/20.500.11822/20830
4. United Nations Climate Change. (2024b). *What is renewable energy?* Retrieved 2024, from https://www.un.org/en/climatechange/what-is-renewable-energy/
5. International Energy Agency. (2024a). *Renewables 2023* [License: CC BY 4.0]. https://www.iea.org/reports/renewables-2023
6. Our world in data. (2024). *Electricity mix*. Retrieved 2024, from https://ourworldindata.org/electricity-mix
7. International Energy Agency. (2024b). *Net zero by 2050* [License: CC BY 4.0]. https://www.iea.org/reports/net-zero-by-2050
8. *Global wind atlas*. (2024). Retrieved 2024, from https://globalwindatlas.info/en
9. renewableUK. (2024). *Wind energy statistics*. Retrieved 2024, from https://www.renewableuk.com/page/UKWEDhome
10. Department for Energy Security and Net Zero and Department for Business and Trade. (2023). *Offshore wind net zero investment roadmap*. Retrieved 2024, from https://assets.publishing.service.gov.uk/media/64a54c674dd8b3000f7fa4c9/offshore-wind-investment-roadmap.pdf
11. Department for Energy Security and Net Zero. (2023, December). *Net Zero Government Initiative UK Roadmap to Net Zero Government Emissions*. https://assets.publishing.service.gov.uk/media/6569cb331104cf000dfa7352/net-zero-government-emissions-roadmap.pdf
12. U.S. Energy Information Administration. (2023, April). *Wind energy explained: History of wind power*. Retrieved 2024, from https://www.eia.gov/energyexplained/wind/history-of-wind-power.php
13. Shea, K., & Howard, B. C. (2012). *Build Your Own Small Wind Power System* (1st ed.). New York: McGraw-Hill.
14. Kaldellis, J. K., & Zafirakis, D. (2011). The wind energy (r)evolution: A short review of a long history. *Renewable Energy*, *36*(7), 1887–1901. https://doi.org/10.1016/j.renene.2011.01.002
15. UNESCO World Heritage Convention. (2024). *Mill Network at Kinderdijk-Elshout*. Retrieved 2024, from https://whc.unesco.org/en/list/818/

16. University of Edinburgh. (2018). *Alumini in history: James blyth (1839 - 1906).* Retrieved 2024, from https://www.ed.ac.uk/alumni/services/notable-alumni/alumni-in-history/james-blyth
17. Scottish Power Renewables. (2024). *Whitelee Wind Farm.* Retrieved 2024, from https://www.whiteleewindfarm.co.uk/
18. equinor. (2024). *Hywind scotland.* Retrieved 2024, from https://www.equinor.com/energy/hywind-scotland
19. Price, T. J. (2005). James Blyth—Britain's first modern wind power pioneer. *Wind Engineering*, *29*(3), 191–200. https://doi.org/10.1260/030952405774354921
20. Garisto, D. (2022, July). *July 1887: James blyth harnesses the wind for electricity.* American Physical Society. Retrieved 2024, from https://www.aps.org/publications/apsnews/202207/blyth_harnesses.cfm
21. University of Massachusetts Amherst. (2008, October). *Wind energy center alumni.* Retrieved 2024, from https://www.umass.edu/windenergy/about/history/alumni
22. Ørsted. (2019a). *Making green energy affordable.* Retrieved 2024, from https://orsted.com/en/insights/white-papers/making-green-energy-affordable
23. IRENA-GWEC. (2013). *30 Years of Policies for Wind Energy: Lessons from 12 Wind Energy Markets* (tech. rep.). https://www.irena.org/publications/2013/Jan/30-Years-of-Policies-for-Wind-Energy-Lessons-from-12-Wind-Energy-Markets
24. Veers, P., Dykes, K., Basu, S., Bianchini, A., Clifton, A., Green, P., Holttinen, H., Kitzing, L., Kosovic, B., Lundquist, J. K., Meyers, J., O'Malley, M., Shaw, W. J., & Straw, B. (2022). Grand challenges: Wind energy research needs for a global energy transition. *Wind Energy Science*, *7*(6), 2491–2496. https://doi.org/10.5194/wes-7-2491-2022
25. Meneveau, C. (2019). Big wind power: Seven questions for turbulence research. *Journal of Turbulence*, *20*, 2–20. https://doi.org/10.1080/14685248.2019.1584664
26. Veers, P., Dykes, K., Lantz, E., Barth, S., Bottasso, C. L., Carlson, O., Clifton, A., Green, J., Green, P., Holttinen, H., Laird, D., Lehtomäki, V., Lundquist, J. K., Manwell, J., Marquis, M., Meneveau, C., Moriarty, P., Munduate, X., Muskulus, M., ... Wiser, R. (2019). Grand challenges in the science of wind energy. *Science*, *366*(6464), eaau2027. https://doi.org/10.1126/science.aau2027
27. Sherry, M., Sheridan, J., & Jacono, D. Horizontal axis wind turbine tip and root vortex measurements. In: 15th Int Symp on Applications of Laser Techniques to Fluid Mechanics. Lisbon, Portugal: Springer, 05-08 July 2010.
28. Sarmast, S., Dadfar, R., Mikkelsen, R. F., Schlatter, P., Ivanell, S., Sørensen, J. N., & Henningson, D. S. (2014a). Mutual inductance instability of the tip vortices behind a wind turbine. *Journal of Fluid Mechanics*, *755*, 705–731. https://doi.org/10.1017/jfm.2014.326
29. Iungo, G. V., Viola, F., Camarri, S., Porté-Agel, F., & Gallaire, F. (2013). Linear stability analysis of wind turbine wakes performed on wind tunnel measurements. *Journal of Fluid Mechanics*, *737*, 499–526. https://doi.org/10.1017/jfm.2013.569
30. Foti, D., Yang, X., Shen, L., & Sotiropoulos, F. (2019a). Effect of wind turbine nacelle on turbine wake dynamics in large wind farms. *Journal of Fluid Mechanics*, *869*, 1–26. https://doi.org/10.1017/jfm.2019.206
31. Debnath, M., Santoni, C., Leonardi, S., & Iungo, G. V. (2017). Towards reduced order modelling for predicting the dynamics of coherent vorticity structures within wind turbine wakes. *Philosophical Transactions of the Royal Society A:*

Mathematical, Physical and Engineering Sciences, *375*(2091), 20160108. https://doi.org/10.1098/rsta.2016.0108
32. Widnall, S. E. (1972). The stability of a helical vortex filament. *Journal of Fluid Mechanics*, *54*(4), 641–663. https://doi.org/10.1017/S0022112072000928
33. Lignarolo, L., Ragni, D., Scarano, F., Simão Ferreira, C., & van Bussel, G. (2015). Tip-vortex instability and turbulent mixing in wind-turbine wakes. *Journal of Fluid Mechanics*, *781*, 467–493. https://doi.org/10.1017/jfm.2015.470
34. Jensen, N. (1983). *A note on wind generator interaction.* (tech. rep.). Risø National Laboratory. Risø-M, No. 2411.
35. Bastankhah, M., & Porté-Agel, F. (2014). A new analytical model for wind-turbine wakes. *Renewable Energy*, *70*, 116–123. https://doi.org/10.1016/j.renene.2014.01.002
36. Barthelmie, R. J., Hansen, K., Frandsen, S. T., Rathmann, O., Schepers, J. G., Schlez, W., Phillips, J., Rados, K., Zervos, A., Politis, E. S., & Chaviaropoulos, P. K. (2009). Modelling and measuring flow and wind turbine wakes in large wind farms offshore. *Wind Energy*, *12*(5), 431–444. https://doi.org/10.1002/we.348
37. Bleeg, J., Purcell, M., Ruisi, R., & Traiger, E. (2018). Wind farm blockage and the consequences of neglecting its impact on energy production. *Energies*, *11*. https://doi.org/10.3390/en11061609
38. Ørsted. (2019b). *Ørsted presents update on its long-term financial targets* [Company Announcement No.28/2019]. Retrieved 2019, from http://web.archive.org/web/20080207010024/http://www.808multimedia.com/winnt/kernel.htm
39. Lundquist, J. K., DuVivier, K. K., Kaffine, D., & Tomaszewski, J. M. (2019). Costs and consequences of wind turbine wake effects arising from uncoordinated wind energy development. *Nature Energy*, *4*, 26–34. https://doi.org/10.1038/s41560-018-0281-2
40. Wu, Y. T., & Porté-Agel, F. (2012). Atmospheric turbulence effects on wind-turbine wakes: An LES study. *Energies*, *5*(12), 5340–5362. https://doi.org/10.3390/en5125340
41. Kleusberg, E., Benard, S., & Henningson, D. S. (2019). Tip-vortex breakdown of wind turbines subject to shear. *Wind Energy*, *22*(12), 1789–1799. https://doi.org/10.1002/we.2403
42. Abkar, M., & Porté-Agel, F. (2014). The effect of atmospheric stability on wind-turbine wakes: A large-eddy simulation study. *Journal of Physics: Conference Series*, *524*(1), 012138. https://doi.org/10.1088/1742-6596/524/1/012138
43. Porté-Agel, F., Bastankhah, M., & Shamsoddin, S. (2020). Wind-turbine and wind-farm flows: A review. *Boundary-Layer Meteorology*, *174*, 1–59. https://doi.org/10.1007/s10546-019-00473-0
44. Zilic de Arcos, F., Vogel, C. R., & Willden, R. H. J. (2020). Extracting angles of attack from blade-resolved rotor CFD simulations. *Wind Energy*, *23*(9), 1868–1885. https://doi.org/10.1002/we.2523
45. Ma, L., Delafin, P.-L., Tsoutsanis, P., Antoniadis, A., & Nishino, T. (2022). Blade-resolved CFD simulations of a periodic array of NREL 5 MW rotors with and without towers. *Wind*, *2*(1), 51–67. https://doi.org/10.3390/wind2010004
46. Churchfield, M. J., Schreck, S. J., Martinez, L. A., Meneveau, C., & Spalart, P. R. An advanced actuator line method for wind energy applications and beyond. In:

35th Wind Energy Symposium. Grapevine, Texas: AIAA, 9-13 January 2017. https://doi.org/10.2514/6.2017-1998

47. Zormpa, M., Clainche, S. L., Ferrer, E., Vogel, C., & Willden, R. (2023). Dynamic mode decomposition of merging wind turbine wakes. *Journal of Physics: Conference Series*, *2505*(1), 012020. https://doi.org/10.1088/1742-6596/2505/1/012020
48. Schluntz, J., & Willden, R. H. (2015). An actuator line method with novel blade flow field coupling based on potential flow equivalence. *Wind Energy*, *18*(8), 1469–1485. https://doi.org/10.1002/we.1770
49. Ouro, P., & Nishino, T. (2021). Performance and wake characteristics of tidal turbines in an infinitely large array. *Journal of Fluid Mechanics*, *925*, A30. https://doi.org/10.1017/jfm.2021.692
50. Vogel, C. R., & Willden, R. H. J. (2020). Investigation of wind turbine wake superposition models using Reynolds-averaged Navier-Stokes simulations. *Wind Energy*, *23*(3), 593–607. https://doi.org/10.1002/we.2444
51. Nishino, T., & Draper, S. (2015). Local blockage effect for wind turbines. *Journal of Physics: Conference Series*, *625*(1), 012010. https://doi.org/10.1088/1742-6596/625/1/012010
52. Kirby, A., Nishino, T., & Dunstan, T. D. (2022). Two-scale interaction of wake and blockage effects in large wind farms. *Journal of Fluid Mechanics*, *953*, A39. https://doi.org/10.1017/jfm.2022.979
53. Wimshurst, A., & Willden, R. H. J. (2017a). Extracting lift and drag polars from blade-resolved computational fluid dynamics for use in actuator line modelling of horizontal axis turbines. *Wind Energy*, *20*(5), 815–833. https://doi.org/10.1002/we.2065
54. de Oliveira, M., Puraca, R., & Carmo, B. (2022). Blade-resolved numerical simulations of the NREL offshore 5 MW baseline wind turbine in full scale: A study of proper solver configuration and discretization strategies. *Energy*, *254*, 124368. https://doi.org/10.1016/j.energy.2022.124368
55. Sun, C., Tian, T., Zhu, X., Hua, O., & Du, Z. (2021). Investigation of the near wake of a horizontal-axis wind turbine model by dynamic mode decomposition. *Energy*, *227*, 120418. https://doi.org/10.1016/j.energy.2021.120418
56. Shen, W. Z., Sørensen, J., & Zhang, J. (2007). Actuator surface model for wind turbine flow computations. *European Wind Energy Conference and Exhibition 2007, EWEC 2007*, *2*.
57. Shen, W. Z., Zhang, J. H., & Sørensen, J. N. (2009). The actuator surface model: A new Navier–Stokes based model for rotor computations. *Journal of Solar Energy Engineering*, *131*(1), 011002. https://doi.org/10.1115/1.3027502
58. Yang, X., & Sotiropoulos, F. (2018). A new class of actuator surface models for wind turbines. *Wind Energy*, *21*(5), 285–302. https://doi.org/10.1002/we.2162
59. Edwards, H., Chen, X., Vogel, C., & Willden, R. (2023). Modelling the effects of boundary proximity on a tidal rotor using the actuator line method. *Proceedings of the European Wave and Tidal Energy Conference*, *15*. https://doi.org/10.36688/ewtec-2023-407
60. Schluntz, J., & Willden, R. (2015). The effect of blockage on tidal turbine rotor design and performance. *Renewable Energy*, *81*, 432–441. https://doi.org/10.1016/j.renene.2015.02.050

61. Troldborg, N. (2009). *Actuator line modeling of wind turbine wakes* [Doctoral dissertation, Technical University of Denmark].
62. Martínez-Tossas, L. A., Churchfield, M. J., & Leonardi, S. (2015). Large eddy simulations of the flow past wind turbines: Actuator line and disk modeling. *Wind Energy*, *18*(6), 1047–1060. https://doi.org/10.1002/we.1747
63. Deskos, G. (2019). *Numerical simulations of wind turbine wakes* [Doctoral dissertation, Imperial College London].
64. Sarlak, H., Meneveau, C., & Sørensen, J. (2015). Role of subgrid-scale modeling in large eddy simulation of wind turbine wake interactions. *Renewable Energy*, *77*, 386–399. https://doi.org/10.1016/j.renene.2014.12.036
65. Stevens, R. J., Martínez-Tossas, L. A., & Meneveau, C. (2018). Comparison of wind farm large eddy simulations using actuator disk and actuator line models with wind tunnel experiments. *Renewable Energy*, *116*(A), 470–478. https://doi.org/10.1016/j.renene.2017.08.072
66. Foti, D., Yang, X., & Sotiropoulos, F. (2018a). Similarity of wake meandering for different wind turbine designs for different scales. *Journal of Fluid Mechanics*, *842*, 5–25. https://doi.org/10.1017/jfm.2018.9
67. Wu, Y. T., & Porté-Agel, F. (2011). Large-eddy simulation of wind-turbine wakes: Evaluation of turbine parametrisations. *Boundary-Layer Meteorology*, *138*, 345–366. https://doi.org/10.1007/s10546-010-9569-x
68. Sørensen, J. N., & Myken, A. (1992). Unsteady actuator disc model for horizontal axis wind turbines. *Journal of Wind Engineering and Industrial Aerodynamics*, *39*(1), 139–149. https://doi.org/10.1016/0167-6105(92)90540-Q
69. Sørensen, J. N., & Shen, W. Z. (2002). Numerical modeling of wind turbine wakes. *Journal of Fluids Engineering*, *124*(2), 393–399. https://doi.org/10.1115/1.1471361
70. Shives, M., & Crawford, C. (2013). Mesh and load distribution requirements for actuator line CFD simulations. *Wind Energy*, *16*(8), 1183–1196. https://doi.org/10.1002/we.1546
71. Sørensen, J. N., Mikkelsen, R. F., Henningson, D. S., Ivanell, S., Sarmast, S., & Andersen, S. J. (2015). Simulation of wind turbine wakes using the actuator line technique. *Philosophical Transactions of the Royal Society A: Mathematical, Physical and Engineering Sciences*, *373*. https://doi.org/10.1098/rsta.2014.0071
72. Wimshurst, A., & Willden, R. (2016). Computational analysis of blockage designed tidal turbine rotors. *Progress in Renewable Energies Offshore : Proceedings of the 2nd International Conference on Renewable Energies*, 587. https://doi.org/10.1201/9781315229256-71
73. Liu, L., Franceschini, L., Oliveira, D. F., Galeazzo, F. C., Carmo, B. S., & Stevens, R. J. A. M. (2022). Evaluating the accuracy of the actuator line model against blade element momentum theory in uniform inflow. *Wind Energy*, *25*(6), 1046–1059. https://doi.org/10.1002/we.2714
74. De Cillis, G., Cherubini, S., Semeraro, O., Leonardi, S., & De Palma, P. (2022). The influence of incoming turbulence on the dynamic modes of an NREL-5MW wind turbine wake. *Renewable Energy*, *183*, 601–616. https://doi.org/10.1016/j.renene.2021.11.037
75. Churchfield, M. J., Lee, S., Michalakes, J., & Moriarty, P. J. (2012). A numerical study of the effects of atmospheric and wake turbulence on wind turbine dynamics. *Journal of Turbulence*, *13*, N14. https://doi.org/10.1080/14685248.2012.668191

76. Apsley, D., Stallard, T., & Stansby, P. (2018). Actuator-line CFD modelling of tidal-stream turbines in arrays. *Journal of Ocean Engineering and Marine Energy*, *4*, 259–271. https://doi.org/10.1007/s40722-018-0120-3
77. Ouro, P., Ramírez, L., & Harrold, M. (2019). Analysis of array spacing on tidal stream turbine farm performance using large-eddy simulation. *Journal of Fluids and Structures*, *91*, 102732. https://doi.org/10.1016/j.jfluidstructs.2019.102732
78. Jost, E., Klein, L., Leipprand, H., Lutz, T., & Krämer, E. (2018). Extracting the angle of attack on rotor blades from CFD simulations. *Wind Energy*, *21*(10), 807–822. https://doi.org/10.1002/we.2196
79. Drela, M. (2013). *Xfoil 6.99*. Retrieved 2024, from http://web.mit.edu/drela/Public/web/xfoil/
80. Bartl, J., Sagmo, K. F., Bracchi, T., & Sætran, L. (2019). Performance of the NREL S826 airfoil at low to moderate Reynolds numbers - a reference experiment for CFD models. *European Journal of Mechanics - B/Fluids*, *75*, 180–192. https://doi.org/10.1016/j.euromechflu.2018.10.002
81. Cakmakcioglu, S. C., Sert, I. O., Tugluk, O., & Sezer-Uzol, N. (2014). 2-D and 3-D CFD investigation of NREL S826 airfoil at low Reynolds numbers. *Journal of Physics: Conference Series*, *524*(1), 012028. https://doi.org/10.1088/1742-6596/524/1/012028
82. Krogstad, P.-Å., & Lund, J. (2012). An experimental and numerical study of the performance of a model turbine. *Wind Energy*, *15*(3), 443–457. https://doi.org/10.1002/we.482
83. Shen, W. Z., Mikkelsen, R., Sørensen, J. N., & Bak, C. (2005). Tip loss corrections for wind turbine computations. *Wind Energy*, *8*(4), 457–475. https://doi.org/10.1002/we.153
84. Wimshurst, A., & Willden, R. H. J. (2017b). Analysis of a tip correction factor for horizontal axis turbines. *Wind Energy*, *20*(9), 1515–1528. https://doi.org/10.1002/we.2106
85. Wimshusrt, A. (2018). *Tip flow corrections for horizontal axis wind and tidal turbine rotors* [Doctoral dissertation, University of Oxford].
86. Glauert, H. (1935). Airplane propellers. In *Aerodynamic Theory: A General Review of Progress Under a Grant of the Guggenheim Fund for the Promotion of Aeronautics* (pp. 169–360). Springer Berlin Heidelberg. https://doi.org/10.1007/978-3-642-91487-4_3
87. Snel, H., Schepers, J. G., & Montgomerie, B. (2007). The MEXICO project (Model Experiments in Controlled Conditions): The database and first results of data processing and interpretation. *Journal of Physics: Conference Series*, *75*(1), 012014. https://doi.org/10.1088/1742-6596/75/1/012014
88. Dag, K. O., & Sørensen, J. N. (2020). A new tip correction for actuator line computations. *Wind Energy*, *23*(2), 148–160. https://doi.org/10.1002/we.2419
89. Martínez-Tossas, L. A., & Meneveau, C. (2019). Filtered lifting line theory and application to the actuator line model. *Journal of Fluid Mechanics*, *863*, 269–292. https://doi.org/10.1017/jfm.2018.994
90. Meyer Forsting, A. R., Pirrung, G. R., & Ramos-García, N. (2019). A vortex-based tip/smearing correction for the actuator line. *Wind Energy Science*, *4*(2), 369–383. https://doi.org/10.5194/wes-4-369-2019
91. Burton, T., Jenkins, N., Sharpe, D., & Bossanyi, E. (2011). *Wind Energy Handbook* (2nd ed.). Wiley & Sons, Ltd. https://doi.org/10.1002/0470846062

92. Martínez-Tossas, L. A., Churchfield, M. J., & Meneveau, C. (2017). Optimal smoothing length scale for actuator line models of wind turbine blades based on gaussian body force distribution. *Wind Energy*, *20*(6), 1083–1096. https://doi.org/10.1002/we.2081
93. Jha, P. K., & Schmitz, S. (2018). Actuator curve embedding - an advanced actuator line model. *Journal of Fluid Mechanics*, *834*, R2. https://doi.org/10.1017/jfm.2017.793
94. Reynolds, O. (1895). On the dynamical theory of incompressible viscous fluids and the determination of the criterion. *Philosophical Transactions of the Royal Society of London. (A.)*, *186*, 123–164. https://doi.org/10.1098/rsta.1895.0004
95. Schmitt, F. (2007). About Boussinesq's turbulent viscosity hypothesis: Historical remarks and a direct evaluation of its validity. *Comptes Rendus - Mecanique*, *335*, 617–627. https://doi.org/10.1016/j.crme.2007.08.004
96. Jones, W., & Launder, B. (1972). The prediction of laminarization with a two-equation model of turbulence. *International Journal of Heat and Mass Transfer*, *15*(2), 301–314. https://doi.org/10.1016/0017-9310(72)90076-2
97. Wilcox, D. C. (1988). Reassessment of the scale-determining equation for advanced turbulence models. *AIAA Journal*, *26*(11), 1299–1310. https://doi.org/10.2514/3.10041
98. Menter, F. R. (1994). Two-equation eddy-viscosity turbulence models for engineering applications. *AIAA Journal*, *32*(8), 1598–1605. https://doi.org/10.2514/3.12149
99. Spalart, P., & Allmaras, S. (1994). A one-equation turbulence model for aerodynamic flows. *La Recherche Aérospeciale*, *1*, 5–21. https://doi.org/10.2514/6.1992-439
100. NASA Langley Research Center. (2021). *Turbulence modeling resource*. Retrieved 2024, from https://turbmodels.larc.nasa.gov
101. Menter, F., Kuntz, M., & Langtry, R. (2003). Ten years of industrial experience with the SST turbulence model. *Turbulence, Heat and Mass Transfer*, *4*, 625–632.
102. Pope, S. B. (2000). *Turbulent Flows*. Cambridge University Press. https://doi.org/10.1017/CBO9780511840531
103. Sagaut, P. (2004). *Large Eddy Simulation for Incompressible Flows* (3rd ed.). Springer. https://doi.org/10.1007/b137536
104. Meneveau, C. (2010). Turbulence: Subgrid-Scale Modeling [revision #153312]. *Scholarpedia*, *5*(1), 9489. https://doi.org/10.4249/scholarpedia.9489
105. Fröhlich, J., & von Terzi, D. (2008). Hybrid LES/RANS methods for the simulation of turbulent flows. *Progress in Aerospace Sciences*, *44*(5), 349–377. https://doi.org/10.1016/j.paerosci.2008.05.001
106. Smagorinsky, J. (1963). General circulation experiments with the primitive equations. *Monthly Weather Review*, *95*, 99–164. https://doi.org/10.1175/1520-0493(1963)091<0099:GCEWTP>2.3.CO;2
107. Lilly, K. E. (1966). The representation of small-scale turbulence in numerical simulation experiments. *In Proceedings of the IBM Scientific Computing Symposium on Environmental Sciences*, 167. https://doi.org/doi:10.5065/D62R3PMM
108. Franck, N., & Ducros, F. (1999). Subgrid-scale stress modelling based on the square of the velocity gradient tensor. *Flow Turbulence and Combustion*, *62*, 183–200. https://doi.org/10.1023/A:1009995426001

109. Germano, M. (1992). Turbulence: The filtering approach. *Journal of Fluid Mechanics*, *238*, 325–336. https://doi.org/10.1017/S0022112092001733
110. Porté-Agel, F., Meneveau, C., & Parlange, M. B. (2000). A scale-dependent dynamic model for large-eddy simulation: Application to a neutral atmospheric boundary layer. *Journal of Fluid Mechanics*, *415*, 261–284. https://doi.org/10.1017/S0022112000008776
111. Meneveau, C., Lund, T. S., & Cabot, W. H. (1996). A lagrangian dynamic subgrid-scale model of turbulence. *Journal of Fluid Mechanics*, *319*, 353–385. https://doi.org/10.1017/S0022112096007379
112. Germano, M., Piomelli, U., Moin, P., & Cabot, W. H. (1991). A dynamic subgrid-scale eddy viscosity model. *Physics of Fluids A: Fluid Dynamics*, *3*(7), 1760–1765. https://doi.org/10.1063/1.857955
113. Krogstad, P.-Å., & Eriksen, P. E. (2013). 'Blind test' calculations of the performance and wake development for a model wind turbine. *Renewable Energy*, *50*, 325–333. https://doi.org/10.1016/j.renene.2012.06.044
114. Pierella, F., Krogstad, P.-Å., & Sætran, L. (2014). Blind test 2 calculations for two in-line model wind turbines where the downstream turbine operates at various rotational speeds. *Renewable Energy*, *70*, 62–77. https://doi.org/10.1016/j.renene.2014.03.034
115. Somers, D. M. (2005, January). *S825 and S826 airfoils: 1994–1995* (tech. rep.). https://doi.org/10.2172/15011671
116. Marten, D., Peukert, J., Pechlivanoglou, G., Nayeri, C., & Paschereit, C. (2013). Qblade: An open source tool for design and simulation of horizontal and vertical axis wind turbines. *International Journal of Emerging Technology and Advanced Engineering*, *3*, 264–269.
117. Zilic de Arcos, F. (2021). *Hydrodynamics of highly-loaded axial flow tidal rotors* [Doctoral dissertation, University of Oxford].
118. Zilic de Arcos, F., Vogel, C., & Willden, R. (2019). Hydrodynamic modelling of flexible tidal turbine blades. *Proceedings of the European Wave and Tidal Energy Conference*, *13*. https://doi.org/10.36688/ewtec-2023-574
119. Forsting, A. R. M., Pirrung, G. R., & Ramos-García, N. (2020). Brief communication: A fast vortex-based smearing correction for the actuator line. *Wind Energy Science*, *5*, 349–353. https://doi.org/10.5194/wes-5-349-2020
120. Mittal, A., Sreenivas, K., Taylor, L. K., & Hereth, L. Improvements to the actuator line modeling for wind turbines. In: 33rd Wind Energy Symposium. Kissimmee, Florida: AIAA, 5-9 January 2017. https://doi.org/10.2514/6.2015-0216
121. NREL. (2012). *SOWFA: Simulator fOr Wind Farm Applications*. Retrieved 2024, from https://www.nrel.gov/wind/nwtc/sowfa.html
122. Guntur, S., & Sørensen, N. N. (2014). An evaluation of several methods of determining the local angle of attack on wind turbine blades. *Journal of Physics: Conference Series*, *555*(1), 012045. https://doi.org/10.1088/1742-6596/555/1/012045
123. Bak, C., Troldborg, N., & Madsen, H. (2011). Dan-aero mw: Measured airfoil characteristics for a mw rotor in atmospheric conditions, 171–175.
124. Mohamed, O., Melani, P. F., Balduzzi, F., Ferrara, G., & Bianchini, A. (2022). An insight on the key factors influencing the accuracy of the actuator line method for use in vertical-axis turbines: Limitations and open challenges. *Energy Conversion*

and Management, *270*(2), 116249.
https://doi.org/10.1016/j.enconman.2022.116249
125. ESI. (2020). *OpenFOAM v.2006*. Retrieved 2020, from
https://www.openfoam.com/
126. Langer, T., Belyaev, A., & Seidel, H.-P. Spherical Barycentric Coordinates. In: Symposium on Geometry Processing. Cagliari, Italy: The Eurographics Association, June 26 - 28, 2006. https://doi.org/10.2312/SGP/SGP06/081-088
127. Yang, X., Zhang, X., Li, Z., & He, G.-W. (2009). A smoothing technique for discrete delta functions with application to immersed boundary method in moving boundary simulations. *Journal of Computational Physics*, *228*(20), 7821–7836.
https://doi.org/10.1016/j.jcp.2009.07.023
128. Hansen, M., Sørensen, N., & Michelsen, J. Extraction of lift, drag and angle of attack from computed 3-D viscous flow around a rotating blade. In: Proceedings of the European wind energy conference. Dublin, Ireland: Irish Wind Energy Association, 6-9 October 1997.
129. Nilsson, K., Shen, W. Z., Sørensen, J. N., Breton, S.-P., & Ivanell, S. (2015). Validation of the actuator line method using near wake measurements of the MEXICO rotor. *Wind Energy*, *18*(3), 499–514. https://doi.org/10.1002/we.1714
130. Nathan, J., Masson, C., & Dufresne, L. (2014). Analysis of the sweeped actuator line method. *E3S Web of Conferences, EDP Sciences*, *5*, 01001.
https://doi.org/10.1051/e3sconf/20150501001
131. Mohammadi, M. M., Olivares-Espinosa, H., Navarro Diaz, G. P., & Ivanell, S. (2023). An actuator sector model for wind power applications: A parametric study [[preprint]]. *Wind Energy Science Discussions*.
https://doi.org/10.5194/wes-2023-16
132. Shen, W. Z., Zhu, W. J., & Sørensen, J. N. (2012). Actuator line/navier–stokes computations for the mexico rotor: Comparison with detailed measurements. *Wind Energy*, *15*(5), 811–825. https://doi.org/10.1002/we.510
133. Schluntz, J., & Willden, R. H. J. (2015). The effect of blockage on tidal turbine rotor design and performance. *Renewable Energy*, *81*(100), 432–441.
https://doi.org/10.1016/j.renene.2015.02.050
134. Wimshurst, A. (2018). *Tip flow corrections for horizontal axis wind and tidal turbine rotors* [Doctoral dissertation, University of Oxford].
135. Jha, P., Churchfield, M., Moriarty, P., & Schmitz, S. (2014). Guidelines for volume force distributions within actuator line modeling of wind turbines on large-eddy simulation-type grids. *Journal of Solar Energy Engineering*, *136*(3), 031003.
https://doi.org/10.1115/1.4026252
136. Foti, D., Yang, X., & Sotiropoulos, F. (2018b). Similarity of wake meandering for different wind turbine designs for different scales. *Journal of Fluid Mechanics*, *842*, 5–25. https://doi.org/10.1017/jfm.2018.9
137. Dag, K. O. (2017). *Combined pseudo-spectral / actuator line model for wind turbine applications* [Doctoral dissertation, DTU Wind Energy].
138. Kleusberg, E., Mikkelsen, R. F., Schlatter, P., Ivanell, S., & Henningson, D. S. (2017). High-order numerical simulations of wind turbine wakes. *Journal of Physics: Conference Series*, *854*(1), 012025.
https://doi.org/10.1088/1742-6596/854/1/012025
139. Sarlak, H., Nishino, T., Martínez-Tossas, L., Meneveau, C., & Sørensen, J. (2016). Assessment of blockage effects on the wake characteristics and power of wind

turbines. *Renewable Energy*, *93*, 340–352. https://doi.org/10.1016/j.renene.2016.01.101
140. Poletto, R., Craft, T., & Revell, A. (2013). A new divergence free synthetic eddy method for the reproduction of inlet flow conditions for LES. *Flow, Turbulence and Combustion*, *91*, 1–21. https://doi.org/10.1007/s10494-013-9488-2
141. Hunter, W., Nishino, T., & Willden, R. H. J. Implementation and validation of an actuator line class for wind and tidal turbines. In: 9th OpenFOAM Workshop. Zagreb, Croatia, 2014.
142. Willden, R., Chen, X., Tucker Harvey, S., Edwards, H., Vogel, C., Bhavsar, K., Allsop, T., Gilbert, J., Mullings, H., Ghobrial, M., Ouro, P., Apsley, D., Stallard, T., Benson, I., Young, A., Schmitt, P., Zilic de Arcos, F., Dufour, M.-A., Choma Bex, C., ... Carmo, B. (2023). Tidal Turbine Benchmarking Project: Stage I - Steady Flow Blind Predictions. *Proceedings of the European Wave and Tidal Energy Conference*, *15*. https://doi.org/10.36688/ewtec-2023-574
143. Sarlak, H. (2014). *Large eddy simulation of turbulent flows in wind energy* [Doctoral dissertation, DTU Wind Energy].
144. Pierella, F., & Sætran, L. (2017). Wind tunnel investigation on the effect of the turbine tower on wind turbines wake symmetry. *Wind Energy*, *20*(10), 1753–1769. https://doi.org/10.1002/we.2120
145. Gao, Z., Li, Y., Wang, T., Ke, S., & Li, D. (2021). Recent improvements of actuator line-large-eddy simulation method for wind turbine wakes. *Applied Mathematics and Mechanics*, *42*(2), 511–526. https://doi.org/10.1007/s10483-021-2717-8
146. Santoni, C., Carrasquillo, K., Arenas-Navarro, I., & Leonardi, S. (2017). Effect of tower and nacelle on the flow past a wind turbine. *Wind Energy*, *20*(12), 1927–1939. https://doi.org/10.1002/we.2130
147. Davidson, L. (2009). Large eddy simulations: How to evaluate resolution. *International Journal of Heat and Fluid Flow*, *30*(5), 1016–1025. https://doi.org/10.1016/j.ijheatfluidflow.2009.06.006
148. Fuchs, A., Kharche, S., Patil, A., Friedrich, J., Wächter, M., & Peinke, J. (2022). An open source package to perform basic and advanced statistical analysis of turbulence data and other complex systems. *Physics of Fluids*, *34*(10), 101801. https://doi.org/10.1063/5.0107974
149. Tabor, G., & Baba-Ahmadi, M. (2010). Inlet conditions for large eddy simulation: A review. *Computers Fluids*, *39*(4), 553–567. https://doi.org/10.1016/j.compfluid.2009.10.007
150. Mann, J. (1994). The spatial structure of neutral atmospheric surface-layer turbulence. *Journal of Fluid Mechanics*, *273*, 141–168. https://doi.org/10.1017/S0022112094001886
151. Bartl, J., & Sætran, L. (2017). Blind test comparison of the performance and wake flow between two in-line wind turbines exposed to different turbulent inflow conditions. *Wind Energy Science*, *2*(1), 55–76. https://doi.org/10.5194/wes-2-55-2017
152. Pierella, F., Eriksen, P. E., Krogstad, P.-Å., & Sætran, L. (2012). Invitation to the 2012 "Blind test 2" workshop calculations for two wind turbines in line. https://www.sintef.no/globalassets/project/nowitech/events/bt2_invite.pdf
153. Shkara, Y., Cardaun, M., Schelenz, R., & Jacobs, G. (2020). Aeroelastic response of a multi-megawatt upwind horizontal axis wind turbine (HAWT) based on

fluid–structure interaction simulation. *Wind Energy Science*, *5*(1), 141–154. https://doi.org/10.5194/wes-5-141-2020

154. Foti, D., Yang, X., Guala, M., & Sotiropoulos, F. (2016). Wake meandering statistics of a model wind turbine: Insights gained by large eddy simulations. *Phys. Rev. Fluids*, *1*, 044407. https://doi.org/10.1103/PhysRevFluids.1.044407
155. Kang, S., Yang, X., & Sotiropoulos, F. (2014). On the onset of wake meandering for an axial flow turbine in a turbulent open channel flow. *Journal of Fluid Mechanics*, *744*, 376–403. https://doi.org/10.1017/jfm.2014.82
156. Abraham, A., Dasari, T., & Hong, J. (2019). Effect of turbine nacelle and tower on the near wake of a utility-scale wind turbine. *Journal of Wind Engineering and Industrial Aerodynamics*, *193*, 103981. https://doi.org/10.1016/j.jweia.2019.103981
157. Neunaber, I., Hölling, M., Stevens, R. J., Schepers, G., & Peinke, J. (2020). Distinct turbulent regions in the wake of a wind turbine and their inflow-dependent locations: The creation of a wake map. *Energies*, *13*(20). https://doi.org/10.3390/en13205392
158. Yang, X., & Sotiropoulos, F. (2019). A review on the meandering of wind turbine wakes. *Energies*, *12*(24). https://doi.org/10.3390/en12244725
159. Ma, L., Nishino, T., & Antoniadis, A. F. (2019). Prediction of the impact of support structures on the aerodynamic performance of large wind farms. *Journal of Renewable and Sustainable Energy*, *11*(6), 063306. https://doi.org/10.1063/1.5120602
160. Foti, D., Yang, X., Shen, L., & Sotiropoulos, F. (2019b). Effect of wind turbine nacelle on turbine wake dynamics in large wind farms. *Journal of Fluid Mechanics*, *869*, 1–26. https://doi.org/10.1017/jfm.2019.206
161. Muchala, S., & Willden, R. H. (2018). Influence of support structures on tidal turbine power output. *Journal of Fluids and Structures*, *83*, 27–39. https://doi.org/10.1016/j.jfluidstructs.2018.08.008
162. De Cillis, G., Cherubini, S., Semeraro, O., Leonardi, S., & De Palma, P. (2021). POD-based analysis of a wind turbine wake under the influence of tower and nacelle. *Wind Energy*, *24*(6), 609–633. https://doi.org/10.1002/we.2592
163. Orlandi, P., & Leonardi, S. (2006). DNS of turbulent channel flows with two- and three-dimensional roughness. *Journal of Turbulence*, *7*, 1–22. https://doi.org/10.1080/14685240600827526
164. Churchfield, M., Lee, S., Schmitz, S., & Wang, Z. (5-9 January 2017). Modeling wind turbine tower and nacelle effects within an actuator line model. https://doi.org/10.2514/6.2015-0214
165. Krogstad, P.-Å., & Eriksen, P. E. (2011). *"Blind test" workshop calculations for a modell wind turbine* (tech. rep.). Department of Energy and Process Engineering, NTNU.
166. ESI. (2024). *Mesh generation with the snappyHexMesh utility*. Retrieved 2024, from https://www.openfoam.com/documentation/user-guide/4-mesh-generation-and-conversion/4.4-mesh-generation-with-the-snappyhexmesh-utility
167. Mukha, T., Rezaeiravesh, S., & Liefvendahl, M. (2019). A library for wall-modelled large-eddy simulation based on OpenFOAM technology. *Computer Physics Communications*, *239*, 204–224. https://doi.org/10.1016/j.cpc.2019.01.016
168. Boileau, M., Duchaine, F., Jouhaud, J. C., & Sommerer, Y. (2013). Large-eddy simulation of heat transfer around a square cylinder using unstructured grids. *AIAA Journal*, *51*(2), 372–385. https://doi.org/10.2514/1.J051800

169. Apsley, D. D. (2024). CFD simulation of tidal-stream turbines in a compact array. *Renewable Energy*, *224*, 120133. https://doi.org/10.1016/j.renene.2024.120133
170. van der Laan, M. P., Sørensen, N. N., Réthoré, P.-E., Mann, J., Kelly, M. C., & Troldborg, N. (2015). The k-ϵ-fp model applied to double wind turbine wakes using different actuator disk force methods. *Wind Energy*, *18*(12), 2223–2240. https://doi.org/10.1002/we.1816
171. ESI. (2021). *Actuation disk*. Retrieved 2024, from https://www.openfoam.com/documentation/guides/latest/doc/guide-fvoptions-sources-actuation-disk.html
172. Rocchio, B., Ciri, U., Salvetti, M. V., & Leonardi, S. (2020). Appraisal and calibration of the actuator line model for the prediction of turbulent separated wakes. *Wind Energy*, *23*(5), 1231–1248. https://doi.org/10.1002/we.2483
173. Stevens, R. J., & Meneveau, C. (2017). Flow Structure and Turbulence in Wind Farms. *49*, 311–339. https://doi.org/10.1146/annurev-fluid-010816-060206
174. Chamorro, L., & Porté-Agel, F. (2009). A wind-tunnel investigation of wind-turbine wakes: Boundary-layer turbulence effects. *Boundary-Layer Meteorology*, *132*, 129–149. https://doi.org/10.1007/s10546-009-9380-8
175. Neunaber, I., Peinke, J., & Obligado, M. (2022). Application of the Townsend-George theory for free shear flows to single and double wind turbine wakes-A wind tunnel study. *Wind Energy Science*, *7*(1), 201–219. https://doi.org/10.5194/wes-7-201-2022
176. Ryi, J., Rhee, W., Hwang, U. C., & Choi, J. S. (2015). Blockage effect correction for a scaled wind turbine rotor by using wind tunnel test data. *Renewable Energy*, *79*(1), 227–235. https://doi.org/10.1016/j.renene.2014.11.057
177. MathWorks. (2024). *ga: Find minimum of function using genetic algorithm*. Retrieved 2024, from https://www.mathworks.com/help/gads/ga.html
178. Kutz, J. N., Brunton, S. L., Brunton, B. W., & Proctor, J. L. (2016). *Dynamic mode decomposition*. Society for Industrial; Applied Mathematics. https://doi.org/10.1137/1.9781611974508
179. Schmid, P. J. (2010). Dynamic mode decomposition of numerical and experimental data. *Journal of Fluid Mechanics*, *656*, 5–28. https://doi.org/10.1017/S0022112010001217
180. Le Clainche, S., & Ferrer, E. (2018). A reduced order model to predict transient flows around straight bladed vertical axis wind turbines. *Energies*, *11*(3). https://doi.org/10.3390/en11030566
181. Hamilton, N., Viggiano, B., Calaf, M., Tutkun, M., & Cal, R. B. (2018). A generalized framework for reduced-order modeling of a wind turbine wake. *Wind Energy*, *21*(6), 373–390. https://doi.org/10.1002/we.2167
182. Le Clainche, S., Lorente, L. S., & Vega, J. M. (2018). Wind predictions upstream wind turbines from a lidar database. *Energies*, *11*(3). https://doi.org/10.3390/en11030543
183. Kleine, V. G., Kleusberg, E., Hanifi, A., & Henningson, D. S. (2019). Tip-vortex instabilities of two in-line wind turbines. *Journal of Physics: Conference Series*, *1256*(1), 012015. https://doi.org/10.1088/1742-6596/1256/1/012015
184. Verhulst, C., & Meneveau, C. (2014). Large eddy simulation study of the kinetic energy entrainment by energetic turbulent flow structures in large wind farms. *Physics of Fluids*, *26*, 025113. https://doi.org/10.1063/1.4865755

185. Bastine, D., Witha, B., Wächter, M., & Peinke, J. (2015). Towards a simplified dynamic wake model using POD analysis. *Energies*, *8*(2), 895–920. https://doi.org/10.3390/en8020895
186. Schmid, P. J. (2022). Dynamic mode decomposition and its variants. *Annual Review of Fluid Mechanics*, *54*, 225–254. https://doi.org/10.1146/annurev-fluid-030121-015835
187. Le Clainche, S., & Vega, J. M. (2017). Higher order dynamic mode decomposition. *SIAM Journal on Applied Dynamical Systems*, *16*(2), 882–925. https://doi.org/10.1137/15M1054924
188. Le Clainche, S., Mao, X., & Vega, J. M. (2019). New method to capture traveling waves in flow passing a wind turbine. *Wind Energy*, *22*(7), 922–931. https://doi.org/10.1137/15M1054924
189. Takens, F. (1981). Detecting strange attractors in turbulence. *Dynamical Systems and Turbulence, Lecture Notes in Mathematics*, *898*, 366–381. https://doi.org/10.1007/BFb0091924
190. Begiashvili, B., Groun, N., Garicano-Mena, J., Le Clainche, S., & Valero, E. (2023). Data-driven modal decomposition methods as feature detection techniques for flow problems: A critical assessment. *Physics of Fluids*, *35*(4), 041301. https://doi.org/10.1063/5.0142102
191. Vega, J. M., & Le Clainche, S. (2020). *Higher Order Dynamic Mode Decomposition and Its Applications*. Elsevier. https://doi.org/10.1016/C2019-0-00038-6
192. Chen, K., Tu, J., & Rowley, C. (2012). Variants of dynamic mode decomposition: Boundary condition, Koopman, and Fourier analyses. *Journal of Nonlinear Science*, *22*(6), 887–915. https://doi.org/10.1007/s00332-012-9130-9
193. Le Clainche, S., Izbassarov, D., Rosti, M., Brandt, L., & Tammisola, O. (2020). Coherent structures in the turbulent channel flow of an elastoviscoplastic fluid. *Journal of Fluid Mechanics*, *888*, A5. https://doi.org/10.1017/jfm.2020.31
194. El-Asha, S., Zhan, L., & Iungo, G. V. (2017). Quantification of power losses due to wind turbine wake interactions through scada, meteorological and wind lidar data. *Wind Energy*, *20*(11), 1823–1839. https://doi.org/10.1002/we.2123
195. Sarmast, S., Dadfar, R., Mikkelsen, R. F., Schlatter, P., Ivanell, S., Sørensen, J. N., & Henningson, D. S. (2014b). Mutual inductance instability of the tip vortices behind a wind turbine. *Journal of Fluid Mechanics*, *755*, 705–731. https://doi.org/10.1017/jfm.2014.326
196. Pierella, F., Krogstad, P.-Å., & S, L. (2014). Blind test 2 calculations for two in-line model wind turbines where the downstream turbine operates at various rotational speeds. *Renewable Energy*, *70*, 62–77. https://doi.org/10.1016/j.renene.2014.03.034
197. Richard, A. (2015). *University of Oxford Advanced Research Computing (ARC)*. 10.5281/zenodo.22558
198. Smyth, A. S. M. (2020). *Three-dimensional unsteady hydrodynamics of tidal turbines* [Doctoral dissertation, University of Cambridge]. https://doi.org/10.17863/CAM.48853